Final Technical Report

Title:
Hangman Catalysis for Photo–and Photoelectro–Chemical Activation of Water Proton-Coupled Electron Transfer Mechanisms of Small Molecule Activation

DOE Award No.:
DE–SC0009758

Period of Performance:
15 March 2013 to 14 March 2017

Journal of Porphyrins and Phthalocyanines
J. Porphyrins Phthalocyanines 2014; **18**: 1–8
DOI: 10.1142/S1088424614501016

Published at http://www.worldscinet.com/jpp/

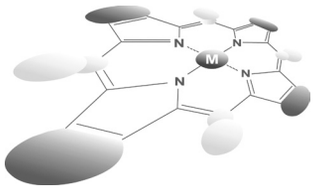

Proton-coupled electron transfer chemistry of hangman macrocycles: Hydrogen and oxygen evolution reactions

Dilek K. Dogutan◊, D. Kwabena Bediako, Daniel J. Graham, Christopher M. Lemon and Daniel G. Nocera*◊

Department of Chemistry and Chemical Biology, Harvard University, 12 Oxford Street, Cambridge, Massachusetts 02138, United States

Dedicated to Professor Shunichi Fukuzumi on the occasion of his retirement

Received 23 September 2014
Accepted 6 October 2014

ABSTRACT: The splitting of water into its constituent elements is an important solar fuels conversion reaction for the storage of renewable energy. For each of the half reactions of the oxygen evolution reaction (OER) and hydrogen evolution reaction (HER), multiple protons and electrons must be coupled to avoid high-energy intermediates. To understand the mechanistic details of the PCET chemistry that underpins HER and OER, we have ~~been~~ designed hangman porphyrin and corrole catalysts. In these hangman constructs, a pendant acid/base functionality within the secondary coordination sphere is "hung" above the macrocyclic redox platform on which substrate binds. The two critical thermodynamic properties of a PCET event, the redox potential and pK_a may be tuned with the macrocycle and hanging group, respectively. This review outlines the synthesis of these catalysts, as well as the examination of the PCET kinetics of hydrogen and oxygen evolution by the hangman catalysts. The insights provided by these systems provide a guide for the design of future HER and OER catalysts that use a secondary coordination sphere to manage PCET.

KEYWORDS: porphyrin, corrole, catalyst, hangman effect, proton-coupled electron transfer (PCET), hydrogen evolution, oxygen evolution, renewable, solar fuels.

INTRODUCTION

The generation of fuels from solar en[illegible] rearrangement of stable chemical bonds with light as the impetus for the fuel-forming reaction. All such transformations of energy consequence require the coupling of protons to an overall multi-electron event. When such coupling is not achieved, large kinetic penalties are associated with the fuel-forming reaction. This is most easily seen for the seemingly simplest of chemical transformations, the reduction of protons to dihydrogen. If this reduction proceeds by sequential *one*-electron steps that are *uncoupled* from the proton, then the reaction confronts a large energetic barrier. On the NHE reference scale, the first reduction proceeds with an uphill potential of 2.3 V; the addition of a second electron and proton then proceeds with a downhill potential of 2.3 V [1, 2]. This is schematically illustrated in Fig. 1. Despite an overall thermodynamic potential of 0 V, the half-reaction confr[illegible]3 V energy barrier if the protons are not coupled to the two-electron process. A catalyst can mediate the coupling of protons to electrons; ~~as well as~~ the catalyst ~~does~~ so, leads to a reduction of the barrier shown in Fig. 1. More generally, this is true of any PCET reaction involving a small molecule substrate. Hence the efficiency of a solar-to-fuels transformation effectively reduces to an issue of catalyst design and the ability of the catalyst to manage PCET.

the ability of

to do

The coupling of the electron to the proton is difficult because, unlike electrons, which can tunnel over long distances, the 2000-fold more massive proton can only

◊SPP full member in good standing

*Correspondence to: Daniel G. Nocera, email: dnocera@fas.harvard.edu, tel: +1 617-495-8904, fax: +1 617-496-0265

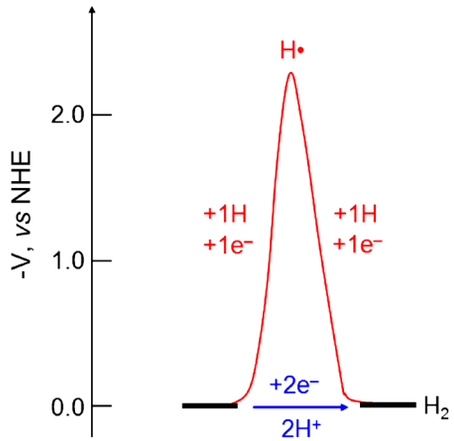

Fig. 1. Energetics for H_2 generation in the absence of PCET

tunnel over very short distances [3]. Despite this inherent quantum mechanical difference between the two particles, they must both tunnel together for their coupling [3–8]. To achieve this coupling, we have developed catalysts in which the secondary coordination sphere is engineered to manage protons and the primary coordination sphere is engineered to manage electrons. By coupling short proton hops to substrates bound to a redox cofactor, PCET activation of the bound substrate may be achieved.

We have designed the hangman macrocycles shown in Fig. 2 to examine the hydrogen evolution reaction (HER), the oxygen evolution reaction (OER) and the oxygen reduction reaction (ORR). The hangman constructs utilize a pendant acid/base functionality within the secondary coordination sphere that is "hung" above the redox platform onto which substrate binds. In this way, we can precisely control the delivery of a proton to the substrate, thus ensuring efficient coupling between the proton and electron. We have examined hangman catalysis with electrochemical techniques to construct a unified mechanistic PCET framework to describe O–O, O–H and H–H bond-breaking and bond-making processes as they pertain to HER and OER processes. This article will present a summary of our efforts to: (1) adapt and elaborate synthetic methods to enable the delivery of hangman macrocycles in sufficiently high yields and quantities to enable PCET studies to be undertaken with facility; (2) design hangman macrocyclic platforms that promote HER with an emphasis on elucidating key intermediates *via* the construction of mechanistic models; and (3) design a hangman macrocycle that promotes OER.

EFFICIENT SYNTHESIS OF HANGMAN PLATFORMS

High yielding syntheses of hangman porphyrins and corroles are needed if PCET studies are to be performed with facility. Our methods have transformed hangman catalyst platforms from difficult-to-make substances, obtained in milligram quantities, to high yielding compounds that can now be made on the hundreds of milligram scale. These compounds thus have been transformed from isolated curiosities to compounds of sufficient quantity for us to undertake PCET studies that are not encumbered by the availability of catalyst.

Hangman porphyrins

The library of metalated hangman porphyrins shown in Fig. 3 was synthesized [9–11, ~~15~~] using refined high-dilution Lindsey reaction conditions [12] and modifications to established procedures. A mixed aldehyde condensation of pyrrole in chloroform in the presence of a Lewis acid furnished the corresponding porphyrinogen intermediate as a result of intermolecular cyclization. *In situ* $6e^-/6H^+$ chemical oxidation of the latter with DDQ afforded the hangman porphyrin with a methyl ester hanging group. Acidic or basic hydrolysis of the methyl ester to the corresponding carboxylic acid

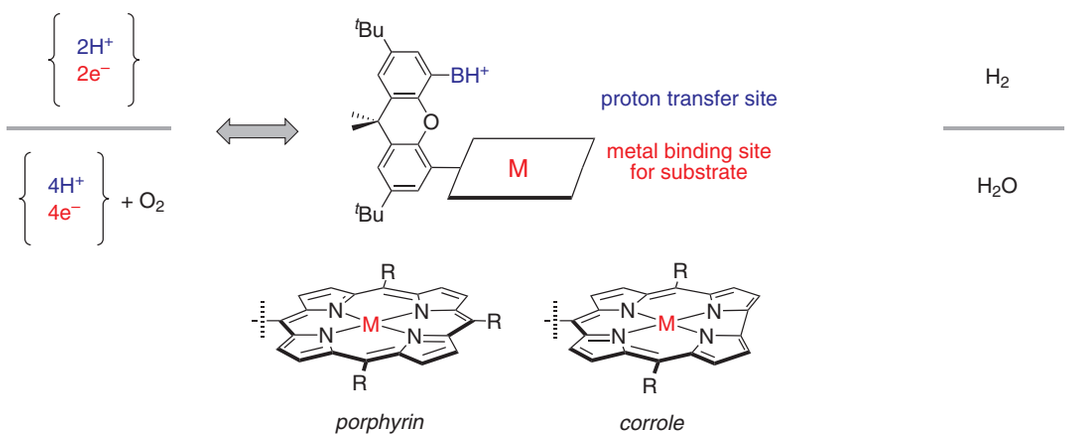

Fig. 2. Hangman platforms permit the study of ~~the~~ PCET mechanisms of HER and OER processes

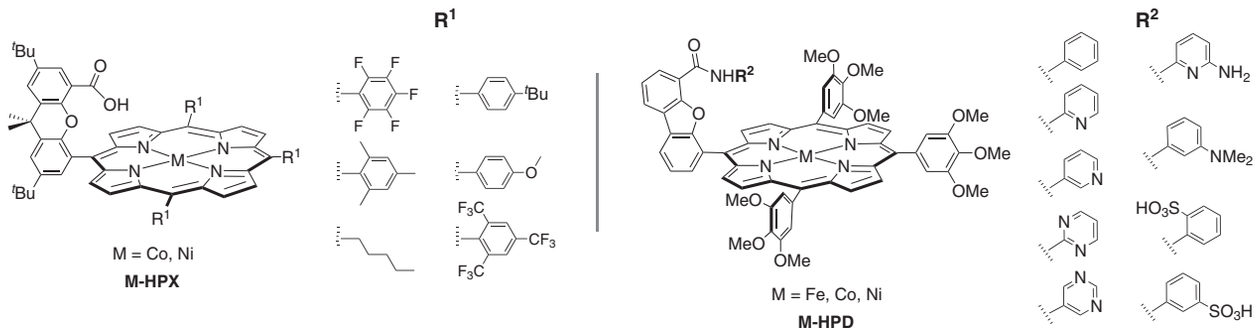

Fig. 3. Hangman porphyrins used in PCET studies for HER and ORR

with conventional heating proceeded with extremely poor yields [13,14]. We found that the introduction of microwave irradiation promoted hydrolysis to overcome this major hurdle confronting general hangman synthesis [15]. Deprotection of the methyl ester group with microwave irradiation was achieved in 6 N NaOH solution with more than 90% yield for the porphyrins shown in Fig. 3. Microwave irradiation also promoted the metalation of free base porphyrins in nearly quantitative yield. The statistical synthesis afforded the target metalloporphyrins in more than 35% overall isolated yield, which is 9× greater yield than our previous methods [15].

Hangman studies have recently been expanded from a xanthene spacer (**HPX**, Fig. 3) to include a dibenzofuran backbone (**HPD**, Fig. 3) [~~16~~]. The larger cleft allowed for the accommodation of a diverse set of hanging groups possessing different steric and acid/base properties. The key step in obtaining the **HPD** library relied on the synthesis of a dibenzofuran precursor that contained an aldehyde functionality and a protected carboxylic acid (methyl ester). The chemistry was carried out in four steps on a decagram scale in 37% overall isolated yield. Using this precursor, the corresponding hangman porphyrins with a hanging carboxylic acid can be obtained in gram quantities. The hanging carboxylic acid on the free base hangman porphyrin was post-synthetically modified to form a carboxamide linker to which the acid/base group was attached. Microwave-assisted metalation furnished the **M-HPD** compounds in good yields.

Hangman corroles

Hangman corroles are attractive candidates for OER chemistry because the π-rich trianionic corrole stabilizes metals in higher oxidation states better than porphyrins do [16, 17]. Furthermore, electron-withdrawing substituents shift the reduction potential of the metal positively. This motivated us to synthesize a new class of compounds — hangman corroles bearing fluorinated β-pyrrolic positions (**Co-H^{F}CX**) [18] *via* the Lindsey [12] and Gryko [19] methods outlined in Scheme 1. The Gryko conditions ~~also delivered~~ were also used to deliver the non-fluoro analog (**Co-HCX**) and had the added advantage of allowing us to enforce the *trans*-A_2B isomer, thus enabling us to establish the regiochemistry of the corrole [20–22]. Deprotection and metalation steps were driven efficiently by microwave irradiation conditions, allowing us to obtain the corroles in 29% overall yield.

HER BY HANGMAN PORPHYRINS

Proton relays are an emerging theme in HER catalysis [23–29]. Key factors that define the kinetics associated with the proton relay are: (i) the pK_a of the metal ion, (ii) the pK_a of the pendant hangman relay, and (iii) the proton transfer distance. The proton can participate in the PCET reaction by stepwise ET and PT steps during catalysis or in a concerted proton-electron transfer (CPET).

We have ascertained the PCET mechanism from electrochemical studies of catalysis, complemented by CV simulation. Heterogeneous ET rate constants ($k_{ET}°$) associated with the electron transfer to the hangman porphyrins have been obtained from "trumpet plots" [30]. Increasing separation between cathodic and anodic peak potentials with scan rate is indicative of deviation from strictly Nernstian (reversible) behavior. Accordingly, the degree of separation for a given scan rate relies on $k_{ET}°$. In the strictly electrochemically irreversible region, the cathodic peak potential is defined by [31]:

$$E_{p,c} = E^{\circ} - 0.78\frac{RT}{aF}\ln\left(k^{\circ}_{ET}\sqrt{\frac{RT}{aF\nu D}}\right) \qquad (1)$$

where α is the transfer coefficient. Complete reversibility is occasionally not attained because of instrumental limitations or the presence of a very fast ET process. In this case, no explicit analytical expression exists for the transitional behavior, but CV simulation software, such as DigiElch [31] provides a reliable means of determining $k_{ET}°$. Beyond simple ET from the electrode, the current and potential dependencies of the catalytic HER wave sheds light on the PCET mechanism for H_2 evolution. There are

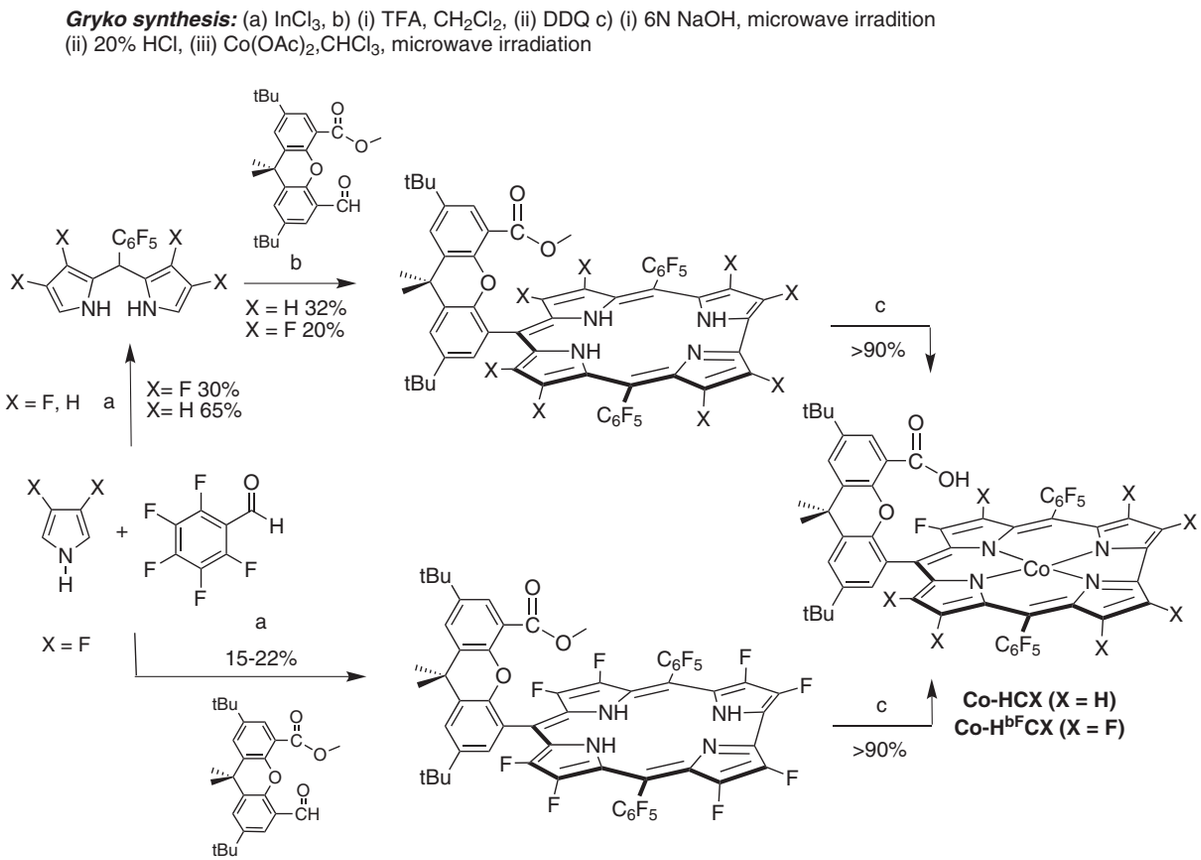

Scheme 1. Synthesis of hangman corroles

two major regimes for catalysis [31]: (i) total-catalysis and (ii) no-substrate-consumption regimes. Case (i) is revealed by a sharp catalytic peak, with a peak potential, E_p, that relates to the catalytic rate constant, k_{cat} by:

$$E_p = E^0_{cat} - 0.409\frac{RT}{F} + \frac{RT}{F}\ln\left(\frac{\mathrm{RT}k_{cat}[\mathrm{cat}]^2}{F\nu[\mathrm{acid}]}\right) \quad (2)$$

where [cat] and [acid] are the bulk concentration of the catalyst and acid, respectively, v is the scan rate, and R, T, and F have their usual meaning. E^0_{cat} represents the reversible catalyst redox couple. In contrast, when catalysis is governed by case (ii), the kinetics parameters may be extracted from the plateau current i_{plat},

$$i_{plat} = \mathrm{FA[cat]}\sqrt{Dk_{cat}[\mathrm{acid}]} \quad (3)$$

where D represents the diffusion coefficient of the acid. By using Equations 1–3, together with CV simulation of catalytic data, we have identified the catalytic PCET mechanism with accompanying rate constants of HER for Co, Ni and Fe hangman porphyrins, and begun unveiling the precise role of the proton relay in HER conversions.

Co hangman porphyrins

We have shown that **Co-HPX** (Fig. 3) catalyzes HER from weak (benzoic) and strong (tosic) acids in acetonitrile solutions [33]. Electrochemical analysis indicated that, regardless of the strength of acid, Co^{II}–H is exclusively involved in the generation of H_2. As summarized in Fig. 4, in weak acid, a Co^0 center is protonated; in strong acid, the Co^I center is protonated and subsequently reduced to deliver the Co^{II}–H. The same result was obtained for other Co macrocycles (*i.e.* tetraazamacrocycle) as well [34]. The mechanisms on the right side of Fig. 4, ~~which is~~ at odds with the more common notion that H_2 is produced from a Co^{III}–H [35], is in line with recent experimental [36, 37] and theoretical [38] findings that Co^{II}–H is the critical intermediate for H_2 generation.

Electrokinetic mechanistic studies of HER are consistent with formation of the Co^{II} hydride by stepwise electron-transfer followed by proton transfer (ET-PT) [39]. The rate constants for the heterogeneous electron transfer to the hangman porphyrin are summarized in Fig. 5. Catalytic enhancement by the hangman moiety arises from a rapid intramolecular rate-limiting PT (*ca.* 8.5×10^6 s^{-1}). This is the first *direct* measure of a proton

(a) *longstanding mechanism:*

$PCo(II) + e^- \longrightarrow [PCo(I)]^-$

$[PCo(I)]^- + H^+ \longrightarrow PCo(III)H$

$PCo(III)H + H^+ \longrightarrow [PCo(III)]^+ + H_2$

$[PCo(III)]^+ + e^- \longrightarrow PCo(II)$

(b) *weak acid:*

$PCo(II) + e^- \longrightarrow [PCo(I)]^-$

$[PCo(I)]^- + e^- \longrightarrow [PCo(0)]^{2-}$

$[PCo(0)]^{2-} + H^+ \longrightarrow [PCo(II)H]^-$

$[PCo(II)H]^- + H^+ \longrightarrow PCo(II) + H_2$

strong acid:

$PCo(II) + e^- \longrightarrow [PCo(I)]^-$

$[PCo(I)]^- + H^+ \longrightarrow PCo(III)H$

$PCo(III)H + e^- \longrightarrow [PCo(II)H]^-$

$[PCo(II)H]^- + H^+ \longrightarrow PCo(II) + H_2$

Fig. 4. (a) Typical mechanism proposed for H_2 generation from Co centers. (b, c) Mechanism for H_2 generation by **Co-HPX** complexes, as determined from electrochemical kinetics analysis

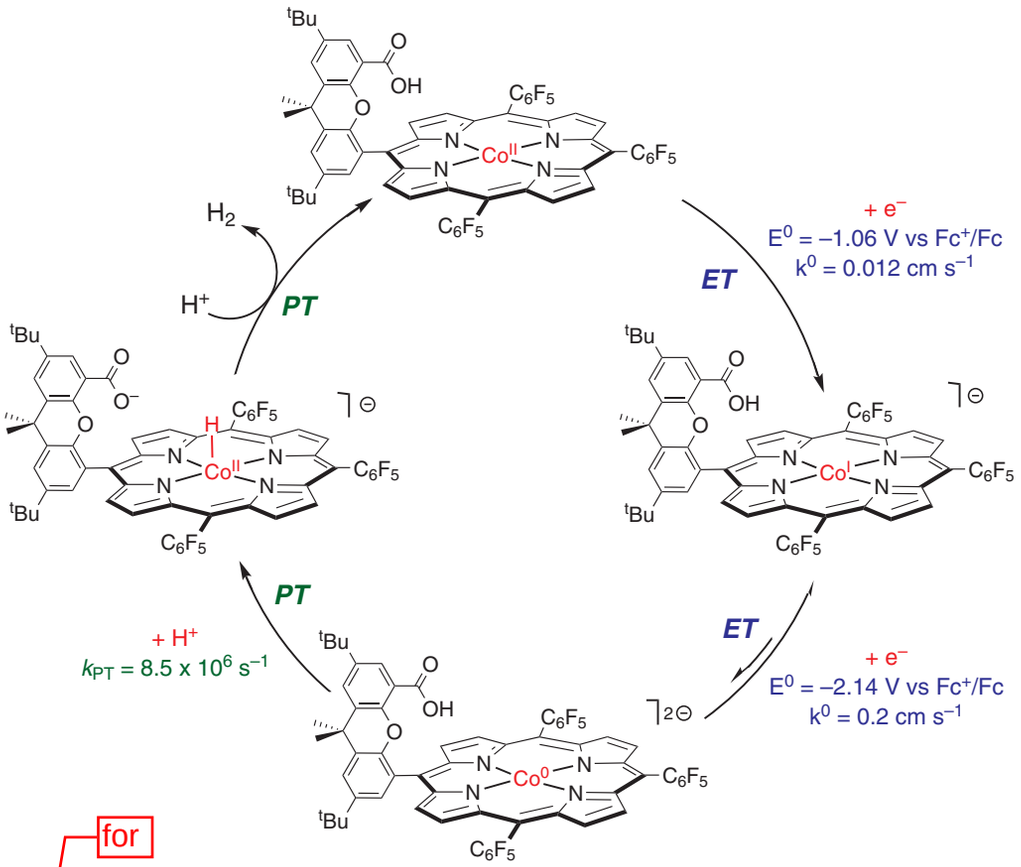

Fig. 5. The rate constants for the PCET mechanism of HER by **Co-HPX**

transfer rate in a HER conversion. Moreover, construction of working curves for a non-hangman congener revealed that the intermolecular (2nd order) proton transfer from benzoic acid to a porphyrin lacking the hanging group proceeded with a rate constant of 1000 $M^{-1}.s^{-1}$. These results indicate that the presence of the pendant proton relay proximate to the metal center gives rise to a rate enhancement that is equivalent to an effective benzoic acid concentration >3000 M. This is the first quantitative measurement of the benefits of a pendant proton transfer in the secondary coorination sphere of a HER catalyst.

Ni hangman porphyrins

The PCET mechanism may be altered owing to the differences in the d-electron count and hence the thermodynamics of proton transfer as has been been computationally discussed [40]. Accordingly, we have targeted Ni hangman porphyrins in order to interrogate the manner in which metal substitution impacts the PCET pathway and kinetics of H_2 production [41]. Because we are able to make the compounds on large scale, we have been able to crystallize the porphyrins, allowing for their structural characterization; the **Ni-HPX** (*meso*-C_6F_5) crystal structure is shown in Fig. 6. Thus structural metrics are available for interpreting the PCET kinetics with this system.

Cyclic voltammetry (CV) of **Ni-HPX** (*meso*-C_6F_5) reveals a shift of the catalytic wave by more than 100 mV to lower overpotential when compared to **Co-HPX** (*meso*-C_6F_5) [33]. This result is indicative of significantly faster catalysis. The CV data and attendant

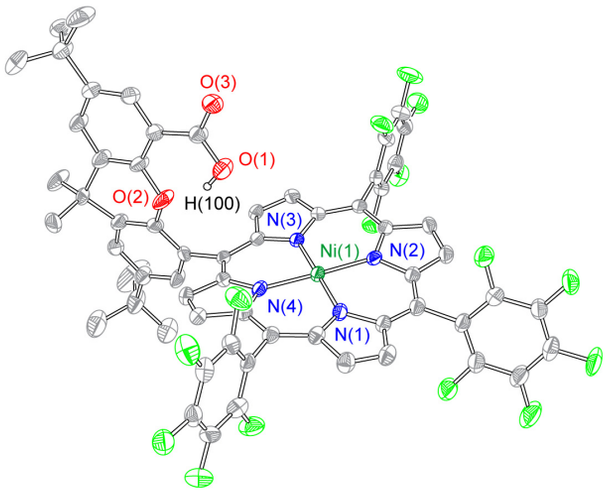

Fig. 6. Crystal structure of **Ni-HPX** with thermal ellipsoids set at 50% probability; hydrogen atoms and crystallization solvents have been omitted for clarity

simulations together with density functional theory (DFT) computational studies are consistent with the occurrence of a stepwise PT followed by ET (PTET) pathway, involving the formation of a formally $Ni^{III}H$, which is subsequently reduced to $Ni^{II}H$. Operation *via* this pathway (involving the protonation of the metal(I) complex as opposed to the metal(0) complex) explains the improved activity of this catalyst relative to its cobalt analog. DFT calculations show that upon reduction of the Ni^{II} complex by one electron, the spin density on Ni is near unity, suggesting that the unpaired electron is localized on the Ni center [41]. Similar calculations on the doubly reduced (formally Ni^{0}) molecule, however, show that only one electron is localized on Ni, and that the other electron is transferred to orbitals predominantly on the porphyrin ring. The non-innocence of the porphyrin ligand in this particular reduction reaction prompted us to consider that the proton may transfer to the ligand prior to H_2 generation and that a transient phlorin intermediate may be involved in HER. This contention is currently under investigation.

Fe hangman porphyrins

We have expanded our studies to the **Fe-HPD** hangman porphyrins shown in Fig. 3 because they enabled the modular installation of a wide range of pendant acid/base moieties, which are sterically imposing. With a phosphine coordinating to the distal face of the reduced porphyrin, these hangman porphyrins channel protons from solution to the catalyst active site *via* the pendant acid/base group. In our study of the catalytic efficacy of these new hangman porphyrins [10], we employed the foot-of-the-wave analysis (FOWA), developed by Costentin and Savéant [42]. Previously, FOWA had been used to analyze the electrocatalytic reduction of H^+ to H_2 [43] and CO_2 to CO and H_2O using Fe porphyrins in the presence of a Brønsted–Lowry acid [42, 44–46]. The application of FOWA to **Fe-HPD**s allowed us to gain insight into the rate of proton transfer from solution to the active site, turnover frequency, and the effect of a pendant proton donor. We found that the steric bulk of the hanging group modulates its pK_a effect. Specifically, the [illegible] acid derivative (strongest acid) was the most active at high acid concentrations. However, at low acid concentrations, the hanging *N*,*N*-dimethylanilinium, though a weaker proton donor, showed higher activity because it was protonated and hence effectively increased the local acid concentration at the Fe center. These are interesting because in cases where H_2 evolution represents a parasitic side reaction, such as carbon dioxide reduction [47, 48], nitrite reduction [49–51] and olefin reduction [52] in acidic solutions, the rate of proton transfer to the catalyst active site might be tailored in order to minimize HER.

OER BY HANGMAN CORROLES

We sought to develop a hangman platform that would allow us to undertake PCET studies of OER. Electrochemical measurements of electron-rich macrocycles, such as mesityl substituted hangmans, showed that they barely had sufficient potential for OER. In order to boost the oxidizing power of the porphyrin subunit, we sought to modify the hangman macrocycle with electron-withdrawing groups. It was known that the introduction of fluorinated phenyl groups onto the *meso*-positions of the porphyrin frameworks increased the reduction potential of oxidized porphyrins by more than 0.4 V [53, 54]. The oxidizing power of the macrocycle can be further augmented by an additional 0.4–0.6 V through fluorination of the β-pyrrole positions [55, 56]. We therefore targeted the design and synthesis of hangman corrole **Co-H$^{\beta F}$CX** (Scheme 1).

Electrochemical experiments established that **Co-$^{\beta F}$HCX** catalyzes water oxidation [18]. The CV (Fig. 7) exhibits two reversible oxidation processes corresponding to the oxidation of the metal center and the corrole ring to produce the corrole cation radical ($corr^{+\bullet}$). Formation of the corrole cation at a redox level of +2 beyond Co(II) corrole was established from EPR studies of an isolated "$Co^{IV}Cl(corr)$", which exhibits hyperfine coupling that is consistent with a $Co^{III}Cl(corr^{+\bullet})$ formulation for the compound [20]. Introduction of a third hole equivalent into the system leads to a catalytic wave for OER. GC traces revealed that only O_2 was produced, and the absence of CO_2 established that the porphyrin did not oxidatively decompose during OER. A steady decrease in pH with no observation of an anomaly also indicated that the catalyst did not decompose to cobalt oxide-like materials, since such species are unstable in acidic solutions. At 1.4 V *vs.* Ag/AgCl, the turnover frequency per Co atom of **Co-$^{\beta F}$HCX** is 0.81 s^{-1}. This

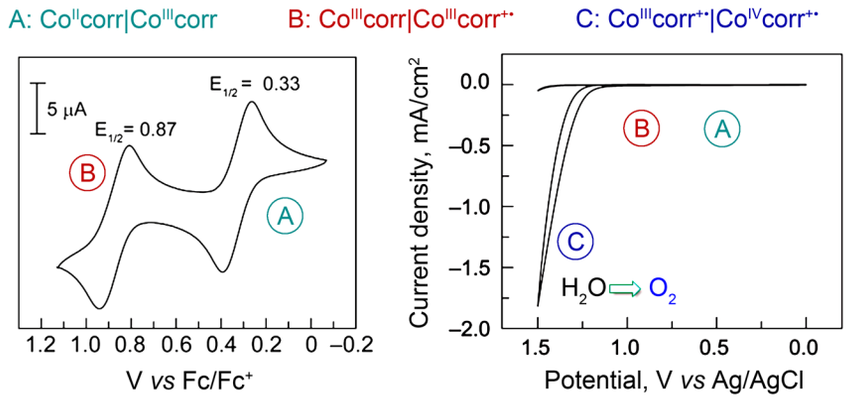

Fig. 7. Cyclic voltammogram of **Co-H^{F}CX** in aqueous solution

number compares favorably with regard to heterogeneous cobalt-based water oxidation catalysts [57].

CONCLUSIONS

Hangman catalysts were created to allow control over proton-coupled electron transfer (PCET) reactions. The hangman constructs utilize a pendant acid/base functionality within the secondary coordination sphere that is positioned above the redox platform onto which substrate binds. On a mechanistic front, the hangman system orthogonalizes PCET and, in doing so, the catalyst permits control of proton transfer over short distances and electron transfer over longer distances. In this way, we can precisely control the delivery of a proton to the substrate, thus ensuring efficient coupling between the proton and electron. Moreover, the two critical thermodynamic properties of a PCET event, the reduction potential and pK_a may be tuned with the macrocycle and hanging group, respectively. By constructing kinetics rate laws using electrochemistry accompanied by simulation, we have begun to develop a unified mechanistic PCET framework to describe O–O, O–H and H–H bond-breaking and bond-making processes, as they pertain to the hydrogen evolution reaction (HER) and the oxygen evolution reaction (OER), the two constituent reactions of the water-to-hydrogen/oxygen fuel forming reaction. To this end, the hangman catalysts offer a unique inroad to providing a succinct framework to guide the design of future HER and OER catalysts that use a secondary coordination sphere to manage PCET.

Acknowledgements

This material is based upon work supported by the U.S. Department of Energy Office of Science, Office of Basic Energy Sciences ~~Energy Frontier Research Centers~~ program under Award Number DE-SC0009758. DJG and CML acknowledge the National Science Foundation (NSF) for Graduate Research Fellowship Program (GRFP) Fellowships.

REFERENCES

1. Stanbury DM. *Adv. Inorg. Chem*. 1989; **33**: 69–138.
2. Schwarz HA. *J. Chem. Ed.* 1981; **58**: 101–105.
3. Cukier RI and Nocera DG. *Annu. Rev. Phys. Chem*. 1998; **49**: 337–369.
4. Mayer JM. *Annu. Rev. Phys. Chem*. 2004; **55**: 363–390.
5. Huynh MVH and Meyer TJ. *Chem. Rev*. 5004–5064.
6. Reece SY and Nocera DG. *Annu. Rev* 2009; **78**: 673–699.
7. Hammes-Schiffer S. *Acc. Chem. Res*. 1881–1889.
8. Hammes-Schiffer S and Stuchebrukhov *Rev*. 2010; **110**: 6939–6960.
9. Lemon CM, Dogutan DK and Nocera DG. In *Handbook of Porphyrin Science*, Vol. 21, Kadish KM, Smith KM and Guilard R. (Eds.) World Scientific Publishing: Singapore, 2012; Chapter 99, pp 1–143.
10. Graham DJ and Nocera DG. *Organometallics* 2014; **33**: 4994–5001.
11. Graham DJ, Zheng S-L and Nocera DG. *ChemSusChem* 2014; **7**: 2449–2452.
12. Lindsey JS and Wagner RW. *J. Org. Chem*. 1989; **54**: 828–836.
13. Rosenthal J, Chng LL, Fried SD and Nocera DG. *Chem. Comm*. 2007; 2642–2644.
14. Chang CJ, Yeh C-Y and Nocera DG. *J. Org. Chem.* 2002; **67**: 1403–1406.
15. Dogutan DK, Bediako DK, Teets TS, Schwalbe M and Nocera DG. *Org. Lett*. 2010; **12**: 1036–1039.
16. Gross Z and Gray HB. *Comm. Inorg. Chem.* 2007; **27**: 61–72.
17. Aviv-Harel I and Gross Z. *Chem. Eur. J.* 2009; **15**: 8382–8394.
18. Dogutan DK, McGuire Jr. R and Nocera DG. *J. Am. Chem. Soc*. 2011; **133**: 9178–9180.
19. Guilard R, Gryko DT, Canard G, Barbe J-M, Koszarna B, Brandès S and Tasior M. *Org. Lett*. 2002; **4**: 4491–4494.

AQ: Please provide the vol. no. Chem Comm did not have volume numbers during this period

111: 15001-15006

20. Dogutan DK, Stoian SA, McGuire Jr. R, Schwalbe M, Teets TS and Nocera DG. *J. Am. Chem. Soc.* 2011; **133**: 131–140.
21. Schwalbe M, Dogutan DK, Stoian SA, Teets TS and Nocera DG. *Inorg. Chem.* 2011; **50**: 1368–1377.
22. Graham DJ, Dogutan DK and Nocera DG. *Chem. Commun*. 2012; **48**: 4175–4177.
23. Helm ML, Stewart MP, Bullock RM, DuBois MR and DuBois DL. *Science* 2011; **333**: 863–866.
24. Appel AM, Pool DH, O'Hagan M, Shaw WJ, Yang JY, DuBois MR, DuBois DL and Bullock RM. *ACS Catal.* 2011; **1**: 777–785.
25. O'Hagan M, Ho M-H, Yang JY, Appel AM, DuBois MR, Raugei S, Shaw WJ, DuBois DL and Bullock RM. *J. Am. Chem. Soc*. 2012; **134**: 19409–19424.
26. Wiedner ES, Appel AM, DuBois DL and Bullock RM. *Inorg. Chem*. 2013; **52**: 14391–14403.
27. Barton BE, Olsen MT and Rauchfuss TB. *J. Am. Chem. Soc*. 2008; **130**: 16834–16835.
28. Wiese S, Kilgore UJ, Ho M-H, Raugei S, DuBois DL, Bullock RM and Helm ML. *ACS Catal*. 2013; **3**: 2527–2535.
29. Barton BE, Olsen MT and Rauchfuss TB. *Curr. Opin. Biotech*. 2010; **21**: 292–297.
30. Costentin C, Robert M, Savéant J-M and Teillout AL. *Proc. Natl. Acad. Sci. U.S.A*. 2009; **106**: 11829–11836.
31. Savéant J-M. *Elements of molecular and biomolecular electrochemistry: An electrochemical approach to electron transfer chemistry*, John Wiley & Sons Inc.: Hoboken, NJ, 2006; Chapter 1, pp 1–75.
32. Rudolf M. *J. Electroanal. Chem.* 2003, **543**: 23–39. DigiElch from Elchsoft under http://www.elchsoft.com.
33. Lee CH, Dogutan DK and Nocera DG. *J. Am. Chem. Soc.* 2011; **133**: 8775–8777.
34. Lee CH, Villagrán D, Cook TR, Peters JC and Nocera DG. *ChemSusChem* 2013; **6**: 1541–1544.
35. Dempsey JL, Winkler JR and Gray HB. *J. Am. Chem. Soc*. 2010; **132**: 1060–1065.
36. Lazarides T, McCormick T, Du P, Luo G, Lindley B and Eisenberg R. *J. Am. Chem. Soc*. 2009; **131**: 9192–9194.
37. Dempsey JL, Brunschwig BS, Winkler JR and Gray HB. *Acc. Chem. Res.* 2009; **42**: 1995–2004.
38. Muckerman JT and Fujita E. *Chem. Commun*. 2011; **47**: 12456–12458.
39. Roubelakis MM, Bediako DK, Dogutan DK and Nocera DG. *Energy Environ. Sci.* 2012; **5**: 7737–7740.
40. Small YA, Dubois DL, Fujita E and Muckerman JT. *Energy Environ. Sci*. 2011; **4**: 3008–3020.
41. Bediako DK, Solis BH, Dogutan DK, Roubelakis MM, Maher AG, Lee CH, Chambers MB, Hammes-Schiffer S and Nocera DG. *Proc. Natl. Acad. Sci. U.S.A*. 2014; ~~DOI: 10.1073/pnas.1414908111~~.
42. Costentin C, Drouet S, Robert M and Savéant J-M. *J. Am. Chem. Soc*. 2012; **134**: 11235–11242.
43. Quentel F and Gloaguen F. *Electrochim. Acta* 2013; **110**: 641–645.
44. Costentin C, Drouet S, Robert M and Savéant J-M. *Science* 2012; **338**: 90–94.
45. Costentin C, Robert M and Savéant J-M. *Chem. Soc. Rev*. 2013; **42**: 2423–2436.
46. Costentin C, Drouet S, Passard G, Robert M and Savéant J-M. *J. Am. Chem. Soc*. 2013; **135**: 9023–9031.
47. Rail MD and Berben LA. *J. Am. Chem. Soc*. 2011; **133**: 18577–18579.
48. Kang P, Cheng C, Chen Z, Schauer CK, Meyer TJ and Brookhart M. *J. Am. Chem. Soc*. 2012; **134**: 5500–5503.
49. Buffington LA, Blackburn DW, Hamilton CL, Jarvis TC, Knowles JJ, Lodwick PA, McAllister LM, Neidhart DJ and Serumgard JL. *J. Am. Chem. Soc.* 1989; **111**: 2451–2454.
50. Brylev O, Sarrazin M, Roué L and Bélanger D. *Electrochim. Acta* 2007; **52**: 6237–6247.
51. Uyeda C and Peters JC. *J. Am. Chem. Soc.* 2013; **135**: 12023–12031.
52. Rasnoshik H, Masarwa A, Cohen H, Zilbermann I, Maimon E and Meyerstein D. *Dalton Trans*. 2010; **39**: 823–833.
53. Neya S and Funasaki N. *J. Heterocyclic Chem*. 1997: **34**: 689–690.
54. Woller EK and DiMagno SG. *J. Org. Chem*. 1997; **62**: 1588–1593.
55. Kadish KM, Van Caemelbeck E and Royal G. In *The Porphyrin Handbook*, Vol. 8, Kadish KM, Smith KM and Guilard R. (Eds.) Academic Press: San Diego, 2000; pp 1–114.
56. Steene E, Dey A and Ghosh A. *J. Am. Chem. Soc.* 2003; **125**: 16300–16309.
57. Jiao F and Frei H. *Angew. Chem. Int. Ed*. 2009; **48**: 1841–1844.

ACS Catalysis

Research Article

pubs.acs.org/acscatalysis

Hydrogen Evolution Catalysis by a Sparsely Substituted Cobalt Chlorin

Andrew G. Maher,[†,‡] Guillaume Passard,[†,‡] Dilek K. Dogutan,[†] Robert L. Halbach,[†] Bryce L. Anderson,[†] Christopher J. Gagliardi,[†] Masahiko Taniguchi,[§] Jonathan S. Lindsey,*[,§] and Daniel G. Nocera*[,†]

[†]Department of Chemistry and Chemical Biology, Harvard University, 12 Oxford Street, Cambridge, Massachusetts 02138, United States

[§]Department of Chemistry, North Carolina State University, Raleigh, North Carolina 27695, United States

Supporting Information

ABSTRACT: A sparsely substituted chlorin macrocycle containing a Co(II) center (**1-Co**) has been synthesized and structurally characterized. The Co(II) atom resides in a square planar coordination environment and induces significant out-of-plane distortion of the chlorin macrocycle. The paramagnetic Co(II) center resides in the macrocycle in a $S = {}^1/_2$ spin state, which displays an axial doublet signal ($g_\perp \approx 2.3$ and $g_\parallel \approx 2.03$) in the X-band EPR spectrum. The open-shell d-orbital configuration is manifest in the transient absorption spectrum, which reveals an excited-state lifetime of 8.6 ± 0.2 ps for **1-Co**. The Co(II) chlorin exhibits a rich oxidation−reduction chemistry with five reversible one-electron waves (three oxidative processes and two reductive processes) observed in the cyclic voltammogram. The reduction processes of **1-Co** drive hydrogen evolution catalysis. Electrochemical kinetics analysis of HER by **1-Co** in trifluoroacetic acid reveals a hydrogen evolution mechanism that proceeds by an ECEC mechanism. Benchmarking the catalytic activity, **1-Co** exhibits higher HER activity at low overpotentials, versus its porphyrin congeners.

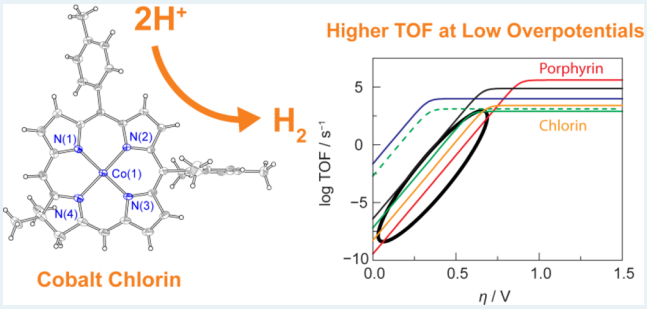

KEYWORDS: *electrocatalysis, macrocycle, chlorin, cobalt, hydrogen evolution reaction, solar fuels*

INTRODUCTION

The macrocyclic ring of chlorins is reduced by two electrons and two protons, relative to its parent porphyrin structure. The reduction occurs at the β-pyrrolic periphery of the macrocycle and thereby preserves an aromatic 18 π-electron conjugated pathway (Chart 1). Structural data of chlorin macrocycles are consistent with this electronic formulation, as the β,β'-bond external to the 18 π-electron network exhibits a C−C distance that is consistent with a more localized π-bond.[1] Hence, the macrocyclic core of chlorins is electronically similar but chemically reduced relative to porphyrins. In view of the exceptional catalytic activity of porphyrins in promoting reductive processes, such as the hydrogen evolution reaction (HER) and the oxygen reduction reaction (ORR),[2] chlorins have presented an interesting new class of catalysts for the activation of small molecules of energy consequence. The extensive literature on the redox properties and reaction chemistry of porphyrins[2−5] is contrasted by a limited number of studies on the electrochemistry of nickel[6,7] and iron[8,9] chlorins. A cobalt chlorin featuring chlorophyll-like substituents is reported to catalyze the two-electron reduction of dioxygen (O_2) to produce hydrogen peroxide (H_2O_2) chemically at activities higher than that observed for cobalt porphyrins,[10,11] which typically drive ORR to H_2O as opposed to H_2O_2. The same cobalt chlorin has been reported to produce H_2 photochemically at the potential of the photoproduced $Ru(bpy)_3^+$ reductant.[12] The potential dependence of the HER catalysis of chlorins remains undefined, especially with regard to how catalytic activity is influenced by potential.

Chart 1. π-Electron Networks in Chlorins and Porphyrins

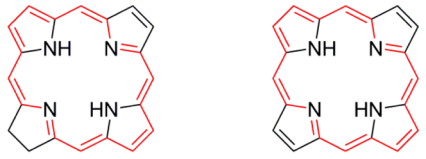

Chlorin Porphyrin

The study of chlorins has been facilitated by advances in the synthesis of the macrocycle that feature various substituents in specific patterns.[13] The sparsely substituted chlorin macrocycle **1** (Chart 2) is available from a concise synthesis in appreciable yields[14] to afford material on scales that permit catalysis studies to be undertaken. Moreover, the gem-dimethyl group in the

Received: March 24, 2017
Published: April 10, 2017

DOI: 10.1021/acscatal.7b00969
ACS Catal. 2017, 7, 3597−3606

Chart 2. Free Base Chlorin 1 and Co Chlorin 1-Co

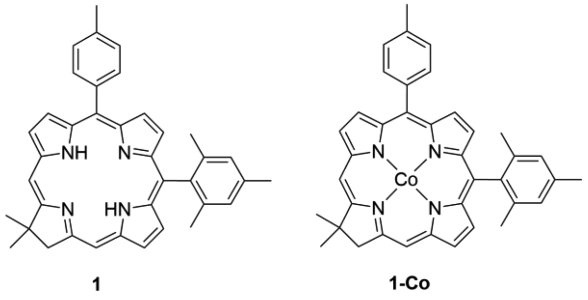

pyrroline ring bestows stability to the chlorin by preventing adventitious dehydrogenation to the porphyrin. We now report the insertion of Co into the chlorin to furnish **1-Co** (Chart 2), which has been structurally characterized. Inasmuch as there are few structurally characterized simple metal chlorin complexes,[15] a comparison of the crystal structure of **1-Co** with that of sparsely substituted chlorin macrocycles furnishes insight into the structural perturbation induced by a centrally chelated metal ion. **1-Co** exhibits a rich redox chemistry, and the various redox species have been correlated to their steady-state and transient electronic spectra. We establish that the redox chemistry of **1-Co** is manifest to an active HER catalysis in the presence of trifluoroacetic acid (TFA). The complex is stable to oxygen, but is unstable in the presence of acid as a promoter of ORR. **1-Co** exhibits a higher turnover frequency for HER catalysis at low overpotentials than its porphyrin congeners, likely due to the increased basicity of the chlorin macrocycle.

RESULTS AND DISCUSSION

Preparation and Characterization of 1-Co. The free base chlorin **1** is delivered by a *de novo* synthetic route.[14] The *de novo* route builds the chlorin from pyrrolic constituents, rather than relying on the more prevalent route wherein a porphyrin is converted to a chlorin.[16] A modified procedure was used to insert Co(II) into the macrocycle.[17] The metalation proceeds quantitatively over 48 h upon treatment of **1** with an 82 mol excess of $Co(OAc)_2$ in CH_2Cl_2/CH_3OH (4:1) mixtures under anaerobic conditions in a glovebox. The metalation of the chlorin is evident by the paramagnetic broadening of the ^1H NMR resonances (Figure S1a in the Supporting Information), which stand in contrast to the sharp resonances observed in the ^1H NMR spectrum of **1** (Figure S1b in the Supporting Information), and the FTIR spectrum. For the latter, the N−H stretching vibration at 3343 cm^{-1} in free base chlorin **1**, which is similar to that for free base porphyrins (3310−3326 cm^{-1}),[18] disappears upon cobalt insertion (Figure S3 in the Supporting Information). On the basis of similar assignments in free base and nickel porphyrin derivatives,[18] two weak bands between 2750 and 3000 cm^{-1} are assigned to the C−H stretching bands of the meso-carbons, intense vibrations at 1595 and 1620 cm^{-1} are assigned to C═C stretching vibrations, and bands at 1350 cm^{-1} are assigned to C−N stretching vibrations. The formulation of **1-Co** has also been confirmed by LC-MS in the positive-ion mode (Figure S4 in the Supporting Information) with m/z = 605.2211 (for M^+, where M = $C_{38}H_{34}CoN_4$, calcd 605.2115).

The paramagnetic properties of **1-Co**, indicated by the broad peaks in the ^1H NMR spectrum, are verified by the EPR spectrum of the complex (Figure 1). Under anaerobic

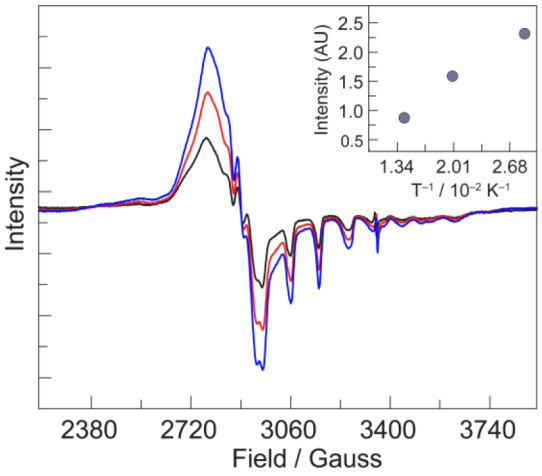

Figure 1. Temperature-dependent EPR spectra (35 K (blue trace), 50 K (red trace), 70 K (black trace)) of **1-Co**.

conditions, **1-Co** exhibits typical EPR signatures for a Co(II) ion in the tetragonal field of the chlorin macrocycle. The X-band EPR spectrum exhibits an axial doublet signal with a quasi-axial g-tensor of $g_\perp \approx 2.3$ and $g_\parallel \approx 2.03$. These g-values are consistent with a low-spin, $S = {}^1/_2$ spin system with the unpaired electron occupying the d_{z^2}-orbital. Strong and well-resolved ^{59}Co hyperfine couplings of 98 G are observed for $A_\parallel$, consistent with other Co(II) macrocycles.[19,20]

Dark green crystals of **1-Co** were obtained by cooling a saturated solution of **1-Co** in pentane at −20 °C. Figure 2 displays the X-ray crystal structure for which the details of structure determination are listed in Table S1 in the Supporting Information. The central Co atom resides in a square planar coordination environment defined by the chlorin macrocycle, which deviates from an ideal planar system. The average Co−N bond distance of the pyrrolic rings is 1.952(3) Å, whereas the

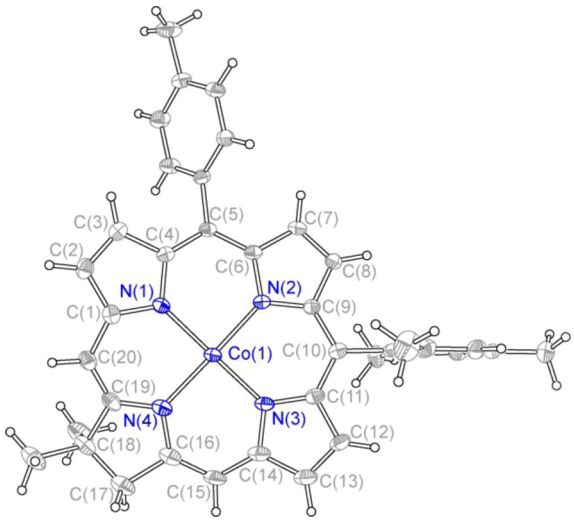

Figure 2. Solid-state structure of **1-Co** with thermal ellipsoids (drawn using SHELX/XP) shown at the 50% probability level. Selected interatomic distances: d(Co1−N1) = 1.9445(17) Å, d(Co1−N2) = 1.9660(17) Å, d(Co1−N3) = 1.9465(18) Å, d(Co1−N4) = 1.9901(18) Å, d(C7−C8) = 1.356(3) Å, d(C17−C18) = 1.520(4) Å. Selected bond angles: ∠(C1−N1−C4) = 104.66(18)°, ∠(C6−N2−C9) = 104.67(17)°, ∠(C11−N3−C14) = 104.82(18)°, ∠(C16−N4−C19) = 107.27(19)°.

DOI: 10.1021/acscatal.7b00969
ACS Catal. 2017, 7, 3597−3606

Co−N bond distance of the pyrroline unit is 1.9901(18) Å. The mesityl substituent is nearly perpendicular (82°) to the mean plane of the macrocycle, whereas the *p*-tolyl substituent is less twisted (51°) (see Figure 2).

The chlorin macrocycle of **1-Co** undergoes significant out-of-plane distortion upon metalation, in contrast to the structure of a related free-base chlorin,[1] **FbC** (analagous to **1** but lacking *meso*-aryl groups), which exhibits an almost-planar macrocycle. The distortions from planarity can be taken into consideration by using the sum of the absolute values of the positive and negative displacements of the N atoms of the chlorin from a plane (defined by the four N atoms).[1] The average out-of-plane distortion of **FbC** is 0.044 Å, whereas the average distortion of **1-Co** is 0.261 Å. Table S2 in the Supporting Information compares the average deviation from planarity to other free-base chlorins as well; in all cases, **1-Co** is more distorted. Metalation also alters the structural metrics of the pyrroline ring, as shown in Table S3 in the Supporting Information; there is a decrease in the C_α−C_β (C16−C17), C_β−C_β (C17−C18), and C_β−C_α (C18−C19) bond distances of the pyrroline ring of **1-Co**, compared to **FbC**. The most notable change in the bond angles between **1-Co** and **FbC** is observed at C17 and C18, where the hybridization changes from sp^2 to sp^3. The bond angles of C16−C17−C18 (103.13(19)°) and C17−C18−C19 (100.27(19)°) in **1-Co** are narrowed by 3.7° and 6.8°, respectively, compared to the corresponding bond angles in **FbC**. Compensation for these narrowed angles (~10.5° in total) in the 5-membered ring occurs by widening of the remaining three angles: C16−N4−C19 (~2.1°), N4−C16−C17 (~1.5°), and C18−C19−N4 (~1.7°). Metalation also leads to a change in the C_α−N−C_α framework bond angles (Table S4 in the Supporting Information), as well as the core shape and core size of the macrocycle (Table S5 in the Supporting Information). As shown in Figure 3, the core size of

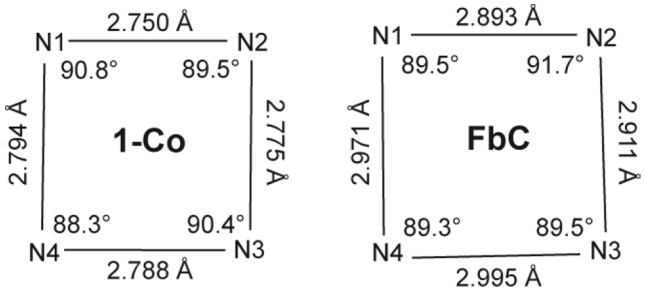

Figure 3. Inner core of sparsely substituted chlorin in the presence and absence of a metal.

1-Co is contracted relative to the free-base species **FbC** and becomes more symmetric upon insertion of Co into the chlorin macrocycle, almost assuming a square, as opposed to the more trapezoidal core of **FbC**. Thus, whereas metal insertion causes the core composed of the four nitrogens to assume a more square-like geometry, there is much greater out-of-plane distortion resulting from the metal insertion.

Another notable structural metric is the bond distance (Table S6 in the Supporting Information) of the pyrrolic C_β−C_β bond C7−C8, which is the double bond external to the 18 π-electron conjugated pathway shown in Chart 1. The C7−C8 double bond of **1-Co** is 1.356(3) Å, which is statistically indistinguishable from the other C_β−C_β bond distances of **1-Co** (C2−C3 = 1.344(3) Å, C12−C13 = 1.345(3) Å), because the differences in bond lengths are not more than three times greater than the estimated standard deviations added in quadrature.[21] A similar comparison of the C7−C8 bond, with respect to the other C_β−C_β bonds, has also been observed in nickel tetramethylchlorin (C7−C8 = 1.362 Å, C2−C3 = 1.353 Å, C12−C13 = 1.351 Å).[15] These results stand in contrast to the trend seen in the free base **FbC**, in which the C7−C8 bond distance of 1.3588(19) Å is shorter than the other C_β−C_β distances (C2−C3 = 1.3704(19) Å, C12−C13 = 1.3680(19) Å) to a statistically significant extent. The shortening of the C7−C8 bond in the free base chlorin could be a manifestation of the exclusion of that bond from the extended π-electron network in order to avoid an antiaromatic 20 π-electron count. In this regard, the lack of shortening of the C7−C8 bond in the metalated chlorins suggests that the presence of the metal center lessens the antiaromaticity of the 20 π-electron network.

The absorption spectra of **1** and **1-Co**, shown in Figure 4, exhibit the signature B (Soret) and Q bands common to

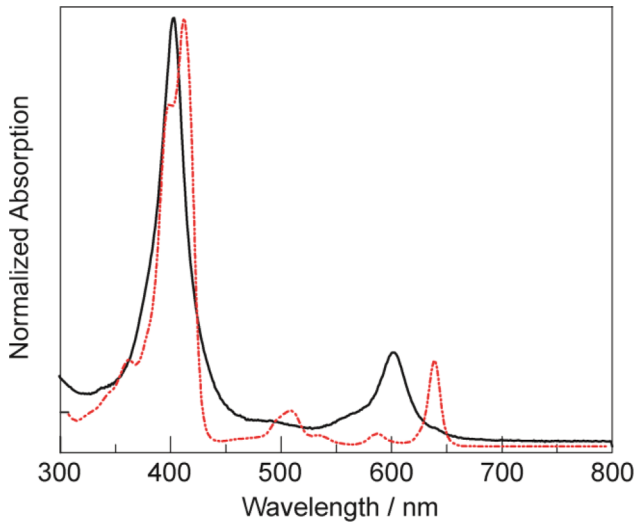

Figure 4. Absorption spectra of **1** (red dotted trace) and **1-Co** (solid black trace) at room temperature in CH_2Cl_2. The spectra are normalized with respect to the Soret band intensities.

tetrapyrrole macrocycles, as well as the enhanced Q-band intensity in the red region particular to chlorins,[22] although the two spectra differ significantly from each other. With respect to the absorption spectrum of **1**, **1-Co** exhibits an ~10 nm hypsochromic shift of the B(0,0) Soret band and an ~40 nm hypsochromic shift of the Q_y(0,0) band. The split in the Soret band of **1**, which is common in free-base chlorins, is due to the partial resolution of the *x*- and *y*-polarized components. The split Soret is not observed for **1-Co**, which is consistent with reports of coalescence of B_x and B_y bands in other metallochlorins, although the exact nature of the relative positioning of the B_x and B_y bands in chlorins is not yet fully understood.[23−25]

Transient Absorption Spectroscopy. The excited state of **1-Co** is short-lived as expected for an open-shell d-orbital metal ion in a π-aromatic system. In the absence of emission, the excited-state dynamics were examined by picosecond transient absorption (TA) spectroscopy. Figure 5 displays the visible light picosecond TA spectrum of **1-Co** in toluene upon excitation with a 400 nm laser pulse at a variety of time delays between <1 and 60 ps. Samples of **1-Co** are indefinitely stable under TA excitation conditions (see Figure S5 in the

DOI: 10.1021/acscatal.7b00969
ACS Catal. 2017, 7, 3597−3606

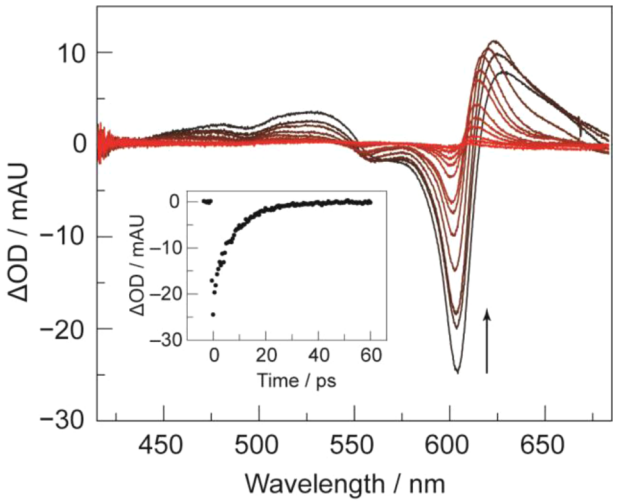

Figure 5. Transient absorption (TA) spectra of **1-Co** at room temperature in toluene at time delays ranging from <1 ps (black) to 60 ps (red), using an excitation wavelength of 400 nm. Inset shows the single wavelength kinetics trace monitored at 604 nm.

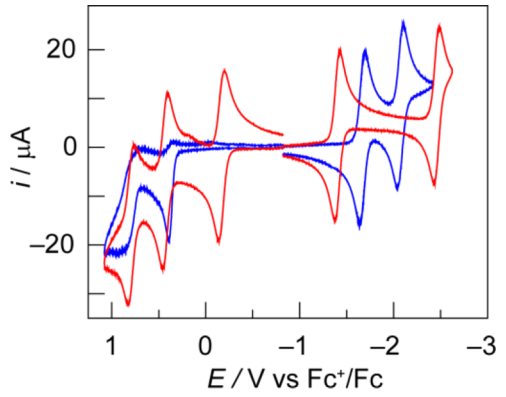

Figure 6. CVs of **1-Co** (red trace) and **1** (blue trace) (1 mM) in CH_3CN (0.1 M $TBAPF_6$) at a scan rate of 0.1 V s^{-1} under an Ar atmosphere with a glassy carbon working electrode (3 mm).

Supporting Information). The transient difference spectrum shows a prompt broad absorption growth (between 425 nm and 550 nm) and bleaches of the ground state Q bands. Additionally, an absorption band slightly to the red of the intense 604 nm ground-state bleach grows in over the first few picoseconds. By 60 ps, the transient spectrum has returned to baseline, indicating that excited **1-Co** completely relaxes back to its electronic ground state during that time interval. A biexponential least-squares fit of the single-wavelength trace at 604 nm (Figure 5 inset) yields time constants of 700 ± 100 fs for the short component decay and 8.6 ± 0.2 ps for the long component decay. A monoexponential fit of the fast growth process at 618 nm yields a time constant of 660 ± 40 fs, which matches the faster component of the biexponential bleach decay at 604 nm. The faster dynamical process is observable for both 400 and 600 nm excitation wavelengths, indicating that it is not due to internal conversion from the $^2B(\pi,^*\pi)$ excited state to the $^2Q(\pi,^*\pi)$ state. Rather, the fast component may reflect vibrational cooling, intersystem crossing to either a doublet $^2T(\pi,^*\pi)$ or quartet $^4T(\pi,^*\pi)$ excited state, or relaxation to a (d,d) or charge-transfer excited state. The 8.6 ps overall excited-state lifetime of the **1-Co** in toluene is similar to those obtained for other Co(II) tetrapyrrole macrocycles such as porphyrins, which typically have lifetimes shorter than 20 ps, attributable to the formation of a low-lying ligand-to-metal charge-transfer (LMCT) state.[26,27] The very short lifetime of **1-Co** is in contrast to the free base and Zn chlorin analogs, which have singlet excited-state lifetimes of 10.7 and 1.6 ns, respectively,[23] underscoring the influence of the open-shell cobalt on the electronic structure of the complex.

Oxidation Reduction Chemistry. Chlorins **1** and **1-Co** exhibit a rich redox chemistry. The cyclic voltammograms (CVs) of **1** and **1-Co**, shown in Figure 6, reveal a number of reductive and oxidative redox processes, all of which are electrochemically reversible in the case of **1-Co**. From the resting state, **1-Co** shows two reduction waves at standard potentials of E^0_{1-} = −1.401 and E^0_{2-} = −2.460 V vs Fc^+/Fc (Figure 6, red line). The compound also exhibits three oxidation waves centered at E^0_{1+} = −0.167, E^0_{2+} = 0.430 and E^0_{3+} = 0.796 V vs Fc^+/Fc. A comparison of the CV of **1-Co** to that of **1** (Figure 6, blue line) shows that the two most negative reduction processes and two most positive oxidative processes are largely associated with the redox chemistry of the chlorin. The E^0_{2+} oxidation process for **1-Co** occurs at a similar potential to the first oxidation of **1**, as well as that of other free base and zinc chlorins,[28] further supporting the assignment of a ligand-centered oxidation. It is interesting to note that while the E^0_{2+} and E^0_{3+} oxidative processes for **1-Co** occur at nearly identical potentials as the two most positive oxidations of **1**, the processes are quasi-reversible for free base **1** but reversible for the metal-containing **1-Co** chlorin. The irreversibility of these oxidation processes in chlorins and isobacteriochlorins has been suggested to stem from oxidative dehydrogenation leading to porphyrin species;[7,29] however, in our case, the presence of geminal methyl groups at the 18 position of the macrocycle makes porphyrin formation unlikely, especially in the absence of a strong acid. The reversibility of the oxidations of **1-Co** suggests that replacing the two *N*-pyrrolic protons with a metal center prevents a ligand-based chemical step, such as deprotonation of the *N*-pyrrolic protons upon oxidation. This contention is supported by the observation that the first oxidation of the analogous Zn chlorin complex, **1-Zn**, which occurs at a similar standard potential (0.30 V vs Fc^+/Fc) to that of **1**, is also reversible.[24] Concerning the reductive processes, we note that an overlay of the CVs (Figure 6) reveals that the reductive processes (E^0_{1-} and E^0_{2-}), in contrast to the two most positive oxidative processes, are perturbed considerably by the presence of the Co ion within the chlorin core, with the first reduction shifting in the positive direction and the second reduction shifting to a more negative potential, with respect to **1**. Thus, the reduction processes likely involve molecular orbitals with considerable admixtures of the Co d-orbitals with the chlorin frontier orbitals. For simplicity and the purposes of the work described herein, we will use a metal oxidation state formalism and describe the reductions as Co(II/I) and Co(I/0) processes with the caveat that these reductions have a parentage involving the chlorin macrocycle.

We ascribe the unique CV wave of **1-Co** at E^0_{1+} = −0.167 V to the Co(III/II) redox process. This value for the first oxidation of **1-Co** falls within the range of reported values for the Co(III/II) couple of cobalt porphyrins, though the reduction potential for the Co(III/II) couple of cobalt tetraphenylporphyrin is highly variant (−0.40 to +0.60 V vs Fc^+/Fc) and is markedly dependent on the solvent and electrolyte used.[30] The Co(III/II) couple of **1-Co** was further

DOI: 10.1021/acscatal.7b00969
ACS Catal. 2017, 7, 3597−3606

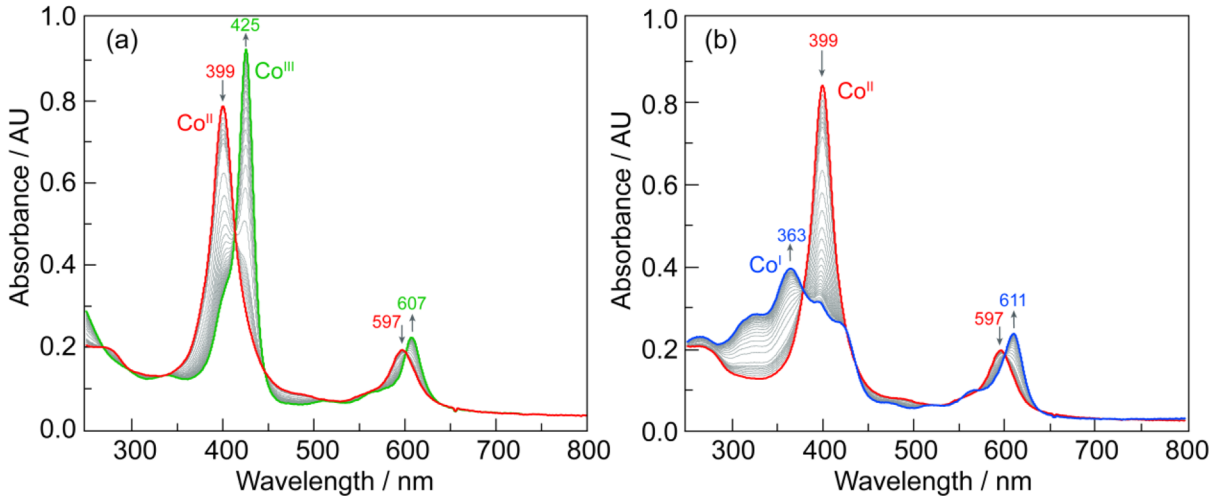

Figure 7. (a) Thin-layer UV-vis spectroelectrochemistry of **1-Co** in CH_3CN and 0.1 M $TBAPF_6$ in a nitrogen-atmosphere glovebox at room temperature: (a) potential held at 0.04 V vs Fc^+/Fc (the Co(III/II) couple is shown with Co(II) (red trace) and Co(III) (green trace)); (b) potential held at −1.51 V vs Fc^+/Fc (the Co(II/I) couple is shown with Co(II) (red trace) and the tentatively assigned Co(I) (blue trace)).

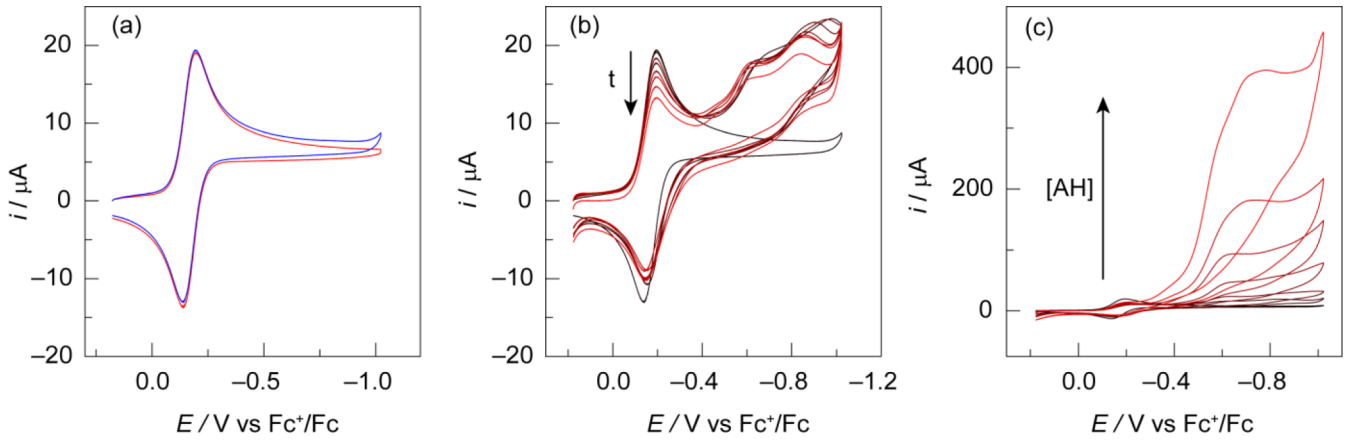

Figure 8. (a) Cyclic voltammograms (CVs) of E^0_{1+} process of **1-Co** (1 mM) in CH_3CN (0.1 M $TBAPF_6$) at a scan rate of 0.1 V s^{-1} with a glassy carbon working electrode (3 mm) under an Ar atmosphere (red trace) and in a saturated O_2 solution (8.1 mM) (blue trace). (b) CVs of **1-Co** (1 mM) in CH_3CN (0.1 M $TBAPF_6$) at a scan rate of 0.1 V s^{-1} with a glassy carbon working electrode (3 mm) in a saturated O_2 solution (8.1 mM) in the presence of 1 mM chloroacetic acid. Evolution with time: from 0 min (black trace) before the addition of acid until 30 min (red trace) (~ 5 min elapsed between each CV). (c) CVs of **1-Co** (1 mM) in CH_3CN (0.1 M $TBAPF_6$) at a scan rate of 0.1 V s^{-1} with a glassy carbon working electrode (3 mm) in a saturated O_2 solution (8.1 mM). Addition of chloroacetic acid (from black to red): 0, 1, 2, 5, 10, 20, and 50 mM.

interrogated using thin-layer UV−vis spectroelectrochemistry by applying an electrochemical potential of 0.04 V vs Fc^+/Fc. Upon application of the potential, the Soret band at λ_{max} = 399 nm bathochromically shifts to λ_{max} = 425 nm with a concomitant increase in molar absorption coefficient. The $Q_y(0,0)$ band also undergoes a bathochromic shift, moving 10 nm, from 597 nm to 607 nm, while maintaining well-anchored isosbestic points (Figure 7a). The shifts of the Soret and Q bands are consistent with spectral changes expected for oxidation of the Co(II) ion to Co(III) within the chlorin macrocycle. In addition, no absorption is observed in the 450−500 nm region of the spectroelectrochemical difference spectrum of Figure 7a; broad growths in this region are observed for π-cations of macrocycles such as porphyrins.[31,32] Indeed, in the transient absorption (TA) spectrum (Figure 5), we do see growths in this region, consistent with an LMCT transition. Thus, the absence of absorptions in this region of the difference spectroelectrochemistry provides further support for an oxidation process occurring largely at the metal center. Consistent with the electrochemical reversibility of this redox couple, the spectrum cleanly reverts to that of Co(II) when the potential is held at open circuit.

The reduced form of the Co(II) chlorin was interrogated similarly, by applying an electrochemical potential of −1.51 V vs Fc^+/Fc. Upon application of potential, the Soret band decreases in intensity and splits, with the new bands forming at 363 and 421 nm. The $Q_y(0,0)$ band shifts 14 to 611 nm (Figure 7b). Such spectral shifts likely correspond to the Co(II/I) redox couple; the shifts are reversible upon returning cleanly back to Co(II) when held at open circuit potential.

The spectral changes observed upon controlled potential electrolysis of **1-Co** at 0.04 V and −1.51 V, especially for the Soret bands, are similar to those observed upon the formation of Co(III) and Co(I) porphyrins, respectively,[33,34] thus supporting the assignment of Co(III) for the one-electron oxidized chlorin complex and of a formal Co(I) chlorin for the one-electron reduced complex. In particular, the split Soret band that we observe for the Co(I) chlorin has also been observed for Co(I) porphyrins, and in the latter case the origin of the higher-energy band has been attributed to a double

DOI: 10.1021/acscatal.7b00969
ACS Catal. 2017, 7, 3597−3606

excited state of charge-transfer character on the basis of magnetic circular dichroism (MCD) experiments.[33,35] The similarity between the spectra of the Co(I) chlorin and those reported for Co(I) porphyrins suggests that the first reduction of each species is similar in nature, with regard to the site of electron transfer. The first reduction of Co(II) porphyrins has conventionally been assigned as being metal-centered because the resulting complexes are diamagnetic.[36,37] However, in light of recent reports detailing the antiferromagnetic coupling of non-innocent macrocycle ligand radicals to metal centers with odd d-electron counts,[38] diamagnetism alone is insufficient to definitively assign whether the nature of the reduction is purely metal-centered, purely ligand-centered, or a combination of the two.

Electrocatalysis. With access to **1-Co** on scales approaching 20−100 mg per synthesis, we were able to undertake exploratory studies of **1-Co** as a small molecule reduction catalyst with emphasis on ORR and HER. With regard to the former, the addition of O_2 has no effect on the Co(III/II) (E^0_{1+}) process, which remains fully reversible and unchanged in potential (Figure 8a) during cyclic voltammetry (CV) cycling. In the presence of both oxygen and acid, however, the catalyst decomposes to a yet unidentified product. This chemical instability is evident by the prompt decrease in the current of the Co(III/II) CV wave upon the addition of 1 mM chloroacetic acid (ClAcOH) to an oxygenated solution of **1-Co**. A catalytic wave is observed to more negative potentials under these conditions, and the current of this wave varies over time. A stable current and reproducible CV is achieved only after 30 min (Figure 8b). The addition of acid results in an increase in catalytic ORR current (Figure 8c). We attribute this catalysis to the decomposition product of **1-Co**. The decomposition may be reproduced chemically when **1-Co** is exposed to humid air over long periods of time. The CV waves of **1-Co** in air-decomposed samples are negligible (Figure S6a in the Supporting Information). Notwithstanding, we observed high ORR activity from the decomposed product (Figure S6b) that is very similar to that shown in Figure 8c, as is evident when the traces are overlaid (see Figure S6c in the Supporting Information). We therefore conclude that **1-Co** decomposes in the presence of oxygen *and* acid, most likely due to a slow reaction with oxygen that is accelerated via an acid-catalyzed process. It is this decomposition product that gives rise to the apparent ORR activity of **1-Co**. We note the recent reports of Co chlorins as selective ORR catalysts for H_2O_2 production from O_2; the chlorins are naturally derived and differ structurally from **1-Co**.[10,11] The generality of the decomposition phenomenon observed herein for **1-Co** is not known across other Co chlorins but warrants investigation.

Whereas the chlorin framework of **1-Co** appears to be unstable in an environment containing both acid *and* oxygen, it is stable in the presence of acid alone, with the caveat that acids that are too strong will lead to demetalation of the chlorin. For example, a CV wave (E_p = −1.3 V vs Fc^+/Fc) appears to potentials positive of the Co(II/I) couple when **1-Co** is titrated with a strong acid such as *p*-toluenesulfonic acid (pTSA, pK_a = 8.6 in CH_3CN),[39] as shown in Figure S7 in the Supporting Information. Bulk electrolysis performed at potentials more negative than −1.3 V vs Fc^+/Fc confirms demetalation of **1-Co**, as the absorption spectrum of the solution following bulk electrolysis shows the presence of **1** (Figure S8); thin layer chromatography (Figure S9 in the Supporting Information) and HR-MS (Figures S10 and S11 in the Supporting Information) also establish the presence of demetalated chlorin. Conversely, bulk electrolysis of **1-Co** performed in the presence of weaker acids, such as ClAcOH (pK_a = 15.3 in CH_3CN)[39] and TFA (pK_a = 12.7 in CH_3CN),[39] show no presence of **1** in absorption spectra of bulk-electrolyzed solutions. Accordingly, to avoid complications arising from demetalation, we undertook the study of HER catalysis by **1-Co** under these weaker acid conditions. In considering the choice of the weaker acid, reduced Co tetrapyrrole macrocycles are known to be strong nucleophiles and thus HER reactions may be complicated by competing S_N2 reactions of weak C-X bonds. Such reactivity has been observed for Co porphyrins and cobalamin complexes, which perform catalytic reductive dechlorination of alkyl chlorides.[40,41] Indeed, the use of ClAcOH as a weak acid in the presence of reduced Co chlorin species showed the presence of chloride formation in competition with HER. Accordingly, studies of HER focused on the use of TFA, which is less prone to nucleophilic attack by the reduced Co chlorin center, because of the presence of stronger C−F vs C−Cl bonds.

Titration of TFA to **1-Co** gives rise to a significant increase in current of the Co(II/I) (E^0_{1-}) wave (Figure 9), indicating

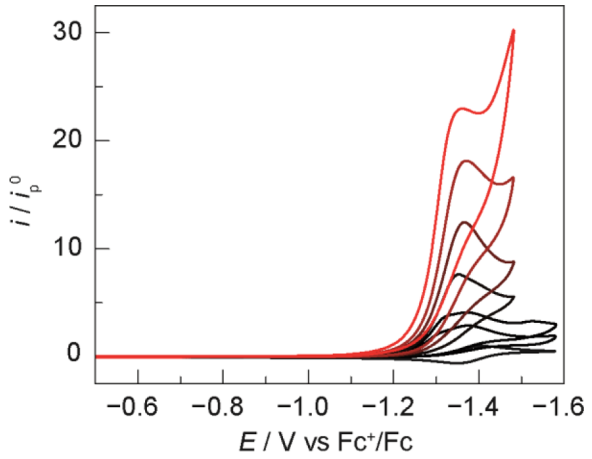

Figure 9. CVs of **1-Co** (1 mM) in CH_3CN (0.1 M $TBAPF_6$) at a scan rate of 0.1 V s^{-1} under an Ar atmosphere with a glassy carbon working electrode (3 mm). Addition of trifluoroacetic acid (from black to red): 0, 1, 2, 5, 10, 20, and 50 mM.

catalysis. Gas chromatography (GC) analysis of the headspace following bulk electrolysis in this case showed H_2 evolution (Figure S12 in the Supporting Information), with a faradaic efficiency of 67%. Analysis of the catalytic CV traces in Figure 9 provides insight into the HER mechanism. Specifically, the half-wave potential of the catalytic wave, which is the potential at which the current is at half of its peak height, may be used to determine the sequence of electrochemical (E) and chemical (C) steps in the mechanism (Scheme 1). Possible sequences include ECEC, EECC, and ECCE mechanisms. Beginning with the Co(II) chlorin, an EECC mechanism would require two one-electron reductions prior to a chemical step. As the catalytic wave occurs after one one-electron reduction, near the Co(II/I) reduction potential and well positive of the Co(I/0) potential, an EECC mechanism from the Co(II) chlorin appears unlikely. An irreversible one-electron wave would be observed in the case of an ECCE mechanism in which the second electron transfer is more difficult than the first.[42] This is not observed in the CVs (Figure 9), so this case is also ruled

DOI: 10.1021/acscatal.7b00969
ACS Catal. 2017, 7, 3597−3606

Scheme 1. Proposed HER Mechanism for 1-Co

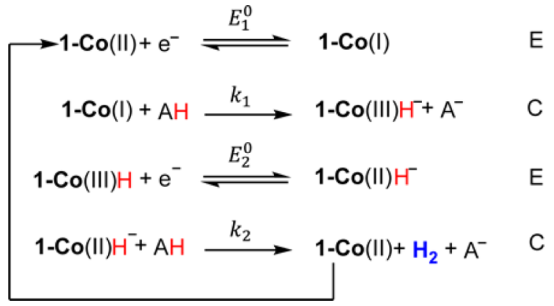

out. An ECCE mechanism in which the second electron transfer is easier than the first is equivalent to an EECC mechanism, in terms of the dependency of the half-wave potential on the rate constants for proton transfer.[42] Conceptually, one could view this type of ECCE mechanism from the Co(II) chlorin as equivalent to an EECC mechanism from the Co(III) chlorin. In such an ECCE or EECC case, the half-wave potential of the catalytic wave could only be shifted positive of the standard potential of the catalyst by a maximum of (RT/F) ln(2) = 17.6 mV, regardless of the values of the rate constants for electron transfer or proton transfer.[42,43] For **1-Co**, the half-wave potential is constant and at a potential positive of the standard potential of the Co(II/I) couple by 99 mV, as shown in Figure 10b. The position of the half-wave potential is

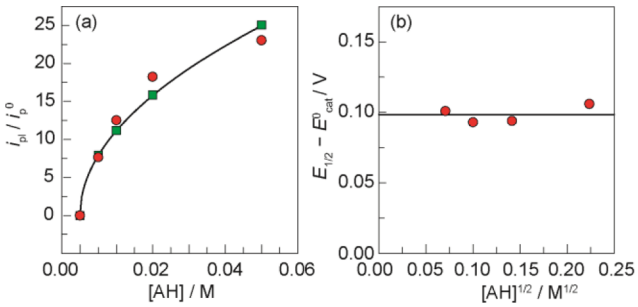

Figure 10. Analysis of the data in Figure 9: (a) Variation of the normalized plateau current (solid red circle) with the acid concentration and least-squares fitting (black line) of the experimental data to eq 1 and expected normalized plateau currents (solid green square) using eq 1 and $k_1 = 5.7 \times 10^6$ M^{-1} s^{-1} and $k_2 = 2.6 \times 10^3$ M^{-1} s^{-1}. (b) The half-wave potential (solid red circle) with the square root of the acid concentration; average value (black line).

therefore inconsistent with an ECCE mechanism with Co(II) chlorin as the initial species. Accordingly, HER catalysis by **1-Co** is most consistent with an ECEC mechanism in which sequential electrochemical reduction and chemical steps occur.

The S-shape of the catalytic wave at high acid concentration (≥5 mM) in Figure 9 is consistent with HER limited only by the kinetics of the catalytic reaction, as opposed to the diffusion of the substrate (the acid).[44] Under such conditions, the plateau current, which is independent of the scan rate, provides invaluable mechanistic insight, particularly with regard to the nature of H_2 production. The two consensus mechanisms for H_2 generation are "heterolytic" or "homolytic" reaction pathways, where the former involves protonation of a metal hydride (a heterocoupling event) and the latter involves homolytic dissociation of the two metal hydride bonds.[45] Costentin, Dridi, and Savéant have shown that these two pathways may be distinguished by analysis of the plateau current and the location of the half-wave potential. In the case of the titration of **1-Co** with TFA, the plateau current is proportional to the square root of the acid concentration (Figure 10a). This observation, in conjunction with the aforementioned observation that the half-wave potential is constant and more positive than the standard potential, is consistent with the prevalence of a heterolytic pathway for H_2 production.[45]

The mechanism for HER by **1-Co** proposed in Scheme 1 reflects a heterolytic pathway that conforms to an ECEC mechanism. In this proposed mechanism, one-electron reduction of the Co(II) species is followed by protonation of Co(I) to deliver a Co(III)H hydride. Subsequent one-electron reduction of Co(III)H to Co(II)H produces an intermediate with increased hydricity, thus driving a second protonation to produce hydrogen and close the catalytic ECEC cycle. We do not see H_2 production from the Co(III)H as has been postulated for a more elaborately substituted Co chlorin.[12] The fact that the catalysis occurs at the first reduction wave rather than at a more negative potential indicates that the second electron transfer occurs at a potential positive of the first ($E_2^0 > E_1^0$).[45] Thus, the catalysis appears to occur at the Co(II/I) wave, as the second CV wave for the second reduction shifts inside (more positive) the first reduction wave upon protonation, following the first reduction process. These results are consistent with the chlorin exhibiting increased basicity, compared to porphyrins, which exhibit HER upon a second reduction that is more negative than the first reduction ($E_1^0 > E_2^0$).[46] Moreover, **1-Co** is also distinct from nature's cobalt tetrapyrrole, cobalamin, which is reduced at too positive a potential for HER, with no further reductions observed, thus resulting in cobalamin being incapable of HER from weak acids.[40] We also note that ligand involvement in the delivery of protons to the metal center to either form or protonate a metal hydride has been proposed in mechanisms for HER catalysts possessing pendant amines,[47] pendant carboxylic acids,[46,48] or even carbon atoms in aromatic ligands.[49] Although protonation of the *meso*- or β-carbon atoms of macrocyclic ligands has been proposed,[50] our present studies of **1-Co** have uncovered no evidence for the chlorin ligand directly participating in proton transfer steps.

The plateau current also gives direct access to the apparent rate constant of the catalytic reaction.[42] In the context of an ECEC mechanism, Savéant and Artero have shown that the rate constants k_1 and k_2 of the first and second chemical steps (proton transfers in Scheme 1) may be deduced from the plateau current (i_{pl}), which is normalized by the current of the one-electron wave in the absence of acid, i_p^0, and the half-wave potential ($E_{1/2}$) according to the following:[43]

$$\frac{i_{pl}}{i_p^0} = 4.48\sqrt{\frac{RT}{Fv}\frac{\sqrt{k_1 k_2[\mathrm{AH}]}}{\sqrt{k_1}+\sqrt{k_2}}} \quad (1)$$

$$E_{1/2} = E_1^0 + \frac{RT}{F}\ln\left(1+\sqrt{\frac{k_1}{k_2}}\right) \quad (2)$$

where v is the scan rate and $E_1^0 = E_{1-}^0 = -1.401$ V vs Fc^+/Fc in this case. The values of the two rate constants can be determined from eqs 1 and 2 by parametrically fitting eq 1 to the experimental data shown in Figure 10a and eq 2 to the average half-wave potential of the data shown in Figure 10b.

DOI: 10.1021/acscatal.7b00969
ACS Catal. 2017, 7, 3597−3606

The details of the fitting procedure are described in Section F of the Supporting Information to furnish the rate constants k_1 = 5.7 × 10^6 M^{-1} s^{-1} and k_2 = 2.6 × 10^3 M^{-1} s^{-1}. Using these calculated rate constants, values of the normalized plateau current from eq 1 agree well with the experimental data (green squares in Figure 10a).

The HER catalytic activity of **1-Co** can be benchmarked by the methods of Savéant and Artero[42,43] to furnish "catalytic Tafel plots", which represent the evolution of the turnover frequency (TOF) as a function of the overpotential (η) of the catalytic reaction. This approach is independent of experimental factors, such as cell configuration, and includes in the calculation of the TOF only the amount of active catalyst present in the reaction diffusion layer, thereby providing a rational method of benchmarking intrinsic catalytic activity. An efficient catalyst will exhibit a high turnover frequency at low overpotential and, consequently, is situated in the top left corner of Figure 11. The TOF, as related to HER, is given by[42,43]

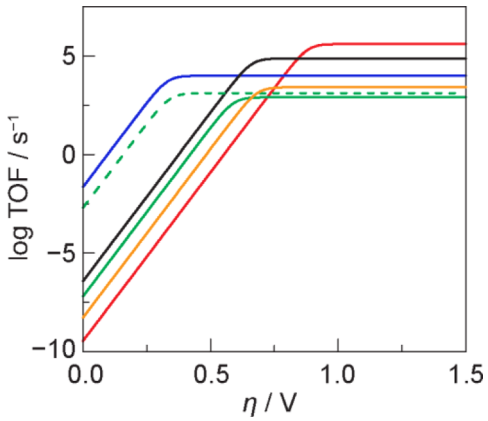

Figure 11. Catalytic Tafel plots for the different electrocatalysts listed in Table 1 of ref 43 and for **1-Co** based on the data in Table 1:[43] FeTPP in DMF and Et_3NH^+(red trace); $Co(dmgH)_2py$ in DMF and Et_3NH^+ (blue trace); $[Ni(P_2^{Ph}N^{Ph})_2]^{2+}$ in CH_3CN and $DMFH^+$ (black trace); $[Ni(P_2^{Ph}N_2^{C_6H_4X})_2]^{2+}$ in CH_3CN and TfOH with X = H (green solid trace) and in CH_3CN and $DMFH^+$ with X = $CH_2P(O)(OEt)_2$ (green dashed trace); 1-Co in CH_3CN and TFA (orange trace).

$$\mathrm{TOF} = \frac{\mathrm{TOF}_{\max}}{1 + \exp\left[\frac{F}{RT}\left(E^0_{H^+/H_2} - E_{1/2}\right)\right]\exp\left(-\frac{F}{RT}\eta\right)} \quad (3)$$

$$\mathrm{TOF}_{\max} = \frac{k_1 k_2}{k_1 + k_2}[\mathrm{AH}] \quad (4)$$

where TOF_{max} is the maximal value of the TOF. From this equation, the previously determined values of k_1 and k_2 yield TOF_{max} for a given concentration of acid. The "catalytic Tafel plots" (Figure 11) are constructed by inputting a concentration of [AH] = 1 M for each catalyst into eq 4. The TOF scales with overpotential, η, as described by eq 3. The thermodynamic standard potential for hydrogen generation, $E^0_{H^+/H_2}$, from TFA at a concentration of 1 M is calculated to be −0.62 V vs Fc^+/Fc using the method established by Fourmond et al.[51] This value of $E^0_{H^+/H_2}$ takes into account the effect of homoconjugation, which is the association of an acid with its conjugate base via hydrogen bonding. The equilibrium constant for homoconjugation of TFA in CH_3CN is 7.9 × 10^3 M^{-1}.[39] $E_{1/2}$ is determined from the CVs in Figure 9a to be −1.302 V vs Fc^+/Fc. From these values, the plot of TOF vs n for HER for **1-Co** can be constructed, and is presented in Figure 11, together with the activity curves of other reported HER catalysts,[52−56] including an Fe porphyrin.[52] **1-Co** is a superior HER catalyst as compared to porphyrins in the low η region. Inasmuch as energy conversion cycles seek to perform catalysis at low overpotential, the connection of η to TOF is the critical metric in catalyst design.

CONCLUSION

Insertion of a Co(II) ion into a sparsely substituted chlorin (**1-Co**) induces significant out-of-plane distortion of the macrocycle. Structural comparisons between metal-free and Co chlorins reveal a constriction of the macrocycle core and a possible mitigation of the destabilizing effect of antiaromaticity in the 20 π-electron conjugated pathway due to the presence of the Co(II) ion. EPR, electronic absorption, and time-resolved absorption spectra are consistent with the presence of an open-shell, $S = {}^1/_2$ metal center residing within the chlorin ligand environment. The electrochemistry of **1-Co** speaks to significant coupling of the Co d-orbitals with those of the electron-rich chlorin macrocycle. Efforts to perform the electrocatalytic oxygen reduction reaction with **1-Co** revealed that the Co chlorin is unstable to the combined presence of oxygen and acid, which are requisite for ORR chemistry. However, the Co chlorin decomposition product formed under such conditions is competent for ORR. **1-Co** is an authentic electrocatalyst for the hydrogen evolution reaction, with the caveat that acids that are too strong will cause demetalation. With weaker acids, such as TFA, **1-Co** performs HER via a proposed mechanism involving the protonation of Co(II) hydride to afford H_2. The ability of the Co chlorin to perform HER via an intermediate that is reduced at a standard potential positive of that of the first reduction of the complex is in contradistinction to Co porphyrins, which catalyze HER from acids, regardless of strength, at potentials well negative of the first reduction (thereby leading to higher overpotentials).[46] The origin for this disparate behavior does not arise from the redox properties of the macrocycle, as **1-Co** and Co tetraphenylporphyrin undergo multiple reduction and oxidations in similar potential ranges.[34] The increased activity of **1-Co**, compared to porphyrins, appears to be derived from the increased electron density of the chlorin macrocycle, thus leading to a more basic Co(I) metal center, in turn, promoting hydride formation and subsequent reduction to Co(II) hydride. The importance of cobalt basicity on such a Co(I) → Co(III)H → Co(II)H reaction sequence for HER has been theoretically established.[57] Examination of the electrochemical kinetics of **1-Co** has revealed HER to proceed by an ECEC mechanism, and allowed us to obtain the key chemical rate constants (k_1 and k_2 in Scheme 1) of the ECEC catalytic cycle. From these rate constants, the catalytic activity, as related by the TOF for HER, has been determined. Upon benchmarking the catalytic activity of molecular HER catalysts, we find that, at low overpotentials, the Co chlorin **1-Co** exhibits superior HER activity as compared to its porphyrin congeners.

ASSOCIATED CONTENT

Supporting Information

The Supporting Information is available free of charge on the ACS Publications website at DOI: 10.1021/acscatal.7b00969.

DOI: 10.1021/acscatal.7b00969
ACS Catal. 2017, 7, 3597−3606

Materials, experimental methods, description of data analysis and instrumentation, mass spectrometry, gas chromatography, and additional UV-vis and cyclic voltammetry data (PDF)
X-ray crystallographic information (CIF)

AUTHOR INFORMATION

Corresponding Authors

*E-mail: jlindsey@ncsu.edu (J. S. Lindsey).
*E-mail: dnocera@fas.harvard.edu (D. G. Nocera).

ORCID

Jonathan S. Lindsey: 0000-0002-4872-2040
Daniel G. Nocera: 0000-0001-5055-320X

Author Contributions

‡These authors contributed equally to this work.

Notes

The authors declare no competing financial interest.

ACKNOWLEDGMENTS

We thank Seung Jun Hwang for assistance with gas chromatography. This material is based upon work supported under the Solar Photochemistry Program of the Chemical Sciences, Geosciences and Biosciences Division, Office of Basic Energy Sciences of the U.S. Department of Energy (D.G.N.) and by Grant No. DE-FG02-05ER15651 from the Chemical Sciences, Geosciences and Biosciences Division, Office of Basic Energy Sciences, of the U.S. Department of Energy (J.S.L.).

REFERENCES

(1) Taniguchi, M.; Mass, O.; Boyle, P. D.; Tang, Q.; Diers, J. R.; Bocian, D. F.; Holten, D.; Lindsey, J. S. *J. Mol. Struct.* **2010**, *979*, 27−45.
(2) Lemon, C. L.; Dogutan, D. K.; Nocera, D. G. In *Handbook of Porphyrin Chemistry*; Kadish, K. M., Smith, K. M., Guilard, R., Eds.; Academic Press: Amsterdam, 2012; Vol. *21*, Ch. 99, p 144.
(3) Rosenthal, J.; Nocera, D. G. *Acc. Chem. Res.* **2007**, *40*, 543−553.
(4) Collman, J. P.; Wagenknecht, P. S.; Hutchison, J. E. *Angew. Chem., Int. Ed. Engl.* **1994**, *33*, 1537−1554.
(5) Brothers, P. J.; Collman, J. P. *Acc. Chem. Res.* **1986**, *19*, 209−215.
(6) Chang, D.; Malinski, T.; Ulman, A.; Kadish, K. M. *Inorg. Chem.* **1984**, *23*, 817−824.
(7) Stolzenberg, A. M.; Stershic, M. T. *Inorg. Chem.* **1987**, *26*, 1970−1977.
(8) Stolzenberg, A. M.; Strauss, S. H.; Holm, R. H. *J. Am. Chem. Soc.* **1981**, *103*, 4763−4778.
(9) Fujita, E.; Fajer, J. *J. Am. Chem. Soc.* **1983**, *105*, 6743−6745.
(10) Mase, K.; Ohkubo, K.; Fukuzumi, S. *J. Am. Chem. Soc.* **2013**, *135*, 2800−2808.
(11) Mase, K.; Ohkubo, K.; Fukuzumi, S. *Inorg. Chem.* **2015**, *54*, 1808−1815.
(12) Aoi, S.; Mase, K.; Ohkubo, K.; Fukuzumi, S. *Chem. Commun.* **2015**, *51*, 15145−15148.
(13) Lindsey, J. S. *Chem. Rev.* **2015**, *115*, 6534−6620.
(14) Taniguchi, M.; Ra, D.; Mo, G.; Balasubramanian, T.; Lindsey, J. S. *J. Org. Chem.* **2001**, *66*, 7342−7354.
(15) Gallucci, J. P.; Swepston, P. N.; Ibers, J. A. *Acta Crystallogr., Sect. B: Struct. Crystallogr. Cryst. Chem.* **1982**, *38*, 2134−2139.
(16) Taniguchi, M.; Lindsey, J. S. *Chem. Rev.* **2017**, *117*, 344−535.
(17) Taniguchi, M.; Kim, H.-J.; Ra, D.; Schwartz, J. K.; Kirmaier, C.; Hindin, E.; Diers, J. R.; Prathapan, S.; Bocian, D. F.; Holten, D.; Lindsey, S. J. *J. Org. Chem.* **2002**, *67*, 7329−7342.
(18) Alben, J. O. *The Porphyrins*; Dolphin, D., Eds.; Academic Press: New York, 1978; Vol. *III*, Physical Chemistry Part A, Ch. 7, p 323.
(19) Collman, J. P.; Berg, K. E.; Sunderland, C. J.; Aukauloo, A.; Vance, M. A.; Solomon, E. I. *Inorg. Chem.* **2002**, *41*, 6583−6596.
(20) Honda, T.; Kojima, T.; Fukuzumi, S. *J. Am. Chem. Soc.* **2012**, *134*, 4196−4206.
(21) Clegg, W., Ed. *Crystal Structure Analysis: Principles and Practice*, 2nd Edition; Oxford University Press: New York, 2009.
(22) Gouterman, M. *J. Mol. Spectrosc.* **1961**, *6*, 138−163.
(23) Kee, H. L.; Kirmaier, C.; Tang, Q.; Diers, J. R.; Muthiah, C.; Taniguchi, M.; Laha, J. K.; Ptaszek, M.; Lindsey, J. S.; Bocian, D. F.; Holten, D. *Photochem. Photobiol.* **2007**, *83*, 1110−1124.
(24) Kee, H. L.; Kirmaier, C.; Tang, Q.; Diers, J. R.; Muthiah, C.; Taniguchi, M.; Laha, J. K.; Ptaszek, M.; Lindsey, J. S.; Bocian, D. F.; Holten, D. *Photochem. Photobiol.* **2007**, *83*, 1125−1143.
(25) Aravindu, K.; Kim, H.-J.; Taniguchi, M.; Dilbeck, P. L.; Diers, J. R.; Bocian, D. F.; Holten, D.; Lindsey, J. S. *Photochem. Photobiol. Sci.* **2013**, *12*, 2089−2109.
(26) Tait, C. D.; Holten, D.; Gouterman, M. *Chem. Phys. Lett.* **1983**, *100*, 268−272.
(27) Yu, H.; Baskin, J.; Steiger, B.; Wan, C.; Anson, F.; Zewail, A. *Chem. Phys. Lett.* **1998**, *293*, 1−8.
(28) Fukuzumi, S.; Ohkubo, K.; Imahori, H.; Shao, J.; Ou, Z.; Zheng, G.; Chen, Y.; Pandey, R. K.; Fujitsuka, M.; Ito, O.; Kadish, K. M. *J. Am. Chem. Soc.* **2001**, *123*, 10676−10683.
(29) Stolzenberg, A. M.; Spreer, L. O.; Holm, R. H. *J. Am. Chem. Soc.* **1980**, *102*, 364−370.
(30) Kadish, K. M.; Royal, G.; Van Caemelbecke, E.; Gueletti, L. In *The Porphyrin Handbook*; Kadish, K. M.; Smith, K. M.; Guilard, R., Eds. Academic Press: San Diego, CA, 2000; Vol. *9*, p 14.
(31) Tait, C. D.; Holten, D.; Gouterman, M. *J. Am. Chem. Soc.* **1984**, *106*, 6653−6659.
(32) Dolphin, D.; Muljiani, Z.; Rousseau, K.; Borg, D. C.; Fajer, J.; Felton, R. H. *Ann. N. Y. Acad. Sci.* **1973**, *206*, 177−200.
(33) Kobayashi, H.; Kaizu, Y.; Hara, T. *Bull. Chem. Soc. Jpn.* **1972**, *45*, 2148−2155.
(34) D'Souza, F.; Villard, A.; Van Caemelbecke, E.; Franzen, M.; Boschi, T.; Tagliatesta, P.; Kadish, K. M. *Inorg. Chem.* **1993**, *32*, 4042−4048.
(35) Gouterman, M. In *The Porphyrins*; Dolphin, D., Eds.; Academic Press: New York, 1978; Vol. *III*, Physical Chemistry Part A, p 1.
(36) Whitlock, H. W.; Bower, B. K. *Tetrahedron Lett.* **1965**, *6*, 4827−4831.
(37) Doppelt, P.; Fischer, J.; Weiss, R. *Inorg. Chem.* **1984**, *23*, 2958−2962.
(38) Lemon, C. M.; Huynh, M.; Maher, A. G.; Anderson, B. L.; Bloch, E. D.; Powers, D. C.; Nocera, D. G. *Angew. Chem., Int. Ed.* **2016**, *55*, 2176−2180.
(39) Izutsu, K. *Acid-Base Dissociation Constants in Dipolar Aprotic Solvents*; Blackwell: Boston, 1990.
(40) Argüello, J. E.; Costentin, C.; Griveau, S.; Savéant, J.- M. *J. Am. Chem. Soc.* **2005**, *127*, 5049−5055.
(41) Costentin, C.; Passard, G.; Robert, M.; Savéant, J.-M. *Chem. Sci.* **2013**, *4* (2), 819−823.
(42) Costentin, C.; Savéant, J.-M. *ChemElectroChem* **2014**, *1*, 1226−1236.
(43) Artero, V.; Savéant, J.-M. *Energy Environ. Sci.* **2014**, *7*, 3808−3814.
(44) Savéant, J.-M. *Elements of Molecular and Biomolecular Electrochemistry: An Electrochemical Approach to Electron Transfer Chemistry*; John Wiley: Hoboken, NJ, 2006; p 106.
(45) Costentin, C.; Dridi, H.; Savéant, J.-M. *J. Am. Chem. Soc.* **2014**, *136*, 13727−13734.
(46) Lee, C. H.; Dogutan, D. K.; Nocera, D. G. *J. Am. Chem. Soc.* **2011**, *133*, 8775−8777.
(47) O'Hagan, M.; Shaw, W. J.; Raugei, S.; Chen, S.; Yang, J. Y.; Kilgore, U. J.; DuBois, D. L.; Bullock, R. M. *J. Am. Chem. Soc.* **2011**, *133*, 14301−14312.
(48) Bediako, D. K.; Solis, B. H.; Dogutan, D. K.; Roubelakis, M. M.; Maher, A. G.; Lee, C. H.; Chambers, M. B.; Hammes-Schiffer, S.; Nocera, D. G. *Proc. Natl. Acad. Sci. U. S. A.* **2014**, *111*, 15001−15006.
(49) Quintana, L. M. A.; Johnson, S. I.; Corona, S. L.; Villatoro, W.; Goddard, W. A.; Takase, M. K.; VanderVelde, D. G.; Winkler, J. R.;

DOI: 10.1021/acscatal.7b00969
ACS Catal. 2017, 7, 3597−3606

Gray, H. B.; Blakemore, J. D. *Proc. Natl. Acad. Sci. U. S. A.* **2016**, *113*, 6409−6414.
(50) Solis, B. H.; Maher, A. G.; Dogutan, D. K.; Nocera, D. G.; Hammes-Schiffer, S. *Proc. Natl. Acad. Sci. U. S. A.* **2016**, *113*, 485−492.
(51) Fourmond, V.; Jacques, P.-A.; Fontecave, M.; Artero, V. *Inorg. Chem.* **2010**, *49*, 10338−10347.
(52) Bhugun, I.; Lexa, D.; Savéant, J.-M. *J. Am. Chem. Soc.* **1996**, *118*, 3982−3983.
(53) Razavet, M.; Artero, V.; Fontecave, M. *Inorg. Chem.* **2005**, *44*, 4786−4795.
(54) Helm, M. L.; Stewart, M. P.; Bullock, R. M.; DuBois, M. R.; DuBois, D. L. *Science* **2011**, *333*, 863−866.
(55) Kilgore, U. J.; Roberts, J. A. S.; Pool, D. H.; Appel, A. M.; Stewart, M. P.; DuBois, M. R.; Dougherty, W. G.; Kassel, W. S.; Bullock, R. M.; DuBois, D. L. *J. Am. Chem. Soc.* **2011**, *133*, 5861−5872.
(56) Wilson, A. D.; Newell, R. H.; McNevin, M. J.; Muckerman, J. T.; Rakowski DuBois, M.; DuBois, D. L. *J. Am. Chem. Soc.* **2006**, *128*, 358−366.
(57) Muckerman, J. T.; Fujita, E. *Chem. Commun.* **2011**, *47*, 12456−12458.

DOI: 10.1021/acscatal.7b00969
ACS Catal. 2017, 7, 3597−3606

Faraday Discussions

Cite this: *Faraday Discuss.*, 2015, **185**, 249

PAPER

Comparison of self-assembled and micelle encapsulated QD chemosensor constructs for biological sensing†

Christopher M. Lemon and Daniel G. Nocera*

Received 23rd May 2015, Accepted 23rd June 2015
DOI: 10.1039/c5fd00093a

Whereas a variety of covalent conjugation strategies have been utilized to prepare quantum dot (QD)-based nanosensors, supramolecular approaches of self-assembly have been underexplored. A major advantage of self-assembly is the ability to circumvent laborious synthetic efforts attendant to covalent conjugation of a chemosensor to functionalized QDs. Here, we combine a CdSe/ZnS core–shell QD with gold(III) corroles using both self-assembly and micelle encapsulation to form QD nanosensors. Appreciable spectral overlap between QD emission and corrole absorption results in efficient Förster resonance energy transfer (FRET), which may be initiated by one- or two-photon excitation. The triplet state of the gold(III) corroles is quenched by molecular oxygen, enabling these constructs to function as optical O_2 sensors, which is useful for the metabolic profiling of tumours. The photophysical properties, including QD and corrole lifetimes, FRET efficiency, and O_2 sensitivity, have been determined for each construct. The relative merits of each conjugation strategy are assessed with regard to their implementation as sensors.

Introduction

The metabolic status of a tumour is well-characterized by the concentration of protons, glucose, and oxygen, as these parameters quantify tumour metabolism, consumption, and respiration, respectively.[1,2] Both pH and pO_2 are particularly relevant because the tumour microenvironment is characterized by low extracellular pH (6.6–6.8)[3] and hypoxia ($pO_2 \leq 5$ Torr).[2] Understanding how these parameters change as a function of disease progression or chemotherapy will enable clinicians to improve patient outcomes. To this end, new sensors are needed to monitor dynamic changes of biologically relevant analyte

Department of Chemistry and Chemical Biology, Harvard University, 12 Oxford Street, Cambridge, Massachusetts 02138, USA. E-mail: dnocera@fas.harvard.edu; Fax: +1-617-496-0265; Tel: +1-617-495-8904

† Electronic supplementary information (ESI) available: Synthetic methods for the preparation of compounds **1** and **2**, as well as NMR spectra, TEM images of CdSe/ZnS quantum dots, additional spectroscopic characterization of the conjugates, and tables of spectroscopic data including binding constants and FRET parameters. See DOI: 10.1039/c5fd00093a

concentrations in real time. Additionally, these sensors must be small enough to penetrate into tumour tissue, enabling precise mapping of analyte gradients in tissue with high spatial resolution.

To meet these criteria, we have selected fluorescent semiconductor quantum dots (QDs) to serve as a platform from which to assemble chemosensors for tumour imaging.[4] Fluorescent semiconductor QDs are ideal scaffolds for optical sensors because they are photostable and possess broad excitation profiles, narrow emission profiles, and high photoluminescence quantum yields.[5] The emission properties of suitably prepared QDs are unperturbed by environmental changes, such as the presence or absence of an analyte.[6] This enables ratiometric sensing, where the concentration of an analyte is determined by measuring changes in emission intensity relative to an internal standard. Moreover, QDs have two-photon absorption cross sections (σ_2) on the order of 10^4 Göppert–Mayer units (1 GM = 10^{-50} cm^4 s per photon),[7,8] which is substantially greater than typical organic fluorophores (σ_2 = 10–100 GM).[9,10] This property makes QD-based constructs superior chemosensors for multiphoton laser scanning microscopy (MPLSM), a technique that uses near-IR light (600–1100 nm) to exploit the tissue transparency window, where endogenous fluorophores do not absorb. Accordingly, MPLSM enables deep tissue penetration (450–600 μm) with approximately 1 μm spatial resolution.[11–13]

Since the photophysical properties of the QD are largely unaffected by analyte, the QD must be paired with an analyte-responsive fluorophore, furnishing a donor–acceptor pair.[14] The QD donor serves as the (multi)photon antenna and subsequently transfers this energy to the chemosensor active site. One of the most common methods of signal transduction in QD-based systems is Förster resonance energy transfer (FRET).[14] In this mechanism, energy is transferred from the donor to the acceptor through space *via* a long-range dipole–dipole interaction,[15] thereby decreasing the emission intensity of the QD donor. For a FRET sensor pair, the donor is selected for its absorption properties in a desired optical window, whereas the acceptor is selected for analyte sensitivity and desired optical properties that serve to measure analyte concentration. To maximize energy transfer in the dyad, the FRET pair must be judiciously selected such that the emission profile of the donor is energetically matched to the absorption profile of the acceptor. In this regard, QDs are ideal FRET donors because their emission profiles are tunable with size,[16] enabling facile matching of the emission spectrum to the absorption spectrum of the acceptor. Using these design principles,[4] we have developed a series of quantum dot based pH sensors,[17–19] as well as high- (160–760 Torr)[20] and low-pressure (0–160 Torr)[21,22] oxygen sensors.

We have exploited a variety of methods to prepare QD donor|acceptor dyads. The most common method is the covalent attachment of the acceptor to a functionalized ligand on the surface of a QD.[23–25] These polymers or dendrimers solubilize the QD in aqueous buffer and provide a functional handle, such as a terminal amine, to covalently attach an acceptor *via* amide bond formation. We have used this method to attach a variety of analyte-responsive dyes to water-soluble QDs: a squaraine dye (pH),[17] SNARF-5F (pH),[18] and Os(II) polypyridyl complexes (O_2).[20] As an alternative to covalent strategies, we have explored supramolecular self-assembly to exploit the surface chemistry of QDs. In this approach, the acceptor molecule has been modified with a functional group, such as a pyridyl ring, that binds directly on the QD surface. This is a rapid method of

preparing conjugates and enables precise control of the donor–acceptor ratio. We have utilized this strategy for the preparation of self-assembled O_2 sensors comprised of *meso*-pyridyl Pd(II) porphyrins.[21] Since this method involves the displacement of hydrophobic surface ligands with hydrophobic fluorophores, self-assembled conjugates are restricted to organic solvents. In order to overcome this limitation, we have employed micelles as a means of transferring the organic-soluble constructs to an aqueous environment. Phospholipids modified with PEG chains were used to encapsulate preformed organic soluble assemblies using sonication processing. Their formation is templated by the QD, using hydrophobic interactions between the surface ligands and the oleate groups of the phospholipid. This method has been used to translate the Pd(II) porphyrin assemblies to an aqueous environment.[22]

Supramolecular approaches of QD donor|acceptor self-assembly bypass laborious synthetic efforts that are needed to covalently conjugate a chemosensor to QDs functionalized with multidentate polymers. Fig. 1 depicts the QD donor|acceptor constructs that pair CdSe/ZnS core–shell QDs with the gold(III) corroles **1** and **2**. With these constructs, the merits (analyte sensitivity, FRET efficiency, *etc.*) of self-assembled and micelle encapsulated constructs may quantitatively be compared. Gold(III) corroles were selected as the FRET acceptor for these conjugates because they have long-lived triplet states (~80 μs), rendering them O_2-sensitive phosphors in the biologically relevant 0–160 Torr O_2 range. Moreover, they emit in the near-IR (~790 nm), which is conducive to biological imaging and

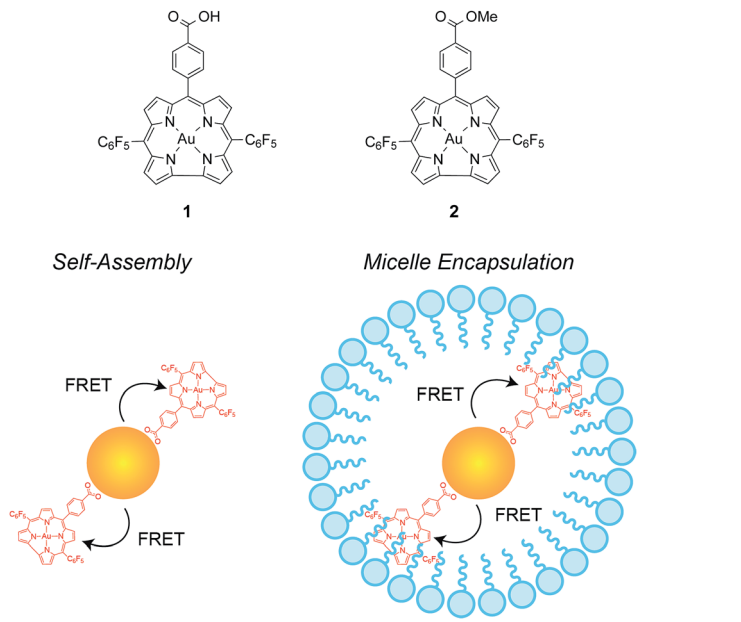

Fig. 1 (Top) Chemical structures of the gold(III) corroles used for the QD sensor constructs. (Bottom) Schematic representations of the different strategies for conjugate formation explored in this study. A CdSe/ZnS core–shell quantum dot is paired with a Au(III) corrole as the O_2-sensitive phosphor. The corrole features a terminal carboxylic acid, which serves as a moiety for surface binding.

sensing in the tissue transparency window. Because these molecules are more red absorbing than isoelectronic palladium(II) and platinum(II) porphyrins, they may be paired with larger, yellow-emitting ($\lambda = 570$ nm) QDs rather than green-emitting ones ($\lambda = 525$ nm). We have recently discussed the difficulties in using *in vivo* intensity data obtained from Pd(II) porphyrin-based sensors.[22] In this system, the green photons from the QD are scattered substantially more than the red photons from the porphyrin, thereby skewing the observed red : green ratio. The red shift of the corrole absorption features decreases the difference in donor and acceptor photon scatter as a function of depth. As a result, constructs with gold(III) corroles may enable *in vivo* intensity data to be used as a quantitative means of determining O_2 concentrations. As a result, dynamic changes may be monitored in real time without the need for measuring lifetimes across the entire field of view.

Compound **1** is well-suited for association to QD surfaces *via* the carboxylic acid moiety at the *meso* position of the corrole ring. The corresponding methyl ester (**2**) serves as a control so that non-specific QD binding may be assessed. Compound **2** also allows us to determine whether surface binding is a prerequisite for micelle incorporation. To the best of our knowledge, the constructs prepared in this study are the first examples of QD|corrole conjugates of any type.

Experimental details

Preparation of self-assembled QD|corrole conjugates

Synthetic details for compounds **1** and **2** are provided in the ESI.† Toluene stock solutions of **1** and **2** (~400 μM) and **QD** (~40 μM) were prepared. An aliquot of the QD stock (typically containing ~0.8 nmol of QDs) was dissolved in 4 mL of toluene; an appropriate volume of the corrole stock was then added to give 10 molar equivalents of corrole per QD. The resultant mixture was stirred overnight at room temperature to allow equilibration of the corrole to the QD surface, furnishing the conjugate **QD1** *via* a specific QD–corrole interaction and **QD2** *via* a non-specific QD–corrole interaction.

Preparation of micelle-encapsulated constructs

To prepare the micelle constructs **QD1-MC** and **QD2-MC**, fresh samples of **QD1** and **QD2** were first prepared. After allowing the solutions to equilibrate overnight, solvent was removed by rotary evaporation and the residue was dissolved in 400 μL of the lipid solution. Solvent was removed and 4 mL of PBS was added. The mixture was then sonicated for 5 min using a VWR Symphony ultrasonic bath to give a red-orange, non-turbid solution. Aggregates were removed by filtering the solution through 0.45 μm and 0.20 μm syringe filters (Pall). The corrole-free construct **QD-MC** was prepared using the same micelle formation protocol outlined above.

Physical measurements

All ^{1}H NMR spectra were recorded on a Varian Inova-500 NMR spectrometer at the Harvard University Department of Chemistry and Chemical Biology Laukien-Purcell Instrumentation Center and internally referenced to the residual solvent signal ($\delta = 7.26$ for $CHCl_3$ in $CDCl_3$).[26] UV-vis absorption spectra were acquired

using a Cary 5000 spectrometer (Agilent). Steady-state emission spectra were recorded on a Photon Technology International (PTI) QM4 fluorometer equipped with a 150 W Xe arc lamp and a Hamamatsu R2658 photomultiplier tube. Quantum yields of the Au(III) corroles were calculated relative to 1,1′,3,3,3′,3′-hexamethylindotricarbocyanine iodide (HITCI) in EtOH ($\Phi_{ref} = 0.283$),[27] while those of the QDs were determined using Rhodamine 6G in EtOH ($\Phi_{ref} = 0.95$)[28] as a reference. Samples for lifetime (τ_0) and quantum yield measurements, as well as for evacuated steady-state emission spectra were prepared using three cycles of freeze–pump–thaw (f–p–t) to pressures below 10^{-5} Torr. Solution oxygen measurements in toluene were made using an Ocean Optics NeoFox Phase measurement system equipped with a HIOXY-R probe for measurements in toluene, or a FOXY-HPT-1-PNA probe for measurements in PBS buffer. Calibration of the probe and determination of solution oxygen concentrations have been described elsewhere.[22] Bright field transmission electron micrographs (TEM) were recorded using a JEOL 2010 transmission electron microscope.

Nanosecond time-resolved emission measurements of corrole lifetimes were acquired using a previously reported system.[29,30] Pump light was provided by the third harmonic (355 nm) of a Quanta-Ray Nd:YAG laser (Spectra-Physics) operating at 10 Hz. The pump light was passed through a BBO crystal in an optical parametric oscillator (OPO), yielding a visible frequency that was tuned to 570 nm. Excitation light was attenuated to 3–4 mJ per pulse for all experiments using neutral density filters. Emitted light was passed to an iHR320 monochromator (Horiba Scientific) and dispersed by a blazed grating (500 nm, 300 grooves per mm) centred at 785 nm. The entrance and exit slits of the monochromator were set to a spectral resolution of 4 nm. The signal was amplified by a photomultiplier tube (R928, Hamamatsu) and collected on a 1 GHz digital oscilloscope (9384CM, LeCroy); acquisition was triggered using a photodiode to collect scattered laser excitation light.

Femtosecond time-resolved emission measurements of QD lifetimes were acquired using a Libra-F-HE (Coherent) chirped-pulse amplified Ti:sapphire laser system, as previously described.[21] Excitation pulses of 480 nm were produced *via* sum-frequency generation of the signal; the pulse power was attenuated to 2–3 mW at the sample. Emission lifetimes were measured on a Hamamatsu C4334 Streak Scope streak camera, which has been described elsewhere.[31] The emission signal was collected over a 140 nm window centred at 575 nm using 100, 50, 20, 10, or 5 ns time windows; delays for these time windows were generated using a Hamamatsu C1097-04 delay unit. Two-photon emission spectra and lifetimes were generated using this Libra-F-HE (Coherent) laser system. Excitation pulses of 965 nm were generated using second harmonic generation of the idler; the pulse power was attenuated to 2–3 mW using neutral density filters and the beam was focused onto the sample using a 100 mm focal length lens. The emission spectrum was collected using a Hamamatsu C4334 Streak Scope streak camera in a 140 nm window centred at 570 nm.

Energy transfer analysis

The efficiency of energy transfer from the QD to the corrole was evaluated using Förster analysis:[15,32]

$$E = \frac{mk_{D-A}}{mk_{D-A} + \tau_D^{-1}} = \frac{mR_0^6}{mR_0^6 + r^6} \quad (1)$$

where k_{D-A} is the rate of energy transfer, r is the average distance between the donor and acceptor, R_0 is the Förster distance, or the distance at which the energy transfer efficiency is 50%, and m is the number of acceptor molecules per donor. This quantity (E) can be measured experimentally:

$$E = 1 - \frac{\tau_{D-A}}{\tau_D} \quad (2)$$

where τ_D is the lifetime of the QD alone and τ_{D-A} is the lifetime of the QD in the presence of corrole. R_0 is determined from the spectral overlap integral,

$$R_0^6 = \frac{9000(\ln 10)\kappa^2\Phi_D}{128\pi^5 N n^4}\int_0^\infty F_D(\lambda)\,\varepsilon_A(\lambda)\,\lambda^4 d\lambda \quad (3)$$

where κ^2 is the relative orientation factor of the dipoles, taken to be 0.476 for static donor–acceptor orientations,[32,33] Φ_D is the quantum efficiency of the donor, N is Avogadro's number, n is the index of refraction of the medium, which is taken to be 1.334 for PBS[34] and 1.4961 for toluene,[35] $F_D(\lambda)$ is the normalized intensity of the donor, and $\varepsilon_A(\lambda)$ is the extinction coefficient of the acceptor at wavelength λ. The latter half of this equation is known as the spectral overlap integral and is denoted by the variable J. The average number of corroles attached to the QD (m) was determined from the optical cross-sections of the QD, the corrole, and the corresponding assembly. The value for m and the concentration of the assemblies was calculated using the individual donor and acceptor absorption spectra, their known ε values, and Beer's law.

Results

Corrole binding studies

Titration experiments were performed to assess the surface binding of gold corroles **1** and **2** to the surface of **QD** in toluene *via* the following equilibrium:

$$QD + Cor \underset{K_D}{\overset{K_A}{\rightleftharpoons}} QD|Cor \quad (4)$$

with an equilibrium binding constant K_A. With increasing concentrations of corrole, the equilibrium is driven to conjugate formation; this process is conveniently monitored using the QD emission. For these studies, the QD was selected so that its emission profile overlaps with the Q(0,0) absorbance feature at 568 nm for corroles **1** and **2**. The absorption and emission spectra for **1** and **2** are provided in Fig. S1.† In order to maximize spectral overlap with the corrole acceptors, the QD used in this study has a first absorption feature at 562 nm and an emission band ($\lambda_{exc} = 470$ nm) centred at 572 nm (Fig. S2†). These QDs are natively capped with a mixture of oleic acid and oleylamine. In order to further characterize these QDs, bright field TEM images were acquired (Fig. S3†) and show that these QDs have a diameter of 5.76 ± 0.62 nm (61 independent QD measurements over 14 different images). The relatively large size of these particles suggests that each QD may easily accommodate several corrole acceptors.

The quenching of QD luminescence *via* energy transfer was examined for corrole **1** bearing a single carboxylic acid and the corresponding methyl ester **2**.

The latter serves as a control to assess non-specific binding interactions with the QD. Titrations were performed in which the same amount of QD (~0.8 nmol or ~200 nM) was treated with 1, 2, 5, or 10 equivalents of **1** or **2**. Each sample point in the titration was prepared independently and incubated overnight to ensure corrole binding. Fig. 2 shows the absorption, steady-state emission, and time-resolved emission profiles for the titration of QD with **1**. Similar data for compound **2** is presented in Fig. S4.†

The absorption profile (Fig. 2a) is dominated by corrole absorption. Both steady state (Fig. 2b) and time-resolved (Fig. 2c) QD emission data shows that the photoluminescence is quenched upon the addition of **1**. The addition of the corrole may be viewed as doping the QD with surface defects.‡ Over the course of the titration, there exists a Poisson distribution of species[21] with varying values of m and corresponding FRET efficiencies. Conveniently, the QD photoluminescence lifetime distills this distribution to a single value and provides a similar equilibrium constant to that derived from the emission intensity using a complementary technique. Using both types of quenching data, the equilibrium

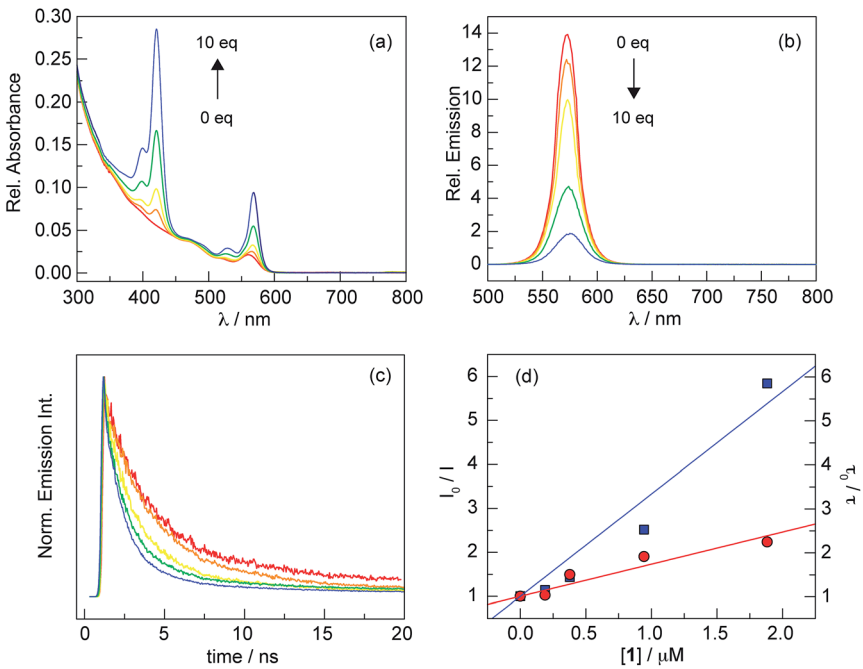

Fig. 2 Spectral changes associated with the titration of a toluene solution of **QD** (—) with 1 (—), 2 (—), 5 (—), and 10 (—) equivalents of **1**. (a) The intensity of the Soret and Q bands of the corrole increases and (b) the QD emission (λ_{ex} = 470 nm) intensity, as well as the photoluminescence decay traces (c) of QD lifetime (λ_{ex} = 480 nm), decrease with increasing concentration of **1**. (d) Stern–Volmer plot to determine the equilibrium binding constants using both the intensity data (■) from (b) and the lifetime data (●) from (c) giving K_A values of 2.33 × 10^6 M^{-1} and 0.73 × 10^6 M^{-1}, respectively.

‡ We thank Prof. Cornelia Bohne for suggesting this analogy.

constant (K_A) for conjugate formation (eqn (4)) was determined. This value may be calculated using the Stern–Volmer equation:

$$\frac{I_0}{I} = \frac{\tau_0}{\tau} = 1 + K_A[\mathrm{Cor}] \quad (5)$$

where I_0 and τ_0 are the emission intensity and lifetime, respectively, in the absence of added corrole, and I and τ are the emission intensity and lifetime, respectively, in the presence of a given corrole concentration [Cor]. The binding constants for compounds **1** and **2** are summarized in Table S1.† Both emission and lifetime quenching titration data were fit to eqn (5) to give the following average values of $K_A = 1.62 \times 10^6\ M^{-1}$ (**1**) and $4.86 \times 10^4\ M^{-1}$ (**2**). As expected, corrole **1** with a carboxylic acid is able to strongly bind to the QD surface and efficiently quench QD luminescence. Conversely, the methyl ester derivative (**2**) interacts non-specifically with the QD and has an effective binding constant that is $\sim 10^2$ times weaker. It should be noted that no binding saturation is observed for either compound over this concentration range. Indeed, a linear quenching response is observed up to 20 equivalents of **1** (Fig. S5†). This implies that all 10

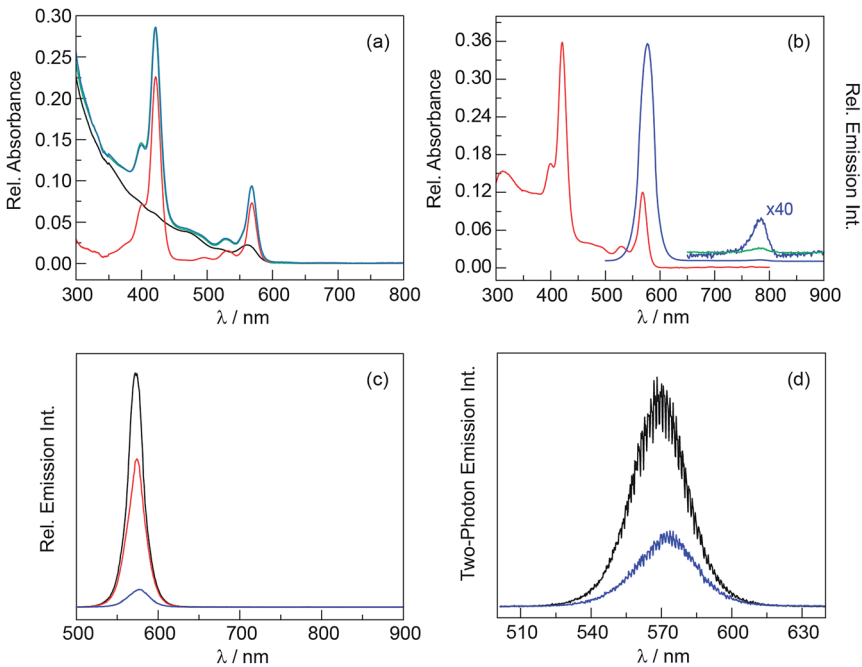

Fig. 3 (a) Comparison of the absorption spectra of **1** (—), QD (—), and **QD1** (—) in toluene, showing that the conjugate is effectively the sum (—) of the two components. (b) Absorption (—) and emission (—) spectra (λ_{exc} = 470 nm) of a freeze–pump–thawed sample of **QD1** in toluene. For clarity, the corrole emission intensity was increased by a factor of 40. To illustrate the FRET enhancement in the conjugate, a concentration-matched sample of **1** (—) is also shown. (c) Emission spectra (λ_{exc} = 470 nm) of **QD** (—), **QD1** (—), and **QD2** (—) in toluene at equivalent quantum dot loading. (d) Two-photon emission spectra (λ_{exc} = 965 nm) of **QD** (—) and **QD1** (—) in toluene at equivalent quantum dot loading.

equivalents of the added corrole are in some way associated with the QD, either surface bound in the case of **1** or intercalated in the exterior capping ligands for **2**.

Characterization of self-assembled constructs

Given the results of the titration studies, corroles **1** and **2** associate with the QD with a high enough binding constant to drive the equilibrium of eqn (4) to conjugate formation. The self-assembled constructs with corroles **1** and **2**, **QD1** and **QD2**, respectively, were prepared using 10 equivalents of donor. The absorption spectrum of the conjugates is a composite of QD and corrole absorption features; the corrole Soret and Q bands are superimposed onto the broad absorption profile of **QD** (Fig. 3a). The emission spectrum ($\lambda_{exc} = 470$ nm) of the conjugates is dominated by emission from the QD (Fig. 3b). In the conjugates, the emission maximum is red shifted 2–6 nm (60–180 cm^{-1}) relative to **QD** (Table 1). While the emission from the acceptor is weak, it is present; the low intensity is due to the low phosphorescence quantum yield of Au(III) corroles (0.2–0.3%). In the 500–900 nm region, the acceptor emission is clearly visible only for **QD1**, as the QD emission is substantially quenched. For **QD2**, QD emission is so strong that phosphorescence from **2** is within the baseline of the spectrum. However, if the scan is limited to the corrole region (650–900 nm), acceptor emission is visible in all cases.

In accordance with titration studies, the QD lifetime is greatly affected by the presence of a corrole acceptor. The QD lifetime data for all constructs is summarized in Table 1. The lifetimes observed for **QD1** are much shorter than that of **QD2**, which reflects the binding efficiency observed in the titration studies due to static quenching of QD photoluminescence. In the absence of acceptor, the QD exhibits monoexponential decay kinetics ($R_{adj}^2 > 0.99$) with a lifetime of about 5 ns. Typically, bi- or tri-exponential kinetics are observed to account for multiple phenomena, such as surface trapped states, exciton emission, and Auger recombination.[36,37] In this case, the observance of monoexponential kinetics is likely due to efficient passivation of surface trapped states due to the presence of a sufficiently thick ZnS shell. Conversely, the conjugates **QD1** and **QD2** exhibit biexponential kinetics ($R_{adj}^2 > 0.99$). This is likely a result of the perturbation of

Table 1 Summary of QD photoluminescence data

Construct	λ_{em} [a]	τ_1 (ns)	A_1 [b] (%)	τ_2 (ns)	A_2 [b] (%)	ϕ_f [c]	E [d]
QD	572	4.93 ± 0.20	100	—	—	0.70	—
QD$_{2h\nu}$	568	15.09 ± 0.23	34	1.48 ± 0.05	66	—	—
QD1	578	2.24 ± 0.07	15	0.55 ± 0.01	85	0.05	0.84
QD1$_{2h\nu}$	572	1.36 ± 0.08	15	0.29 ± 0.01	85	—	0.93
QD2	574	7.22 ± 0.52	19	3.06 ± 0.28	81	0.44	0.22
QD-MC	575	14.81 ± 3.61	37	5.96 ± 0.45	63	0.14	—
QD1-MC	577	2.17 ± 0.16	12	0.43 ± 0.04	88	0.01	0.93
QD2-MC	577	7.99 ± 0.86	16	2.19 ± 0.37	84	0.02	0.66

[a] Observed transitions with $\lambda_{exc} = 470$ nm (or 965 nm for $2h\nu$ excitation). [b] Relative contribution to the biexponential fit. [c] Fluorescence quantum yield, relative to Rhodamine 6G in EtOH ($\phi_f = 0.95$). [d] FRET efficiency calculated using eqn (2). Errors associated with each measurement are reflective of 1 standard deviation.

the QD surface as a result of corrole binding, which induces surface-trapped states that were not present in the absence of acceptor. Indeed, the long component of the fit (~7 ns, 20%) is consistent with surface-trapped states, whereas the short component (~3 ns, 80%) is comparable to the exciton emission lifetime observed for **QD** (~5 ns).

QD photoluminescence quenching is a direct result of Förster resonance energy transfer (FRET) as a result of significant spectral overlap between QD emission and acceptor absorption (Fig. S6†). This interaction has been characterized using both steady-state and time-resolved methods. For **QD1** and **QD2**, the photoluminescence intensity is decreased by 93% and 38%, respectively, compared to native QD (Fig. 3c). This data is consistent with the observed decreases in photoluminescence quantum yield (Table 1). **QD2** exhibits only a 37% decrease in quantum yield relative to QD, whereas a 93% decrease is observed for **QD1**. Using the lifetime data of Table 1 and eqn (2), the FRET efficiency in each conjugate is determined to be 84% for **QD1** and 22% for **QD2**. A summary of FRET parameters is presented in Table S2.† For both constructs, the spectral overlap integral (J) and Förster distance (R_0) are quite similar. However, the less efficient binder **QD2** has an average donor–acceptor distance (r) that is ~3.4 nm longer than for **QD1** ($r = 5.70$ nm).

FRET is supported by excitation spectra (Fig. S7†) recorded by monitoring the corrole emission at 780 nm. The collected emission is attributed to corrole, as QD emission is spectrally separated by over 200 nm. At wavelengths where **1** and **2** do not readily absorb ($\lambda < 370$ nm), a substantial emission signal is observed. QD absorbance dominates in this spectral region, demonstrating that it is the donor in the FRET process. Additional evidence for FRET is revealed upon comparison of the corrole emission in the conjugate relative to the free acceptor. Under linear excitation at 470 nm where the QD is the primary absorber, there is a six-fold enhancement in T(0,0) emission intensity for **QD1** relative to a concentration-matched solution of **1** (Fig. 3b). In the conjugate, the QD serves as a photon antenna and the absorbed energy is transferred to the appended corrole, resulting in a FRET-based enhancement in acceptor emission.

In addition to characterization of the system under linear excitation, the conjugates were studied under two-photon excitation ($\lambda_{exc} = 965$ nm). The integrated emission intensity from the QD in **QD1** is reduced by 63% relative to **QD** alone (Fig. 3d). Additionally, QD lifetime measurements were made under two-photon excitation conditions (Table 1). In this case, **QD** exhibits the expected biexponential decay kinetics ($R_{adj}^2 > 0.99$), with a long component of 15 ns due to surface trapped states and a short component of 1.5 ns due to exciton emission. The observed difference in lifetime under one- and two-photon excitation is a result of a difference in selection rules.[38,39] The QD lifetime for **QD1** is substantially quenched. Using the amplitude-weighted average lifetimes, a FRET efficiency of 93% is calculated, assuming that the quantum yield of the QD is the same under both linear and two-photon excitation. This corresponds to an average donor–acceptor distance (r) of 4.88 nm (Table S2†), which is approximately 1 nm shorter than the value calculated under linear excitation.

Triplet lifetimes of the free corroles and conjugates **QD1** and **QD2** were recorded in toluene for aerated and f–p–t samples and the data is presented in Table 2. Decay traces at $t > 100$ ns were fit to a monoexponential decay function ($R_{adj}^2 > 0.99$). Corroles **1** and **2** exhibit natural radiative lifetimes of 82–84 μs. The

Table 2 Summary of Au corrole phosphorescence data

Construct	τ_{air} (μs)	τ_0[a] (μs)	k_q[b]	ϕ_p[c] (×10²)	k_r[d] (s^{-1})	k_{nr}[d] (s^{-1})
1	0.63 ± 0.01	84.2 ± 0.5	8.6×10^8	0.24	28	1.18×10^4
2	0.62 ± 0.01	82.0 ± 1.7	8.3×10^8	0.32	39	1.22×10^4
QD1	0.88 ± 0.04	100.3 ± 0.9	6.5×10^8	0.43	42	0.99×10^4
QD2	0.78 ± 0.05	93.7 ± 2.6	1.0×10^9	0.50	54	1.06×10^4
QD1-MC$_{long}$[e]	2.32 ± 0.04 (75)[f]	81.9 ± 2.7 (85)	1.6×10^9	0.33	40	1.22×10^4
QD1-MC$_{short}$	0.52 ± 0.05 (25)	21.1 ± 4.1 (15)	8.4×10^9	0.33	155	4.72×10^4
QD2-MC$_{long}$	2.02 ± 0.19 (57)	103.8 ± 4.3 (85)	2.1×10^9	0.37	36	0.96×10^4
QD2-MC$_{short}$	0.59 ± 0.11 (43)	30.7 ± 5.4 (15)	9.3×10^9	0.37	120	3.25×10^4

[a] Freeze–pump–thawed samples (f–p–t) ($<10^{-5}$ Torr) with $\lambda_{ex} = 570$ nm. [b] Calculated using eqn (7). [c] Phosphorescence quantum yield, relative to HITCI in EtOH ($\phi = 0.283$) for f–p–t samples. [d] Calculated using eqn (6). [e] Biexponential kinetics were observed for the micelle constructs; long and short refer to the two components. [f] Relative contribution to the biexponential fit. Errors associated with each measurement are reflective of a 95% confidence interval.

phosphorescence quantum yields for this transition was measured to be 0.24% and 0.32% for compounds **1** and **2**, respectively. Upon conjugate formation, the lifetime is increased by 16 μs for **QD1** and 12 μs for **QD2**. This increase in lifetime is accompanied by a ~1.7 fold increase in the phosphorescence quantum yield to 0.43% for **QD1** and 0.50% for **QD2**. The quantum yield and lifetime are correlated according to the following equation:

$$\phi = \frac{k_r}{k_r + k_{nr}} = k_r \tau_0 \quad (6)$$

where ϕ is the phosphorescence quantum yield, τ_0 is the phosphorescence lifetime, k_r is the radiative rate constant, and k_{nr} is the nonradiative rate constant. Using the data of Table 2, these rate constants may be estimated for both the compounds and their conjugates. Upon conjugate formation, k_{nr} decreases by ~15% while k_r increases by 40–50%.

Quenching of the triplet state by molecular oxygen was quantified using the Stern–Volmer relation:

$$\frac{\tau_0}{\tau} = 1 + k_q \tau_0 [O_2] \quad (7)$$

where τ_0 is the natural radiative lifetime of the phosphor in the absence of quencher, τ is the lifetime of the phosphor at a given oxygen concentration $[O_2]$, and k_q is the bimolecular quenching rate constant. Each construct was studied in toluene, purging the sample with five different gases to construct a Stern–Volmer plot: ambient air (1930 μM O_2), 10% O_2 (919 μM O_2), 5% O_2 (460 μM O_2), 1% O_2 (92 μM O_2), and argon (0 μM O_2). Variable O_2 measurements were made using a HIOXY fibre optic oxygen sensor after purging the sample with argon for corroles **1** and **2**. The Stern–Volmer data is presented for compound **1** in Fig. 4a and for constructs **QD1** and **QD2** in Fig. 4b. The bimolecular quenching constant for **1** was found to be 8.6×10^8 M^{-1} s^{-1}, and that of **2** is 8.3×10^8 M^{-1} s^{-1}. Upon conjugate formation, k_q decreases by ~25% for **QD1**, whereas k_q increases by ~25% for **QD2**, relative to the free phosphor. Thus, the oxygen sensitivity of the corrole is minimally perturbed in the conjugate.

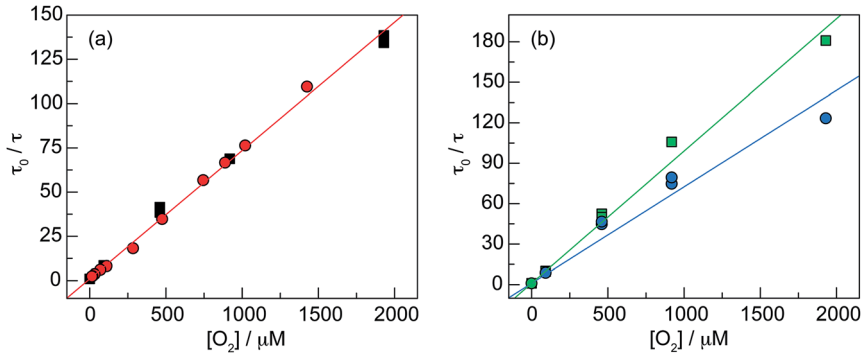

Fig. 4 (a) Stern–Volmer plot for compound **1** in toluene, constructed from data using pre-mixed gases (■) and variable O_2 concentrations (●), as measured using a fiber optic probe. (b) Stern–Volmer plot for **QD1** (●) and **QD2** (■) in toluene using pre-mixed gases.

Characterization of micelle constructs

In order to prepare the water-soluble micelle constructs, preformed conjugates **QD1** and **QD2** were encapsulated in a phosphoethanolamine lipid modified with a PEG-2000 chain[40] using sonication processing[22] to afford micelles **QD1-MC** and **QD2-MC**, respectively. For comparison, corrole-free micelles **QD-MC** were prepared in an analogous way without the addition of an acceptor (Fig. S8†). The steady-state absorption and emission spectra of these constructs are quite similar to the toluene-soluble analogues. Examination of the absorbance spectra reveals that 10 and 9 equivalents of acceptor are incorporated into **QD1-MC** and **QD2-MC**, respectively (Fig. S9†). With regard to the emission spectra (λ_{exc} = 470 nm), corrole emission is barely perceptible above the baseline when scanning over the 500–900 nm region for **QD1-MC** and **QD2-MC**. When examining the corrole region (650–900 nm) separately, acceptor emission is visible.

For these CdSe/ZnS QDs, micelle encapsulation drastically diminishes the photoluminescence quantum yield, from 70% for **QD** in toluene to only 14% for **QD-MC** in PBS. This perturbation of the QD surface also manifests in the photoluminescence decay kinetics (Table 1). Whereas a monoexponential decay was observed for **QD**, **QD-MC** displays biexponential kinetics with a long ~15 ns component reflective of surface trapped states and a short ~6 ns component due to exciton emission. The relative amplitudes of these components are nearly identical to that observed for **QD** under two-photon excitation. Upon incorporation of corrole acceptors, the lifetime decreases; the relative amplitudes of both components are similar to those observed for **QD1** and **QD2**. As expected, the decrease in photoluminescence lifetime is more substantial for **QD1-MC** than **QD2-MC**, akin to the results observed for the organic soluble constructs.

The FRET interaction between the QD donor and corrole acceptors in the micelle constructs was characterized using both steady-state and time-resolved methods. Due to a 3 nm (90 cm^{-1}) red shift in the emission spectrum of **QD-MC** relative to QD, the spectral overlap in the micelle constructs is nominally decreased (Fig. S10†). For **QD1-MC** and **QD2-MC**, the photoluminescence intensity is decreased by 90% and 78%, respectively, compared to **QD-MC** (Fig. 5a). Using the lifetime data of Table 1 and eqn (2), the FRET efficiency for **QD1-MC** is

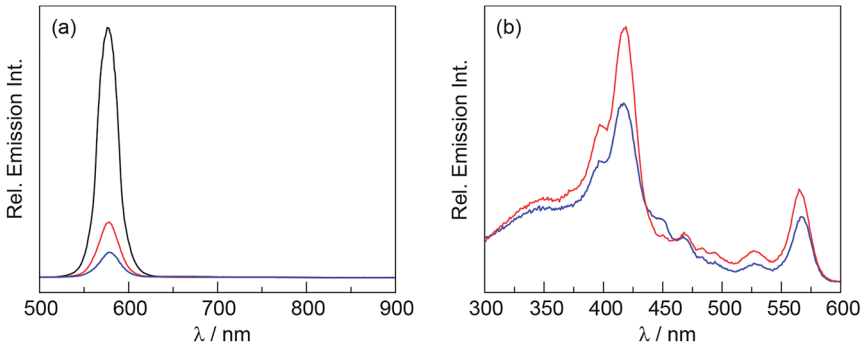

Fig. 5 (a) Emission spectra (λ_{ex} = 470 nm) of QD-MC (▬), QD1-MC (▬), and QD2-MC (▬) in PBS at equivalent quantum dot loading. (b) Excitation spectra (λ_{em} = 780 nm) of concentration matched solutions of QD1-MC (▬) and QD2-MC (▬) in PBS.

93% while this value is 66% for **QD2-MC**, which is a substantial increase relative to **QD2** in toluene (22%). A summary of the FRET parameters is presented in Table S2.† The Förster distance (R_0) for the micelles is ~1 nm shorter than for the self-assembled constructs. The primary reason for this is the substantial decrease in the photoluminescence quantum yield of the donor (see eqn (3)). This manifests in a substantial decrease in the average donor–acceptor distance r for both micelle constructs. However, the distance r for **QD2-MC** is ~1.3 nm longer than that for **QD1-MC** (r = 3.94 nm). The FRET interaction is also observed in the excitation spectra of the micelles (Fig. 5b). As observed for the organic soluble assembles, a substantial emission signal is observed at λ < 370 nm where QD absorption dominates, indicating that it is the FRET donor.

Triplet corrole lifetimes were measured for both aerated and f–p–t samples of **QD1-MC** and **QD2-MC** in PBS. Decay traces at t > 100 ns were fit to a biexponential decay function (R_{adj}^2 > 0.99) and the results are summarized in Table 2. For f–p–t samples, the long component (85% relative amplitude) of **QD1-MC** is similar to the lifetime of **1** alone; in the case of **QD2-MC**, it is longer than that observed for either **2** or **QD2**. In both cases, the short component (15% relative amplitude) is substantially shorter (20–30 μs). The phosphorescence quantum yields are higher than the free acceptor (1.4 fold increase for **QD1-MC**), but they are not as high as those observed for the toluene soluble analogues. Using the lifetimes and quantum yields, we may estimate k_{nr} and k_r using eqn (6). Since the lifetimes are biexponential and the quantum yield is a steady-state measurement that cannot disentangle the two components, the values for the rate constants can only be bracketed. For both micelle constructs, the values of both the radiative and non-radiative rate constants are similar: k_r = 35–155 s^{-1} and k_{nr} = 1–5 × 10^4 s^{-1}.

The oxygen sensitivity of **QD1-MC** and **QD2-MC** is maintained in PBS. Each sample was purged with five different gases to construct a Stern–Volmer plot: ambient air (255 μM O_2), 10% O_2 (121 μM O_2), 5% O_2 (61 μM O_2), 1% O_2 (12 μM O_2), and argon (0 μM O_2). All data fit to a biexponential decay function and each component was analysed according to eqn (7). The data from these experiments is plotted in Fig. 6 for both the long and short component of each construct. The long component is well-behaved and exhibits a bimolecular quenching rate

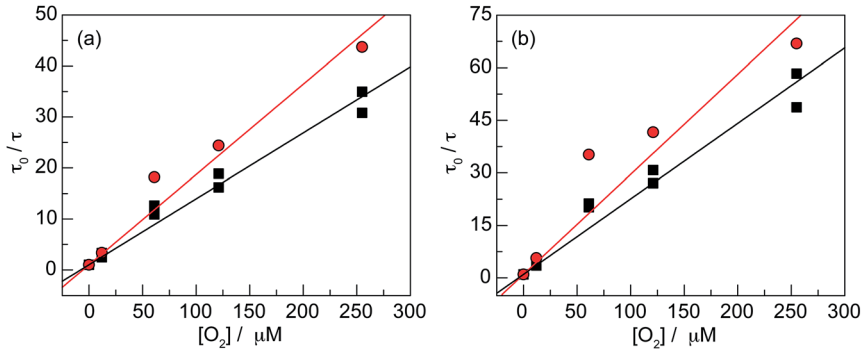

Fig. 6 Stern–Volmer plots for (a) **QD1-MC** and (b) **QD2-MC** in PBS. These plots were constructed using pre-mixed gases. Each plot shows the long (■) and short (●) components of the biexponential fit.

constant that is 1.9–2.5 times longer than the k_q determined for the free corroles (2×10^9 M^{-1} s^{-1}). The short component is substantially more variable, but reasonable fits ($R_{adj}^2 > 0.938$) were obtained. It was found that this data gave values of k_q that are near the diffusion limit (8–9 $\times$ 10^9 M^{-1} s^{-1}).

Discussion

Supramolecular assembly of QD-based donor–acceptor FRET pairs represents a rapid and facile method of conjugate formation. It enables precise control over the donor–acceptor ratio and circumvents the laborious synthesis of multidentate amphiphilic polymers. Consistent with the observation that fluorophores with terminal carboxylic acids efficiently bind to the surface of QDs,[41,42] the equilibrium constant for the association of **1** to QD is 1.62×10^6 M^{-1}. The binding of the carboxylic acid moiety of **1** proceeds by ligand exchange at surface Zn(II) ions, displacing the native oleic acid ligand. This value is quite similar to the K_A for the surface binding of a Pd(II) porphyrin with a single 4-pyridyl substituent: 1.36×10^6 M^{-1}.[21] For porphyrins, we[21] and others[43,44] have shown that two adjacent binding groups in a *cis* disposition have binding constants that are an order of magnitude higher. As a result, a *cis*-A_2B derivative of **1** or an A_3 tri-carboxylic acid corrole, though synthetically more challenging,[45] will likely further increase the association constant and lead to higher FRET efficiencies, and by extension, the emission signal from the acceptor. Based on the lower $K_A = 4.86 \times 10^4$ M^{-1} for **2**, non-specific binding of corrole to QD is not significant. Quenching of QD emission by **2** only occurs at high equivalency of the acceptor. The substantially longer FRET distance r between the QD and **2** (9.12 nm) as compared to **1** (5.70 nm) suggests that the non-specific interaction is derived from the intercalation of compound within the hydrophobic capping ligands of the QD.

The phosphorescence lifetimes of **QD1** and **QD2** in toluene exhibit mono-exponential decay kinetics, indicating a homogeneous environment (surface bound to the QD for **1** or dispersed in the capping ligands for **2**). The lifetimes of the corroles in conjugates **QD1** and **QD2** are longer than the free phosphor, thus leading to an increase in the phosphorescence quantum yield. The greater

increase for **QD1** as compared to **QD2** indicates that surface binding constrains the geometry of the corrole and results in attenuated nonradiative decay processes relative to non-specifically associated corrole with the surface ligands.

Encapsulation of the pre-formed organic soluble conjugates **QD1** and **QD2** proceeds facilely by sonication. All of the corrole equivalents in **QD1** are associated to the QD surface, and hence they are carried into the micelle **QD1-MC**. We note, however, that high loadings are also achieved for **QD2-MC**; the absorption spectrum of the construct indicates that 9 out of the 10 added equivalents of **2** were incorporated into the micelle, demonstrating that surface binding is not a pre-requisite for incorporation of the acceptor into the micelle: non-specific interactions with the QD surface ligand are sufficient. Notwithstanding, surface binding of the acceptor leads to a high FRET efficiency: $E = 0.93$ for **QD1-MC** *vs.* $E = 0.66$ for **QD2-MC**. With the increase in FRET efficiency of **QD1-MC** relative to **QD1**, in conjunction with the decrease in quantum yield of **QD-MC** relative to the native QD, the average donor–acceptor distance decreases from 5.70 nm in **QD1** to 3.94 nm in the micelle. This distance corresponds to the measured metrics of each component. Based on the bright field TEM data of Fig. S3,† the radius of the QD is 2.88 nm. From the crystal structure of compound **2**, the distance between the methyl group of the ester (in order to approximate the bond between the carboxylate group and the metal atom on the QD surface) and the gold centre is 1.11 nm. The QD to corrole centre-to-centre distance based on structural metrics is 3.99 nm, which is remarkably similar to the calculated value of 3.94 nm obtained from FRET measurements.

The phosphorescence lifetime of the corrole in both constructs, **QD1-MC** and **QD2-MC**, exhibits biexponential decay kinetics, indicating that the corrole resides in two distinct environments within the micelle. The long component is attributed to corrole associated with the QD surface, while the short component is ascribed to free corrole residing within the micelle. These results are consistent with our observations for the QD|porphyrin micelles, where biexponential kinetics were observed for the Pd(II) porphyrin.[22] For the corrole conjugates, each component exhibits a linear Stern–Volmer relationship as a function of oxygen. The long component is well behaved and exhibits a bimolecular quenching constant (k_q) that is $\sim 2 \times 10^9\ M^{-1}\ s^{-1}$; the short component of $\sim 9 \times 10^9\ M^{-1}\ s^{-1}$ is at the diffusion limit. For sensing applications only corroles at the surface of the QD can be excited *via* FRET by two-photon excitation because the QD is the two-photon antenna. Free corrole within the micelle cannot be excited, and hence emission decay from this population is absent under two-photon excitation conditions. In this regard, the two-photon experiment is ideal for *in vivo* sensing for self-assembled chemosensors, as the experiment naturally selects for a single population of chemosensors which are associated to the QD. Background signal from unassociated chemosensors is absent, since this population cannot directly be excited under two-photon conditions. This is a powerful property of the micelle approach for sensing applications.

Conclusions

Micelle encapsulation represents a scalable method of synthesizing QD nanosensors and circumvents laborious multi-step polymer syntheses required for coating QDs for covalent conjugation to a chemosensor. Using this technique, we

prepare self-assembled and micelle encapsulated conjugates of Au(III) corroles and CdSe/ZnS QDs. For the organic soluble assemblies, all of the corrole equivalents associate with the QD in some way: surface bound in the case of the carboxylic acid **1**, or loosely associated with the capping ligand at the solvent interface for the methyl ester **2**. Because of the efficient surface binding of **1**, static quenching of QD photoluminescence and FRET efficiency are much greater than for **2**. Due to the large size of the QD, all of the added corrole equivalents are associated with the QD as supported by the observation of monoexponential decay kinetics of corrole phosphorescence and the incorporation of all the added corrole equivalents into the micelle. Within the micelle, the corrole phosphorescence exhibits biexponential decay owing to the acceptor residing in two distinct environments within the micelle: corrole tightly bound or associated with the QD surface (long component) and free corrole dispersed in the lipids of the micelle (short component). In terms of O_2 sensing, the long component is well behaved and may serve as a robust metric for sensing oxygen, as this is the only population that may be excited under two-photon conditions. These results establish micelle encapsulation as an ideal vehicle to implement sensing *via* FRET signal transduction pathways in QD-donor|acceptor constructs.

Acknowledgements

This material is based upon work supported by the U.S. Department of Energy Office of Science, Office of Basic Energy Sciences under Award No. DE-SC0009758. C. M. L. acknowledges the National Science Foundation's Graduate Research Fellowship Program. We thank Yue Chen for preparing the CdSe/ZnS quantum dots, Andrew Maher for assistance with experiments using the Libra-F-He laser system, and Dr Thomas Kempa for acquiring the TEM images.

References

1 P. Vaupel, F. Kallinowski and P. Okunieff, *Cancer Res.*, 1989, **49**, 6449–6465.
2 G. Helmlinger, F. Yuan, M. Dellian and R. K. Jain, *Nat. Med.*, 1997, **3**, 177–182.
3 G. Helmlinger, A. Sckell, M. Dellian, N. S. Forbes and R. K. Jain, *Clin. Cancer Res.*, 2002, **8**, 1284–1291.
4 C. M. Lemon, P. N. Curtin, R. C. Somers, A. B. Greytak, R. M. Lanning, R. K. Jain, M. G. Bawendi and D. G. Nocera, *Inorg. Chem.*, 2014, **53**, 1900–1915.
5 C. B. Murray, D. J. Norris and M. G. Bawendi, *J. Am. Chem. Soc.*, 1993, **115**, 8706–8715.
6 G. W. Walker, V. C. Sundar, C. M. Rudzinski, A. W. Wun, M. G. Bawendi and D. G. Nocera, *Appl. Phys. Lett.*, 2003, **83**, 3555–3557.
7 S. A. Blanton, A. Dehestani, P. C. Lin and P. Guyot-Sionnest, *Chem. Phys. Lett.*, 1994, **229**, 317–322.
8 D. R. Larson, W. R. Zipfel, R. M. Williams, S. W. Clark, M. P. Bruchez, F. W. Wise and W. W. Webb, *Science*, 2003, **300**, 1434–1436.
9 C. Xu and W. R. Zipfel, Multiphoton Excitation of Fluorescent Probes, *Handbook of Biomedical Nonlinear Optical Microscopy*, ed. B. R. Master and P. T. C. So, Oxford University Press, 2008, pp. 311–333.
10 C. Xu and W. W. Webb, *J. Opt. Soc. Am. B*, 1996, **13**, 481–491.

11 C. Xu, W. Zipfel, J. B. Shear, R. M. Williams and W. W. Webb, *Proc. Natl. Acad. Sci. U. S. A.*, 1996, **93**, 10763–10768.
12 W. R. Zipfel, R. M. Williams and W. W. Webb, *Nat. Biotechnol.*, 2003, **21**, 1369–1377.
13 R. K. Jain, M. F. Booth, T. P. Padera, L. L. Munn, D. Fukumura and E. Brown, Applications of Nonlinear Intravital Microscopy in Tumor Biology, *Handbook of Biomedical Nonlinear Optical Microscopy*, ed. B. R. Master and P. T. C. So, Oxford University Press, 2008, pp. 735–756.
14 R. C. Somers, M. G. Bawendi and D. G. Nocera, *Chem. Soc. Rev.*, 2007, **36**, 579–591.
15 T. Förster, *Ann. Phys.*, 1948, **437**, 55–75.
16 A. P. Alvisatos, *J. Phys. Chem.*, 1996, **100**, 13226–13239.
17 P. T. Snee, R. C. Somers, G. Nair, J. P. Zimmer, M. G. Bawendi and D. G. Nocera, *J. Am. Chem. Soc.*, 2006, **128**, 13320–13321.
18 R. C. Somers, R. M. Lanning, P. T. Snee, A. B. Greytak, R. K. Jain, M. G. Bawendi and D. G. Nocera, *Chem. Sci.*, 2012, **3**, 2980–2985.
19 E. R. Kay, J. Lee, D. G. Nocera and M. G. Bawendi, *Angew. Chem., Int. Ed.*, 2013, **52**, 1165–1169.
20 E. J. McLaurin, A. B. Greytak, M. G. Bawendi and D. G. Nocera, *J. Am. Chem. Soc.*, 2009, **131**, 12994–13001.
21 C. M. Lemon, E. Karnas, M. G. Bawendi and D. G. Nocera, *Inorg. Chem.*, 2013, **52**, 10394–10406.
22 C. M. Lemon, E. Karnas, X. Han, O. T. Bruns, T. J. Kempa, D. Fukumura, M. G. Bawendi, R. K. Jain, D. G. Duda and D. G. Nocera, *J. Am. Chem. Soc.*, 2015, **137**, 9832–9842.
23 W. Liu, M. Howarth, A. B. Greytak, Y. Zheng, D. G. Nocera, A. Y. Ting and M. G. Bawendi, *J. Am. Chem. Soc.*, 2008, **130**, 1274–1284.
24 W. Liu, A. B. Greytak, J. Lee, C. R. Wong, J. Park, L. F. Marshall, W. Jiang, P. N. Curtin, A. Y. Ting, D. G. Nocera, D. Fukumura, R. K. Jain and M. G. Bawendi, *J. Am. Chem. Soc.*, 2010, **132**, 472–483.
25 K. Susumu, H. T. Uyeda, I. L. Medintz, T. Pons, J. B. Delehanty and H. Mattoussi, *J. Am. Chem. Soc.*, 2007, **129**, 13987–13996.
26 G. R. Fulmer, A. J. M. Miller, N. H. Sherden, H. E. Gottlieb, A. Nudelman, B. M. Stoltz, J. E. Bercaw and K. I. Goldberg, *Organometallics*, 2010, **29**, 2176–2179.
27 K. Rurack and M. Spieles, *Anal. Chem.*, 2011, **83**, 1232–1242.
28 M. Grabolle, M. Spieles, V. Lesnyak, N. Gaponik, A. Eychmüller and U. Resch-Genger, *Anal. Chem.*, 2009, **81**, 6285–6294.
29 A. A. Pizano, D. A. Lutterman, P. G. Holder, T. S. Teets, J. Stubbe and D. G. Nocera, *Proc. Natl. Acad. Sci. U. S. A.*, 2012, **109**, 39–43.
30 P. G. Holder, A. A. Pizano, B. L. Anderson, J. Stubbe and D. G. Nocera, *J. Am. Chem. Soc.*, 2012, **134**, 1172–1180.
31 Z. H. Loh, S. E. Miller, C. J. Chang, S. D. Carpenter and D. G. Nocera, *J. Phys. Chem. A*, 2002, **106**, 11700–11708.
32 J. R. Lakowicz, *Principles of Fluorescence Spectroscopy*, Springer, 3rd edn, 2006.
33 I. Z. Steinberg, *Annu. Rev. Biochem.*, 1971, **40**, 83–114.
34 F. C. Chen and S. J. Chen, *Opt. Lett.*, 2006, **31**, 187–189.
35 *CRC Handbook of Chemistry and Physics*, CRC Press, 84th edn, 2003.

36 A. Javier, D. Magana, T. Jennings and G. F. Strouse, *Appl. Phys. Lett.*, 2003, **83**, 1423–1425.
37 M. Jones, S. S. Lo and G. D. Scholes, *Proc. Natl. Acad. Sci. U. S. A.*, 2009, **106**, 3011–3016.
38 K. D. Bonin and T. J. McIlrath, *J. Opt. Soc. Am. B*, 1984, **1**, 52–55.
39 S. A. Blanton, M. A. Hines, M. E. Schmidt and P. Guyot-Sionnest, *J. Lumin.*, 1996, **70**, 253–268.
40 B. Dubertret, P. Skourides, D. J. Norris, V. Noireaux, A. H. Brivanlou and A. Libchaber, *Science*, 2002, **298**, 1759–1762.
41 T. Ren, P. K. Mandal, W. Erker, Z. Liu, Y. Avlasevich, L. Puhl, K. Müllen and T. Basché, *J. Am. Chem. Soc.*, 2008, **130**, 17242–17243.
42 L. Dworak, V. V. Matylitsky, T. Ren, T. Basché and J. Wachtveitl, *J. Phys. Chem. C*, 2014, **118**, 4396–4402.
43 E. Zenkevich, F. Cichos, A. Shulga, E. P. Petrov, T. Blaudeck and C. von Borczyskowski, *J. Phys. Chem. B*, 2005, **109**, 8679–8692.
44 E. I. Zenkevich, E. I. Sagun, V. N. Knyukshto, A. S. Stasheuski, V. A. Galievsky, A. P. Stupak, T. Blaudeck and C. von Borczyskowski, *J. Phys. Chem. C*, 2011, **115**, 21535–21545.
45 C. M. Lemon and P. J. Brothers, *J. Porphyrins Phthalocyanines*, 2011, **15**, 809–834.

ACS Catalysis

Research Article

pubs.acs.org/acscatalysis

Theoretical Analysis of Cobalt Hangman Porphyrins: Ligand Dearomatization and Mechanistic Implications for Hydrogen Evolution

Brian H. Solis,[†] Andrew G. Maher,[‡] Tatsuhiko Honda,[‡] David C. Powers,[‡] Daniel G. Nocera,[‡] and Sharon Hammes-Schiffer*[,†]

[†]Department of Chemistry, University of Illinois at Urbana-Champaign, 600 South Mathews Avenue, Urbana, Illinois 61801, United States

[‡]Department of Chemistry and Chemical Biology, Harvard University, 12 Oxford Street, Cambridge, Massachusetts 02138-2902, United States

Supporting Information

ABSTRACT: The design of molecular electrocatalysts for hydrogen evolution has been targeted as a strategy for the conversion of solar energy to chemical fuels. In cobalt hangman porphyrins, a carboxylic acid group on a xanthene backbone is positioned over a metalloporphyrin to serve as a proton relay. A key proton-coupled electron transfer (PCET) step along the hydrogen evolution pathway occurs via a sequential ET-PT mechanism in which electron transfer (ET) is followed by proton transfer (PT). Herein theoretical calculations are employed to investigate the mechanistic pathways of these hangman metalloporphyrins. The calculations confirm the ET-PT mechanism by illustrating that the calculated reduction potentials for this mechanism are consistent with experimental data. Under strong-acid conditions, the calculations indicate that this catalyst evolves H_2 by protonation of a formally Co(II) hydride intermediate, as suggested by previous experiments. Under weak-acid conditions, however, the calculations reveal a mechanism that proceeds via a phlorin intermediate, in which the *meso* carbon of the porphyrin is protonated. In the first electrochemical reduction, the neutral Co(II) species is reduced to a monoanionic singlet Co(I) species. Subsequent reduction leads to a dianionic doublet, formally a Co(0) complex in which substantial mixing of Co and porphyrin orbitals indicates ligand redox noninnocence. The partial reduction of the ligand disrupts the aromaticity in the porphyrin ring. As a result of this ligand dearomatization, protonation of the dianionic species is significantly more thermodynamically favorable at the *meso* carbon than at the metal center, and the ET-PT mechanism leads to a dianionic phlorin species. According to the proposed mechanism, the carboxylate group of this dianionic phlorin species is reprotonated, the species is reduced again, and H_2 is evolved from the protonated carboxylate and the protonated carbon. This proposed mechanism is a guidepost for future experimental studies of proton relays involving noninnocent ligand platforms.

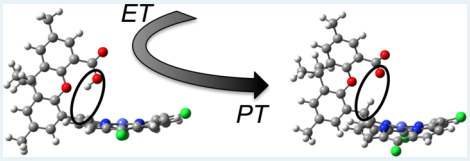

KEYWORDS: *proton-coupled electron transfer, hydrogen evolution reaction, hangman porphyrin, electrocatalyst, proton relay, dearomatization, phlorin*

INTRODUCTION

Efficient conversion of solar energy into chemical bonds is important for global sustainability.[1] The hydrogen evolution reaction (HER), oxidation of water to oxygen, and reduction of CO_2 to hydrocarbons are multielectron, multiproton processes.[2] In these reactions, electron transfer (ET) and proton transfer (PT) steps often occur as proton-coupled electron transfer (PCET) reactions.[3−9] PCET can occur sequentially, with the initial ET or PT forming a stable intermediate, or concertedly, with ET and PT occurring simultaneously. Incorporating proton relays into molecular electrocatalysts facilitates PCET by juxtaposing the proton donor and acceptor.[10−16] A fundamental understanding of PCET through molecular proton relays can assist in the design of efficient HER electrocatalysts.[17−23]

A series of metalloporphyrins has been studied as HER electrocatalysts in acetonitrile.[24,25] In the case of the cobalt "hangman" porphyrin ([**1**-H], Chart 1), in which a carboxylic acid group affixed to a xanthene backbone is positioned over a metalloporphyrin capable of electrochemical reduction, a PCET step along the HER pathway was shown to occur by a sequential ET-PT mechanism. Specifically, the formal Co(I) state was proposed to be reduced to Co(0) and then quickly protonated intramolecularly from the hangman moiety to form a Co(II) hydride intermediate. Electrokinetic studies revealed the intramolecular PT rate constant to be ca. 8.5×10^6 s^{-1}.[25] The non-hangman analogue [**2**] (Chart 1) behaves similarly to [**1**-H] electrochemically but evolves hydrogen at a more negative potential (E_{cat}[**1**] ≈ −1.9 V vs Fc^+/Fc; E_{cat}[**2**] ≈ −2.1 V vs Fc^+/Fc) with benzoic acid due to the lack of an internal proton relay.[24]

Received: September 24, 2014
Revised: November 3, 2014
Published: November 6, 2014

   dx.doi.org/10.1021/cs501454y | ACS Catal. 2014, 4, 4516−4526

Chart 1. Structure of Cobalt Porphyrins

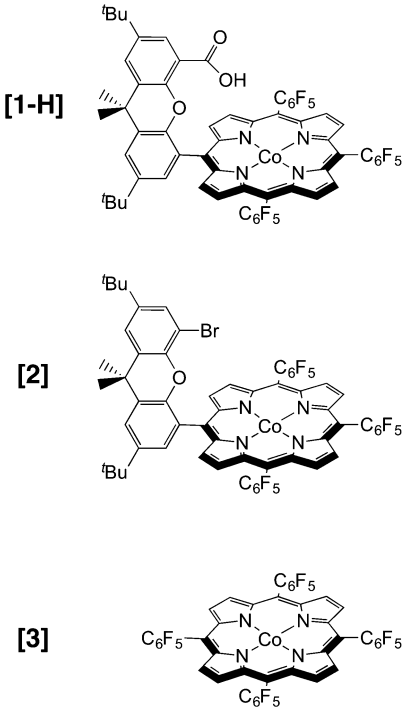

In this work, we employ computational methods to investigate potential mechanisms of hydrogen evolution catalyzed by cobalt metalloporphyrins. NMR experiments were performed to probe the spin state of $[\mathbf{3}]^-$ (Chart 1) to assist in the selection of a suitable level of theory. We investigate several intramolecular PT pathways by allowing the proton to transfer from the hangman moiety of [**1-H**] to the cobalt center, a pyrrolic nitrogen, or the closest *meso* carbon. Calculated relative pK_as are used to explore additional intermolecular PT steps preceding H_2 production. Reduction potentials are calculated for the ET steps in the ET-PT, PT-ET, and concerted PCET mechanisms for all proton acceptors. Additionally, we calculate a transition state structure for the PT reaction within the experimentally proposed ET-PT mechanism and employ transition state theory to calculate a first-order PT rate constant to compare to previous experimental results. On the basis of the calculations, we propose mechanisms for the HER catalyzed by Co hangman porphyrins in both weak- and strong-acid regimes.

COMPUTATIONAL METHODS

The complexes were optimized with density functional theory (DFT), primarily with the BP86 functional.[26,27] Additional benchmarking was performed with the following functionals and is presented in the Supporting Information: B3P86,[26,28] B3LYP,[28,29] BLYP,[27,29] TPSSh,[30] M06L,[31] and ωB97XD.[32−35] Geometry optimizations were performed with the 6-31+G(d,p)[36] basis set for the transferring proton and the 6-31+G(d)[37−39] basis set for all remaining atoms with default options in Gaussian 09.[40] The results presented in the main paper are based on the structures optimized in solution; structures optimized in the gas phase are provided in the Supporting Information and are similar to those optimized in solution. Calculations in acetonitrile solvent utilized the conductor-like polarizable continuum model (C-PCM)[41,42] with Bondi radii and included nonelectrostatic interactions resulting from dispersion,[43,44] repulsion,[44] and cavity formation.[45] Entropic and zero-point energy effects from the vibrational frequencies at T = 298.15 K were included in the calculation of the reaction free energies. The free energies of the solvated molecules calculated with geometries optimized in the gas phase, which are presented in the Supporting Information, employed a Born−Haber thermodynamic cycle that combined gas-phase free energies with single-point solvation free energies of the reactant and product species.[46,47] For computational tractability, the pentafluorophenyl groups were replaced with chlorines and the *tert*-butyl groups were replaced with methyl groups. These substitutions were chosen on the basis of similar electron-donating or electron-withdrawing properties as determined by their Hammett constants (Table S1, Supporting Information).[48,49]

Reduction potentials were calculated using the relation $\Delta G^\circ_{redox} = -nFE^\circ$, where n is the number of transferring electrons, F is Faraday's constant, and ΔG°_{redox} is the free energy of reduction. The free energies of reduction were calculated using the expression $\Delta G^\circ_{redox} = \Delta H^\circ - T\Delta S^\circ$ for structures optimized in solution. Reference reactions were utilized in the calculation of reduction potentials to eliminate systematic errors in DFT, limitations in the basis sets and exchange-correlation functionals, and changes in standard states.[46,47] All reduction potentials were calculated with respect to the ferrocenium/ferrocene couple (Fc^+/Fc) in acetonitrile. Axial solvent ligands may bind to an open octahedral site of cobalt d^7 complexes, consistent with the crystal structure of a related Co(II) hangman porphyrin that contains an axial ligand.[50] Given the excellent agreement of the calculated Co(II/I) and Co(I/0) reduction potentials with experiment, however, no axial solvent ligands were explicitly included in the calculations. In some cases, an explicit water molecule was included to test the effects of residual water on possible intramolecular proton transfer mechanisms.

The pK_a calculations were performed using the relation $\Delta G^\circ_{pK_a} = [\ln(10)RT]pK_a$, where $\Delta G^\circ_{pK_a}$ is the free energy of deprotonation. The free energies of deprotonation were calculated using the expression $\Delta G^\circ_{pK_a} = \Delta H^\circ - T\Delta S^\circ$ for structures optimized in solution. Relative pK_as were calculated with experimentally known references: the deprotonation of $[\mathbf{1}\text{-}\mathbf{H}]^0$ (determined to be 20.2 in acetonitrile)[51] and the deprotonation of the Co hydride $[\mathbf{3}\text{-}\mathbf{H}_{Co}]^0$ (estimated to be 15.0). This latter estimate stems from the rise in a catalytic wave of [**1-H**] and [**2**] at ca. −1.5 V vs Fc^+/Fc with *p*-toluenesulfonic (tosic) acid (pK_a = 8.0)[52] but not benzoic acid (pK_a = 20.7),[53] providing a range of plausible Co(III) hydride pK_a values.[24] The choice of pK_a = 15.0 for $[\mathbf{3}\text{-}\mathbf{H}_{Co}]^0$ is validated by calculations of relative pK_as that fall in the appropriate range. As with reduction potentials, systematic errors in DFT cancel in the calculation of relative pK_as.[47] Two pK_a references are needed in the calculations to obtain reasonable pK_a values of singly and multiply protonated complexes. All calculations that result in the deprotonated $[\mathbf{1}]^-$, $[\mathbf{1}]^{2-}$, or $[\mathbf{1}]^{3-}$ are calculated with respect to the $[\mathbf{1}\text{-}\mathbf{H}]^0$ pK_a reference, while all other calculated relative pK_as are calculated with respect to the $[\mathbf{3}\text{-}\mathbf{H}_{Co}]^0$ pK_a reference.

A transition state for PT was calculated with the synchronous transit-guided quasi-Newton method.[54,55] The reactant and product states were aligned in Cartesian space and interpolated to obtain the average structure, which was used as a guess for the transition state geometry. The transition state structure was

dx.doi.org/10.1021/cs501454y | ACS Catal. 2014, 4, 4516−4526

confirmed to contain a single imaginary frequency corresponding to the PT mode. The intrinsic reaction coordinate was followed backward and forward to the expected reactant and product species. The free energy barrier for PT was used in conjunction with transition state theory to calculate the PT rate constant:

$$k_{PT} = \frac{k_B T}{h} \exp\left(\frac{-\Delta G^{\ddagger}}{k_B T}\right) \quad (1)$$

where k_B is Boltzmann's constant, T is the temperature, h is Planck's constant, and $\Delta G^{\ddagger}$ is the free energy barrier. Here we are neglecting the effects of dynamical barrier recrossings and tunneling.

RESULTS AND DISCUSSION

Electronic Structure and H_2 Evolution Mechanism of [3]. Analyses of the spin densities and molecular orbitals of [3] provide insight into the electronic structure of the cobalt porphyrins along the hydrogen evolution reaction pathway. The low-spin Co(II) complex $[3]^0$ is reduced to singlet Co(I) $[3]^-$, the spin state of which was determined by ^{1}H NMR (Figure S1, Supporting Information) and is consistent with literature reports for other one-electron-reduced Co porphyrins.[56,57] The formally Co(0) structure $[3]^{2-}$ was calculated to be a doublet with spin density on the cobalt approximately 0.5, suggesting substantial metal−ligand orbital mixing with partial reduction of the ligand. On the basis of the computed spin density, we describe the formally Co(0) structure as Co("0.5"). The highest occupied molecular orbitals (HOMOs) of $[3]^-$ and $[3]^{2-}$ are depicted in Figure 1. The HOMO of $[3]^-$ is a cobalt-centered d_{z^2} orbital, which indicates that $[3]^0$ is reduced at cobalt to form Co(I). This observation is consistent with previous calculations performed with BLYP indicating a cobalt-centered d_{z^2} lowest unoccupied molecular orbital of $[3]^0$.[58] The HOMO of $[3]^{2-}$ has mixed metal/ligand character, suggesting that $[3]^-$ is reduced equally at both the metal and the porphyrin, forming Co("0.5"). This characterization differs from our previous calculations on the nickel analogue of [3] indicating that the singly occupied molecular orbital (SOMO) of the monoanion is σ^* $d_{x^2-y^2}$ on the nickel and the highest SOMO of the triplet dianion is nearly entirely ligand based.[59] For both cobalt and nickel, the HOMO of the lowest-energy dianion has some ligand character, breaking the aromaticity in the porphyrin ring.

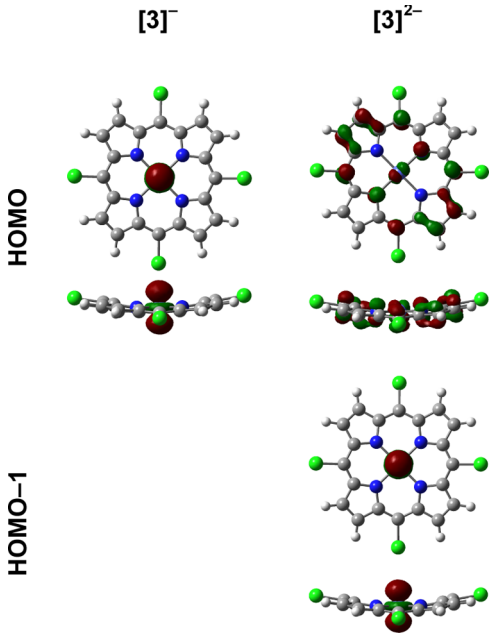

Figure 1. Top (upper structures) and side (lower structures) views of HOMOs of $[3]^-$ and $[3]^{2-}$ and HOMO-1 of $[3]^{2-}$ (isovalue 0.05). The HOMO of $[3]^-$ and the HOMO-1 of $[3]^{2-}$, corresponding to the paired α spin orbital, have d_{z^2} character. The HOMO of $[3]^{2-}$, corresponding to the unpaired α spin orbital, has mixed metal−ligand character. Color scheme: purple, Co; blue, N; gray, C; green, Cl; white, H.

Relative free energies of protonated $[3]^-$ and $[3]^{2-}$ were calculated for three proton acceptor sites: the cobalt center, a pyrrolic nitrogen, and a carbon at the *meso* position of the ring (Table 1 and Table S6 (Supporting Information)). The three protonated species are denoted $[3\text{-}H_{Co}]$, $[3\text{-}H_N]$, and $[3\text{-}H_C]$ for protonation at cobalt, nitrogen, and carbon, respectively. $[3\text{-}H]^0$, which corresponds to protonated $[3]^-$, is most stable when protonated at the cobalt center ($[3\text{-}H_{Co}]^0$) as a singlet. $[3\text{-}H]^-$, which corresponds to protonated $[3]^{2-}$, is most stable when protonated at the *meso* carbon, forming the phlorin complex $[3\text{-}H_C]^-$. Note that the aromaticity in the porphyrin ring of Co("0.5") in $[3]^{2-}$ is already broken because the unpaired electron is shared nearly equally by the metal and ligands. Formation of a phlorin stabilizes the remaining conjugation in the ring. Due to the puckering of the porphyrin ring, two protonated structures are possible when protonating at the *meso* carbon, and both structures were considered.

Table 1. Calculated Relative Free Energies and Spin Densities on Cobalt for [3-H]

complex	S^a	rel free energy^b	$\rho_{Co}{}^c$
$[3\text{-}H_{Co}]^0$	0	0.00	0.00
$[3\text{-}H_N]^0$	0	15.4	0.00
$[3\text{-}H_C]^{0\,d}$	0	13.3	0.00
$[3\text{-}H_{Co}]^0$	1	32.3	0.19
$[3\text{-}H_N]^0$	1	20.9	1.30
$[3\text{-}H_C]^{0\,d}$	1	4.3	1.05
$[3\text{-}H_{Co}]^-$	1/2	0.00	0.03
$[3\text{-}H_N]^-$	1/2	13.4	0.47
$[3\text{-}H_C]^{-\,d}$	1/2	−12.2	0.96

^{a}*S* indicates the total spin of the system. ^{b}Free energies in kcal/mol relative to the closed-shell singlet $[3\text{-}H_{Co}]^0$ for the neutral species and $[3\text{-}H_{Co}]^-$ for the monoanions. ^{c}Mulliken spin density on Co. ^{d}Geometry in which the proton binds from the top. When the proton binds from the bottom, the relative free energy of singlet $[3\text{-}H_C]^0$ is 7.9 kcal/mol, and the chlorine atom dissociates for triplet $[3\text{-}H_C]^0$ and for $[3\text{-}H_C]^-$.

H_2 evolution mechanisms by [3] can be analyzed from the calculated reduction potentials and pK_as of the relevant intermediates. Selected calculated pK_as are given in Table 2, and the calculated reduction potentials are given in Table 3. Additional relative pK_as and reduction potentials calculated from structures optimized in the gas phase are provided in Tables S12−S15 (Supporting Information). The agreement between the calculated and experimental reduction potentials provides validation of the computational methodology. Cyclic voltammograms (CVs) of [3] showed that the second reduction peak ($E_{1/2}$ = −1.98 V vs Fc^+/Fc) becomes catalytic upon addition of benzoic acid (pK_a = 20.7 in acetonitrile).[25] On

dx.doi.org/10.1021/cs501454y | ACS Catal. 2014, 4, 4516−4526

Table 2. Calculated Relative pK_as[a]

complex	pK_a
[**1**-***H***]^0	*20.2* (20.2)[b]
[**1**-***H***]$^-$	22.3
[**1**-***H***]$^{2-}$	22.5
[**1**-***H***$_{Co}$]$^-$	16.6
[**1**-***H***$_{Co}$]$^{2-}$	22.5
[**1**-***H***$_C$]$^-$	12.2
[**1**-***H***$_C$]$^{2-}$	31.0
[**3**-***H***$_{Co}$]^0	*15.0* (8.0−20.7)[c]
[**3**-***H***$_{Co}$]$^-$	24.1 (>20.7)[c]
[**3**-***H***$_C$]^0	9.2
[**3**-***H***$_C$]$^-$	33.1
[**3**-H$_C$***H***$_{Co}$]^0	10.6
[**3**-H$_C$***H***$_{Co}$]$^-$	27.6
[**1**-H***H***$_{Co}$]^0	16.2 (8.0−20.7)[c]
[**1**-H***H***$_{Co}$]$^-$	24.9 (>20.7)[c]
[**1**-H***H***$_C$]^0	10.5
[**1**-H***H***$_C$]$^-$	30.5
[**1**-H$_C$***H***$_{Co}$]^0	3.3
[**1**-H$_C$***H***$_{Co}$]$^-$	14.4
[**1**-***H***H$_C$]^0	20.6
[**1**-***H***H$_C$]$^-$	22.0

[a]Calculated relative pK_as are given in acetonitrile for the deprotonation of the italicized proton relative to the pK_a of [**1**-***H***]^0 or [**3**-***H***$_{Co}$]^0. (See Computational Methods for an explanation of the choice of references.) The experimental values are given in parentheses. The italicized calculated pK_as were used as references and agree with experiment by construction. [b]Experiment from ref 51. [c]Estimate from experimental range in ref 24.

Table 3. Calculated Reduction Potentials[a]

ox	red	$E°$	mechanism
[**3**]^0	[**3**]$^-$	−*1.00* (−1.00)[b]	
[**3**]$^-$	[**3**]$^{2-}$	−1.98 (−1.98)	
[**2**]^0	[**2**]$^-$	−1.01 (−1.10)	
[**2**]$^-$	[**2**]$^{2-}$	−2.10 (−2.14)	
[**1**-**H**]^0	[**1**-**H**]$^-$	−1.03 (−1.08)	
[**1**-**H**]$^-$	[**1**-**H**]$^{2-}$	−2.00	ET-PT
[**1**-**H**]$^-$	[**1**-**H**$_{Co}$]$^{2-}$	−2.00	concerted
[**1**-**H**]$^-$	[**1**-**H**$_N$]$^{2-}$	−2.50	concerted
[**1**-**H**]$^-$	[**1**-**H**$_C$]$^{2-}$ [c]	−1.50	concerted
[**1**-**H**$_{Co}$]$^-$	[**1**-**H**$_{Co}$]$^{2-}$	−1.66	PT-ET
[**1**-**H**$_N$]$^-$	[**1**-**H**$_N$]$^{2-}$	−2.35	PT-ET
[**1**-**H**$_C$]$^-$ [c]	[**1**-**H**$_C$]$^{2-}$ [c]	−0.90	PT-ET
[**3**-**H**$_{Co}$]^0	[**3**-**H**$_{Co}$]$^-$	−1.44	
[**3**-**H**$_C$]$^-$	[**3**-**H**$_C$]$^{2-}$	−1.61	
[**3**-**H**$_C$**H**$_{Co}$]$^-$	[**3**-**H**$_C$**H**$_{Co}$]$^{2-}$	−1.96	
[**1**-**HH**$_{Co}$]^0	[**1**-**HH**$_{Co}$]$^-$	−1.49 (−1.5)	
[**1**-**HH**$_C$]$^-$	[**1**-**HH**$_C$]$^{2-}$	−1.65	

[a]Values are given in volts vs Fc$^+$/Fc in acetonitrile. Experimental values of $E_{1/2}$ are given in parentheses, as obtained from ref 50 for [**3**] and ref 24 for [**1**-**H**] and [**2**]. [b]$E_{1/2}$([**3**]^0/[**3**]$^-$) was used as the reference and agrees by construction. [c]The value is for the geometry without the large structural rearrangement. With the large structural rearrangement, $E°$([**1**-**H**]$^-$/[**1**-**H**$_C$]$^{2-}$) = −1.51 V vs Fc$^+$/Fc for the concerted mechanism and is the same to within the numerical accuracy given for the PT-ET mechanism. Thus, the values for the two geometries are the same to within the accuracy of the computational method.

the basis of our calculations, Co("0.5") in [**3**]$^{2-}$ would become protonated predominantly at the *meso* carbon to form [**3**-**H**$_C$]$^-$ (pK_a = 33), although it is thermodynamically favorable for [**3**-**H**$_{Co}$]$^-$ to be formed as well (pK_a = 24). With a sufficiently strong acid, Co(I) in [**3**]$^-$ could become protonated to form a Co(III) hydride intermediate, [**3**-**H**$_{Co}$]^0.

Figure 2 presents the experimental CVs for [**1**-**H**] and [**2**] in the absence of external acid as well as in the presence of

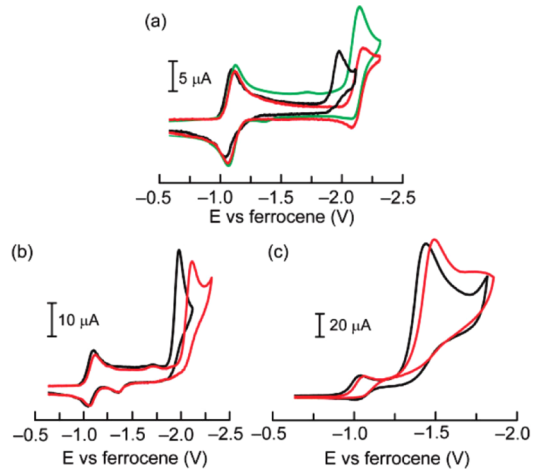

Figure 2. (a) CVs of 0.5 mM [**1**-**H**] (black line), [**2**] (red line), and [**2**] in the presence of 0.5 mM benzoic acid (green line) in acetonitrile. (b) CVs of 0.5 mM [**1**-**H**] in the presence of 2.5 mM benzoic acid (black line) and 0.5 mM [**2**] in the presence of 3.0 mM benzoic acid (red line) in acetonitrile. (c) CVs of 0.8 mM [**1**-**H**] (black line) and [**2**] (red line) in the presence of 10 mM tosic acid. Reproduced with permission from ref 24. Copyright 2011 American Chemical Society.

benzoic acid or tosic acid. For [**1**-**H**] and [**2**], addition of tosic acid (pK_a = 8.0 in acetonitrile)[52] gives rise to a new catalytic peak at ca. −1.5 V vs Fc$^+$/Fc in cyclic voltammetry (depicted in Figure 2c), proposed to be the Co(III/II) hydride peak.[24] The calculated reduction potential $E°$([**3**-**H**$_{Co}$]^0/[**3**-**H**$_{Co}$]$^-$) = −1.44 V vs Fc$^+$/Fc is consistent with the Co(III/II) hydride assignment in these complexes. Free energy diagrams for thermodynamically favorable H_2 evolution catalyzed by [**3**] with tosic and benzoic acid are provided in Figures S4 and S5 (Supporting Information), respectively.

Electronic Structure and Characterization of [1-H]. The complex [**1**-**H**] differs from [**3**] in that one pentafluorophenyl group is replaced with a xanthene group that contains the hangman moiety. The calculated spin densities on Co for [**1**-**H**]^0 and [**1**-**H**]$^{2-}$, which are both doublets, are 1.06 and 0.42, respectively. These spin densities are very similar to those calculated for [**3**]^0 and [**3**]$^{2-}$ (1.00 and 0.40, respectively). Because of the presence of the xanthene group, the puckering of the porphyrin ring of [**1**-**H**] can adopt two structural minima not present in [**3**]. The global minima for [**1**-**H**]^0 and [**1**-**H**]$^-$ correspond to the porphyrin ring puckered upward ($\Delta G°$ = −0.5 and −0.1 kcal/mol, respectively), while the global minimum for [**1**-**H**]$^{2-}$ corresponds to the porphyrin ring puckered downward ($\Delta G°$ = −1.3 kcal/mol). Additional local minima ($\Delta G°$ = ∼3−4 kcal/mol for each puckering conformation) were found in which the proton in the hanging moiety is positioned over the porphyrin ring instead of pointing toward the xanthene ether oxygen. Figure 3 depicts optimized structures of [**1**-**H**]$^-$ (puckered upward) and [**1**-**H**]$^{2-}$ (puckered downward) with the proton pointing toward the xanthene ether oxygen or hanging over the porphyrin ring. The puckering of the ring and the position of the hanging proton

dx.doi.org/10.1021/cs501454y | ACS Catal. 2014, 4, 4516−4526

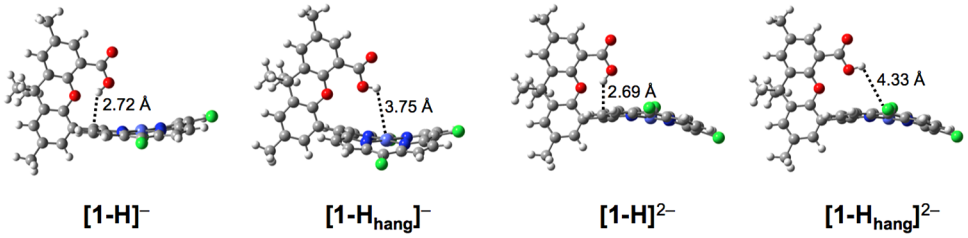

Figure 3. Optimized structures of $[\mathbf{1}\text{-H}]^-$ with the porphyrin ring puckered upward and $[\mathbf{1}\text{-H}]^{2-}$ with the porphyrin ring puckered downward. The global minimum for each species is the structure with the proton pointing toward the xanthene ether oxygen with the porphyrin ring puckering shown here. The H−C and H−Co distances are provided for the structures with the carboxylic acid proton pointing toward the xanthene ether oxygen (left) and hanging over the porphyrin ring (right), respectively, for each species. The associated O−C and O−Co distances are given in the main text. Color scheme: purple, Co; blue, N; gray, C; green, Cl; red, O; white, H.

may affect the identity of the proton acceptor and the structure of $[\mathbf{1}\text{-H}]$ after intramolecular PT. Note that all of these minima may be thermally accessible at 298.15 K, although the equilibrium populations of the minima with the carboxylic acid proton positioned over the porphyrin rings will be 150−850 times lower than those with the proton pointing toward the xanthene ether oxygen for both puckering conformations.

We explored three proton acceptor sites: the cobalt center, a pyrrolic nitrogen, and a carbon at the *meso* position of the ring. The calculated proton donor−acceptor distances and donor−proton−acceptor angles for the global and local minima of $[\mathbf{1}\text{-H}]^-$, which is the relevant species for both the sequential PT-ET mechanism and the concerted PCET mechanism, are given in Table S8 (Supporting Information). Intramolecular PT is favored in geometries with a short equilibrium proton donor−acceptor distance. In the global minimum geometry, the ideal proton acceptor candidate is the *meso* carbon, which has a proton donor−acceptor distance of 3.54 Å. The donor−proton−acceptor angle is also the most linear at 139.6°. If the proton were to transfer to the cobalt or a pyrrolic nitrogen, the proton would most likely need to be positioned over the porphyrin ring, as in the local minimum geometry $[\mathbf{1}\text{-H}_{\mathbf{hang}}]^-$ (ΔG° = +3.1 kcal/mol) depicted in Figure 3. In this local minimum geometry, PT to the cobalt center as well as to the two pyrrolic nitrogen atoms farthest from the xanthene becomes more probable due to the decrease in the proton donor−acceptor distance and increase in the donor−proton−acceptor angle. The H−C and H−Co distances with the proton pointing toward the xanthene ether oxygen and hanging over the porphyrin ring, respectively, are shown in Figure 3 for $[\mathbf{1}\text{-H}]^-$ and $[\mathbf{1}\text{-H}]^{2-}$.

The proton donor−acceptor distances and donor−proton−acceptor angles for the global and local minima of $[\mathbf{1}\text{-H}]^{2-}$, the relevant species for the sequential ET-PT mechanism, are given in Table S9 (Supporting Information). Similar to $[\mathbf{1}\text{-H}]^-$, the global minimum of $[\mathbf{1}\text{-H}]^{2-}$ favors transfer of the proton to the nearest *meso* carbon, which has the shortest proton donor−acceptor distance (3.51 Å) and the most linear donor−proton−acceptor angle (139.6°). Adoption of the local minimum in which the proton is hanging over the porphyrin ring (ΔG° = +3.9 kcal/mol) does not drastically improve the proton donor−acceptor interface for any of the remaining acceptors. Thus, for any of the proposed mechanisms, structural features of the hangman moiety suggest that the likely proton acceptor is the closest *meso* carbon.

The relative free energies and spin densities on Co of $[\mathbf{1}\text{-H}]$ after intramolecular PT, denoted $[\mathbf{1}\text{-H}_{\mathbf{Co}}]$, $[\mathbf{1}\text{-H}_{\mathbf{N}}]$, and $[\mathbf{1}\text{-H}_{\mathbf{C}}]$ for cobalt, nitrogen, and carbon acceptors, respectively, were also calculated for the monoanion and dianion (Table 4 and Table S10 (Supporting Information)). For the monoanion, the proton is most stable on the nitrogen acceptor ($[\mathbf{1}\text{-H}_{\mathbf{N}}]^-$) as a singlet, although this species is still higher in free energy than if the proton had remained on the oxygen acceptor ($[\mathbf{1}\text{-H}]^-$; ΔG°_{PT} = +3.4 kcal/mol). For the dianion, the proton is most stable on the carbon acceptor ($[\mathbf{1}\text{-H}_{\mathbf{C}}]^{2-}$; ΔG°_{PT} = −11.6 kcal/mol), and the spin density on Co is approximately unity. As in the case for [**3**], two different structures are possible following PT. When the porphyrin ring is puckered downward, a large structural rearrangement occurs in which the porphyrin ring bends away from the hangman moiety. When the porphyrin ring is puckered upward, this structural rearrangement does not occur. The latter structure is 0.4 kcal/mol lower in free energy than the former structure. Most importantly, the phlorin $[\mathbf{1}\text{-H}_{\mathbf{C}}]^{2-}$ is the global minimum for the doubly reduced species (ΔG°_{PT} = −11.6 kcal/mol), while $[\mathbf{1}\text{-H}_{\mathbf{Co}}]^{2-}$ has a free energy nearly identical with that of $[\mathbf{1}\text{-H}]^{2-}$ (ΔG°_{PT} = −0.02 kcal/mol).

Table 4. Calculated Relative Free Energies and Spin Densities on Cobalt for $[\mathbf{1}\text{-H}]$ after Intramolecular Proton Transfer

complex	S^a	rel free energy^b	$\rho_{Co}{}^c$
$[\mathbf{1}\text{-H}_{\mathbf{Co}}]^-$	0	7.8	0.00
$[\mathbf{1}\text{-H}_{\mathbf{N}}]^-$	0	3.4	0.00
$[\mathbf{1}\text{-H}_{\mathbf{C}}]^{-\,d}$	0	18.4	0.00
$[\mathbf{1}\text{-H}_{\mathbf{C}}]^{-\,e}$	0	21.9	0.00
$[\mathbf{1}\text{-H}_{\mathbf{Co}}]^-$	1	42.2	0.19
$[\mathbf{1}\text{-H}_{\mathbf{N}}]^-$	1	20.9	1.35
$[\mathbf{1}\text{-H}_{\mathbf{C}}]^{-\,d}$	1	14.2	1.09
$[\mathbf{1}\text{-H}_{\mathbf{C}}]^{-\,e}$	1	13.8	1.17
$[\mathbf{1}\text{-H}_{\mathbf{Co}}]^{2-}$	1/2	−0.02	0.04
$[\mathbf{1}\text{-H}_{\mathbf{N}}]^{2-}$	1/2	11.4	0.47
$[\mathbf{1}\text{-H}_{\mathbf{C}}]^{2-\,d}$	1/2	−11.2	0.99
$[\mathbf{1}\text{-H}_{\mathbf{C}}]^{2-\,e}$	1/2	−11.6	1.08

^{a}*S* indicates the total spin of the system. ^{b}Free energies are given in kcal/mol relative to the closed-shell singlet $[\mathbf{1}\text{-H}]^-$ for the monoanions and $[\mathbf{1}\text{-H}]^{2-}$ for the dianions. ^{c}Mulliken spin density on Co. ^{d}Geometry with large structural rearrangement. ^{e}Geometry without large structural rearrangement.

To determine if residual water may impact the thermodynamics, we also performed calculations with an explicit water molecule that can hydrogen bond with the hangman moiety and thereby potentially facilitate proton transfer (Table S11 (Supporting Information)). The relative free energies of the monoanion and dianion Co hydrides and phlorin complexes

dx.doi.org/10.1021/cs501454y | ACS Catal. 2014, 4, 4516−4526

changed by at most 1.5 kcal/mol in the presence of a water molecule. Thus, the addition of water has little effect on the thermodynamics of cobalt hydride formation. Qualitatively, the only difference that arises due to the addition of water is the energetic ordering of the local minima that differ in the position of the carboxylic acid proton of the hangman moiety. When a water molecule is present, the carboxylic acid proton is more stable when it is positioned over the porphyrin ring because it can readily hydrogen bond with the water molecule, whereas when a water molecule is not present, it is more stable when it is positioned toward the xanthene ether oxygen.

The calculated reduction potentials of the Co porphyrins are provided in Table 3. This table includes the reduction potentials of [**2**], which behaves electrochemically similarly to [**1-H**] but lacks the proton relay. The excellent agreement with experimentally measured reduction potentials provides further validation of the computational methods. For [**1-H**], the reduction potentials were calculated for the structures before and after intramolecular PT as well as for concerted PCET. The reduction potential before PT, $E^\circ([\mathbf{1\text{-}H}]^-/[\mathbf{1\text{-}H}]^{2-}) = -2.00$ V vs Fc^+/Fc, is equivalent to the reduction potential for concerted PCET to the metal center, $E^\circ([\mathbf{1\text{-}H}]^-/[\mathbf{1\text{-}H_{Co}}]^{2-})$, because the dianionic products have nearly identical free energies. For the concerted PCET mechanism, $E^\circ([\mathbf{1\text{-}H}]^-/[\mathbf{1\text{-}H_N}]^{2-}) = -2.50$ V vs Fc^+/Fc is very negative due to the high free energy $[\mathbf{1\text{-}H_N}]^{2-}$ product, and $E^\circ([\mathbf{1\text{-}H}]^-/[\mathbf{1\text{-}H_C}]^{2-}) = -1.50$ V vs Fc^+/Fc is more positive due to the stability of the $[\mathbf{1\text{-}H_C}]^{2-}$ phlorin product. For the PT-ET mechanism, $E^\circ([\mathbf{1\text{-}H_C}]^-/[\mathbf{1\text{-}H_C}]^{2-}) = -0.90$ V vs Fc^+/Fc (for either conformer) is very positive because the oxidized state $[\mathbf{1\text{-}H_C}]^-$ is the product of a thermodynamically unfavorable PT. These reduction potentials will be analyzed in the context of possible PCET mechanisms in the next subsection.

PCET Mechanism of [1-H]. The PCET mechanism of [**1-H**] was previously investigated with experimental and simulated CVs.[25] The hypothesis that PCET proceeds via the ET-PT mechanism was studied by analysis of the catalytic peak potential, E_p, which has the following form for a fast, reversible ET followed by intramolecular PT:

$$E_p = E^\circ - 0.78\frac{RT}{F} + \frac{RT}{2F}\ln\left(\frac{RT}{F}\frac{k_{PT}}{\nu}\right) \quad (2)$$

where E° is the reversible potential of the ET step, k_{PT} is the proton transfer rate constant, and ν is the scan rate of the CV. If the mechanism is ET-PT, the plot of $(E_p - E^\circ)F/RT$ versus $\ln \nu$ should be linear with a slope of -0.5. Experimental CVs revealed a linear plot at low scan rates but a distinct curvature at high scan rates, which can be ascribed to kinetic competition between the ET and PT steps. The experimentally observed anodic shift of ~200 mV of the catalytic wave of [**1-H**] relative to [**2**] (depicted in Figure 2a by the black and red CVs), called the "hangman effect,"[30] arises from two distinct phenomena: the positive charge of the proton proximal to the metal center, which causes a shift in $E^\circ([\mathbf{1\text{-}H}]^-/[\mathbf{1\text{-}H}]^{2-})$ relative to $E^\circ([\mathbf{2}]^-/[\mathbf{2}]^{2-})$, and the effect of the ET-PT mechanism, which causes a shift in the peak position relative to $E^\circ([\mathbf{1\text{-}H}]^-/[\mathbf{1\text{-}H}]^{2-})$, as described by eq 2.[25]

The proton transfer rate constant, k_{PT}, was extracted from the simulated CVs that reproduced the experimental peak positions as a function of scan rate. Because the formally Co(I/0) couple of [**1-H**] is irreversible (Figure 2), the reduction potential $E^\circ([\mathbf{1\text{-}H}]^-/[\mathbf{1\text{-}H}]^{2-})$ was assumed to be similar to that of [**2**] in the CV simulations.[25] Our calculations show that the formal reduction potential $E^\circ([\mathbf{1\text{-}H}]^-/[\mathbf{1\text{-}H}]^{2-})$ is ~100 mV less negative than $E^\circ([\mathbf{2}]^-/[\mathbf{2}]^{2-})$ (Table 3). This shift in the thermodynamic reduction potential is most likely due to the presence of the proton proximal to the metal center. Additional CV simulations could be performed to determine the sensitivity of the extracted intramolecular PT rate constant to the thermodynamic reduction potential. In comparison to the experimental $E_{cat}[\mathbf{1}] \approx -1.9$ V vs Fc^+/Fc with benzoic acid (Figure 2b), our calculated $E^\circ([\mathbf{1\text{-}H}]^-/[\mathbf{1\text{-}H}]^{2-}) = -2.00$ V vs Fc^+/Fc implies an additional anodic shift of 100 mV in peak position due to the subsequent PT step, as described by eq 2. According to our calculated relative free energies of the dianion, PT is only thermodynamically favorable from $[\mathbf{1\text{-}H}]^{2-}$ to $[\mathbf{1\text{-}H_C}]^{2-}$ ($\Delta G^\circ = -11.6$ kcal/mol, $K_{eq} = 3.2 \times 10^8$ at 298.15 K).

To determine the rate constant of intramolecular PT from $[\mathbf{1\text{-}H}]^{2-}$ to $[\mathbf{1\text{-}H_C}]^{2-}$, which is thermodynamically favorable, we calculated the transition state structure. The porphyrin ring of the global minimum structure of $[\mathbf{1\text{-}H_C}]^{2-}$ ($S = 1/2$, spin density of 1.08 on Co) is puckered upward. We found a local minimum of $[\mathbf{1\text{-}H}]^{2-}$ that is similarly puckered upward and denote this local minimum structure $[\mathbf{1'\text{-}H}]^{2-}$ ($\Delta G^\circ = +1.3$ kcal/mol, $K_{eq} = 0.1$ at 298.15 K). The puckering of the porphyrin ring in $[\mathbf{1\text{-}H}]^{2-}$ does not affect the spin density on the cobalt ($\rho_{Co} = 0.42$ for both puckering configurations) according to the calculations. We calculated the transition state structure associated with PT from $[\mathbf{1'\text{-}H}]^{2-}$ to $[\mathbf{1\text{-}H_C}]^{2-}$. The resulting transition state structure, denoted $[\mathbf{1}^\ddagger]^{2-}$, has a single imaginary frequency of 1377 cm^{-1} that corresponds to the PT mode and a spin density of 0.59 on Co. The proton is positioned 1.22 Å from the donor oxygen and 1.51 Å from the acceptor carbon at a proton donor–acceptor distance of 2.69 Å and a donor–proton–acceptor angle of 161°. Following the intrinsic reaction coordinate (IRC) from this transition state structure leads to the minima corresponding to $[\mathbf{1'\text{-}H}]^{2-}$ and $[\mathbf{1\text{-}H_C}]^{2-}$. The free energy of $[\mathbf{1}^\ddagger]^{2-}$ is 9.0 kcal/mol higher than that of $[\mathbf{1'\text{-}H}]^{2-}$. According to transition state theory, the resulting PT rate constant is 1.4×10^6 s^{-1} at 298.15 K. This rate constant is consistent with the experimentally determined intramolecular PT rate constant of ca. 8.5×10^6 s^{-1}, which corresponds to an 8.0 kcal/mol free energy barrier.[25] The reaction free energy pathway for intramolecular PT from the carboxylic acid to the *meso* carbon in $[\mathbf{1\text{-}H}]^{2-}$ is depicted in Figure 4. Note that the free energy barrier for PT to the Co center is expected to be much larger on the basis of the H–Co distance of 4.33 Å, in contrast to the H–C distance of 2.69 Å at the global minimum.

The results of these computational studies are consistent with the experiments suggesting that the PCET reaction proceeds via an ET-PT mechanism. The PT-ET mechanism can be discounted due to the unfavorable thermodynamics of PT from the Co(I) species to certain potential proton acceptors (Table 4 and Table S10 (Supporting Information)), the structure of the proton donor–acceptor interface (Table S8 (Supporting Information)), and the subsequent reduction potentials (Table 3). Experimentally, $E_{cat}[\mathbf{1}] \approx -1.9$ V vs Fc^+/Fc with benzoic acid, which is anodically shifted ~200 mV from the Co(I/0) potential. Proton transfer to the carbon, $\Delta G^\circ([\mathbf{1\text{-}H}]^- \rightarrow [\mathbf{1\text{-}H_C}]^-) = \sim 14$ kcal/mol, is thermodynamically unfavorable. As a result, the subsequent reduction potential, $E^\circ([\mathbf{1\text{-}H_C}]^-/[\mathbf{1\text{-}H_C}]^{2-}) = -0.90$ V vs Fc^+/Fc, is artificially positive. Proton transfer to the cobalt,

dx.doi.org/10.1021/cs501454y | ACS Catal. 2014, 4, 4516–4526

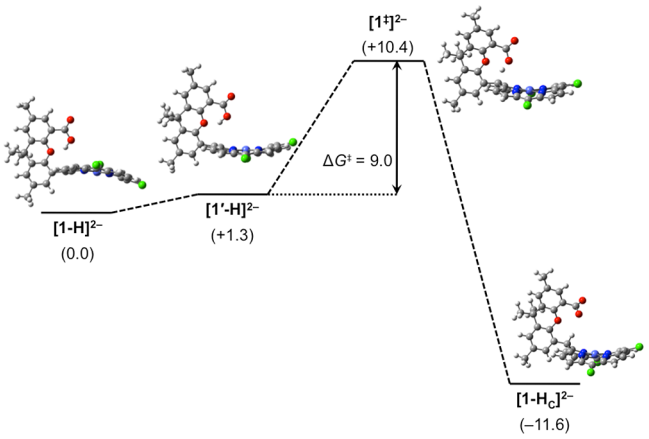

Figure 4. Calculated reaction free energy pathway for intramolecular PT of $[\mathbf{1}\text{-H}]^{2-}$. Free energies are given in kcal/mol relative to $[\mathbf{1}\text{-H}]^{2-}$. Ring puckering forms the local minimum $[\mathbf{1}'\text{-H}]^{2-}$, after which the proton transfers to generate $[\mathbf{1}\text{-H}_\mathbf{C}]^{2-}$ through the transition state $[\mathbf{1}^{\ddagger}]^{2-}$. Color scheme: purple, Co; blue, N; gray, C; green, Cl; red, O; white, H.

$\Delta G^\circ([\mathbf{1}\text{-H}]^- \rightarrow [\mathbf{1}\text{-H}_{Co}]^-)$ = 7.8 kcal/mol, is also thermodynamically unfavorable. The subsequent reduction potential, $E^\circ([\mathbf{1}\text{-H}_{Co}]^-/[\mathbf{1}\text{-H}_{Co}]^{2-})$ = −1.66 V vs Fc^+/Fc, is reasonable, although the proton donor−acceptor interface does not structurally favor formation of a cobalt hydride. Finally, proton transfer to a nitrogen, $\Delta G^\circ([\mathbf{1}\text{-H}]^- \rightarrow [\mathbf{1}\text{-H}_N]^-)$ = 3.4 kcal/mol, is thermodynamically accessible but is followed by reduction at $E^\circ([\mathbf{1}\text{-H}_N]^-/[\mathbf{1}\text{-H}_N]^{2-})$ = −2.35 V vs Fc^+/Fc, which is much too negative in comparison to the catalytic potential $E_{cat}[\mathbf{1}] \approx$ −1.9 V vs Fc^+/Fc with benzoic acid.

The concerted PCET reaction can also be excluded on the basis of our calculations. The calculated reduction potentials for concerted PCET from $[\mathbf{1}\text{-H}]^-$ to $[\mathbf{1}\text{-H}_\mathbf{C}]^{2-}$ or $[\mathbf{1}\text{-H}_N]^{2-}$ are −1.50 V vs Fc^+/Fc and −2.50 V vs Fc^+/Fc, respectively. The phlorin product is highly stabilized, leading to a reduction potential that is too positive in comparison to $E_{cat}[\mathbf{1}] \approx$ −1.9 V vs Fc^+/Fc with benzoic acid, whereas the nitrogen acceptor product is highly destabilized, leading to a reduction potential that is too negative. Concerted PCET from $[\mathbf{1}\text{-H}]^-$ to $[\mathbf{1}\text{-H}_{Co}]^{2-}$ (E° = −2.00 V vs Fc^+/Fc) is unlikely, due to the long proton donor−acceptor distance (O−Co = 4.21 Å), as the rate constant of concerted PCET is proportional to the square of the overlap integral between the proton vibrational wave functions localized on the proton donor and acceptor, respectively.[6,9] Thus, although electrochemical PCET rate theory[6,14,60] could be used to analyze the kinetics of the concerted PCET mechanism, the calculated reduction potentials and structural characteristics are not consistent with this mechanism.

Hydrogen Evolution by [1-H]. Experimental studies have shown that [**1**-H] and [**2**] evolve H_2 at ca. −1.5 V vs Fc^+/Fc with tosic acid and at more negative potentials (−1.9 V vs Fc^+/Fc and −2.1 V vs Fc^+/Fc, respectively) with benzoic acid, as depicted in Figure 2. Complex [**2**] lacks an internal proton relay and is thus expected to evolve H_2 in a fashion similar to that for [**3**]. The precise mechanism for H_2 evolution by [**1**-H], however, is complicated by the "hangman" moiety of the xanthene backbone. The calculated free energy diagrams for H_2 evolution by [**1**-H] and a complete mechanistic cycle are depicted in Figure 5.

The top left of Figure 5 corresponds to the reaction with benzoic acid and an applied potential of −1.9 V vs Fc^+/Fc. In this case, after the PCET reaction discussed above (steps 2 and 3 in Figure 5), the resulting dianionic phlorin $[\mathbf{1}\text{-H}_\mathbf{C}]^{2-}$ can become protonated at the carboxylate from benzoic acid to form the doubly protonated $[\mathbf{1}\text{-HH}_\mathbf{C}]^-$ (step 4). Note that the calculated pK_a is 22.0 for deprotonation of the carboxylate in $[\mathbf{1}\text{-HH}_\mathbf{C}]^-$ and is 14.4 for deprotonation of Co in $[\mathbf{1}\text{-H}_\mathbf{C}\text{H}_{Co}]^-$ (Table 2). Because the pK_a of benzoic acid is 20.7, the carboxylate is much more likely to become protonated than the Co of $[\mathbf{1}\text{-H}_\mathbf{C}]^{2-}$. The calculated reduction potential of this species, $[\mathbf{1}\text{-HH}_\mathbf{C}]^-$, is −1.65 V vs Fc^+/Fc, which is less negative than the experimental catalytic potential $E_{cat}[\mathbf{1}] \approx$ −1.9 V vs Fc^+/Fc with benzoic acid and will occur spontaneously (step 5). At this point the free energy diagram branches into two possible pathways that involve either direct H_2 elimination (step 5′) or another reduction followed by H_2 elimination (steps 5 and 6). The calculated free energies for H_2 elimination from $[\mathbf{1}\text{-HH}_\mathbf{C}]^-$ (step 5′) and $[\mathbf{1}\text{-HH}_\mathbf{C}]^{2-}$ (step 6) are 5.7 and −5.9 kcal/mol, respectively. The H−H distance is 1.95 Å for both species; although this H−H distance is relatively long, thermal fluctuations of the molecule will enable sampling of shorter distances. Following the latter pathway, protonation of the carboxylate of $[\mathbf{1}]^{2-}$ (step 7) closes the catalytic cycle, re-forming $[\mathbf{1}\text{-H}]^-$. Following the former pathway, protonation of $[\mathbf{1}]^-$ (step 8′) closes the catalytic cycle, re-forming $[\mathbf{1}\text{-H}]^0$. The pathway that involves $[\mathbf{1}\text{-HH}_\mathbf{C}]^{2-}$ (steps 5−7) is more thermodynamically favorable than the pathway that involves $[\mathbf{1}\text{-HH}_\mathbf{C}]^-$ (steps 5′ and 8′) or than the pathway that requires oxidation of $[\mathbf{1}]^{2-}$ to $[\mathbf{1}]^-$ (step 7′; ΔG° = +17.3 kcal/mol at the applied potential). The proposed mechanistic cycle for H_2 evolution by [**1**-H] and benzoic acid, in conjunction with the formal oxidation states of the metal and formal charges of the ligands of the intermediates, is summarized in Figure 6.

The top right of Figure 5 corresponds to the reaction with tosic acid and an applied potential of −1.49 vs Fc^+/Fc. As for [**2**] and [**3**], addition of tosic acid to [**1**-H] results in protonation of $[\mathbf{1}\text{-H}]^-$ at the Co center, forming $[\mathbf{1}\text{-HH}_{Co}]^0$ (step 9). This species can be reduced at a less negative catalytic potential of $E^\circ([\mathbf{1}\text{-HH}_{Co}]^0/[\mathbf{1}\text{-HH}_{Co}]^-)$ = −1.49 V vs Fc^+/Fc (step 10) to evolve hydrogen with tosic acid (ΔG° = −18.5 kcal/mol, step 11). Note that protonation of $[\mathbf{1}\text{-H}]^-$ by tosic acid is more thermodynamically favorable at the Co center than at the *meso* carbon, as indicated by the calculated pK_as for deprotonation of $[\mathbf{1}\text{-HH}_{Co}]^0$ at the Co center (16.2, Table 2) and for deprotonation of $[\mathbf{1}\text{-HH}_\mathbf{C}]^0$ at the carbon (10.5, Table 2).

CONCLUSIONS

This paper presents a theoretical analysis of a series of cobalt porphyrins, focusing on the impact of the electronic structure on the HER mechanism. The Co(II) porphyrin $[\mathbf{3}]^0$ is electrochemically reduced to the Co(I) porphyrin $[\mathbf{3}]^-$. The ^{1}H NMR spectrum of the chemically reduced tetrabutylammonium salt $\mathbf{TBA}^+[\mathbf{3}]^-$ exhibits a sharp proton peak in the aromatic region, consistent with a diamagnetic Co(I) complex. Subsequent reduction produces a formally Co(0) complex with substantial ligand-based reduction. Calculations indicate that the unpaired electron in the doubly reduced species occupies a molecular orbital with nearly equal contributions from the Co center and the ligands. In contrast to the nickel analogue of [**3**], for which the formally Ni(0) intermediate is a triplet, the monoanionic and dianionic states of [**3**] remain low spin.

dx.doi.org/10.1021/cs501454y | ACS Catal. 2014, 4, 4516−4526

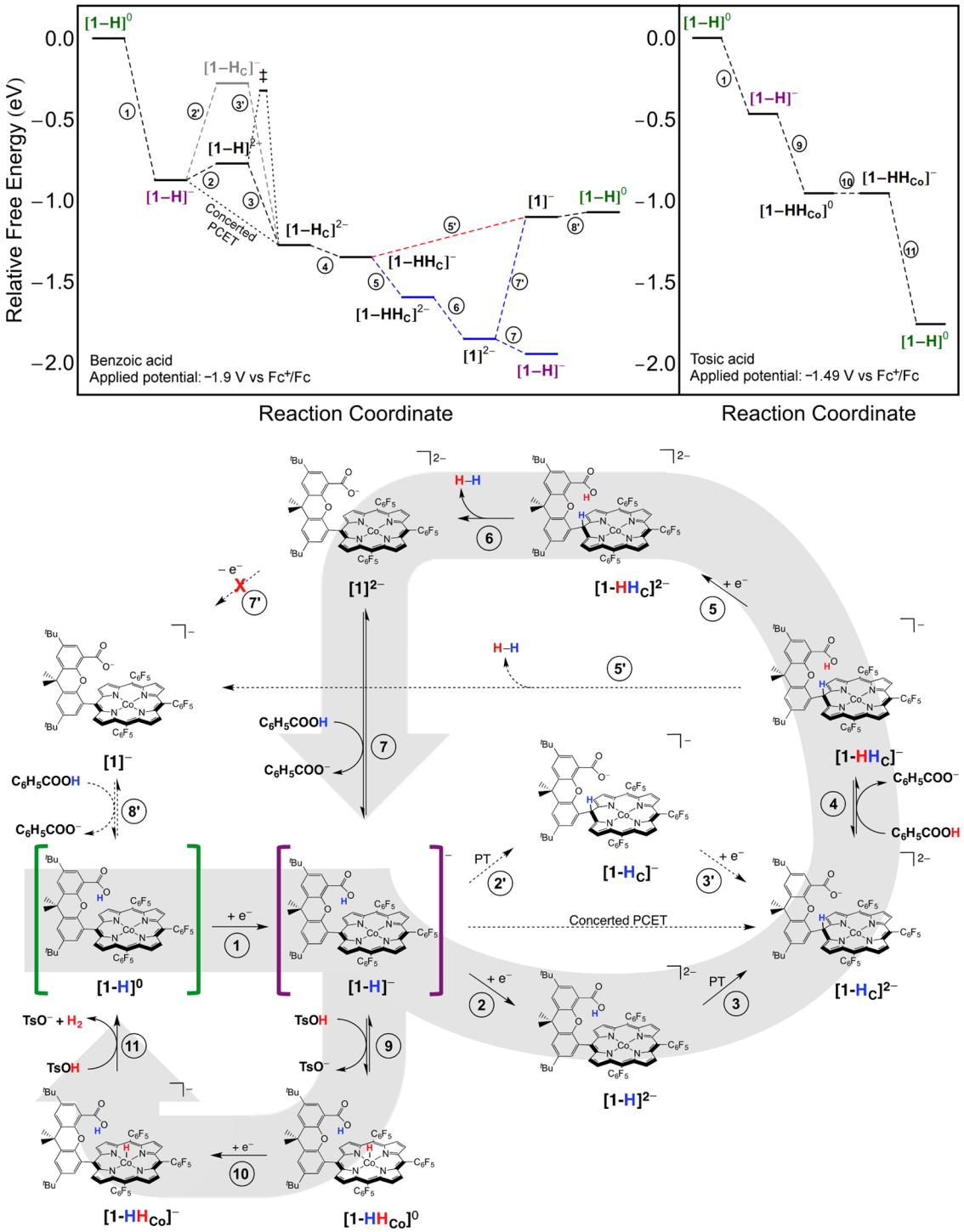

Figure 5. Free energy diagrams (top) for H_2 production catalyzed by [**1**-**H**] with benzoic acid (C_6H_5COOH, pK_a = 20.7)[53] and an applied potential of −1.9 V vs Fc^+/Fc (left) and tosic acid (TsOH, pK_a = 8.0)[52] with an applied potential of −1.49 V vs Fc^+/Fc (right). Complete mechanistic cycle of proposed mechanisms (bottom), where solid arrows indicate thermodynamically favorable pathways and dotted arrows represent thermodynamically unfavorable pathways. The proposed catalytic pathways with weak and strong acids follow the gray arrows in the background of the full catalytic cycle. The catalytic cycle starts with $[\mathbf{1}\text{-}\mathbf{H}]^0$ (shown in green) and is reduced (step 1) to $[\mathbf{1}\text{-}\mathbf{H}]^-$ (shown in purple). With benzoic (weak) acid, the mechanism continues with a PCET step. The proposed PCET mechanism is the sequential ET-PT mechanism (steps 2−3). The intramolecular PT barrier is labeled ‡ in the free energy diagram (top left), and the alternative sequential PT-ET mechanism (steps 2′ and 3′) is shown in gray. The carboxylate of $[\mathbf{1}\text{-}\mathbf{H}_\mathbf{C}]^{2-}$ is protonated (step 4) to form the doubly protonated $[\mathbf{1}\text{-}\mathbf{HH}_\mathbf{C}]^-$. Self-elimination of H_2 from $[\mathbf{1}\text{-}\mathbf{HH}_\mathbf{C}]^-$ (step 5′) is thermodynamically unfavorable, necessitating the reduction to $[\mathbf{1}\text{-}\mathbf{HH}_\mathbf{C}]^{2-}$ (step 5) before H_2 elimination (step 6). The deprotonated $[\mathbf{1}]^{2-}$ is protonated by acid to form $[\mathbf{1}\text{-}\mathbf{H}]^-$ and close the catalytic cycle in step 7. Oxidation of $[\mathbf{1}]^{2-}$ to $[\mathbf{1}]^-$ (step 7′) is very thermodynamically unfavorable (denoted with a red "X") at the applied catalytic potential (ΔG° = +17.3 kcal/mol). If $[\mathbf{1}]^-$ were formed, it could be protonated to form $[\mathbf{1}\text{-}\mathbf{H}]^0$ (step 8′) to close the catalytic cycle. With tosic (strong) acid, $[\mathbf{1}\text{-}\mathbf{H}]^-$ (shown in purple) is protonated at the Co center (step 9), forming the doubly protonated Co(III) hydride $[\mathbf{1}\text{-}\mathbf{HH}_\mathbf{Co}]^0$. After further reduction (step 10), H_2 is evolved with tosic acid (step 11).

dx.doi.org/10.1021/cs501454y | ACS Catal. 2014, 4, 4516−4526

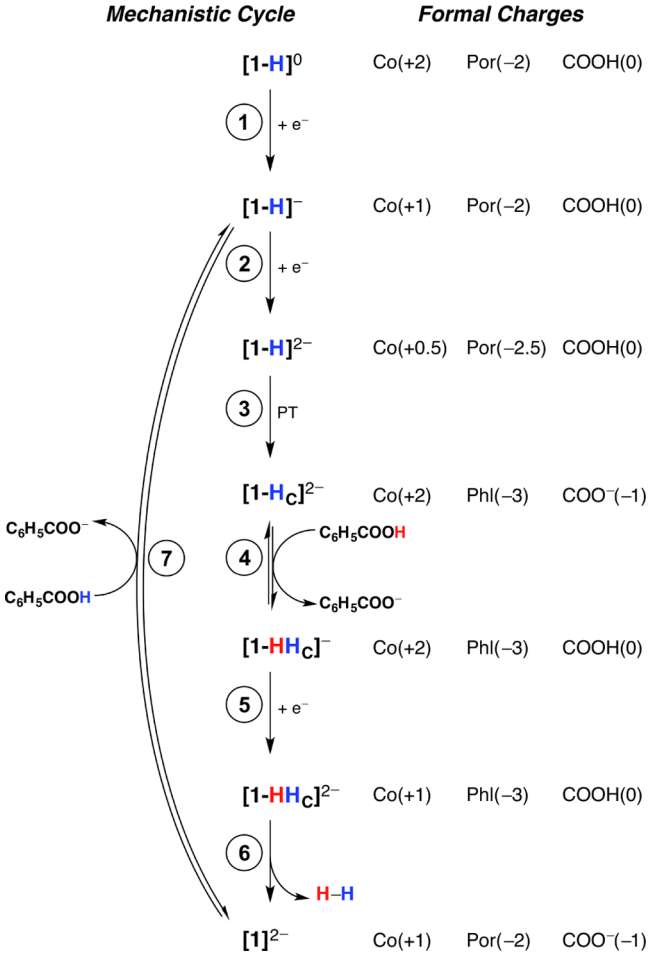

Figure 6. Proposed mechanistic cycle of H_2 evolution catalyzed by [**1**-H] with benzoic acid (left) and formal charges of the intermediates (right). The formal oxidation state of the metal center (Co) and formal charges of the porphyrin ring (Por), phlorin (Phl), carboxylic acid (COOH), and carboxylate (COO^-) are shown.

Formally Co(0) and Ni(0) porphyrin complexes both display some metal(I) character, indicating a significant degree of ligand noninnocence.

These properties of the electronic structure have mechanistic implications, owing to the broken aromaticity in the porphyrin ring of $[\mathbf{3}]^{2-}$. In particular, the ligand dearomatization affects the thermodynamics of the various protonated species. The Co(III) hydride structure $[\mathbf{3}\text{-}\mathbf{H}_{Co}]^0$ was found to be most stable upon protonation of $[\mathbf{3}]^-$, whereas the phlorin product $[\mathbf{3}\text{-}\mathbf{H}_C]^-$ was found to be most stable upon protonation of $[\mathbf{3}]^{2-}$. For $[\mathbf{3}]^-$, which is in the Co(I) oxidation state, protonation at the *meso* carbon would result in breaking the porphyrin aromaticity. For $[\mathbf{3}]^{2-}$, formulated as a mixed Co(I)/Co(0) species with a partially reduced porphyrin ligand, the aromaticity is already broken, and the formation of a phlorin stabilizes the remaining conjugation in the macrocycle.

The related hangman porphyrin [**1**-H], which is enhanced with a proton relay, was found to exhibit similar behavior. Specifically, the formally Co(0) $[\mathbf{1}\text{-H}]^{2-}$ is a mixed Co(I)/Co(0) species with partial ligand reduction. In this case, the HER mechanism is thought to involve an intramolecular PT from the carboxylic acid to another atom within the catalyst. The closest *meso* carbon is the most structurally and thermodynamically favorable proton acceptor site within the proton relay, forming the phlorin $[\mathbf{1}\text{-}\mathbf{H}_C]^{2-}$. As for [**3**], the phlorin stabilizes the ring conjugation due to ligand dearomatization in $[\mathbf{1}\text{-H}]^{2-}$. These properties of the hangman porphyrin have significant implications for the HER mechanism.

The H_2 evolution mechanism was explored for all of these Co porphyrins in weak- and strong-acid regimes, corresponding to experiments performed with benzoic and tosic acids. Under strong-acid conditions, [**1**-H], [**2**], and [**3**] all behave similarly and can evolve H_2 from a Co hydride intermediate. Under weak-acid conditions, [**1**-H] evolves hydrogen at a potential 100−200 mV less negative than that for [**2**] or [**3**].[24] The calculations were consistent with previous experiments indicating that the PCET step following the initial reduction of $[\mathbf{1}\text{-H}]^0$ to $[\mathbf{1}\text{-H}]^-$ occurs by a sequential ET-PT pathway. In this ET-PT pathway, the reduction of $[\mathbf{1}\text{-H}]^-$ to $[\mathbf{1}\text{-H}]^{2-}$ is followed by intramolecular PT. According to the calculations, the most thermodynamically and structurally favorable intramolecular PT reaction produces the dianonic phlorin $[\mathbf{1}\text{-}\mathbf{H}_C]^{2-}$, which differs from the previous proposal of a cobalt hydride intermediate.[25] The calculated free energy barrier and associated rate constant for the PT reaction from the carboxylic acid to the *meso* carbon (9.0 kcal/mol; $k_{PT} = 1.4 \times 10^6\ s^{-1}$) are consistent with the experimentally measured rate constant ($k_{PT} \approx 8.5 \times 10^6\ s^{-1}$). This agreement provides further support for an ET-PT mechanism that generates a phlorin intermediate rather than a metal hydride. Following the sequential ET-PT pathway, the dianionic phlorin $[\mathbf{1}\text{-}\mathbf{H}_C]^{2-}$ may be protonated at the carboxylate to form the doubly protonated species $[\mathbf{1}\text{-}\mathbf{HH}_C]^-$. This complex can be spontaneously reduced at the catalytic potential $E_{cat}[\mathbf{1}] \approx -1.9$ V vs Fc^+/Fc to $[\mathbf{1}\text{-}\mathbf{HH}_C]^{2-}$. Subsequent elimination of H_2 is thermodynamically favorable, yielding a deprotonated $[\mathbf{1}]^{2-}$, which can be protonated from benzoic acid to form $[\mathbf{1}\text{-H}]^-$.

Storing reducing equivalents by reductive dearomatization and carbon-centered protonation, as exemplified in the conversion of $[\mathbf{1}\text{-H}]^0$ to $[\mathbf{1}\text{-}\mathbf{H}_C]^{2-}$, is similar to known strategies for storing formal hydride equivalents in both biology and synthetic chemistry. NADH, the reduction currency in biology, is generated by $2e^-/1H^+$ delivery to NAD^+.[61,62] Reductive protonation of NAD^+ dearomatizes a pyridyl ring and stores reduction equivalents as a hydride on an sp^3 carbon center (Figure 7a). Hantzsch esters represent synthetic analogues of NADH and have been employed as H_2 surrogates in transfer hydrogenation reactions.[63] The reducing equivalents of Hantzsch esters can be generated by reductive dearomatiza-

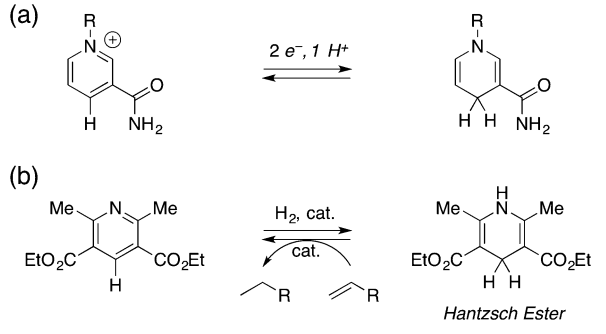

Figure 7. (a) Two-electron, one-proton reduction of NAD^+ generates NADH, in which a reducing equivalent is stored as a hydride at an sp^3 center (R = ADP-ribo). (b) Hantzsch esters are synthetic analogues of NADH and function as hydrogen surrogates in transfer hydrogenation.

dx.doi.org/10.1021/cs501454y | ACS Catal. 2014, 4, 4516−4526

tion of appropriately substituted pyridines (Figure 7b). Similar ligand-centered management of hydride equivalents have also been demonstrated in C-centered frustrated Lewis pair reactions for cleavage of H_2[64] and in dearomative M−L cooperation in Ru-pincer complexes.[65]

Thus, these calculations, supported by related examples from the literature, suggest that the HER mechanism of [**1**-**H**] could involve a phlorin intermediate under weak-acid conditions. This proposed mechanism will require testing and validation by further experimental studies aimed at identifying and characterizing a phlorin intermediate. Free-base phlorins are well-known, isolable compounds, which have been demonstrated to participate in multielectron redox chemistry.[66−70] Unique spectroscopic signatures of the phlorin complexes have been discovered and can be used in future experiments aimed at probing the proposed transient phlorin intermediate.[71] Furthermore, the analogous nickel hangman porphyrins, which have been proposed to follow a sequential PT-ET pathway,[59] may also evolve hydrogen through a phlorin intermediate.

■ ASSOCIATED CONTENT

Supporting Information

The following file is available free of charge on the ACS Publications website at DOI: 10.1021/cs501454y.

Discussion of computational benchmarking, calculation of H_2 production free energies, experimental methods, calculated relative free energies of structures optimized in the gas phase and solution, calculated bond distances and angles, calculated reduction potentials and relative pK_as, ^{1}H NMR and crystal structures of [**3**]$^-$, free energy diagrams of H_2 evolution catalyzed by [**3**] with tosic and benzoic acids, coordinates and energies of structures optimized in solution (PDF)

■ AUTHOR INFORMATION

Corresponding Author

*E-mail for S.H.-S.: shs3@illinois.edu.

Notes

The authors declare no competing financial interest.

■ ACKNOWLEDGMENTS

We are grateful to Thomas B. Rauchfuss, D. Kwabena Bediako, Mioy T. Huynh, Soumya Ghosh, and Alexander Soudackov for meaningful discussion and helpful advice. B.H.S. and S.H.-S. acknowledge support for the computational work by the Center for Chemical Innovation of the National Science Foundation (Solar Fuels, Grant No. CHE-1305124). The contributions by A.G.M., T.H., D.C.P., and D.G.N. are based on work supported by the U.S. Department of Energy Office of Science, Office of Basic Energy Sciences Energy Frontier Research Centers program under Award Number DE-SC0009758.

■ REFERENCES

(1) Lewis, N. S.; Nocera, D. G. *Proc. Natl. Acad. Sci. U.S.A.* **2006**, *103*, 15729−15735.
(2) Nocera, D. G. *Inorg. Chem.* **2009**, *48*, 10001−10017.
(3) Cukier, R. I.; Nocera, D. G. *Annu. Rev. Phys. Chem.* **1998**, *49*, 337−369.
(4) Mayer, J. M. *Annu. Rev. Phys. Chem.* **2004**, *55*, 363−390.
(5) Huynh, M. H. V.; Meyer, T. J. *Chem. Rev.* **2007**, *107*, 5004−5064.
(6) Hammes-Schiffer, S.; Soudackov, A. V. *J. Phys. Chem. B* **2008**, *112*, 14108−14123.
(7) Costentin, C. *Chem. Rev.* **2008**, *108*, 2145−2179.
(8) Costentin, C.; Robert, M.; Savéant, J.-M. *Chem. Rev.* **2010**, *110*, PR1−PR40.
(9) Hammes-Schiffer, S.; Stuchebrukhov, A. A. *Chem. Rev.* **2010**, *110*, 6939−6960.
(10) Wilson, A. D.; Shoemaker, R. K.; Miedaner, A.; Muckerman, J. T.; DuBois, D. L.; Rakowski DuBois, M. *Proc. Natl. Acad. Sci. U.S.A.* **2007**, *104*, 6951−6956.
(11) Barton, B. E.; Rauchfuss, T. B. *Inorg. Chem.* **2008**, *47*, 2261−2263.
(12) DuBois, D. L.; Bullock, R. M. *Eur. J. Inorg. Chem.* **2011**, 1017−1027.
(13) O'Hagen, M.; Shaw, W. J.; Raugei, S.; Chen, S.; Yang, J. Y.; Kilgore, U. J.; DuBois, D. L.; Bullock, R. M. *J. Am. Chem. Soc.* **2011**, *133*, 14301−14312.
(14) Horvath, S.; Fernandez, L. E.; Soudackov, A. V.; Hammes-Schiffer, S. *Proc. Natl. Acad. Sci. U.S.A.* **2012**, *109*, 15663−15668.
(15) Fernandez, L. E.; Horvath, S.; Hammes-Schiffer, S. *J. Phys. Chem. Lett.* **2013**, *4*, 542−546.
(16) Chen, S.; Ho, M.-H.; Bullock, R. M.; DuBois, D. L.; Dupuis, M.; Rousseau, R.; Raugei, S. *ACS Catal.* **2014**, *4*, 229−242.
(17) Le Goff, A.; Artero, V.; Jousselme, B.; Tran, P. D.; Guillet, N.; Métayé, R.; Fihri, A.; Palacin, S.; Fontecave, M. *Science* **2009**, *326*, 1384−1387.
(18) Dempsey, J. L.; Brunschwig, B. S.; Winkler, J. R.; Gray, H. B. *Acc. Chem. Res.* **2009**, *42*, 1995−2004.
(19) Liu, T.; Li, B.; Popescu, C. V.; Bilko, A.; Pérez, L. M.; Hall, M. B.; Darensbourg, M. Y. *Chem.—Eur. J.* **2010**, *16*, 3083−3089.
(20) McNamara, W. R.; Han, Z.; Alberin, P. J.; Brennessel, W. W.; Holland, P. L.; Eisenberg, R. *J. Am. Chem. Soc.* **2011**, *133*, 15368−15371.
(21) McNamara, W. R.; Han, Z.; Yin, C.-J.; Brennessel, W. W.; Holland, P. L.; Eisenberg, R. *Proc. Natl. Acad. Sci. U.S.A.* **2012**, *109*, 15594−15599.
(22) Valdez, C. N.; Dempsey, J. L.; Brunschwig, B. S.; Winkler, J. R.; Gray, H. B. *Proc. Natl. Acad. Sci. U.S.A.* **2012**, *109*, 15589−15593.
(23) Andreiadis, E. S.; Jacques, P.-A.; Tran, P. D.; Leyris, A.; Chavarot-Kerlidou, M.; Jousselme, B.; Matheron, M.; Pécaut, J.; Palacin, S.; Fontecave, M.; Artero, V. *Nat. Chem.* **2013**, *5*, 48−53.
(24) Lee, C. H.; Dogutan, D. K.; Nocera, D. G. *J. Am. Chem. Soc.* **2011**, *133*, 8775−8777.
(25) Roubelakis, M. M.; Bediako, D. K.; Dogutan, D. K.; Nocera, D. G. *Energy Environ. Sci.* **2012**, *5*, 7737−7740.
(26) Perdew, J. P. *Phys. Rev. B* **1986**, *33*, 8822−8824.
(27) Becke, A. D. *Phys. Rev. A* **1988**, *38*, 3098−3100.
(28) Becke, A. D. *J. Chem. Phys.* **1993**, *98*, 5648−5652.
(29) Lee, C.; Yang, W.; Parr, R. G. *Phys. Rev. B* **1988**, *37*, 785−789.
(30) Tao, J. M.; Perdew, J. P.; Staroverov, V. N.; Scuseria, G. E. *Phys. Rev. Lett.* **2003**, *91*, 146401.
(31) Zhao, Y.; Truhlar, D. G. *J. Chem. Phys.* **2006**, *125*, 194101.
(32) Grimme, S. *J. Comput. Chem.* **2006**, *27*, 1787−1799.
(33) Becke, A. D. *J. Chem. Phys.* **1997**, *107*, 8554−8560.
(34) Kamiya, M.; Tsunea, T.; Hirao, K. *J. Chem. Phys.* **2002**, *117*, 6010−6015.
(35) Chai, J.-D.; Head-Gordon, M. *Phys. Chem. Chem. Phys.* **2008**, *10*, 6615−6620.
(36) Hariharan, P. C.; Pople, J. A. *Theor. Chim. Acta* **1973**, *28*, 213−222.
(37) Hehre, W. J.; Ditchfield, R.; Pople, J. A. *J. Chem. Phys.* **1972**, *56*, 2257−2261.
(38) Francl, M. M.; Pietro, W. J.; Hehre, W. J.; Binkley, J. S.; Gordon, M. S.; DeFrees, D. J.; Pople, J. A. *J. Chem. Phys.* **1982**, *77*, 3654−3665.
(39) Clark, T.; Chandrasekhar, J.; Spitznagel, G. W.; Schleyer, P. v. R. *J. Comput. Chem.* **1983**, *4*, 294−301.
(40) Frisch, M. J.; Trucks, G. W.; Schlegel, H. B.; Scuseria, G. E.; Robb, M. A.; Cheeseman, J. R.; Scalmani, G.; Barone, V.; Mennucci, B.; Petersson, G. A.; Nakatsuji, H.; Caricato, M.; Li, X.; Hratchian, H.

P.; Izmaylov, A. F.; Bloino, J.; Zheng, G.; Sonnenberg, J. L.; Hada, M.; Ehara, M.; Toyota, K.; Fukuda, R.; Hasegawa, J.; Ishida, M.; Nakajima, T.; Honda, Y.; Kitao, O.; Nakai, H.; Vreven, T.; Montgomery, J. A., Jr.; Peralta, J. E.; Ogliaro, F.; Bearpark, M.; Heyd, J. J.; Brothers, E.; Kudin, K. N.; Staroverov, V. N.; Kobayashi, R.; Normand, J.; Raghavachari, K.; Rendell, A.; Burant, J. C.; Iyengar, S. S.; Tomasi, J.; Cossi, M.; Rega, N.; Millam, J. M.; Klene, M.; Knox, J. E.; Cross, J. B.; Bakken, V.; Adamo, C.; Jaramillo, J.; Gomperts, R.; Stratmann, R. E.; Yazyev, O.; Austin, A. J.; Cammi, R.; Pomelli, C.; Ochterski, J. W.; Martin, R. L.; Morokuma, K.; Zakrzewski, V. G.; Voth, G. A.; Salvador, P.; Dannenberg, J. J.; Dapprich, S.; Daniels, A. D.; Farkas, Ö.; Foresman, J. B.; Ortiz, J. V.; Cioslowski, J.; Fox, D. J. *Gaussian 09, Revision C.1*; Gaussian, Inc., Wallingford, CT, 2009.

(41) Barone, V.; Cossi, M. *J. Phys. Chem. A* **1998**, *102*, 1995−2001.

(42) Cossi, M.; Rega, N.; Scalmani, G.; Barone, V. *J. Comput. Chem.* **2003**, *24*, 669−681.

(43) Floris, F.; Tomasi, J. *J. Comput. Chem.* **1989**, *10*, 616−627.

(44) Floris, F. M.; Tomasi, J.; Ahuir, J. L. P. *J. Comput. Chem.* **1991**, *12*, 784−791.

(45) Pierotti, R. A. *Chem. Rev.* **1976**, *76*, 717−726.

(46) Solis, B. H.; Hammes-Schiffer, S. *Inorg. Chem.* **2011**, *50*, 11252−11262.

(47) Solis, B. H.; Hammes-Schiffer, S. *Inorg. Chem.* **2014**, *53*, 6427−6443.

(48) Hansch, C.; Leo, A.; Taft, R. W. *Chem. Rev.* **1991**, *91*, 165−195.

(49) Solis, B. H.; Hammes-Schiffer, S. *J. Am. Chem. Soc.* **2011**, *133*, 19036−19039.

(50) McGuire, R., Jr.; Dogutan, D. K.; Teets, T. S.; Suntivich, J.; Shao-Horn, Y.; Nocera, D. G. *Chem. Sci.* **2010**, *1*, 411−414.

(51) Roubelakis, M. M.; Nocera, D. G., unpublished results.

(52) Hu, X.; Brunschwig, B. S.; Peters, J. C. *J. Am. Chem. Soc.* **2007**, *129*, 8988−8998.

(53) Fourmond, V.; Jacques, P.-A.; Fontecave, M.; Artero, V. *Inorg. Chem.* **2010**, *49*, 10338−10347.

(54) Peng, C.; Schlegel, H. B. *Isr. J. Chem.* **1993**, *33*, 449−454.

(55) Peng, C.; Ayala, P. Y.; Schlegel, H. B.; Frisch, M. J. *J. Comput. Chem.* **1996**, *17*, 49−56.

(56) Whitlock, H. W.; Bower, B. K. *Tetrahedron Lett.* **1965**, *52*, 4827−4831.

(57) Kobayashi, H.; Hara, T.; Kaizu, Y. *Bull. Chem. Soc. Jpn.* **1972**, *45*, 2148−2155.

(58) Baran, J. D.; Grönbeck, H.; Hellman, A. *J. Am. Chem. Soc.* **2014**, *136*, 1320−1326.

(59) Bediako, D. K.; Solis, B. H.; Dogutan, D. K.; Roubelakis, M. M.; Maher, A. G.; Lee, C. H.; Chambers, M. B.; Hammes-Schiffer, S.; Nocera, D. G. *Proc. Natl. Acad. Sci. U.S.A.* **2014**, *111*, 15001−15006.

(60) Venkataraman, C.; Soudackov, A. V.; Hammes-Schiffer, S. *J. Phys. Chem. C* **2008**, *112*, 12386−12397.

(61) Belenky, P.; Bogan, K. L.; Brenner, C. *Trends Biochem. Sci.* **2007**, *32*, 12−19.

(62) Pollak, N.; Dölle, C.; Ziegler, M. *Biochem. J.* **2007**, *402*, 205−218.

(63) Zheng, C.; You, S.-L. *Chem. Soc. Rev.* **2012**, *41*, 2498−2518.

(64) Boone, M. P.; Stephan, D. W. *Chem. Eur. J.* **2014**, *20*, 3333−3341.

(65) Zhang, J.; Leitus, G.; Ben-David, Y.; Milstein, D. *J. Am. Chem. Soc.* **2005**, *127*, 10840−10841.

(66) O'Brien, A. Y.; McGann, J. P.; G. Richard Geier, I. *J. Org. Chem.* **2007**, *72*, 4084−4092.

(67) Flint, D. L.; Fowler, R. L.; LeSaulnier, T. D.; Long, A. C.; O'Brien, A. Y.; G. Richard Geier, I. *J. Org. Chem.* **2010**, *75*, 553−563.

(68) Pistner, A. J.; Yap, G. P. A.; Rosenthal, J. *J. Phys. Chem. C* **2012**, *116*, 16918−16924.

(69) Pistner, A. J.; Lutterman, D. A.; Ghidiu, M. J.; Ma, Y.-Z.; Rosenthal, J. *J. Am. Chem. Soc.* **2013**, *135*, 6601−6607.

(70) Bruce, A. M.; Weyburne, E. S.; Engle, J. T.; Ziegler, C. J.; G. Richard Geier, I. *J. Org. Chem.* **2014**, *79*, 5664−5672.

(71) Pistner, A. J.; Lutterman, D. A.; Ghidiu, M. J.; Walker, E.; Yap, G. P. A.; Rosenthal, J. *J. Phys. Chem. C* **2014**, *118*, 14124−14132.

ChemPubSoc Europe

DOI: 10.1002/cssc.201402242

Post-Synthetic Modification of Hangman Porphyrins Synthesized on the Gram Scale

Daniel J. Graham, Shao-Liang Zheng, and Daniel G. Nocera*[a]

We report a multi-gram scale synthesis of methyl 6-formyl-4-dibenzofurancarboxylate and its subsequent use in the gram scale synthesis of a dibenzofuran-functionalized hangman porphyrin containing a pendant carboxylic acid (**HPD-CO_2H**). **HPD-CO_2H** can be isolated as a free carboxylic acid in high purity with minimal purification. Post-synthetic modification of **HPD-CO_2H** allows for the introduction of any desired pendant group in good yields, resulting in a practical amount of hangman porphyrin ligand with an easily customizable second coordination sphere. The cobalt complexes of these hangman porphyrins are shown to be active proton reduction electrocatalysts.

Ligand design for the purpose of controlling the secondary coordination sphere of a metal site is a popular strategy to enhance catalytic activity. The effect of placing a pendant acid/base moiety in the second coordination sphere of metallocycles on ligand binding,[1–3] as well as on the catalytic transformations of peroxide dismutation,[4–12] H_2 generation,[13,14] H_2O oxidation,[15,16] and O_2 reduction,[16–22] has been an intense topic of study. The concept of using the secondary coordination sphere to influence activity of redox reactions involving protons has subsequently been generalized to a variety of metal centers and secondary coordination spheres.[23] The strategy has been especially important for promoting the hydrogen evolution reaction (HER), which involves coupling the reduction of a metal center to proton transfer.[24–29] In our hangman approach, xanthene has been a preferred scaffold for the assembly of macrocycles such as porphyrins or salens with a pendant acid/base group, which has primarily been a carboxylic acid. We have sought to expand the hangman methodology to include more sterically imposing pendant groups that not only assist in proton transfer, but also shield the metal center from the bulk solution and effectively create a substrate binding pocket. In order to accommodate larger hanging groups, we have turned our attention to the dibenzofuran scaffold. The dibenzofuran precursor that is needed for macrocyclic construction can be synthesized on the gram scale from inexpensive starting materials. Whereas this dibenzofuran spacer has been employed in the construction of Pacman complexes,[30,31] the use of dibenzofuran as a platform for appending acid/base functionalities above a single transition metal complex has been largely unexplored and limited to hanging carboxylic acids.[4,32] Building on our experience with hangman ligands containing carboxylic acids, we chose to pursue a modification strategy to post-synthetically attach hanging groups via carboxamide formation. Herein, we report the high yielding synthesis of greater-than-one-gram of hanging porphyrin dibenzofuran with a pendant carboxylic acid (**HPD-CO_2H**) using a modified Lindsey method[33] and 3,4,5-trimethoxy-benzaldehyde (TMB) as the second aldehyde. The origin of this unusually high yield for a porphyrin compound is presumably due to similar electronic properties of TMB and dibenzofuran aldehyde. **HPD-CO_2H** can be cleanly isolated with minimal purification and post-synthetically modified through carboxamide formation with any primary amine, allowing for rapid generation of a library of hangman porphyrins with systematic variation of proton donor properties and/or steric hindrance. We further show that cobalt complexes of HPD are competent proton reduction electrocatalysts.

1. Scaffold synthesis: the synthesis of **HPD-CO_2H** requires an asymmetric dibenzofuran containing an aldehyde functionality and a pendant methyl ester, which can be subsequently hydrolyzed after porphyrin formation to yield the free carboxylic acid. The synthesis of methyl 6-formyl-dibenzofuran-4-carboxylate (**4**) is carried out in 4 steps on the multigram scale. First, dibenzofuran was selectively deprotonated at the 4 and 6 positions using the combination of *n*-BuLi and TMEDA in refluxing hexanes. The resulting dilithio salt was quenched with CO_2 at −78 °C, yielding 4,6-dibenzofuran dicarboxylic acid (**1**) after acidic workup. Impure **1** was often used directly in the next step after removal of excess water *in vacuo*. **1** was converted to dimethyl-4,6-dibenzofuran dicarboxylate (**2**) by acid-catalyzed esterification in refluxing methanol (MeOH) with trimethyl orthoformate as a dehydrating agent (Scheme 1). **2** is easily isolated by precipitation upon addition of excess water followed by filtration and drying *in vacuo*. Column chromatography yields analytically pure **2**. However, it was found that impure **2** could be used in the following step after sufficient drying in vacuo.

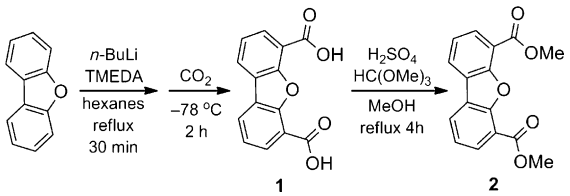

Scheme 1. Synthesis of **2** from dibenzofuran.

[a] *D. J. Graham, Dr. S.-L. Zheng, Dr. D. G. Nocera*
Department of Chemistry and Chemical Biology
Harvard University
12 Oxford St, Cambridge, MA 02138 (USA)
E-mail: dnocera@fas.harvard.edu

Supporting Information for this article is available on the WWW under http://dx.doi.org/10.1002/cssc.201402242.

Following published methods,[34] statistical reduction of **2** was accomplished by treatment with $NaBH_4$ in a refluxing THF/MeOH solution to yield 6-(hydroxy-methyl)dibenzofuran-4-carboxylate methyl ester (**3**). Subsequent oxidation of **3** with TEMPO and bis(acetoxy)iodosylbenzene (BAIB) in DCM gave the desired porphyrin precursor (**4**) in 38% overall yield starting from dibenzofuran (Scheme 2).

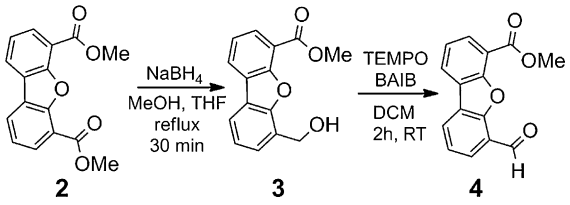

Scheme 2. Synthesis of hangman porphyrin precursor **4** by the statistical reduction and subsequent oxidation of **2**.

In an attempt to synthesize the desired asymmetric aldehyde in three steps, **2** was treated with one equivalent of DIBAL-H. Curiously, regardless of solvent, reaction time, or temperature, only starting material was recovered. An additional equivalent of DIBAL-H resulted in a 1:1 mixture of **2** and fully reduced dialcohol, 4,6-di(hydroxymethyl)dibenzofuran (**5**) (Scheme 3).

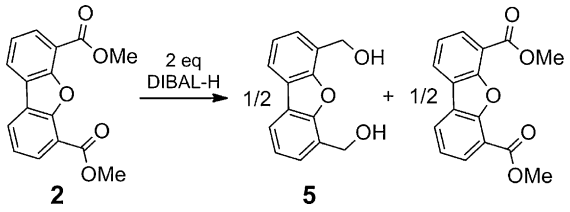

Scheme 3. Attempted selective reduction of **2** by DIBAL-H.

2. Porphyrin construction: porphyrins are notoriously difficult to synthesize on a large scale, especially those featuring multiple *meso*-substituents. Whereas all previous reported syntheses of hanging dibenzofuran ligands have employed Pd-catalyzed cross coupling, we decided to attempt statistical porphyrin formation with **4** because the products of Pd cross-coupling reactions retain minute amounts of Pd that are capable of driving the HER catalytically.[35] Our most common means of hangman porphyrin synthesis employs the Lindsey method in a highly dilute solution containing excess pyrrole and non-hangman aldehyde in order to maximize the yield of hangman porphyrin.[36,37] Following this published strategy, treatment of a 0.53 mM solution of **4**, containing an overall 1:15:16 ratio of **4**/TMB/pyrrole, with $BF_3{\cdot}OEt_2$ resulted in an unusually high combined yield of tetrakis(3,4,5-trimethoxyphenyl)porphyrin (**A4**) and hanging porphyrin dibenzofuran methyl ester (**A3B**, **HPD-CO_2Me**) with few other byproducts. Given the surprising ability of TMB and **4** to form porphyrin rings in a respectably selective fashion, statistical synthesis was attempted by subjecting a 2.1 mM solution of **4** in $CHCl_3$, with a 1:7:8 ratio of **4**/TMB/pyrrole, to the Lindsey method (Scheme 4). The higher reagent concentrations resulted in more non-porphyrinic byproducts, but still gave remarkably high yields of porphyrin. Notably, this method gives relatively poor yields of hangman porphyrin when other aldehydes, such as pentafluorobenzaldehyde (10%), mesitylaldehyde (12%), or 2,4,6-trimethoxybenzaldehyde (7%), were used in the same ratios in conjunction with **4**.

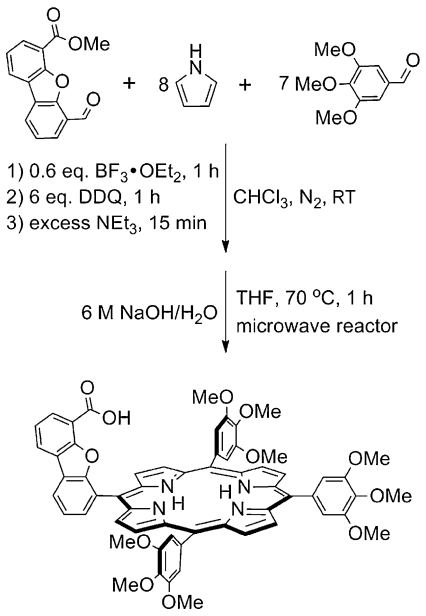

Scheme 4. Formation for the porphyrin from pyrrole, TMB, and **4**.

HPD-CO_2Me is difficult to separate from other porphyrinic byproducts due to similar elution properties, but hangman porphyrin could be isolated cleanly by carrying the entire porphyrin mixture directly through to the next step and hydrolyzing the hanging methyl ester (Scheme 4). After filtering off a majority of the pyrrolic byproducts, microwave-assisted basic hydrolysis[37] converted **HPD-CO_2Me** to the corresponding **HPD-CO_2H**, which is easily separated from unreacted **HPD-CO_2Me** and **A4** porphyrin on a silica column. Starting with a 2.1 mM solution of **4** in 1.5 L of $CHCl_3$, **HPD-CO_2H** was isolated in 33% over two steps on a gram scale. The yield of **HPD-CO_2H** increased to 41% if performed on a smaller scale in 560 mL of $CHCl_3$, keeping all reagent concentrations the same.

In addition to **HPD-CO_2H**, 1.64 g (30% yield with respect to total available TMB) of **A4** was isolated and identified by ^{1}H NMR. Even though it is a byproduct, the yield of **A4** is similar to its synthesis by published methods.[38,39]

3. Hanging group attachment: the presence of 3,4,5-trimethoxyphenyl *meso*-substituents on **HPD-CO_2H** precludes the use of thionyl chloride in carboxamide formation.[40,41] Instead, a combination of *p*-toluenesulfonyl chloride (TsCl) and *N*,*N*-dimethylaminopyridine (DMAP) was employed to prepare the acyl transfer reagent. Treatment of **HPD-CO_2H** with 2–5 equivalents of TsCl and 4–10 equivalents of DMAP followed by addition of excess aryl amine afforded the functionalized hangman porphyrins, which were easily purified and isolated in good yield (Scheme 5).

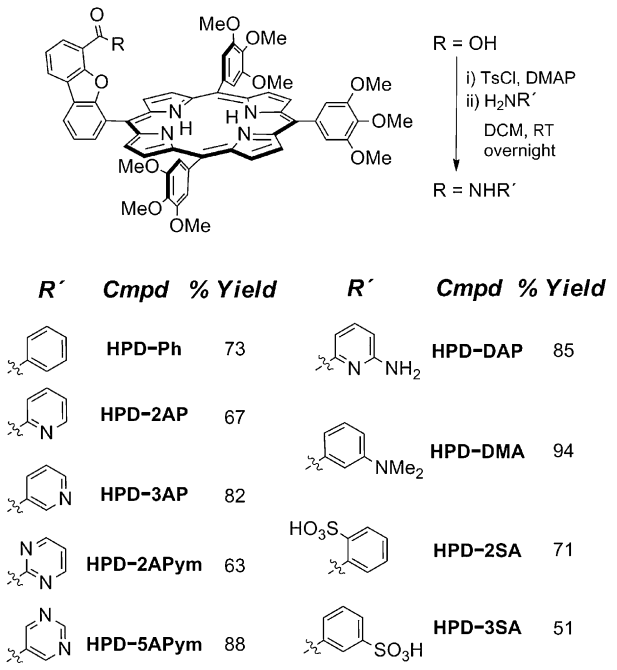

Scheme 5. Post-synthetic modification of hanging group with isolated yields for each hangman porphyrin derivative.

Crystals suitable for X-ray diffraction studies were grown from slow evaporation of an acetonitrile (CH_3CN) solution of **HPD-Ph**. The porphyrin crystallized as a dimer and displayed the expected connectivity (Figure 1). The center of the hanging phenyl ring is positioned 4.474(2) Å above the mean porphyrin plane. The porphyrin ring is slightly saddled, which has the effect of tilting the hangman scaffold inward and decreasing the distance between the hanging group and the porphyrin plane. The presence of an intramolecular NH···O hydrogen bond is apparent between the carboxamide NH group and the central dibenzofuran O atom, with an N–O distance of 2.791(3) Å and N–H–O bond angle of 141.90(1)°. This hydrogen bond may provide an anchor to prevent rotation around the C–C(O)NHR bond and maintain the desired second coordination sphere.

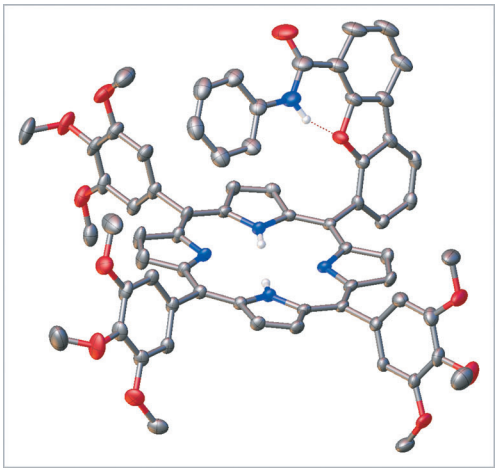

Figure 1. Solid state molecular structure of **HPD-Ph** with 50% ellipsoids. All carbon-bound hydrogens are removed for clarity.

4. Cobalt insertion and HER electrocatalysis: the Co^{II} complexes are synthesized using published microwave-assisted metallation procedures.[37] The Co complex **HPDCo-2AP** displays waves in the cyclic voltammogram (CV) that correspond to $Co^{III/II}$, $Co^{II/I}$, and $Co^{I/"0"}$ electron transfer events. The CV of the **HPDCo-2AP** changes dramatically upon the titration of $HBF_4{\cdot}OEt_2$ into a CH_3CN solution of 0.1 M tetraethylammonium *p*-toluenesulfonate ($[TEA]^+[TsO]^-$), which generates tosic acid (TsOH) *in situ*. A catalytic wave appears at the $Co^{II/I}$ reduction (Figure 2). This behavior differs significantly from that of other

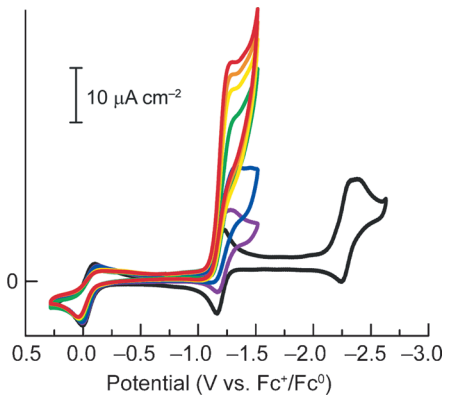

Figure 2. Cyclic voltammograms of a 0.5 mM solution of **HPDCo-2AP** in CH_3CN (0.1 M $[TEA^+][TsO^-]$) with 0 mM (——), 1 mM (——), 2 mM (——), 5 mM (——), 10 mM. (——), 15 mM (——), and 20 mM (——) of added $HBF_4{\cdot}OEt_2$. Scan rates are 50 mV s^{-1}.

Co-hangman porphyrins with a pendant carboxylic acid in the presence of TsOH,[13] in which a catalytic wave is observed at potentials significantly negative of the $Co^{II/I}$ reduction wave, suggesting that $Co^{III}H$, generated from protonation of Co^{I}, must be reduced to $Co^{II}H$ before H_2 evolution occurs. The hanging pyridine is a significantly stronger proton donor than the xanthene carboxylic acid, and may be capable of protonating $Co^{III}H$ directly. Further studies concerning the differences in proton reduction rates with different hanging groups are underway.

In summary, HPD-hangman porphyrins with 3,4,5-trimethoxyphenyl *meso*-substituents can be synthesized from inexpensive starting materials that are either commercially available or easily made on a multigram scale; and they can be isolated on a gram scale with minimal purification. Using these hangman porphyrins as ligands for transition metals allows one to control the nature of the secondary coordination sphere. Subsequent functionalization of **HPD-CO_2H** allows for the installation of any pendant group with tunable steric, electronic, and/or proton donating properties. Cobalt complexes of these new hangman porphyrins are capable of reducing protons electrocatalytically. Studies on the mechanism for H_2 evolution and on the use of other metalloporphyrins derived from hanging porphyrin dibenzofuran are currently underway.

Acknowledgements

DJG is thankful for the financial support offered by the NSF GRFP and for insightful discussions with Christopher Lemon and Dr. David Powers. We are also grateful for funding from the DOE award number DE-SC0009758.

Keywords: electrocatalysis · gram scale · hangman porphyrin · hydrogen · porphyrin

[1] C. K. Chang, M. P. Kondylis, *J. Chem. Soc. Chem. Commun.* **1986**, 316 – 318.
[2] Y. Liang, C. K. Chang, *Tetrahedron Lett.* **1995**, *36*, 3817 – 3820.
[3] Y. Liang, C. K. Chang, *J. Mol. Recognit.* **1996**, *9*, 149 – 157.
[4] C. J. Chang, L. L. Chng, D. G. Nocera, *J. Am. Chem. Soc.* **2003**, *125*, 1866 – 1876.
[5] J. Rosenthal, L. L. Chng, S. D. Fried, D. G. Nocera, *Chem. Commun.* **2007**, 2642 – 2644.
[6] S.-Y. Liu, D. G. Nocera, *J. Am. Chem. Soc.* **2005**, *127*, 5278 – 5279.
[7] L. L. Chng, C. J. Chang, D. G. Nocera, *Org. Lett.* **2003**, *5*, 2421 – 2424.
[8] M. Schwalbe, D. K. Dogutan, S. A. Stoian, T. S. Teets, D. G. Nocera, *Inorg. Chem.* **2011**, *50*, 1368 – 1377.
[9] D. J. Graham, D. K. Dogutan, M. Schwalbe, D. G. Nocera, *Chem. Commun.* **2012**, *48*, 4175 – 4177.
[10] J. D. Soper, S. V. Kryatov, E. V. Rybak-Akimova, D. G. Nocera, *J. Am. Chem. Soc.* **2007**, *129*, 5069 – 5075.
[11] B. Zyska, M. Schwalbe, *Chem. Commun.* **2013**, *49*, 3799 – 3801.
[12] A. Mahammed, Z. Gross, *Catal. Sci. Technol.* **2011**, *1*, 535 – 540.
[13] C. H. Lee, D. K. Dogutan, D. G. Nocera, *J. Am. Chem. Soc.* **2011**, *133*, 8775 – 8777.
[14] M. M. Roubelakis, D. K. Bediako, D. K. Dogutan, D. G. Nocera, *Energy Environ. Sci.* **2012**, *5*, 7737 – 7740.
[15] D. K. Dogutan, R. McGuire, D. G. Nocera, *J. Am. Chem. Soc.* **2011**, *133*, 9178 – 9180.
[16] J. D. Baran, H. Gronbeck, A. Hellman, *J. Am. Chem. Soc.* **2014**, *136*, 1320 – 1326.
[17] D. K. Dogutan, S. A. Stoian, R. McGuire, Jr., M. Schwalbe, T. S. Teets, D. G. Nocera, *J. Am. Chem. Soc.* **2011**, *133*, 131 – 140.
[18] R. McGuire Jr., D. K. Dogutan, T. S. Teets, J. Suntivich, Y. Shao-Horn, D. G. Nocera, *Chem. Sci.* **2010**, *1*, 411 – 414.
[19] J. Rosenthal, D. G. Nocera, *Acc. Chem. Res.* **2007**, *40*, 543 – 553.
[20] C. M. Lemon, D. K. Dogutan, D. G. Nocera in *Handbook of Porphyrin Science Vol. 21* (Eds.: K. M. Kadish, K. M. Smith, R. Guilard), World Scientific Publishing Singapore, **2012**, pp. 1 – 143.
[21] J. G. Liu, Y. Shimizu, T. Ohta, Y. Naruta, *J. Am. Chem. Soc.* **2010**, *132*, 3672 – 3673.
[22] W. Z. Lai, R. Cao, G. Dong, S. Shaik, J. N. Yao, H. Chen, *J. Phys. Chem. Lett.* **2012**, *3*, 2315 – 2319.
[23] M. Zhao, H.-B. Wang, L.-N. Ji, Z.-W. Mao, *Chem. Soc. Rev.* **2013**, *42*, 8360 – 8375.
[24] J. Y. Yang, R. M. Bullock, M. R. DuBois, D. L. DuBois, *MRS Bull.* **2011**, *36*, 39 – 47.
[25] D. L. DuBois, R. M. Bullock, *Eur. J. Inorg. Chem.* **2011**, 1017 – 1027.
[26] M. L. Helm, M. P. Stewart, R. M. Bullock, M. R. DuBois, D. L. DuBois, *Science* **2011**, *333*, 863 – 866.
[27] M. O'Hagan, M.-H. Ho, J. Y. Yang, A. M. Appel, M. R. DuBois, S. Raugei, W. J. Shaw, D. L. DuBois, R. M. Bullock, *J. Am. Chem. Soc.* **2012**, *134*, 19409 – 19424.
[28] A. M. Appel, D. H. Pool, M. J. O'Hagan, W. J. Shaw, J. Y. Yang, M. R. DuBois, D. L. DuBois, R. M. Bullock, *ACS Catal.* **2011**, *1*, 777 – 785.
[29] B. E. Barton, M. T. Olsen, T. B. Rauchfuss, *J. Am. Chem. Soc.* **2008**, *130*, 16834 – 16835.
[30] J. Rosenthal, D. G. Nocera, *Prog. Inorg. Chem.* **2007**, *55*, 483 – 544.
[31] J. Rosenthal, B. J. Pistorio, L. L. Chng, D. G. Nocera, *J. Org. Chem.* **2005**, *70*, 1885 – 1888.
[32] J. Y. Yang, S.-Y. Liu, I. V. Korendovych, E. V. Rybak-Akimova, D. G. Nocera, *ChemSusChem* **2008**, *1*, 941 – 949.
[33] J. S. Lindsey, R. W. Wagner, *J. Org. Chem.* **1989**, *54*, 828 – 836.
[34] J. Rochford, E. Galoppini, *Langmuir* **2008**, *24*, 5366 – 5374.
[35] C. H. Lee, D. Villagran, T. R. Cook, J. C. Peters, D. G. Nocera, *ChemSusChem* **2013**, *6*, 1541 – 1544.
[36] C. J. Chang, C.-Y. Yeh, D. G. Nocera, *J. Org. Chem.* **2002**, *67*, 1403 – 1406.
[37] D. K. Dogutan, D. K. Bediako, T. S. Teets, M. Schwalbe, D. G. Nocera, *Org. Lett.* **2010**, *12*, 1036 – 1039.
[38] R. A. W. Johnstone, M. L. P. G. Nunes, M. M. Pereira, A. M. d'A. Rocha Gonsalves, A. C. Serra, *Heterocycles* **1996**, *43*, 1423 – 1437.
[39] S. Banfi, E. Caruso, S. Caprioli, L. Mazzagatti, G. Canti, R. Ravizza, M. Gariboldi, E. Monti, *Bioorg. Med. Chem.* **2004**, *12*, 4853 – 4860.
[40] K. H. Bell, *Aust. J. Chem.* **1985**, *38*, 1209 – 1221.
[41] K. H. Bell, L. F. McCaffery, *Aust. J. Chem.* **1992**, *45*, 1213 – 1224.

Received: March 28, 2014
Published online on June 27, 2014

Inorganic Chemistry

Article

pubs.acs.org/IC

Electron-Transfer Studies of a Peroxide Dianion

Andrew M. Ullman,[†] Xianru Sun,[‡] Daniel J. Graham,[†] Nazario Lopez,[§] Matthew Nava,[§] Rebecca De Las Cuevas,[§] Peter Müller,[§] Elena V. Rybak-Akimova,[‡] Christopher C. Cummins,*[,§] and Daniel G. Nocera*[,†]

[†]Department of Chemistry and Chemical Biology, Harvard University, 12 Oxford Street, Cambridge, Massachusetts 02138, United States

[§]Department of Chemistry, Massachusetts Institute of Technology, 77 Massachusetts Avenue, Cambridge, Massachusetts 02139, United States

[‡]Department of Chemistry, Tufts University, 62 Talbot Avenue, Medford, Massachusetts 02155, United States

Supporting Information

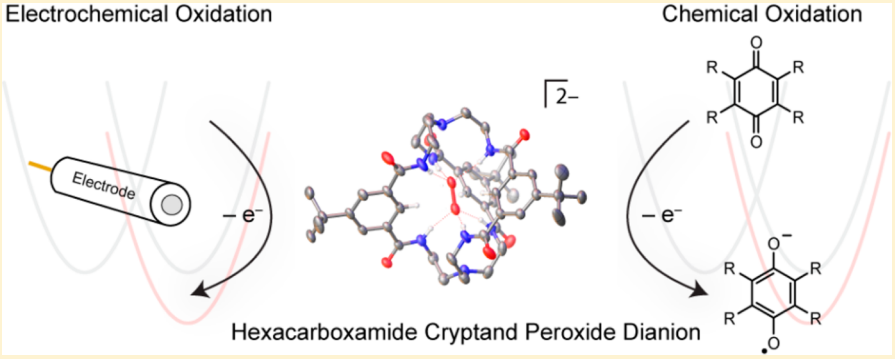

ABSTRACT: A peroxide dianion (O_2^{2-}) can be isolated within the cavity of hexacarboxamide cryptand, $[(O_2)\subset$mBDCA-5t-$H_6]^{2-}$, stabilized by hydrogen bonding but otherwise free of proton or metal-ion association. This feature has allowed the electron-transfer (ET) kinetics of isolated peroxide to be examined chemically and electrochemically. The ET of $[(O_2)\subset$mBDCA-5t-$H_6]^{2-}$ with a series of seven quinones, with reduction potentials spanning 1 V, has been examined by stopped-flow spectroscopy. The kinetics of the homogeneous ET reaction has been correlated to heterogeneous ET kinetics as measured electrochemically to provide a unified description of ET between the Butler–Volmer and Marcus models. The chemical and electrochemical oxidation kinetics together indicate that the oxidative ET of O_2^{2-} occurs by an outer-sphere mechanism that exhibits significant nonadiabatic character, suggesting that the highest occupied molecular orbital of O_2^{2-} within the cryptand is sterically shielded from the oxidizing species. An understanding of the ET chemistry of a free peroxide dianion will be useful in studies of metal–air batteries and the use of $[(O_2)\subset$mBDCA-5t-$H_6]^{2-}$ as a chemical reagent.

INTRODUCTION

Aerobic life is driven by the thermodynamic potential provided by dioxygen (O_2). In its ground state, O_2 is kinetically stable with respect to the chemical bonds found in living organisms. The controlled activation of O_2 in nature is therefore mediated by electron transfer (ET) to produce its diatomic congeners of superoxide ($O_2^{\bullet-}$) and peroxide (O_2^{2-}).[1] In nonaqueous environments, superoxide is stable in the absence of electrophilic species such as protons or metal ions, and the anion exhibits reversible ET behavior; accordingly, the outer-sphere oxidation of superoxide has been comprehensively studied using chemical and electrochemical techniques.[2−4] The ET chemistry of peroxide as an isolated species, however, remains ill-defined because the dianion is not readily available in free form. Peroxide is extremely unstable under nonaqueous conditions because of its ability to act as a strong Brønsted base.[5] For example, the electrochemical reduction of superoxide at a gold electrode in dimethyl sulfoxide (DMSO), and in the presence of tetraethylammonium (TEA) perchlorate, results in deprotonation-induced decomposition of the TEA cation to form protonated peroxide (HO_2^-), which in turn, oxidizes DMSO to dimethyl sulfone ($DMSO_2$).[6] Peroxide is therefore stabilized by coordination to a metal ion, and hence the intrinsic oxidation–reduction properties of the isolated dianion are difficult to establish because of metal–oxygen orbital mixing and electrostatic effects. Given the importance of peroxide as a deleterious intermediate in the biochemical reduction of molecular O_2,[7] as a valuable industrial feedstock,[8] and, in particular, as a primary discharge product in nonaqueous lithium–air batteries,[9,10] it is desirable to understand the basic

Received: April 5, 2014
Published: April 28, 2014

   dx.doi.org/10.1021/ic500759g | Inorg. Chem. 2014, 53, 5384−5391

ET properties of peroxide uncoupled from the complicating effects of protons or metal ions.

We have discovered that a soluble source of discrete O_2^{2-} units can be isolated by using hexacarboxamide cryptand (*m*BDCA-5t-H_6) as a sequestering agent (Figure 1).[11] The

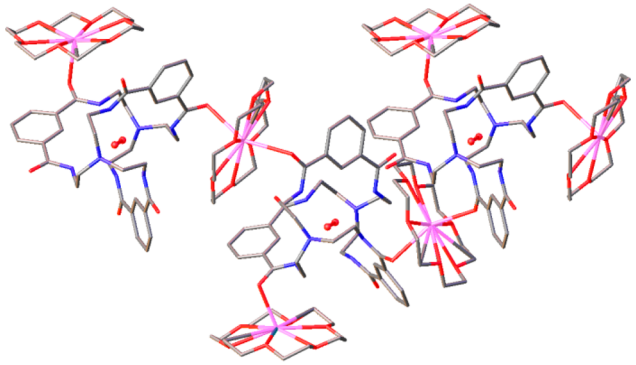

Figure 1. View of the crystal structure of [K(18-crown-6)]$_2$[(O_2)⊂*m*BDCA-5t-H_6] depicting the 1D coordination polymer formed in the solid state. Solvents of crystallization, *tert*-butyl groups, and hydrogen atoms are omitted for clarity. Color code: C, gray; N, blue; O, red; K, pink.

dianion does not interact with surrounding cations, and O_2 is released upon chemical oxidation of the sequestered dianion. This simple oxidative ET serves as a model for the desired half-reaction needed for a rechargeable lithium–air battery, for which a large overpotential is required. This overpotential has been the subject of numerous studies[12−14] and remains a hurdle in the pursuit of a practical metal–air battery.[15] Herein, we report the ET kinetics of chemical and electrochemical oxidation of [(O_2)⊂*m*BDCA-5t-H_6]$^{2-}$, with the goal of providing insight into the inherent properties germane to peroxide oxidation. Knowledge of the ET behavior from discrete O_2^{2-} is useful not only for the design of metal–air batteries capable of recharging at lower overpotentials but also for the informed use of a cryptand-encapsulated O_2^{2-} oxidant and/or atom-transfer reagent, in chemical transformations.

EXPERIMENTAL SECTION

General Methods. All manipulations were performed either with use of Schlenk techniques or in a nitrogen-atmosphere glovebox. All reagents were purchased from Aldrich. Quinones were sublimed three times. Solvents (EMD Chemicals) were either used as received or purified on a Glass Contour Solvent Purification System built by SG Water USA, LLC. IR spectra were recorded on a Bruker Tensor 37 Fourier transform infrared (FTIR) spectrometer. NMR solvents were obtained from Cambridge Isotope Laboratories, and ^{1}H and ^{13}C{^{1}H} NMR spectra were obtained on a Varian 300 MHz or a Bruker 400 MHz spectrometer and are referenced to residual solvent signals. Elemental analyses were performed by Midwest Microlabs, LLC.

Crystallography. Low-temperature diffraction data were collected on a three-circle diffractometer coupled to a Bruker-AXS Smart Apex charged-coupled-device (CCD) detector with graphite-monochromated Mo Kα radiation (λ = 0.71073 Å) for the structure of [K(18-crown-6)]$_2$[(O_2)⊂*m*BDCA-5t-H_6], performing φ and ω scans. The structures were solved by direct methods using *SHELXS* and refined against F^2 on all data by full-matrix least squares with *SHELXL-97* using established methods.[16] All non-hydrogen atoms were refined anisotropically.[17]

Preparative Methods. For [K(18-crown-6)]$_2$[(O_2)⊂*m*BDCA-5t-H_6], *m*BDCA-5t-H_6 (0.587 mmol, 1.00 equiv), 18-crown-6 (1.292 mmol, 2.2 equiv), and KO_2 (1.292 mmol, 2.2 equiv) were loaded into a 100 mL Schlenk flask and 30 mL of dry tetrahydrofuran (THF) was added. This reaction mixture was stirred under N_2 with the vessel connected to the Schlenk line. The contents formed a white-yellow slurry. A yellow solution was formed after 12 h. This reaction mixture was stirred for 24 h with no evident color change. The contents were subjected to three cycles of freeze–pump–thaw and brought into the glovebox. The remaining insoluble materials were removed by filtration, and the solid was washed with 3 × 5 mL of THF to dissolve any peroxide adduct that might have precipitated. THF was removed under a dynamic vacuum. The contents were redissolved in a minimum amount of THF (10 mL). The product was induced to precipitate by adding Et_2O dropwise with stirring. Excess 18-crown-6 was removed by washing the yellow solid with 3 × 10 mL of Et_2O. A sample of the yellow solid was dissolved in DMSO-d_6, and a ^{1}H NMR spectrum was taken. The ^{1}H NMR spectrum indicated complete conversion to the peroxide adduct. Single crystals were obtained after 4 days by vapor diffusion of diethyl ether into a THF solution of [K(18-crown-6)]$_2$[(O_2)⊂*m*BDCA-5t-H_6]. Yield: 0.80 g (0.54 mmol, 91%). ATR-FTIR on solid: (N–H) 3272 cm^{-1}. ^{1}H NMR (300 MHz, DMSO-d_6, δ): 14.63 (s, 6 H), 10.10 (s, 3 H), 8.16 (s, 6 H), 3.53 (s, 48 H), 3.39 (br, 6 H), 2.60 (br d, 6 H), 2.33 (br d, 12 H), 1.32 (s, 27 H). NMR (100 MHz, DMSO-d_6, δ): 165.56, 148.90, 134.99, 126.70, 124.23, 69.39, 59.97, 40.79, 34.40, 31.19. Anal. Calcd (found) for $C_{72}H_{114}N_8O_{20}K_2$: C, 58.04 (57.90); H, 7.71 (7.72); N, 7.52 (7.44).

Stopped-Flow Kinetic Measurements. THF solutions of the reagents were prepared in an MBraun glovebox filled with ultrahigh-purity argon (Airgas) and placed in Hamilton gastight syringes equipped with three-way valves. Time-resolved spectra (380–800 nm) were acquired over a range of temperatures using a Hi-Tech Scientific KinetAsyst SF-61DX2 Multi-Mixing CryoStopped-Flow system (TgK Scientific Ltd.) equipped with a quartz tungsten halogen light source, a J&M TIDAS diode-array detector, and a Brandenburg 4479 series PMT monochromator. The instrument was equipped with poly(ether ether ketone) tubing fitted inside stainless steel plumbing, a 1.00 cm^3 quartz mixing cell submerged in an ethanol cooling bath, and an anaerobic kit purged with argon. The temperature in the mixing cell was maintained to ±0.1 °C, and the mixing time was 2–3 ms. All flow lines of the instrument were extensively washed with degassed, anhydrous THF before charging the driving syringes with reactant solutions. The reactions were studied by rapid-scanning spectrophotometry under second-order conditions with a 1:1 molar ratio of the two reactants. All of the experiments were performed in a single-mixing mode of the instrument, with a 1:1 (v/v) mixing ratio. A series of three or four measurements gave an acceptable standard deviation (within 10%). Data analysis was performed with Kinetic Studio (TgK Scientific Ltd.) and IGOR Pro 5.0 (Wavemetrics, Inc.).

Electrochemical Methods. Cyclic voltammograms (CVs) were collected using a CH Intstruments (Austin, TX) 730C potentiostat. Solutions of 0.5 mM [TBA]$_2$[(O_2)⊂*m*BDCA-5t-H_6] in *N*,*N*-dimethylformamide (DMF; 0.1 M [TBA][PF_6]) were prepared in a nitrogen glovebox. The cell was covered with a Teflon cap containing the electrodes and sealed with parafilm. It was then removed from the glovebox and immediately placed under a blanket of argon. The temperature was controlled by placing the cell in an ethylene glycol bath kept at 298 K. The working electrode was freshly polished glassy carbon (area = 0.07 cm^2), the counter electrode was a platinum wire, and a fresh silver wire in DMF (0.1 M [TBA][PF_6]) separated from the working solution by a vycor frit was used as a pseudoreference electrode. Prior to use, DMF had been dried by passage through an alumina column followed by exposure to activated 4 Å sieves overnight. At the conclusion of the experiments, ferrocene was added and all potentials were referenced to the ferrocenium/ferrocene ($Fc^{+/0}$) couple.

Electrochemical Modeling. The diffusion coefficient (D) and reduction potential (E_0) of O_2 were determined from a CV of a 4.6 mM (saturated) solution of O_2 in DMF (0.1 M [TBA][PF_6]). The diffusion coefficient of $O_2^{\bullet-}$ was approximated as $^1/_3D(O_2)$.[18] The literature value for the heterogeneous rate constant (k_s) of 0.093 cm/s O_2 in DMSO (0.1 M [TBA][ClO_4]) was used.[19] All other quantities

dx.doi.org/10.1021/ic500759g | *Inorg. Chem.* 2014, 53, 5384–5391

were varied in the *DigiElch* software suite[21] until a satisfactory fit to the experimental data was achieved with reasonable values.

RESULTS

Synthesis. The sequestration of K^+ ions of $[K_2(DMF)_5][(O_2)\subset m\text{BDCA-5t-H}_6]$ by 18-crown-6 affords the appropriation of $[K(18\text{-crown-}6)]_2[(O_2)\subset m\text{BDCA-5t-H}_6]$ in 73% isolated yield and engenders good solubility of the complex in THF.[11] Alternatively, a more facile preparative route of $[K(18\text{-crown-}6)]_2[(O_2)\subset m\text{BDCA-5t-H}_6]$ was found, which avoids the extra step of isolating $[K_2(DMF)_5][(O_2)\subset m\text{BDCA-5t-H}_6]$. For this method, a slurry of *m*BDCA-5t-H_6 and 2.2 equiv of 18-crown-6 is treated with 2.2 equiv of KO_2 in THF, resulting in a 91% isolated yield for the peroxide-guest complex. The ^1H NMR spectra of compounds obtained by either of these preparative methods are identical except for the additional resonances corresponding to 18-crown-6 (Figure S1 in the Supporting Information, SI). Single crystals of the complex were obtained by vapor diffusion of Et_2O into a THF solution of $[K(18\text{-crown-}6)]_2[m\text{BDCA-5t-H}_6]$. The solid-state structure reveals two environments for the K^+ ions: one ion is coordinated to the CO of neighboring cryptands, forming a 1D coordination polymer, and the other one is bound terminally (Figure 1).

Electrochemical Oxidation. CVs of $[TBA]_2[(O_2)\subset m\text{BDCA-5t-H}_6]$ under an atmosphere of argon exhibit oxidation and reduction features (Figure 2). The

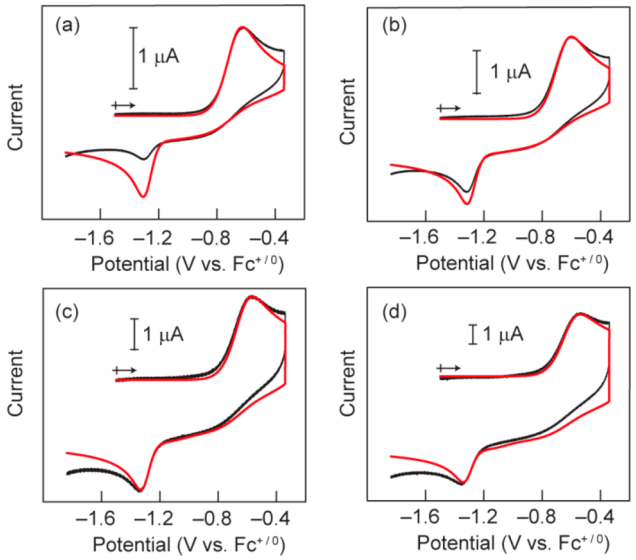

Figure 2. Experimental (black solid line) and simulated (red solid line) CVs of 0.5 mM $[TBA]_2[(O_2)\subset m\text{BDCA-5t-H}_6]$ in DMF (0.1 M $[TBA][PF_6]$) at (a) 50, (b) 100, (c) 250, and (d) 500 mV/s. Crosses and arrows depict the initial point and direction of the scan.

reduction wave, which we have attributed to the chemically irreversible reduction of O_2, only appears after oxidation of $[(O_2)\subset m\text{BDCA-5t-H}_6]^{2-}$ (Figures S2 and S3 in the SI).[11] The oxidation peak current (i_p) displayed a linear variation with the square root of the scan rate (ν; Figure S4 in the SI), indicating well-defined Cottrell kinetics for a soluble diffusion-controlled species. The oxidation peak potential (E_p) varied linearly with $\log(\nu)$ with a slope equal to 95 mV/decade (Figure S5 in the SI), which is inconsistent with an electrochemically reversible ET or an ET followed by a chemical step (30 mV/decade) according to Butler–Volmer kinetics for $\alpha = 0.5$.[20] This result, together with the broadness of the oxidation wave, indicates that ET attendant to the cryptand peroxide oxidation process is not an electrochemically or chemically facile process.

The broad oxidation wave may be modeled according to the Butler–Volmer formalism using $\alpha = 0.38$ for the one-electron oxidation of $[TBA]_2[(O_2)\subset m\text{BDCA-5t-H}_6]$.[11] The data can also be described using the Marcus–Hush model of electrode kinetics. Figure 2 shows that a satisfactory representation of the data is achieved for all scan rates using electrochemical simulation software, such as *DigiElch*,[21] with a reorganization energy $\lambda = 0.79$ eV, an ET rate constant of $k_s = 2.7 \times 10^{-5}$ cm/s, and a standard reduction potential of $O_2^{\bullet-}/O_2^{2-}$ within the cryptand of −0.85 V versus $Fc^{+/0}$ (Table S1a,b in the SI). The poor fit at low scan rates of the reduction of free O_2 is ascribed to unwanted convection contributions to the current.

Chemical Oxidation with Quinones. Quinones are rapidly reduced by $[(O_2)\subset m\text{BDCA-5t-H}_6]^{2-}$, requiring the use of stopped-flow spectroscopy at low temperature in order to determine the ET reaction rate. Dichlorodicyanoquinone (DDQ) cleanly reacts with $[K_2(DMF)_5][(O_2)\subset m\text{BDCA-5t-H}_6]$ in DMF under stoichiometric conditions to produce free O_2 (quantified by gas chromatography), free cryptand, and the DDQ dianion, DDQ^{2-}.[11] However, DMF could not be used as a solvent in the stopped-flow measurements because of the solvent's relatively high freezing point, relatively high viscosity, and incompatibility with some materials used to seal the flow lines of the instrument. Thus, THF was employed instead, necessitating the use of the more soluble $[K(18\text{-crown-}6)]_2[(O_2)\subset m\text{BDCA-5t-H}_6]$ complex.

The kinetics of the reaction between $[K(18\text{-crown-}6)]_2[(O_2)\subset m\text{BDCA-5t-H}_6]$ and DDQ was measured over a broad temperature range (−85 to +25 °C) under second-order conditions with equal concentrations of reactants. Reaction times varied when the stopped-flow experiment was performed in the diode-array mode as opposed to reproducible reaction times when the experiment was performed in the single-wavelength mode. Intense illumination with white light was used in the former case, whereas low-intensity, monochromatic visible light was used in the latter. These effects indicate photosensitivity of the reaction, which is circumvented in single-wavelength-mode detection. Thus, only single-wavelength data measured at $\lambda = 601$ nm was used for kinetic analyses.

Figure 3a shows the time-resolved visible absorption trace of the formation of a species at low temperature (−85 °C) with absorption maxima at $\lambda = 445$, 561, and 601 nm. These features are consistent with $DDQ^{\bullet-}$,[22] which forms rapidly. The kinetics for the prompt appearance of $DDQ^{\bullet-}$ is in accordance with the ET reaction

$$LO_2^{2-} + DDQ \xrightarrow{k_{ET}} LO_2^{-} + DDQ^{\bullet-} \quad (1)$$

where L = mBDCA-5t-H_6. The initial rate of formation of the anion (inset in Figure 3a) fits pseudo-first-order reaction kinetics,

$$\text{rate} = ae^{-k_{1obs}t} \quad (2)$$

to yield the observed rate constants k_{1obs} (Figure S6 in the SI), from which second-order ET rate constants k_{ET} were estimated using $k_{ET} = k_{1obs}/[DDQ] = 4 \times 10^6\ M^{-1}\ s^{-1}$. No pronounced differences in the values of k_{ET} were found at the three temperatures studied (Table S2 in the SI), which is likely due

dx.doi.org/10.1021/ic500759g | Inorg. Chem. 2014, 53, 5384−5391

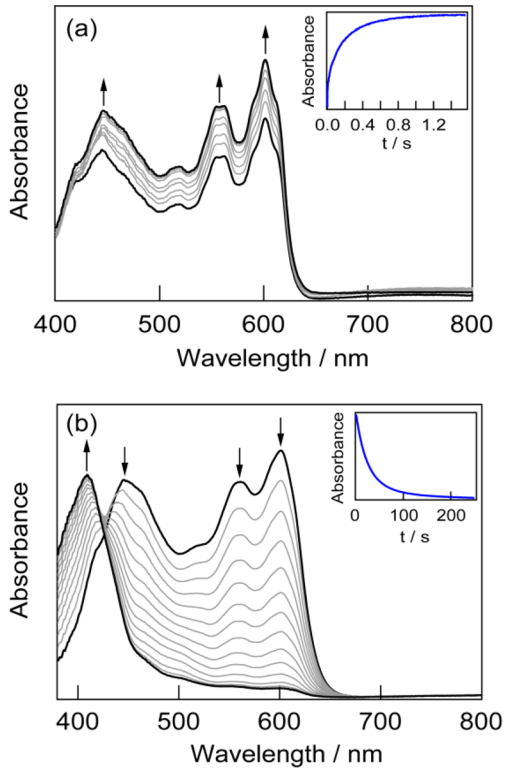

Figure 3. (a) Time-resolved spectral changes obtained upon mixing THF solutions of $[K(18\text{-crown-}6)]_2[(O_2)\subset m\text{BDCA-5t-H}_6]$ (0.05 mM) and DDQ (0.05 mM) at −85 °C, showing rapid formation of the $DDQ^{\bullet-}$ radical anion. (b) Time-resolved spectral changes obtained upon mixing THF solutions of $[K(18\text{-crown-}6)]_2[(O_2)\subset m\text{BDCA-5t-H}_6]$ (0.1 mM) and DDQ (0.1 mM) at 20 °C. The insets are the kinetic traces at λ = 601 nm. All concentrations are reported after mixing in the stopped-flow cell.

to our inability to accurately observe a difference in the rate with sufficient fidelity over this small temperature range. Accordingly, accurate activation parameters could not be obtained.

After the initial absorption rapidly increased because of the formation of $DDQ^{\bullet-}$, more quinone anion appeared in two slower steps (Figures S7 and S8 in the SI). The formation of the quinone monoanion on slower time scales is consistent with the bimolecular reaction of the superoxide cryptand complex produced from reaction (1)

$$LO_2^- + DDQ \xrightarrow{k_2} L + DDQ^{\bullet-} + O_2 \quad (3)$$

or from the disproportionation reaction of the superoxide adduct

$$2LO_2^- \rightarrow LO_2^{2-} + L + O_2 \quad (4)$$

followed by the reaction of LO_2^{2-} with DDQ per reaction (1). Superoxide in the presence of free cryptand rapidly produces LO_2^{2-} and O_2. Hence, we believe that superoxide disproportionation is facile and that one of the slower events that leads to $DDQ^{\bullet-}$ is most likely due to reaction (4), followed by reaction (1). This slower growth of $DDQ^{\bullet-}$ appeared to be complete within tens of seconds (Figure S7 in the SI). Because the time scale for this event was well separated from the initial kinetic phase, the slow process could be examined independently from reaction (1) over a broad temperature range (−85 to −59 °C). Activation parameters for this event are extracted from the data presented in Figure S9 in the SI and are summarized in Table S2 in the SI. Monitoring the reaction for several minutes at low temperature (see Figure S8 in the SI) revealed yet an additional, though minor, absorption growth phase. Because these secondary growth phases associated with reactions (3) and (4) were slow with respect to the kinetics of reaction (1), they posed no interference to analysis of the ET kinetics of peroxide as described by reaction (1).

Whereas $DDQ^{\bullet-}$ persists at low temperature, it disproportionates to DDQ and DDQ^{2-} at higher temperatures, as evidenced by growth of the dianion's characteristic spectral features, the most prominent of which is a band at $\lambda_{max} \sim 417$ nm.[22] Figure 3b shows this conversion at 20 °C. Figure S10 in the SI presents the time-dependent bleach at λ = 601 nm that accompanies this transformation at 5 °C. Formation of DDQ^{2-} may occur by either the reaction of $DDQ^{\bullet-}$ with the cryptand superoxide or cryptand peroxide complex. The activation parameters for the appearance of DDQ^{2-} are derived from the kinetic data in Figure S11 in the SI, and they are summarized in Table S2 in the SI. Because conversion of DDQ^- to DDQ^{2-} occurs over long time scales and only at higher temperature, this process does not interfere with examination of the ET kinetics of reaction (1).

To further elucidate the ET chemistry of the LO_2^{2-} adduct, the ET reactions of six additional quinones (Br_4Q, Cl_4Q, F_4Q, Cl_2Q, ClQ, and H_4Q; see Table 1) were examined by the stopped-flow method. The overall driving force of the reaction

$$Q + LO_2^{2-} \xrightarrow{k_{ET}} Q^{\bullet-} + LO_2^- \quad (5)$$

Table 1. Driving-Force and ET Rate Constants of Quinone/LO_2^{2-} at −80 °C for Reaction (5)

Quinone		E_{red} [a]	ΔG° (V)	k_{ET} (M^{-1} s^{-1}) [b]
	DDQ	0.13	−0.98	$3.83(27)\times10^6$
	Cl_4Q	−0.37	−0.48	$3.03(8)\times10^6$
	Br_4Q	−0.38	−0.47	$7.98(84)\times10^5$
	F_4Q	−0.42	−0.43	$2.35(22)\times10^6$
	Cl_2Q	−0.56	−0.29	$1.67(11)\times10^4$
	ClQ	−0.72	−0.13	$3.20(24)\times10^2$
	H_4Q	−0.89	0.04	2.57 [c]

[a]Reduction potentials of quinones are referenced versus $Fc^{+/0}$. [b]Measured in DMF at −80 °C. [c]The rate constant for the H_4Q/peroxide reaction at −80 °C was obtained by extrapolation from measurements at +25 to −50 °C using the activation parameters (E_a) obtained from the higher temperature data (see Table S2 in the SI).

dx.doi.org/10.1021/ic500759g | Inorg. Chem. 2014, 53, 5384−5391

spans 1 V with this set of quinone reactants. The free-energy change (ΔG°) of ET from $[K(18\text{-crown-6})]_2[(O_2)\subset m\text{BDCA-5t-H}_6]$ to members of the quinone series is obtained from

$$\Delta G^\circ = -e(E_{red} - E_1) \quad (6)$$

where $E_1 = -0.85$ V versus $Fc^{+/0}$ (in DMF) is the reduction potential of $[(O_2)\subset m\text{BDCA-5t-H}_6]^{2-}$ and E_{red} is the first reduction potential of the quinones listed in Table 1.[23,24] The reactions were performed under second-order conditions with identical concentrations of reactants in all cases. The time-resolved diode-array spectra of reactions of the seven quinones and $[K(18\text{-crown-6})]_2[(O_2)\text{-}\subset m\text{BDCA-5t-H}_6]$ in THF were acquired at −80 °C, except for H_4Q, which required higher temperatures for the reaction to proceed readily (−50 to +25 °C). The spectral changes accompanying the ET reaction are shown in Figures 4 and S12−S16 in the SI. To avoid

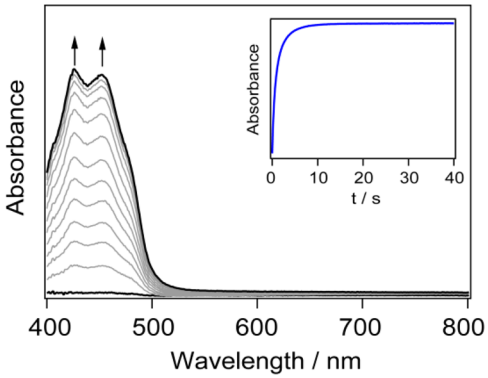

Figure 4. Time-resolved spectral changes obtained upon mixing THF solutions of $[K(18\text{-crown-6})]_2[(O_2)\subset m\text{BDCA-5t-H}_6]$ (0.1 mM) and Cl_2Q (0.1 mM) at −80 °C, showing rapid formation of the $Cl_2Q^{\bullet-}$ radical anion. Inset: Kinetic trace at 452 nm acquired in a single-wavelength registration mode. All concentrations are reported after mixing in the stopped-flow cell.

contributions from photochemistry, single-wavelength kinetic traces were acquired at $\lambda = 610$ nm for DDQ, $\lambda = 448$ nm for Cl_4Q and Br_4Q, $\lambda = 432$ nm for F_4Q, $\lambda = 452$ nm for Cl_2Q, $\lambda = 451$ nm for ClQ, and $\lambda = 449$ nm for H_4Q. The kinetic traces in Figures S17−S23 in the SI were analyzed with the bimolecular expression

$$\text{rate} = ae^{-k_{1obs}t} + be^{-k_{2obs}t} \quad (7)$$

We note that the kinetic traces for the fastest reactions, Q = Cl_4Q and F_4Q, were not fit well by eq 7. In this case, the traces were better fit by eq 2 to yield k_{1obs}, from which the second-order rate constant was then estimated from $k_{ET} = k_{1obs}/[Q]$. For consistency, kinetic traces from the other four reactions, Q = Br_4Q, Cl_2Q, ClQ, and H_4Q, were treated in a similar manner. The rate constant obtained from eq 7 and those estimated from the first-order fitting of the initial segment of the kinetic traces with eq 2 were in accordance with each other.

DISCUSSION

The ability to encapsulate a peroxide dianion within the cage of hexacarboxamide cryptand (mBDCA-5t-H_6) permits the ET chemistry of an isolated peroxide ion to be investigated. The homologous quinone series listed in Table 1 allows ET reaction (5) to be analyzed by Marcus theory over a larger driving force. The second-order rate constants listed in Table 1 vary over 6 orders of magnitude, from the mildly endergonic H_4Q system to the most exergonic DDQ system. The driving-force dependence of the ET rate constants is shown in Figure 5,

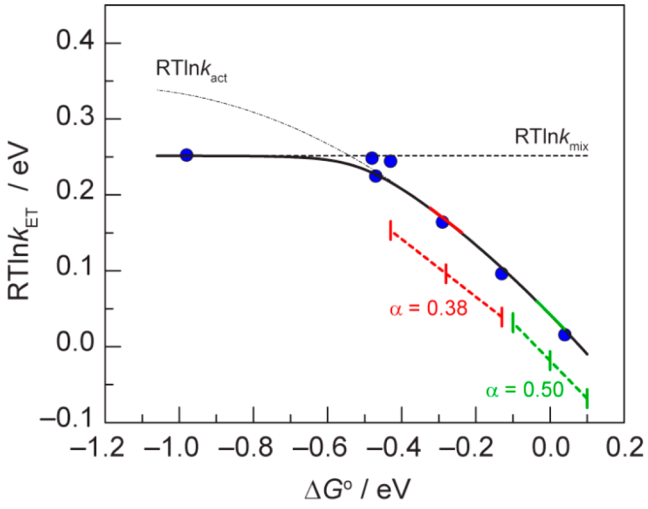

Figure 5. Dependence of RT ln k_{ET} on ΔG° for the first one-electron oxidation of $[K(18\text{-crown-6})]_2[(O_2)\subset m\text{BDCA-5t-H}_6]$ with seven different quinones in THF at −80 °C. (black solid line) Marcus curve, eq 11, with $k_{mix} = 3.8 \times 10^6$ M^{-1} s^{-1}, $\lambda_{(LO_2^{2-}/Q)} = 1.2$ eV, and $Z = 9 \times 10^8$ M^{-1} s^{-1}. The linear regions denoted by $\alpha = 0.38$ (red) and $\alpha = 0.5$ (green) are the tangents of the Marcus curve at the points directly above the midpoints of the lines. Their slopes are −0.38 and −0.5, respectively.

where the values of RT ln k_{ET} are plotted against the driving force (ΔG°). An increase of the RT ln k_{ET} values as a function of ΔG° is observed over more than 5 orders of magnitude of k_{ET} in the less exergonic region (−0.48 eV < ΔG° < 0.04 eV). For the strongest oxidant, DDQ (at $\Delta G^\circ = -0.98$ eV), the ET rate appears to level off. However, the ET rate for reaction (1) could not be measured accurately because the mixing time of the stopped-flow instrument has a limiting value, k_{mix}, which we have approximated with 3.8×10^6 M^{-1} s^{-1}.

The activation free energy, $\Delta G^\ddagger$, for outer-sphere ET,[25−27]

$$\Delta G^\ddagger = \frac{(\Delta G^\circ + \lambda)^2}{4\lambda} \quad (8)$$

is related in the Marcus formalism to the free energy of the reaction, ΔG°, and the reorganization energy, λ. In its simplest elaboration, Marcus theory provides the ET rate constant via the Eyring equation

$$k_{act} = Z \exp\left(-\frac{\Delta G^\ddagger}{RT}\right) \quad (9)$$

where Z is the bimolecular collision frequency, often taken as ~10^{11} M^{-1} s^{-1}. In semiclassical expressions of Marcus theory, Z is replaced by nuclear and electronic tunneling terms. In either classical or semiclassical formalisms, by utilizing a series of structurally related quinones, we assume with good confidence that the values for Z and λ are the same for all reactions in the present study. Under this supposition, only changes in ΔG° will influence the magnitude of the measured rate constants.

λ was estimated using the activation energy measured for reaction between ClQ and $[(O_2)\subset m\text{BDCA-5t-H}_6]^{2-}$ (Figure S26 in the SI). Assuming that the activation entropy is minimal,

dx.doi.org/10.1021/ic500759g | Inorg. Chem. 2014, 53, 5384−5391

$\Delta G^{\ddagger} = \Delta H^{\ddagger} = 24.0$ kJ/mol (0.249 eV), and the reorganization energy for reaction (5) is calculated to be $\lambda_{(LO_2^{2-}/Q)} = 1.2$ eV. Furthermore, because λ for a cross-reaction is an average of the λ values of the relevant self-exchange reactions,[28] the component contributions from the reactant partners $[(O_2)\subset m\text{BDCA-5t-H}_6]^{2-}$ and the quinone are furnished from

$$\lambda_{(LO_2^{2-}/Q)} = \frac{\lambda_{(LO_2^{2-}/LO_2^{-})} + \lambda_{(Q/Q^{\bullet-})}}{2} \tag{10}$$

Values for the self-exchange $\lambda_{(Q/Q^{\bullet-})}$ are known to depend on the nature of the countercation due to ion-pairing effects.[29] Though $\lambda_{(Q/Q^{\bullet-})}$ has not been measured with K(18-crown-6)$^+$ as the cation, it has been measured for quinones with countercations of K([2,2,2]cryptand)$^+$, $\lambda_{(Q/Q^{\bullet-})} = 0.42$ eV, and $K(THF)_4^+$, $\lambda_{(Q/Q^{\bullet-})} = 0.99$ eV.[29] Taking an average of these two values to approximate $\lambda_{(Q/Q^{\bullet-})} = 0.71$ eV for K(18-crown-6)$^+$, then the estimate of $\lambda_{(LO_2^{2-}/LO_2^{-})} = 1.7$ eV is determined from eq 10.

For the stopped-flow experiment, the observed ET rate constant is convoluted with the mixing time of the reactants. The equation that governs the observable ET kinetics is

$$\frac{1}{k_{ET}} = \frac{1}{k_{mix}} + \frac{1}{k_{act}} = \frac{1}{k_{mix}} + \frac{1}{Z\exp\left[\frac{-(\Delta G^{\circ} + \lambda)^2}{4\lambda RT}\right]} \tag{11}$$

This equation is a double-reciprocal model for the observable kinetics in a stopped-flow instrument, which has an inherent mixing time defined by k_{mix}.[30] Using $\lambda_{(LO_2^{2-}/Q)} = 1.2$ eV, which was deduced from the temperature dependence of the reaction with ClQ and the driving force for the ET reactions, the observed measurements are approximated by eq 11 for $Z = 9 \times 10^8$ M^{-1} s^{-1} (Figure 5). Figure S26 in the SI shows a comparison of the plots derived from eq 11 for a range of Z values.

The differentiated Marcus expression yields

$$\frac{\partial RT \ln k_{ET}}{\partial \Delta G^{\circ}} = \frac{\partial}{\partial \Delta G^{\circ}}\left[RT \ln Z - \left(\frac{\lambda}{4} + \frac{\Delta G^{\circ}}{2} + \frac{\Delta G^{\circ 2}}{4\lambda}\right)\right] = -\frac{1}{2}\left(1 + \frac{\Delta G^{\circ}}{\lambda}\right) \tag{12}$$

This equation defines the local slope in the activation controlled regime of the curve in Figure 5 at any driving-force value. For the driving-force range of $\lambda \gg |\Delta G^{\circ}|$, as depicted in the green region in Figure 5, a linear free-energy relationship (LFER) is obtained with a slope −0.5. For a regime in which the average driving force is $^1/_4$ the magnitude of λ, as depicted by the red region of Figure 5, then a LFER is obtained with a slope of −0.38. In this study, the specific quinones were chosen such that a large range of driving force was explored and, therefore, we prefer to model the Marcus kinetics with the quadratic Marcus equation (eq 11), as shown by the black solid line in Figure 5. The data in the activation control region fit this expected curve, with a limiting region eventually achieved because of the mixing time of the stopped-flow spectrometer.

The homogeneous ET kinetics of LO_2^{2-}, as explained by Figure 5, is related to its heterogeneous ET reaction at an electrode surface, as defined by the CVs of Figure 2. The Butler−Volmer model of electrode kinetics accounts for a rate-limiting ET and is characterized by the symmetry factor, α, also known as the transfer coefficient. This transfer coefficient is the linchpin between the Butler−Volmer model and the Marcus ET formalism.[31,32] Formally, the transfer coefficient is defined as

$$\alpha = \frac{\partial \Delta G^{\ddagger}}{\partial \Delta G^{\circ}} \tag{13}$$

Within the context of Butler−Volmer kinetics, it is assumed, without any theoretical basis, that a linear relationship exists between $\Delta G^{\ddagger}$ and ΔG°. In Marcus theory, $\Delta G^{\ddagger}$ has a quadratic dependence on ΔG°, according to eq 8, leading to

$$\alpha = \frac{1}{2}\left(1 + \frac{\Delta G^{\circ}}{\lambda}\right) \tag{14}$$

Excursions in the potential around the standard reduction potential involving small molecules are typically small, in the range of 30−200 mV, and thus $\lambda \gg |\Delta G^{\circ}|$. Therefore, in most electrochemical experiments, the transfer coefficient is in the linear Marcus regime where $\alpha = 0.5$ (green region of Figure 5) and a Butler−Volmer approximation with $\alpha = 0.5$ is often appropriate. However, when the electrode kinetics is sluggish owing to poor coupling to the electrode, large driving-force overpotentials are required to produce a peak current response in a CV, despite moderate or low values of λ. Therefore, according to eq 14, as the absolute magnitude of ΔG° approaches λ, the value of the transfer coefficient will decrease from $\alpha = 0.5$ to a lower value, depending precisely on the ratio of $\Delta G^{\circ}/\lambda$. In a graphical sense, the measured current response is then occurring in a region of the Marcus curve that is closer to the curve's apex, for example, in the red region of Figure 5.

The electrode kinetics of $[TBA]_2[(O_2)\text{-}\subset m\text{BDCA-5t-H}_6]$ is consistent with this latter case. Simulation of the CVs of $[(O_2)\subset m\text{BDCA-5t-H}_6]^{2-}$ yields a heterogeneous ET rate constant of $k_s = 2.7 \times 10^{-5}$ cm/s, which places ET on the border of what is commonly accepted as an electrochemically quasi-irreversible or irreversible ET.[33] The broadness of the wave is in accordance with the attenuated transfer coefficient of $\alpha = 0.38$, as determined from the Butler−Volmer model.[11] By modeling the CV features using the Marcus−Hush model of electrokinetics, λ may be obtained, where α is treated as a variable according to eq 14.[34] We find a heterogeneous reorganization energy of $\lambda_{el} = 0.79$ eV from the electrochemical simulations (vide supra). This electrochemical-derived reorganization energy can be compared to the homogeneous reorganization energy derived from the fit of the Marcus curve in Figure 5, though not directly. The homogeneous reorganization energy, $\lambda_{(LO_2^{2-}/LO_2^{-})}$, is defined for a bimolecular self-exchange reaction, which includes contributions from two reactant molecules, whereas the electrochemical reorganization energy involves only a single-molecule reactant (there is no contribution from the electrode surface). Therefore, the correct comparison is between the electrochemical reorganization energy, λ_{el}, and $^1/_2\lambda_{(LO_2^{2-}/LO_2^{-})}$,[35]

$$\frac{1}{2}\lambda_{(LO_2^{2-}/LO_2^{-})} = 0.85 \text{ eV} \tag{15}$$

The agreement between the two reorganization energies is quite good considering that the assumption of an intermediate reorganization energy for quinones in the presence of the cation, K(18-crown-6)$^+$, was needed to arrive at the homogeneous reorganization energy for $[(O_2)\subset m\text{BDCA-5t-H}_6]^{2-}$ oxidation (vide supra).

dx.doi.org/10.1021/ic500759g | Inorg. Chem. 2014, 53, 5384−5391

With the heterogeneous rate constant, k_s, and reorganization energy, a heterogeneous preexponential factor, Z_{el}, can also be derived using eq 9 with $\Delta G^{\ddagger} = \lambda_{el}/4$. We find $Z_{el} = 0.059$ cm/s, which is 5 orders of magnitude lower than the collision frequency $Z_{el} = (RT/2\pi M)^{1/2} = 2000$ cm/s, where M is the molar mass of $[(O_2)\subset m\text{BDCA-5t-H}_6]^{2-}$. This disparity is consistent with the results of homogeneous ET, in which a preexponential factor of $Z = 9 \times 10^8$ M^{-1} s^{-1} was found to be 2 orders of magnitude lower than the classical value. The diminished preexponential factor, whether ET by LO_2^{2-} occurs to a molecule or electrode, is attributed to poor electronic coupling[36] because of steric shielding of O_2^{2-} within the hexacarboxamide cryptand. Because the electron acceptor in the homogeneous reaction, the quinone, is small and may have partial access to the cavities presented by the cryptand molecule, whereas the heterogeneous electron acceptor, the electrode, does not, it is not surprising that the heterogeneous ET event exhibits even greater nonadiabatic character than the homogeneous ET.

CONCLUSIONS

A free peroxide ion may be isolated within the cage of a hexacarboxamide cryptand, thus allowing for the ET reactivity of this dianion of oxygen to be examined. Enhanced solubility of $[(O_2)\subset m\text{BDCA-5t-H}_6]^{2-}$ in THF is enabled by sequestration of the K^+ counterions by 18-crown-6, thus allowing for the study of homogeneous ET via the stopped-flow method. The ET reaction of the encapsulated peroxide with quinones is consistent with a highly nonadiabatic outer-sphere transfer owing to steric shielding of peroxide from its reacting partner by the hexacarboxamide cryptand. These results correlate well with the heterogeneous ET rate measurements, which exhibit an apparent transfer coefficient of $\alpha < 0.5$. Modeling the $[(O_2)\subset m\text{BDCA-5t-H}_6]^{2-}$ electrochemical response within a Marcus theory framework yields a consistent set of results for the homogeneous and heterogeneous ET reactions. We have emphasized in this study the direct relationship between the local slope of the Marcus curve and α. For nonadiabatic ET, α can be treated as a variable that depends on the driving force. The λ value thus obtained is consistent with that obtained in homogeneous Marcus analysis. This is one of the few cases[37,38] where a direct comparison between homogeneous and heterogeneous ET reactions for a given species has been made. Understanding the intrinsic parameters that govern the kinetics of ET from this unique species will facilitate its development as a reagent for oxidations, reductions, and/or atom-transfer chemistries.

The most fundamental reaction of all molecular oxygen species is ET. Owing to our success in using a macro-bicyclic anion receptor[39] to furnish an isolated peroxide dianion species that is soluble in aprotic organic media, the kinetics of the transfer of an electron from the peroxide dianion in the absence of an intimately bound proton or metal ion has now been established. Considering the importance of peroxide as an intermediate in biochemical redox processes, as a valuable industrial feedstock, and as a primary discharge product in nonaqueous lithium−air batteries, the results reported herein provide a basis for elucidating the chemistry of peroxide in a range of subjects pertaining to oxygen and ET.

ASSOCIATED CONTENT

Supporting Information

X-ray crystallographic data in CIF format, CVs, parameters used for simulation of CVs, stopped-flow kinetic traces, decay kinetics and summary of stopped-flow data, ^{1}H NMR spectra, electrochemical plots of the potential and current versus scan rate, kinetic traces for the formation of quinone anions, time-resolved stopped-flow spectral changes accompanying ET between LO_2^{2-} and quinones, Cl_4Q, F_4Q, Br_4Q, ClQ, and H_4Q, Arrhenius and Eyring plots, and Marcus curve plots with different Z factors. This material is available free of charge via the Internet at http://pubs.acs.org. Complete crystallographic data were deposited in the Cambridge Crystallographic Database Centre (CCDC 983504).

AUTHOR INFORMATION

Corresponding Authors

*E-mail: ccummins@mit.edu.
*E-mail: dnocera@fas.harvard.edu.

Funding

D.G.N. acknowledges support of the Department of Energy (DOE; Grant DE-SC0009758). C.C.C. acknowledges support of the NSF-CCI (Grant CHE-0802907). E.V.R.-A. acknowledges support of the DOE (Grant DE-FG02-06ER15799). Grants from the NSF also provided instrument support to the DCIF at MIT (Grants CHE-9808061 and DBI-9729592) and to E.V.R.-A. at Tufts (Grants CRIF CHE-0639138 and MRI CHE-1229426). D.J.G. acknowledges the support of the NSF's Graduate Research Fellowship Program. The authors also acknowledge the Robert Bosch Company for partial financial support.

Notes

The authors declare no competing financial interest.

REFERENCES

(1) Sawyer, D. T. *Oxygen Chemistry*; Oxford University Press: New York, 1991.
(2) Sawyer, D. T.; Valentine, J. S. *Acc. Chem. Res.* **1981**, *14*, 393−400.
(3) Sawyer, D. T.; Chiericato, G.; Angelis, C. T.; Nanni, E. J.; Tsuchiya, T. *Anal. Chem.* **1982**, *54*, 1720−1724.
(4) Stanbury, D. M.; Mulac, W. A.; Sullivan, J. C.; Taube, H. *Inorg. Chem.* **1980**, *19*, 3735−3740.
(5) Costentin, C.; Evans, D. H.; Robert, M.; Savéant, J.-M.; Singh, P. S. *J. Am. Chem. Soc.* **2005**, *127*, 12490−12491.
(6) Goolsby, A. D.; Sawyer, D. T. *Anal. Chem.* **1968**, *40*, 83−86.
(7) Imlay, J. A. *Annu. Rev. Biochem.* **2008**, *77*, 755−776.
(8) Jones, C. W. *Applications of Hydrogen Peroxide and Derivatives*; Royal Society of Chemistry: Cambridge, U.K., 1999.
(9) Huff, L. A.; Rapp, J. L.; Zhu, L.; Gewirth, A. A. *J. Power Sources* **2013**, *235*, 87−94.
(10) Abraham, K. M.; Jiang, Z. *J. Electrochem. Soc.* **1996**, *143*, 1−5.
(11) Lopez, N.; Graham, D. J.; McGuire, R.; Alliger, G. E.; Shao-Horn, Y.; Cummins, C. C.; Nocera, D. G. *Science* **2012**, *335*, 450−453.
(12) Chen, Y.; Freunberger, S. A.; Peng, Z.; Fontaine, O.; Bruce, P. G. *Nat. Chem.* **2013**, *5*, 489−494.
(13) McCloskey, B. D.; Scheffler, R.; Speidel, A.; Girishkumar, G.; Luntz, A. C. *J. Phys. Chem. C* **2012**, *116*, 23897−23905.
(14) Lu, Y.-C.; Gallant, B. M.; Kwabi, D. G.; Harding, J. R.; Mitchell, R. R.; Whittingham, M. S.; Shao-Horn, Y. *Energy Environ. Sci.* **2013**, *6*, 750−768.
(15) Christensen, J.; Albertus, P.; Sanchez-Carrera, R. S.; Lohmann, T.; Kozinsky, B.; Liedtke, R.; Ahmed, J.; Kojic, A. *J. Electrochem. Soc.* **2012**, *159*, R1−R30.
(16) Sheldrick, G. M. *Acta Crystallogr., Sect. A* **2008**, *64*, 112−122.
(17) Müller, P. *Crystallogr. Rev.* **2009**, *15*, 57−83.

(18) Wilshire, J.; Sawyer, D. T. *Acc. Chem. Res.* **1979**, *12*, 105−110.
(19) Ortiz, M. E.; Nuñez-Vergara, L. J.; Squella, J. A. *J. Electroanal. Chem.* **2003**, *549*, 157−160.
(20) Savéant, J.-M. *Elements of Molecular and Biomolecular Electrochemistry*; John Wiley: Hoboken, NJ, 2006; p 105.
(21) Rudolf, M. *J. Electroanal. Chem.* **2003**, *543*, 23−39. *DigiElch* from Elchsoft under http://www.elchsoft.com.
(22) Miller, J. S.; Krusic, P. J.; Dixon, D. A.; Reiff, W. M.; Zhang, J. H.; Anderson, E. C.; Epstein, A. J. *J. Am. Chem. Soc.* **1986**, *108*, 4459−4466.
(23) Eberson, L. *Acta Chem. Scand.* **1999**, *53*, 584−593.
(24) Peover, M. E. *J. Chem. Soc.* **1962**, 4540−4548.
(25) Marcus, R. A. *Annu. Rev. Phys. Chem.* **1964**, *15*, 155−196.
(26) Marcus, R. A. *Angew. Chem., Int. Ed.* **1993**, *32*, 1111−1121.
(27) Marcus, R. A.; Sutin, N. *Biochim. Biophys. Acta* **1985**, *811*, 265−322.
(28) Sutin, N. In *Inorganic Reaction and Methods*; Zuckerman, J. J., Ed.; Wiley-VCH: Weinheim, Germany, 1986; Vol. *15*, pp 41−45.
(29) Lu, J.-M.; Rosokha, S. V.; Neretin, I. S.; Kochi, J. K. *J. Am. Chem. Soc.* **2006**, *128*, 16708−16719.
(30) Nemeth, M. T.; Fogelman, K. D.; Ridley, T. Y.; Margerum, D. W. *Anal. Chem.* **1987**, *59*, 283−291.
(31) Bard, A.; Faulkner, L. R. *Electrochemical Methods: Fundamentals and Applications*, 2nd ed.; John Wiley: Hoboken, NJ, 2001; pp 121−124.
(32) Savéant, J.-M. *Elements of Molecular and Biomolecular Electrochemistry*; John Wiley: Hoboken, NJ, 2006; pp 30−44.
(33) Geiger, W. E. In *Inorganic Reaction and Methods*, Zuckerman, J. J., Ed.; Wiley-VCH: Weinheim, Germany, 1986; Vol. *15*, pp 88−91.
(34) Feldberg, S. W. *Anal. Chem.* **2010**, *82*, 5176−5183.
(35) Weaver, M. J. In *Inorganic Reaction and Methods*; Zuckerman, J. J., Ed.; Wiley-VCH: Weinheim, Germany, 1986; Vol. *15*, pp 153−163.
(36) Costentin, C. *Chem. Rev.* **2008**, *108*, 2145−2179.
(37) Kojima, H.; Bard, A. J. *J. Am. Chem. Soc.* **1975**, *97*, 6317−6324.
(38) Costentin, C.; Hajj, V.; Louault, C.; Robert, M.; Savéant, J.-M. *J. Am. Chem. Soc.* **2011**, *133*, 19160−19167.
(39) Sessler, J. L.; Gale, P. A.; Cho, W.-S. *Anion Receptor Chemistry*; Royal Society of Chemistry: Cambridge, U.K., 2006.

Inorganic Chemistry

Article

pubs.acs.org/IC

Photophysical Properties of β-Substituted Free-Base Corroles

Christopher M. Lemon, Robert L. Halbach, Michael Huynh, and Daniel G. Nocera*

Department of Chemistry and Chemical Biology, Harvard University, 12 Oxford Street, Cambridge, Massachusetts 02138, United States

Supporting Information

ABSTRACT: Corroles are an emergent class of fluorophores that are finding an application and reaction chemistry to rival their porphyrin analogues. Despite a growing interest in the synthesis, reactivity, and functionalization of these macrocycles, their excited-state chemistry remains undeveloped. A systematic study of the photophysical properties of β-substituted corroles was performed on a series of free-base β-brominated derivatives as well as a β-linked corrole dimer. The singlet and triplet electronic states of these compounds were examined with steady-state and time-resolved spectroscopic methods, which are complemented with density functional theory (DFT) and time-dependent DFT calculations to gain insight into the nature of the electronic structure. Selective bromination of a single molecular edge manifests in a splitting of the Soret band into *x* and *y* polarizations, which is a consequence of asymmetry of the molecular axes. A pronounced heavy atom effect is the primary determinant of the photophysical properties of these free-base corroles; bromination decreases the fluorescence quantum yield (from 15% to 0.47%) and lifetime (from 4 ns to 80 ps) by promoting enhanced intersystem crossing, as evidenced by a dramatic increase in k_{nr} with bromine substitution. The nonbrominated dimer exhibits absorption and emission features comparable to those of the tetrabrominated derivative, suggesting that oligomerization provides a means of red-shifting the spectral properties akin to bromination but without decreasing the fluorescence quantum yield.

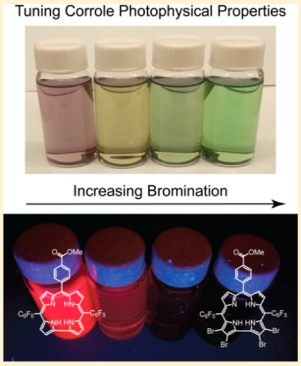

INTRODUCTION

Porphyrins possess unique electronic and photophysical properties that engender their use as imaging agents,[1−4] photosensitizers for photodynamic therapy,[5−7] light-harvesting antennas,[8−11] and optical sensors.[12−15] A related class of molecules is corroles, which, like porphyrins, are 18 π-electron tetrapyrrole macrocycles but with a contracted 23-atom core versus the 24-atom core of porphyrins. This contracted core arises from a direct pyrrole−pyrrole linkage to yield three meso carbons bridging pyrrole units, unlike the four meso carbons of a porphyrin. Corroles have been historically difficult to synthesize with the first preparations involving the cyclization of the linear precursor biladiene-*ac*.[16,17] With the advent of facile one-pot methods,[18−21] corrole chemistry has expanded with emphasis on both the synthesis and peripheral functionalization of the macrocycle.[22−27] The availability of corroles as a result of these synthetic methods has led to many applications,[28−30] including their function as molecular catalysts,[31−36] photosensitizers,[37−39] singlet oxygen photogenerators,[40,41] and imaging agents.[42] Despite these advances, there have been comparatively few photophysical studies of free-base corroles. Some of these studies include the elucidation of photophysics as a function of meso-substitution,[40,41,43−46] N−H tautomerization,[47−50] and higher order architectures such as corrole−fluorophore dyads.[51−53]

A desirable property of any fluorophore is the ability to tune its absorbance and emission wavelengths, as well as the excited-state lifetime. Modulation of spectral features to achieve a desired optical window is important for any imaging or sensing application, especially for those that function in the biological milieu. Free-base corroles have appreciable fluorescence quantum yields and excited-state lifetimes of several nanoseconds.[40,43] The effect of substitution at the meso positions of the corrole appears to have a more pronounced influence on photophysical properties than it does for porphyrins. Spurred by these observations, we were interested in delineating the effect of β-substitution on the electronic structure and excited-state properties of corroles. We find that the electronic spectral properties are governed by the (*x*,*y*) asymmetry of the corrole ring. As observed by Gross and co-workers for Al and Ga corroles,[54] β-substitution with halogen causes a severe perturbation to the photophysics of the corrole, arising from a pronounced heavy atom effect. Corrole dimerization at the β-position provides a means of red-shifting the spectral properties akin to bromination but without decreasing the fluorescence quantum yield. Such design principles are useful for the implementation of corroles for sensing applications.

EXPERIMENTAL SECTION

Materials. The following materials were used as received: hexanes, acetone, ethanol (EtOH), methanol (MeOH), chloroform ($CHCl_3$), dichloromethane (CH_2Cl_2), pentane, inhibitor-free tetrahydrofuran (THF), acetonitrile (MeCN), toluene, benzonitrile (PhCN), dimethyl sulfoxide (DMSO), pyrrole, indium(III) chloride ($InCl_3$), sodium hydroxide (NaOH) beads, methyl 4-formylbenzoate, 2,3-dichloro-5,6-dicyano-1,4-benzoquinone (DDQ), *N*-bromosuccinimide (NBS), and pentafluorobenzaldehyde from Sigma-Aldrich; sodium bicarbonate ($NaHCO_3$), sodium sulfate (Na_2SO_4), and sodium chloride (NaCl)

Received: December 4, 2014
Published: February 25, 2015

DOI: 10.1021/ic502860g
Inorg. Chem. 2015, 54, 2713−2725

from Mallinckrodt; hydrochloric acid (HCl) from EMD; silica gel 60 Å 230−400 mesh ASTM from Whatman; and chloroform-*d* ($CDCl_3$) from Cambridge Isotope Laboratories. Argon gas (Airgas) was passed over a Drierite column prior to use. The compounds 5-pentafluorophenyldipyrromethane (**1**)[55,56] and 5,10,15,20-tetraphenylporphyrin (H_2TPP)[57] were prepared according to literature procedures or slight modifications thereof.

Corrole Synthesis. In a 1 L round-bottom flask, 1.58 g of 5-pentafluorophenyldipyrromethane (**1**) (5.06 mmol) and 0.41 g of methyl 4-formylbenzoate (2.5 mmol) were dissolved in 250 mL of MeOH. A solution of HCl was prepared by dissolving 12.5 mL of concentrated HCl (12 M) in 250 mL of H_2O. The acid solution was added to the MeOH solution and stirred at room temperature for 1 h. Over the course of the reaction, the solution became cloudy, and a red-brown color developed. The reaction mixture was poured into a 2 L separatory funnel, and the product was extracted with $CHCl_3$ (200 mL ×3). The combined organics were washed with water (×2), dried over Na_2SO_4, and the solution was diluted to a volume of 1 L with $CHCl_3$; 1.71 g of DDQ (2.51 mmol) was added, and this solution immediately turned dark. The reaction mixture was stirred overnight at room temperature. The crude reaction mixture was concentrated to a volume of ∼200 mL and then poured onto a silica gel column packed with hexanes. All fluorescent material was collected using $CHCl_3$ as the eluent. The product was purified on a silica gel column packed with hexanes, using hexanes then 1:1 hexanes/CH_2Cl_2 to elute **2** as a purple solution. A second macrocyclic product (**3**) was identified at the top of the column and was isolated using 100% CH_2Cl_2 as the eluent to afford a green solution. After solvent removal, 0.33 g (17% yield) of **3** was isolated as a shiny purple solid. Compound **2**, which was initially obtained as a black solid, was further purified on a silica gel column packed with hexanes, using hexanes then 1:1 hexanes/CH_2Cl_2 as the eluent. After solvent removal, 0.98 g (51% yield) of **2** was obtained as a purple solid.

*10-(4-Methoxycarbonylphenyl)-5,15-bis(pentafluorophenyl)-corrole (**2**).* ^{1}H NMR (500 MHz, $CDCl_3$) δ 4.10 (s, 3H), 8.27 (d, J = 8.1 Hz, 2H), 8.45 (d, J = 8.1 Hz, 2H), 8.59 (bs, 2H), 8.66 (d, J = 4.8 Hz, 2H), 8.73 (d, J = 4.6 Hz, 2H), 9.14 (d, J = 4.3 Hz, 2H). ^{19}F NMR (376 MHz, CH_2Cl_2) δ −163.98 (m, 4F), −155.15 (m, 2F), −140.15 (dd, J^1 = 28.9 Hz, J^2 = 6.5 Hz, 4F). Anal. Calcd for $(M + H)^+$, M = $C_{39}H_{18}F_{10}N_4O_2$: 765.1270; Found ESI-MS: 765.1252. UV−vis (toluene), λ in nm (ε in 10^3 M^{-1} cm^{-1}): 424 (99), 525 (7.3), 565 (16), 615 (9.3), 640 (5.8).

*3-[10′-(4-Methoxycarbonylphenyl)-5′,15′-bis-(pentafluorophenyl)corrole-3′-yl]-10-(4-methoxycarbonylphenyl)-5,15-bis(pentafluorophenyl)corrole (**3**).* ^{1}H NMR (500 MHz, $CDCl_3$) δ 4.07 (s, 6H), 8.21 (d, J = 7.7 Hz, 4H), 8.25 (d, J = 8.0 Hz, 2H), 8.41 (d, J = 8.2 Hz, 4H), 8.47 (d, J = 4.8 Hz, 2H), 8.60 (d, J = 4.7 Hz, 2H), 8.71 (d, J = 4.7 Hz, 2H), 8.74 (d, J = 4.3 Hz, 2H), 9.16 (s, 2H), 9.17 (d, J = 4.2 Hz, 2H). ^{19}F NMR (376 MHz, CH_2Cl_2) δ −167.62 (bs, 2F), −165.29 (m, 2F), −163.97 (m, 4F), −157.03 (bs, 2F), −155.10 (m, 2F), −141.33 (bs, 2F), −139.98 (dd, J^1 = 25.9 Hz, J^2 = 6.5 Hz, 4F),−139.49 (bs, 2F). Anal. Calcd for $(M + H)^+$, M = $C_{78}H_{34}F_{20}N_8O_4$: 1527.2384; Found ESI-MS: 1527.2322. UV−vis (toluene), λ in nm (ε in 10^3 M^{-1} cm^{-1}): 418 (144), 448 (91), 547 (20), 582 (34), 627 (27), 656 (34).

Preparation of Bromocorroles. In a 100 mL round-bottom flask, 82 mg (0.11 mmol) of **2** was dissolved in 20 mL of CH_2Cl_2. A solution of *N*-bromosuccinimide (NBS) was prepared by dissolving 52 mg (0.29 mmol) of the compound in 10 mL of MeCN. The NBS solution was slowly added to the corrole solution, ∼1 mL at a time, using a pipet over the course of ∼5 min. The resultant blue-green solution was stirred at room temperature for 1 h. The crude reaction mixture was extracted with $CHCl_3$, washed with water, saturated $NaHCO_3$, and brine, then dried over Na_2SO_4 and brought to dryness. The residue was purified on a silica gel column packed with hexanes using 1:1 hexanes/$CHCl_3$ as the eluent. Fractions were collected in 100 mL aliquots. Fractions 1−3 were blue-green in color and were identified as compound **5** by ^{1}H NMR, affording 27 mg (25% yield) of the product. Fractions 5−9 were violet in color and were identified as compound **4** by ^{1}H NMR, affording 35 mg (35% yield) of the product. Later-eluting fractions were identified as monobrominated corroles (2-bromo-**2** and 3-bromo-**2**), as well as putative decomposition products on the basis of ^{1}H NMR.

*2,3-Dibromo-10-(4-methoxycarbonylphenyl)-5,15-bis-(pentafluorophenyl)corrole (**4**).* ^{1}H NMR (500 MHz, $CDCl_3$) δ 4.08 (s, 3H), 8.26 (d, J = 8.1 Hz, 2H), 8.44 (d, J = 8.1 Hz, 2H), 8.57 (d, J = 4.4 Hz, 1H), 8.62 (d, J = 4.8 Hz, 1H), 8.66 (overlapping d, J = 5.0 Hz, 1H), 8.67 (overlapping d, J = 4.8 Hz, 1H), 8.81 (d, J = 4.7 Hz, 1H), 9.39 (d, J = 4.4 Hz, 1H). ^{19}F NMR (376 MHz, CH_2Cl_2) δ −164.64 (m, 2F), −163.42 (m, 2F), −155.02 (m, 1F), −154.07 (m, 1F), −140.31 (d, J = 27.2 Hz, 2F), −140.11 (d, J = 27.1 Hz, 2F). Anal. Calcd for $(M + H)^+$, M = $C_{39}H_{16}Br_2F_{10}N_4O_2$: 922.9460; Found ESI-MS: 922.9462. UV−vis (toluene), λ in nm (ε in 10^3 M^{-1} cm^{-1}): 427 (93), 528 (7.5), 565 (15), 597 (8.9), 648 (14).

*2,3,17-Tribromo-10-(4-methoxycarbonylphenyl)-5,15-bis-(pentafluorophenyl)corrole (**5**).* ^{1}H NMR (500 MHz, $CDCl_3$) δ 4.09 (s, 3H), 8.24 (d, J = 8.1 Hz, 2H), 8.45 (d, J = 8.0 Hz, 2H), 8.58 (d, J = 4.8 Hz, 1H), 8.63 (d, J = 4.6 Hz, 2H), 8.73 (d, J = 4.7 Hz, 1H), 9.34 (s, 1H). ^{19}F NMR (376 MHz, CH_2Cl_2) δ −164.38 (m, 2F), −164.09 (m, 2F), −154.60 (m, 1F), −154.01 (m, 1F), −140.92 (d, J = 27.0 Hz, 2F), −140.14 (d, J = 27.3 Hz, 2F). Anal. Calcd for $(M + H)^+$, M = $C_{39}H_{15}Br_3F_{10}N_4O_2$: 1000.8565; Found ESI-MS: 1000.8555. UV−vis (toluene), λ in nm (ε in 10^3 M^{-1} cm^{-1}): 423 (100), 437 (92), 531 (7.3), 570 (16), 598 (11), 650 (19).

*2,3,17,18-Tetrabromo-10-(4-methoxycarbonylphenyl)-5,15-bis-(pentafluorophenyl)corrole (**6**).* In a 100 mL round-bottom flask, 80 mg (0.10 mmol) of **2** was dissolved in 15 mL of MeCN. A solution of NBS was prepared by dissolving 87 mg (0.49 mmol) of the compound in 15 mL of CH_2Cl_2. The NBS solution was slowly added to the corrole solution, ∼1 mL at a time using a pipet over the course of ∼5 min. The resultant blue-green solution was stirred at room temperature for 1 h. The crude reaction mixture was washed with water, saturated $NaHCO_3$, and brine, then dried over Na_2SO_4, and brought to dryness. The residue was purified on a silica gel column packed with hexanes using hexanes then 1:1 hexanes/CH_2Cl_2 as the eluent. The product eluted as a blue-green solution. The solvent was removed to afford 67 mg (62% yield) of the title compound as a purple solid. ^{1}H NMR (500 MHz, $CDCl_3$) δ 4.08 (s, 3H), 8.20 (d, J = 8.0 Hz, 2H), 8.43 (d, J = 8.1 Hz, 2H), 8.51 (d, J = 4.7 Hz, 2H), 8.59 (d, J = 4.6 Hz, 2H). ^{19}F NMR (376 MHz, CH_2Cl_2) δ −164.04 (m, 4F), −154.03 (m, 2F), −140.46 (dd, J^1 = 27.9 Hz, J^2 = 6.2 Hz, 4F). Anal. Calcd for $(M + H)^+$, M = $C_{39}H_{14}Br_4F_{10}N_4O_2$: 1080.7650; Found ESI-MS: 1080.7699. UV−vis (toluene), λ in nm (ε in 10^3 M^{-1} cm^{-1}): 423 (98), 440 (88), 538 (8.1), 575 (19), 607 (13), 655 (19).

Physical Measurements. ^{1}H NMR spectra were recorded at 23 °C on a Varian Inova-500 NMR spectrometer at the Harvard University Department of Chemistry and Chemical Biology Laukien-Purcell Instrumentation Center. All spectra were internally referenced to the residual solvent signal (δ = 7.26 for $CHCl_3$ in $CDCl_3$).[58] ^{19}F NMR spectra were recorded at 25 °C on a Varian Mercury-400 NMR spectrometer and externally referenced to α,α,α-trifluorotoluene (δ = −63.72). Mass spectra were recorded on a Bruker micrO-TOF-QII LCMS ESI-TOF mass spectrometer in positive ion mode. All spectra were externally calibrated with sodium formate. UV−vis absorption spectra were acquired using a Cary 5000 spectrometer (Agilent). Steady-state emission spectra were recorded on a Photon Technology International (PTI) QM 4 fluorometer equipped with a 150 W Xe arc lamp and a Hamamatsu R2658 photomultiplier tube. Relative quantum yields of corroles in toluene were calculated using H_2TPP in toluene as the reference according to the following equation

$$\Phi_{sam} = \Phi_{ref}\left(\frac{\nabla_{sam}}{\nabla_{ref}}\right)\left(\frac{\eta_{sam}}{\eta_{ref}}\right)^2 \quad (1)$$

where ∇ is the slope of the plot of integrated fluorescence intensity versus absorbance (constructed using 5 points), η is the refractive index of the solvent (taken to be 1.4961 for toluene),[59] and Φ_{ref} is the emission quantum yield of the reference. Φ_{ref} was taken to be 0.11 for an aerated sample of H_2TPP in toluene.[60] Corrole samples for lifetime (τ_0) measurements and transient absorbance spectra were prepared

DOI: 10.1021/ic502860g
Inorg. Chem. 2015, 54, 2713−2725

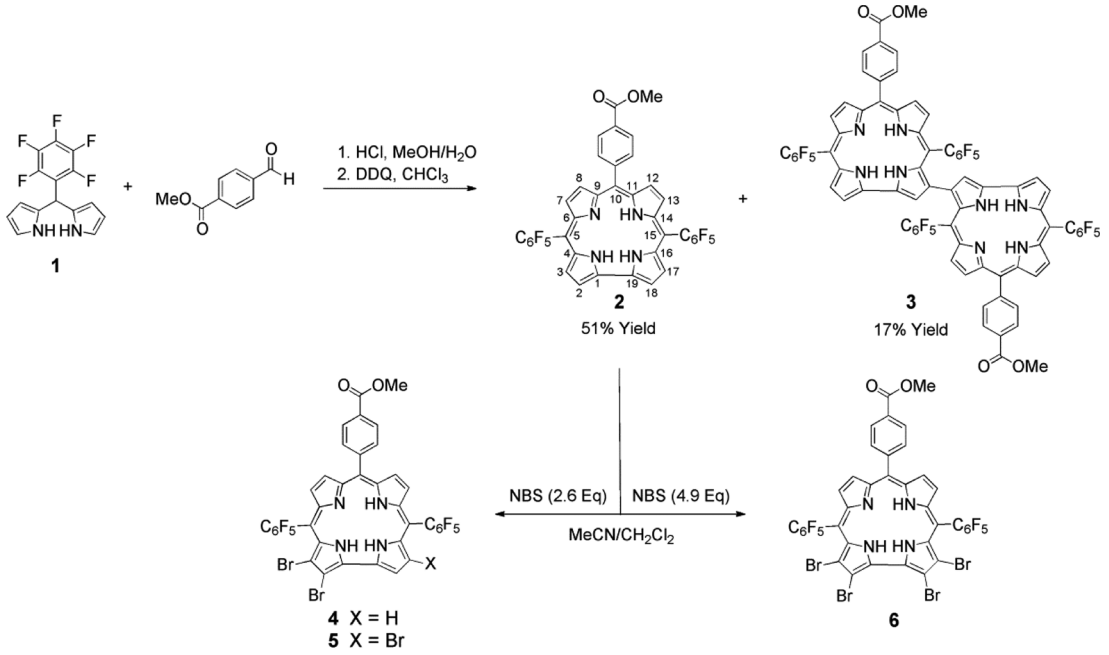

Figure 1. Synthesis of free-base corrole **2** and subsequent bromination with NBS to afford a series of β-brominated corroles **4**–**6**.

using three freeze–pump–thaw (fpt) cycles at vacuum pressures below 10^{-4} Torr.

Femtosecond emission lifetime measurements were acquired using a Libra-F-HE (Coherent) chirped–pulse amplified Ti:sapphire laser system.[61] The 800 nm laser output was used to pump an OperA Solo (Coherent) optical parametric amplifier (OPA); excitation pulses of 400 nm were produced via fourth harmonic generation of the signal using a BBO crystal, and the pulse power was attenuated to 2–6 mW at the sample using neutral density filters. Emission lifetimes were measured on a Hamamatsu C4334 Streak Scope streak camera, which has been described elsewhere.[62] The emission signal was collected over a 140 nm window centered at 680 or 700 nm with 50, 20, 2, or 1 ns time windows using a Stanford Research Systems DG535 delay generator.

Nanosecond transient absorption (TA) spectra of corroles were acquired using a previously reported system.[63,64] Pump light was provided by the third harmonic (355 nm) of a Quanta-Ray Nd:YAG laser (Spectra Physics) operating at 10 Hz. The pump light was passed through a BBO crystal in an optical parametric oscillator (OPO), yielding a visible frequency that was tuned to 430 nm to excite the sample. Excitation light was attenuated to 100–300 μJ per pulse for all experiments using neutral density filters. Probe white light was generated using a 75 W Xe-arc lamp (PTI). The probe beam was aligned with the sample, while the laser pump beam was positioned at 15° with respect to the white light probe, and both beams were focused on the sample. After exiting the sample, the light entered either a Triax 320 (Jobin Yvon Horiba) or a iHR320 monochromator (Horiba Scientific) and was dispersed by a blazed grating (500 nm, 300 grooves/mm) centered at 500 nm. The entrance and exit slits of the monochromator were set to provide a spectral resolution of 4 nm. TA spectra were collected using a gated intensified CCD camera (DH520–25F-01, Andor Technology). Acquisition delays and gate times for the CCD were set using a Stanford Research Systems DG535 delay generator, which was synchronized to the Q-switch output of the laser. The final data were calculated from a combination of four spectra: I (pump on/probe on), I_F (pump on/probe off), I_0 (pump off/probe on), and I_B (pump off/probe off). The resultant TA spectra were obtained using the following equation:

$$\Delta OD = -\log\left(\frac{I - I_F}{I_0 - I_B}\right) \quad (2)$$

thereby correcting for both sample emission and extraneous background light. To acquire these four spectra, pump and probe beams were selectively exposed to the sample using electronically controlled shutters (Uniblitz T132, Vincent Associates), which were triggered using a Stanford Research Systems DG535 delay generator synchronized to the Q-switch output of the laser. For TA single wavelength kinetics, output signal from the sample was passed through a 450 nm long pass filter and then amplified by a photomultiplier tube (R928, Hamamatsu) and collected on a 1 GHz digital oscilloscope (9384CM, LeCroy); acquisition was triggered using a photodiode to collect scattered laser excitation light.

Computational Details. Density functional theory (DFT) calculations were performed with the hybrid functional Becke-3 parameter exchange functional[65−67] and the Lee–Yang–Parr nonlocal correlation functional (B3LYP)[68] as implemented in the Gaussian 09, Revision D.01 software package.[69] For light atoms (H, C, N, O, and F), a polarized split-valence triple-ζ basis set that includes p functions on hydrogen atoms and d functions on other atoms (i.e., 6-311G(d,p) or 6-311G** basis set) was used. The LANL2DZ basis set was used for bromine atoms with the inclusion of an effective core potential (ECP).[70,71] All calculations were performed with a polarizable continuum (PCM) solvation model in toluene using a polarizable conductor calculation model (CPCM).[72,73] All geometries were confirmed as local minima structures by calculating the Hessian matrix and ensuring that no imaginary eigenvalues were present. Excited-state calculations were performed using time-dependent DFT (TD-DFT)[74−78] with the same functionals, basis sets, and solvation details as the ground state, but with the inclusion of diffuse functions on all light atoms (i.e., 6-311++G** basis set). Excited-state energies were computed for the 10 or 15 lowest singlet and triplet excited states. All optimized geometries and molecular orbitals were rendered in the program Avogadro.[79] Simulated UV–vis spectra were generated in the program Gauss View 5 by broadening transition lines with Gaussian functions with a half width of 0.08 eV.

X-ray Crystallographic Details. Diffraction-quality crystals of **2** were obtained by slow evaporation of a 1:1 mixture of pentane and THF under N_2 at 20 °C, affording crystals as purple blocks; a single crystal was cut from a larger one for the X-ray diffraction study. Crystals of **3** and **6** were obtained by dissolving each compound in a minimal amount of a 1:1 mixture of pentane and THF and cooling the resultant solutions to −40 °C, affording crystals as purple blocks. Low-temperature (100 K) X-ray diffraction data were collected on a Bruker

DOI: 10.1021/ic502860g
Inorg. Chem. 2015, 54, 2713–2725

three-circle platform goniometer equipped with an Apex II CCD detector and an Oxford cryostream cooling device, performing φ and ω scans. Radiation was generated from a graphite fine focus sealed tube Mo Kα (0.710 73 Å) source. Crystals were mounted on a cryoloop using Paratone-N oil. Data were processed and refined using the program SAINT supplied by Siemens Industrial Automation. Structures were solved by intrinsic phasing methods in SHELXT and refined by standard difference Fourier techniques in the SHELXTL program suite.[80] Hydrogen atoms were located in the difference map and were refined isotropically using a riding model; all non-hydrogen atoms were refined anisotropically. The structure of **3** contains a pentafluorophenyl group that is disordered over two positions in a ratio of ~0.6:0.4, as well as three molecules of disordered THF and one molecule of disordered pentane per molecule of **3**. Since the solvent disorder could not be modeled satisfactorily, the associated electron density was removed using the program SQUEEZE. The structure of **6** contains two molecules of THF, one molecule of *N*-methyl-2-pyrrolidone, and one disordered molecule of pentane per two molecules of **6**. Since the disordered pentane molecule of **6** could not be satisfactorily modeled, this electron density was removed using the program SQUEEZE. Unit cell parameters, morphology, and solution statistics for the structure are summarized in Supporting Information, Table S1. Thermal ellipsoid plots are drawn at the 50% probability level with hydrogen atoms removed for clarity.

RESULTS

Corrole Synthesis and Structure. Bromination of the corrole periphery affords a convenient method of functionalization and a useful synthetic handle for cross-coupling chemistry as a means of further elaboration of the corrole macrocycle.[21,81−87] Compound **2** was prepared by the HCl-catalyzed condensation of dipyrromethane **1** and methyl 4-formylbenzoate (Figure 1), following the procedure of Koszarna and Gryko.[88] This method furnishes corroles in high yield (up to 32% yield for 5,10,15-triphenylcorrole) and facilitates the preparation of *trans*-A_2B corroles without scrambling (i.e., circumventing the formation of the *cis*-A_2B isomer). The desired product was obtained in 51% yield, giving quantities of ~1 g in a typical synthesis. This yield is greatly improved over previous preparative methods,[51] which used TFA as the acid catalyst and gave **2** in 18% yield (~300 mg of isolated product).

An additional fluorescent macrocyclic product, obtained in 17% isolated yield, was assigned as the 3,3′ linked dimer **3** on the basis of mass spectrometry and ^{1}H NMR. Seven unique β-pyrrole protons in the ^{1}H NMR spectrum established that the lower-symmetry 2,3′-linked dimer had not formed. The chemical shift of the singlet (δ 9.16 ppm), attributed to the proton adjacent to the corrole−corrole linkage, suggested a 3,3′ linkage as it compared well to δ 9.12 ppm for the 3,3′ dimer of 5,10,15-tris(pentafluorophenyl)corrole (H_3TPFC).[89] A resonance comparable to that of the 2,2′ dimer of H_3TPFC (δ 9.66 ppm) was also absent,[90] precluding formation of this derivative as a byproduct. H_3TPFC has recently been observed to undergo regioselective oxidative coupling in the presence of quinone oxidants to give 3,3′-linked oligomers,[91] thus offering a plausible explanation for the formation of **3** as a byproduct in the preparation of **2**.

Serial bromination of **2** generated brominated corroles **4**−**6**. The majority of bromination reactions have been performed on metallocorroles by using a significant excess of Br_2 to deliver the β-octabromo derivatives.[81−83] A notable exception is germanium corrole, which gave hexabromo, pentabromo, or tribromo derivatives (each as a single regioisomer), depending on the amount of Br_2 added.[84] As an alternative to Br_2, there has been a report on the bromination of H_3TPFC using NBS; the extent of bromination is proportional to the amount of added NBS.[85] Unlike H_3TPFC, we find that treatment of corrole **2** with NBS is not straightforward. Addition of small volumes of NBS to **2** prompted the reaction mixture to turn from violet to blue-green, and the observed fluorescence intensity of the solution, as observed using a hand-held UV lamp (365 nm) as the excitation source, dramatically decreased.

In an attempt to better control the distribution of brominated products, the amount of NBS was varied from 1.9 to 2.7 equiv (Figure 1). In all cases, a mixture of products (mono-, di-, and tribromo corroles) was obtained. However, this reaction, as with nearly all corrole peripheral functionalization reactions,[26] is regioselective, producing four unique species: 2-bromo-**2**, 3-bromo-**2**, **4**, and **5**. This result suggests that bromination is not sequential and that all products are formed in the course of the reaction. Indeed, monobromo corroles were identified in reaction mixtures that used more than 3 equiv of NBS. The best results were achieved when using 2.6 equiv of NBS. All of these species have very similar R_f values by thin-layer chromatography (TLC, 1:1 hexanes/$CHCl_3$) and appear as a single spot on the TLC plate. Fortunately, each species has a distinctive color, making it possible to separate these compounds by column chromatography. Compound **5** elutes first as a blue-green solution, followed by **4** as a violet solution with a gold-amber hue (see TOC image). These two products were obtained as pure species by careful column chromatography. The two monobrominated corroles (violet-brown solution) eluted next as a mixture, as identified by ^{1}H HMR, along with decomposition products. These late-eluting fractions were discarded because each contained a mixture of several products, as evidenced by multiple methyl ester resonances in the ^{1}H HMR spectrum. Monobrominated corrole isomers are inseparable,[85] and therefore no efforts were made to further purify or characterize these compounds, as mixtures are not suitable for photophysical characterization. Small fraction volumes were collected to ensure that pure compounds were isolated. We note that reported yields represent the isolated yields of pure compounds; the actual reaction yields are presumably higher, as fractions identified as mixtures of products were discarded. Compound **6** was isolated as the exclusive product when more than 4 equiv of NBS were used. This suggests that the excess NBS reacts with any remaining corrole with fewer than four bromine atoms to give a single product. Moreover, this result also demonstrates that the unique axis of the corrole (i.e., the 2, 3, 17, and 18 positions) is the most reactive and that excess NBS does not react at the opposite side (i.e., the 7, 8, 12, and 13 positions), a result that is consistent with known corrole reactivity.[26]

Diffraction-quality crystals of compounds **2**, **3**, and **6** were obtained as purple blocks from THF and pentane. The thermal ellipsoid plots of the refined structures are shown in Figures 2, 3, and 4, and a summary of the crystallographic data is presented in Supporting Information, Table S1. The solid-state structure of **2** (Figure 2) exhibits structural metrics that fall within the range observed for other C_6F_5-substituted free-base corroles.[19,92,93] Three of the four pyrrole rings are nearly coplanar, while the fourth cants out of the plane and hydrogen bonds with a THF solvent molecule. The macrocycle has a mean deviation of 0.170 ± 0.144 Å from the mean 23-atom plane, with a maximum deviation of 0.501 Å for the pyrrole that participates in hydrogen bonding. The solid-state structure of **3** unambiguously confirms the 3,3′ linkage of the dimer (Figure

DOI: 10.1021/ic502860g
Inorg. Chem. 2015, 54, 2713−2725

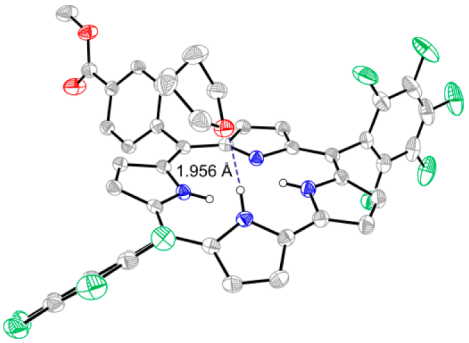

Figure 2. Solid-state structure of **2**, showing a THF molecule hydrogen bonded to the corrole core. Thermal ellipsoids are drawn at the 50% probability level, and carbon-bound hydrogen atoms were removed for clarity.

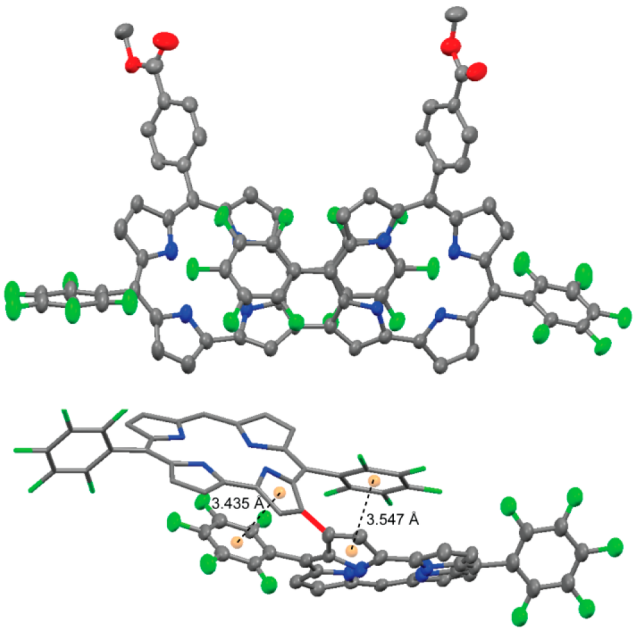

Figure 3. Solid-state crystal structure of compound **3**. Thermal ellipsoids are drawn at the 50% probability level. The lower structure highlights the π-aryl interaction by showing the centroids of the relevant rings and their corresponding distances. To better illustrate this conformation, one corrole unit is drawn with ellipsoids while the other uses capped sticks. Additionally, the 3,3′ linkage is highlighted in red. For clarity, hydrogen atoms and the 10 meso substituents were removed from the lower structure.

3, top). The structure is highly contorted to enable a favorable π-aryl interaction between a pentafluorophenyl ring and a pyrrole unit of the macrocycle (Figure 3, bottom), giving 3.435 and 3.547 Å distances between the centroids of these rings. This is atypical of meso-aryl corroles and porphyrins, which usually have these substituents orthogonal to the macrocycle plane. This close contact results in a 42.09° separation between the mean 23-atom planes of the corrole units. This is comparable to that observed for the 3,3′-linked dimer of H_3TPFC (CCDC No. 842519),[91] which displays a 47.60° separation of the corrole planes. Despite this close contact, the corrole units adopt a highly planar structure, with three of the pyrrole units being largely coplanar, while the fourth pyrrole unit (i.e., the one participating in dimer formation) cants out of the corrole plane. The crystal structure of **6** displays two corroles in the asymmetric unit that display differing degrees of

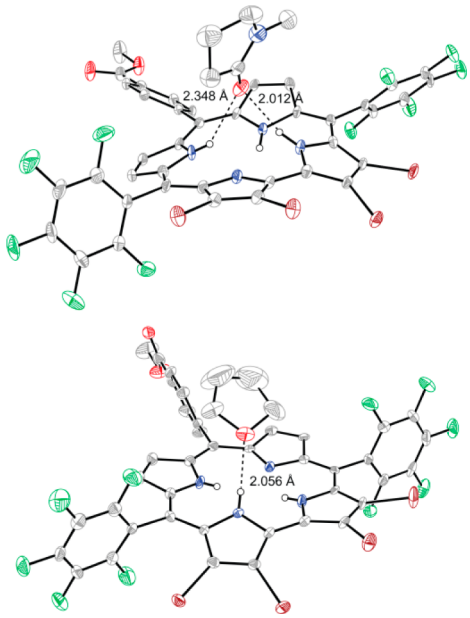

Figure 4. Solid-state crystal structure of compound **6** showing the two independent corrole molecules in the asymmetric unit. Thermal ellipsoids are drawn at the 50% probability level, and carbon-bound hydrogen atoms were removed for clarity. One corrole is highly nonplanar, exhibiting a molecule of *N*-methyl-2-pyrrolidone bound to the core (upper), while the other corrole (lower) features a hydrogen bonded THF molecule, akin to the structure of **2** (Figure 2).

nonplanarity. One molecule (Figure 4, top) is highly nonplanar, exhibiting a mean deviation of 0.259 ± 0.214 Å from the mean 23-atom plane, with a maximum deviation of 0.639 Å (a pyrrole carbon bearing a bromine atom). This large deviation may originate from a crystal packing effect, as this molecule has a molecule of *N*-methyl-2-pyrrolidone hydrogen bonded to the macrocycle core. Two pyrrole units cant out of the plane to result in this large deviation from planarity. Conversely, the other corrole (Figure 4, bottom) has a THF molecule hydrogen bonded to the macrocycle core; it exhibits mean deviation of 0.126 ± 0.111 Å from the mean 23-atom plane, with a maximum deviation of 0.388 Å (a pyrrole carbon bearing a bromine atom). This observation is consistent with what is observed in the solid-state structure of **2** and may be more representative of corrole conformations.

Absorbance Spectroscopy. The electronic absorption spectra of corroles **2**, **4**, **5**, and **6**, which are shown in Figure 5a, exhibit intense Soret or B bands in the near-UV and weaker Q bands in the visible spectral regions. Supporting Information, Table S2 lists the absorbance maxima for these compounds. The Soret band of **2** is quite broad (43 nm fwhm), and the line shape displays a plateau rather than a Gaussian profile, suggestive of overlapping transitions (i.e., B_x and B_y polarizations), which is expected for lower-symmetry corrole molecules. With the inclusion of two bromine atoms along the same face of the corrole (compound **4**), the Soret red-shifts by 3 nm and broadens (46 nm fwhm), establishing that the B_x and B_y transitions are energetically more separated upon bromination. Sequential bromination further separates these transitions such that the two bands are clearly resolved in **6** (Supporting Information, Figure S1a). In this progression of compounds, the edge defined by the 2, 3, 17, 18 positions of the molecule is perturbed, while the other edge (2, 3, 7, 8 positions) is much less perturbed. For clarity, the *y* axis is taken

DOI: 10.1021/ic502860g
Inorg. Chem. 2015, 54, 2713−2725

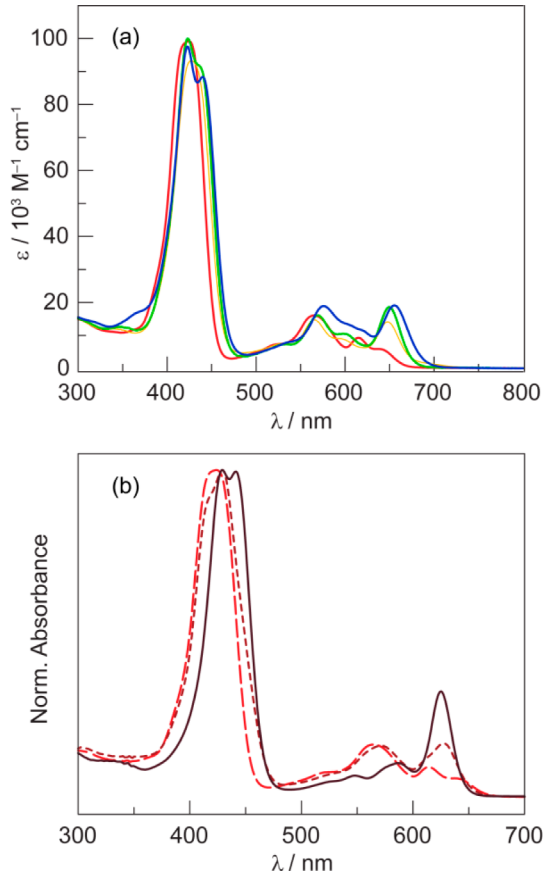

Figure 5. (a) Comparison of the steady state absorption spectra of a series of corroles in toluene: **2** (red —), **4** (yellow —), **5** (green —), and **6** (blue —). With an increasing extent of bromination, the Soret band splits, and these transitions exhibit a spectral red shift. See Supporting Information, Figure S1 for an expansion of the Soret and Q-band regions. (b) Steady-state absorption spectra of **2** in toluene (red – –), PhCN (maroon - - -), and DMSO (purple —).

as the C_2 pseudorotational axis and is aligned through the 10 position, whereas the *x* axis is perpendicular to it in the plane of the corrole and passes through the 5 and 15 positions.

All four corroles exhibit four Q bands in the 500–700 nm region. Consistent with what is observed for porphyrins, there are two fundamental bands $Q_x(0,0)$ and $Q_y(0,0)$ at 565 and 650 nm, respectively, each with vibrational overtones $Q_x(1,0)$ and $Q_y(1,0)$ at 530 and 600 nm, respectively (Supporting Information, Figure S1b). This nomenclature is in line with that used to describe porphyrin transitions. An energy difference of ~1200–1350 cm^{-1} is observed for each Q(1,0) and Q(0,0) pair in this series of molecules, with an average energy separation of 1277 cm^{-1} ± 63 cm^{-1}; this is consistent with the energy separation of ~1250 cm^{-1} observed for porphyrins.[94] Additionally, there is an energy spacing of ~2100–2200 cm^{-1} between corresponding *x* and *y* bands (i.e., $Q_x(0,0)$ and $Q_y(0,0)$) with an average separation of 2148 cm^{-1} ± 64 cm^{-1}. The splitting of *x* and *y* Q bands is ~3000 cm^{-1} for porphyrins, and this separation is known to be smaller for other tetrapyrrolic macrocycles.[94]

While the *x* and *y* polarizations of these compounds should be distinguished as a result of symmetry, the Soret band of corroles does not typically reflect an (*x*, *y*) polarization, and a single, sometimes broad, absorption feature is observed, as in the case of **2**. The Soret band clearly resolves to two distinct peaks when the compound is dissolved in solvents of increasing dielectric constant (Figure 5b), as has also been observed for both 5,10,15-triphenylcorrole (H_3TPC) and 5,10,15-tris(4-methoxyphenyl)-corrole (H_3TMPC).[43]

The steady-state absorbance spectrum of dimer **3** (Figure 6) is comparable to the monomeric corroles, except the optical

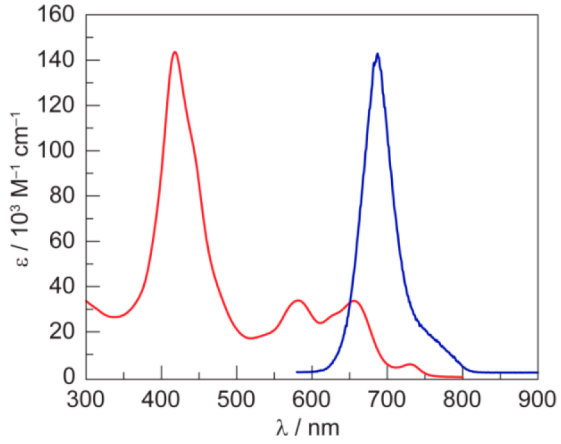

Figure 6. Steady-state absorption (red) and emission (blue) spectra (λ_{exc} = 560 nm) of dimer **3** in toluene. Qualitatively, these spectra are similar to that of the monomer **2**, but the transitions are more intense; an additional feature at ~750 nm is observed, indicative of a dimeric structure.

absorption transitions are considerably more intense than the corrole monomer. This increased optical absorbance is due to the presence of two fluorophores in a single molecule. The Soret band displays a shoulder, indicative of two overlapping transitions. The most intense peak of **3** is blue-shifted by 338 cm^{-1} relative to **2**. Conversely, all of the Q transitions of **3** are red-shifted relative to **2**: 517 and 766 cm^{-1} for Q_y transitions and 311 and 381 cm^{-1} for Q_x. Additionally, compound **3** exhibits a feature at 731 nm (ε = 5700 M^{-1} cm^{-1}) that is unique to a dimeric structure. A similar feature has been observed for corrole dimers and higher order oligomers,[89,91] and it is likely due to transitions between corrole subunits.

Fluorescence Spectroscopy. Steady-state emission spectra (λ_{exc} = 440 nm) were recorded for toluene solutions of compounds **2**, **4**, **5**, and **6**. Table 1 summarizes the emission data for these corroles, and Figure 7a displays the normalized emission spectra, which exhibit an intense band with a vibrational shoulder to the red; expansion of the Q-band region for compound **2** is presented in Supporting Information, Figure S2. On the basis of the assignment of the Q-band absorption profile, the intense fluorescence band is assigned to $Q_x(0,0)$, and the shoulder is assigned to $Q_x(0,1)$. This nomenclature is consistent with that used to describe fluorescence transitions for free-base porphyrins.[94] A constant energy gap of ~1300–1400 cm^{-1} between $Q_x(0,0)$ and $Q_x(0,1)$ is observed, with an average separation of 1335 cm^{-1} ± 32 cm^{-1}, which is comparable to that observed between $Q_x(0,0)$ and $Q_x(1,0)$ in the absorption spectra. The observed Stokes shift between the $Q_x(0,0)$ absorption and emission features is ~400 cm^{-1} for **2**, **4**, and **5**, whereas that of **6** is ~650 cm^{-1}. Paralleling trends in the absorption profile, the emission spectra exhibit a red shift with increasing bromination. As observed for the absorbance Q bands, the steady-state emission Q features for **3** are red-shifted relative to **2** by 644 and 795 cm^{-1} for $Q_x(0,0)$ and $Q_x(0,1)$, respectively. The fluorescence quantum

DOI: 10.1021/ic502860g
Inorg. Chem. 2015, 54, 2713–2725

Table 1. Photophysical Data for Free-Base Corroles

corrole[a]	$Q_x(0,0)^b$	$Q_x(0,1)^b$	$\tau_o{}^c$ (ps)	$\Phi_f{}^d \times 10^2$	$k_r{}^e$ (s^{-1})	$k_{nr}{}^e$ (s^{-1})
2	657	722	4111 ± 24[f]	15	4.06×10^7	2.30×10^8
4	664	728	235 ± 7	1.1	4.74×10^7	4.26×10^9
5	668	732	121 ± 3	0.51	4.15×10^7	8.10×10^9
6	684	770	84 ± 3	0.47	5.66×10^7	1.20×10^{10}
3	686	766	3285 ± 20	27	8.86×10^7	2.40×10^8

[a]Toluene solution, transition wavelengths are in units of nm. [b]Observed transitions with λ_{exc} = 440 nm. [c]Freeze–pump–thawed samples (<10^{-4} Torr) with λ_{exc} = 400 nm. [d]Fluorescence quantum yield, relative to H_2TPP in toluene (ϕ_f = 0.11). [e]Calculated using eq 3. [f]95% confidence interval.

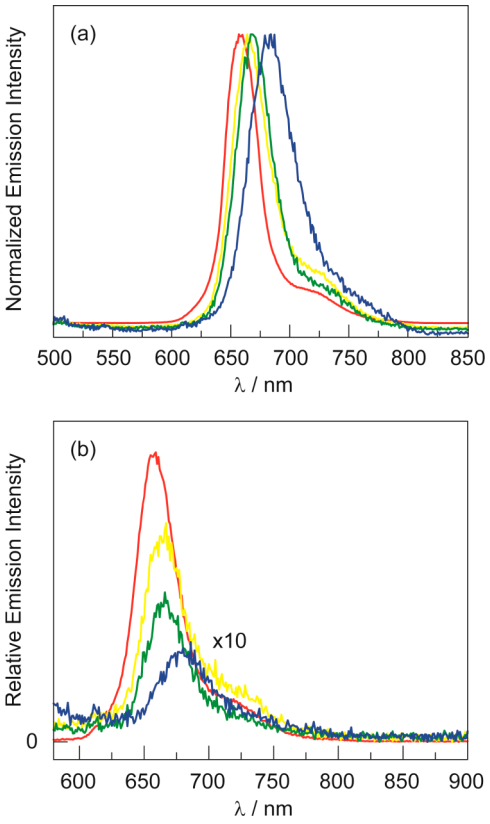

Figure 7. Steady-state emission for a series of corroles in toluene: **2** (red), **4** (yellow), **5** (green), and **6** (blue). (a) Normalized steady-state emission spectra (λ_{exc} = 440 nm), demonstrating a red shift in the emission maximum. (b) Absorbance-matched (A_{560} = 0.100 ± 0.002) emission spectra (λ_{exc} = 560 nm), reflecting fluorescence quenching upon bromination. For clarity, the emission intensity of compounds **4**, **5**, and **6** was increased by a factor of 10.

yield also exhibits a pronounced decrease with increasing bromination. Figure 7b shows the steady-state emission spectra (λ_{exc} = 560 nm) for absorbance-matched toluene solutions of **2**, **4**–**6** at the excitation wavelength of λ_{exc} = 560 nm (A_{560} = 0.100 ± 0.002). The fluorescence quantum yields are provided in Table 1, where eq 1 was used to determine Φ with H_2TPP in toluene as the reference (Φ_{ref} = 0.11). No phosphorescence was observed from the triplet manifold of these corroles.

Consistent with emission intensity results, the emission lifetime also exhibits a marked decrease with bromination. The fluorescence lifetimes of nonbrominated corroles listed in Table 1 were determined from fitting the data with a monoexponential decay (R^2 > 0.99). For the brominated derivatives, the lifetimes were so short that the decay is on the order of the instrument response function, as illustrated in Supporting Information, Figure S3. As a result, these traces were fit with an exponential-modified Gaussian (R^2 > 0.99). Using eq 3, the radiative and nonradiative rate constants k_r and k_{nr}, respectively, may be determined for each compound:

$$\Phi = \frac{k_r}{k_r + k_{nr}} = k_r\tau \tag{3}$$

where Φ is the is emission quantum yield, and τ is the natural fluorescence lifetime. Whereas k_r is effectively invariant for all monomeric corroles, k_{nr} increases significantly with bromination. Although the quantum yield of **3** is nearly twice that of **2**, the radiative lifetime is similar, indicating that additional deactivation pathways are present in the dimer.

Transient Absorption Spectroscopy. In the absence of phosphorescence, nanosecond transient absorption (TA) was utilized to probe the spectral features of the triplet state and its relaxation dynamics. The TA spectra of corroles **2** and **4**–**6** in toluene, shown in Figure 8 for aerated samples and Supporting Information, Figures S4–S7 for freeze–pump–thawed (fpt) samples, were recorded by pumping the Soret band of the ground state absorption spectrum (λ_{exc} = 430 nm). The spectral data is summarized in Table 2. The TA spectra are dominated by bleaches of the ground state Soret and Q bands with a concomitant growth of two features: one centered at ~380 nm and the other at ~470 nm. The normalized triplet absorption spectra of compounds **2** and **4**–**6** is presented in Supporting Information, Figure S8. The two major features in the spectrum red shift upon bromination, although the observed differences among the brominated derivatives **4**–**6** are nominal. This suggests that the nature of the triplet state is quite similar across this series of corroles. Consistent with trends from the ground state electronic absorption spectrum, the higher energy band of **3** in the TA spectrum (Supporting Information, Figures S9 and S10) is nominally (~140 cm^{-1}) blue-shifted whereas the lower energy band around 505 nm is significantly red-shifted (~1660 cm^{-1}) relative to that observed for **2**.

The temporal evolution of the TA spectra was determined from monitoring single wavelength kinetics for the prominent spectral feature at ~470 nm for each species. Lifetime data are given in Table 2. Compounds **4**–**6** obey monoexponential decay kinetics ($R_{adj}{}^2$ > 0.99) whereas **2** and **3** exhibit biexponential decay kinetics with the shorter lifetime component dominating the fit. The biexponential decay indicates the presence of two distinct triplet states for **2** and **3**. The lifetime of the triplet excited state decreases with increasing bromination. Introduction of oxygen into solution leads to significant quenching of the long-lived triplet feature in all samples. The decreased lifetime furnishes a diffusional rate constant ($k_q \approx 2 \times 10^{-9}$ M^{-1} s^{-1}) for the quenching of the triplet excited state by oxygen.

Density Functional Theory Calculations. DFT calculations were performed using the B3LYP functional to gain insight into the nature of the electronic structure and the effect

DOI: 10.1021/ic502860g
Inorg. Chem. 2015, 54, 2713–2725

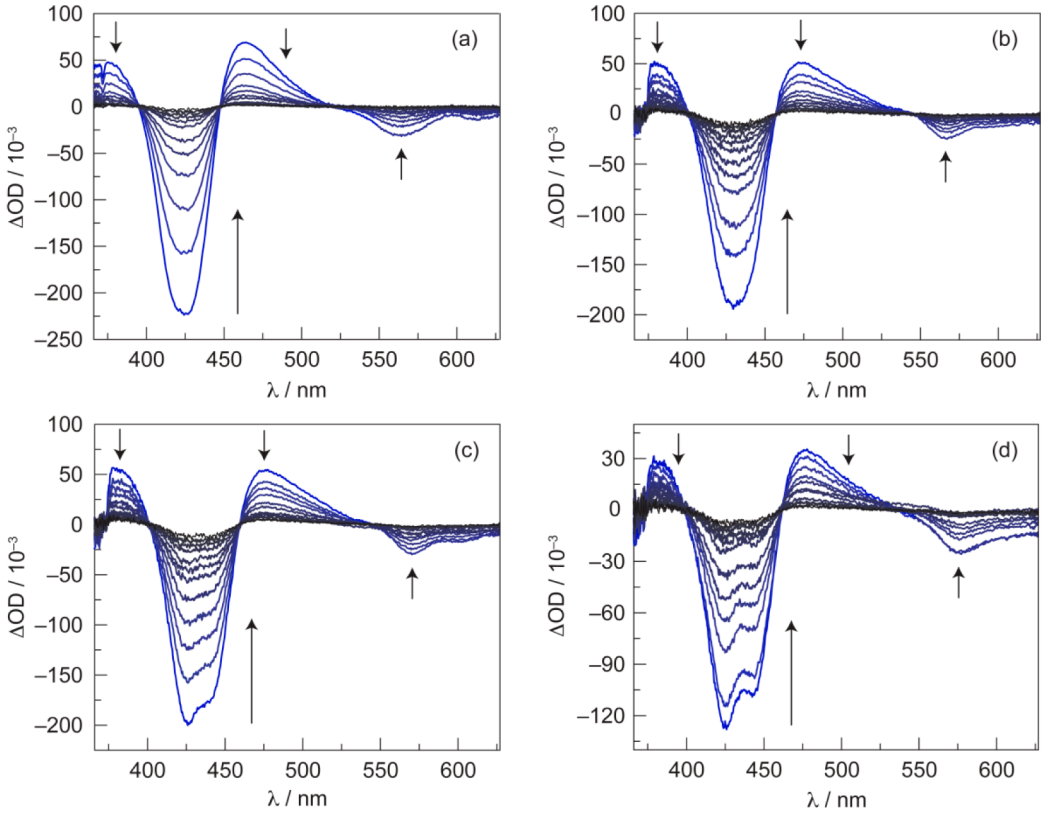

Figure 8. Nanosecond transient absorption (TA) spectra (λ_{exc} = 430 nm) of aerated toluene solutions of (a) **2**, (b) **4**, (c) **5**, and (d) **6**, showing the bleach of the ground state with concomitant growth of the triplet state. The temporal evolution of each spectrum is from 20 to 735 ns in 65 ns intervals. The corresponding spectra of fpt samples are presented in Supporting Information, Figures S4–S7.

Table 2. Summary of Transient Absorption Kinetics Data for Corroles

corrole[a]	Abs_1[b]	Abs_2[b]	τ_{o1}[c] (μs), %[d]	τ_{o2} (μs), %[d]	τ_{air} (ns)	k_q (M^{-1} s^{-1})
2	377	465	151 ± 5[e] (21)	19.2 ± 0.6 (79)	230 ± 3	2.2×10^9
4	385	470	12.2 ± 0.1 (100)		263 ± 3	1.9×10^9
5	384	474	8.8 ± 0.1 (100)		283 ± 5	1.8×10^9
6	382	473	5.4 ± 0.1 (100)		298 ± 2	1.6×10^9
3	375	504	88.3 ± 9.1 (29)	22.8 ± 1.3 (71)	267 ± 5	1.9×10^9

[a]Toluene solution, transition wavelengths are in units of nm. [b]Measured from transient absorption spectra with λ_{exc} = 430 nm. [c]Freeze–pump–thawed samples (<10^{-4} Torr). [d]Relative contribution to the biexponential fit. [e]95% confidence interval.

of bromination on the frontier molecular orbitals. Ground-state geometry optimization for compounds **2** and **4**–**6** was carried out using the 6-311G** basis set and a CPCM solvation model in toluene. The optimized structures, which are presented in Supporting Information, Figures S11–S14 with the Cartesian coordinates listed in Supporting Information, Tables S3–S6, were verified as local minima by performing frequency calculations and ensuring that there were no imaginary frequencies. Qualitatively, the structures are quite similar and exhibit a single pyrrole ring (the so-called A or D ring) that largely deviates from the mean 23-atom plane, irrespective of bromination. The calculated structure of **2** is consistent with the solid-state structure of **2** and other free-base corroles, as typified by H_3TPFC.[19,92,93] In these crystal structures, three of the pyrrole units are nearly coplanar while the fourth (the A or D ring) cants out of the plane. The root-mean-square (RMS) deviation between the calculated and solid-state structures of **2** is 0.430 Å; the overlay of the structures is presented in Supporting Information, Figure S15. Although the calculated distortion of the macrocycle upon bromination is not as pronounced as it is in the crystal structure (Figure 4, top), the solid-state (Figure 4, bottom) and calculated structures of **6** are quite similar (Supporting Information, Figure S16), with an RMS deviation of 0.566 Å. This larger deviation relative to **2** is primarily due to a different conformation of the 10-meso substituent rather than the corrole ring itself.

The frontier molecular orbitals of the corroles (HOMO−1, HOMO, LUMO, and LUMO+1) are shown in Figure 9 for **2** and Supporting Information, Figures S17–S19 for **4**–**6.** Qualitatively, the frontier orbitals are all π-type symmetry with significant orbital density at the β positions. The LUMO and HOMO−1 orbitals possess the greatest amount of density at the β positions, suggesting that these two orbitals are most affected by β substitution. As shown in Supporting Information, Figure S20 and Table S7, the frontier orbitals are energetically well-separated from the rest of the molecular orbital manifold. The calculated HOMO–LUMO gap decreases with increasing bromination, consistent with the observed red shift of spectral features: 2.51 eV (494 nm) for compound **2** to 2.43 eV (510 nm) for compound **6** (see Supporting Information, Table S7).

DOI: 10.1021/ic502860g
Inorg. Chem. 2015, 54, 2713–2725

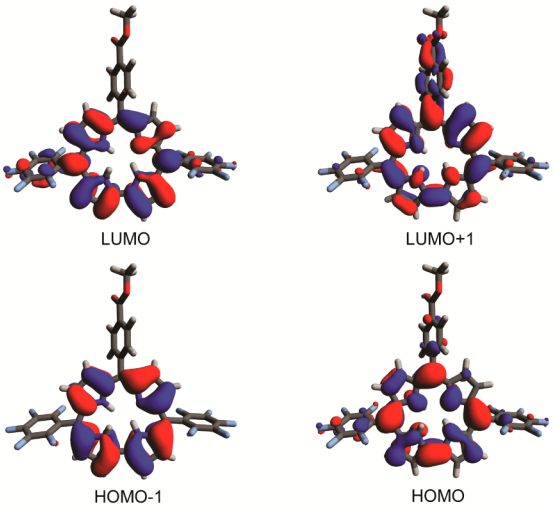

Figure 9. Four frontier molecular orbitals calculated for compound **2**, illustrating that all four orbitals possess electron density at the β positions.

Whereas the trend is captured, the absolute values of the calculated HOMO−LUMO gap deviate from the observed energies of the lowest-energy electronic transitions. Conversely, the observed and calculated spectra are in better agreement with TD-DFT calculations (vide infra).

The ground-state geometry optimization of the dimer **3** was performed as a full molecule without truncation (presented in Supporting Information, Figure S21 and Cartesian coordinates in Supporting Information, Table S8) and validated as a local minimum by a frequency calculation. The calculated structure displays a more splayed geometry than that of the solid-state structure, with a 65.46° separation between the mean 23-atom planes of the corrole (as compared to 42.09° of Figure 3). The π-aryl interaction of the pentafluorophenyl and pyrrole rings is not captured in the calculation, with a 4.119 Å distance between the centroids of these rings (compared to 3.435 Å in Figure 3). This results in a longer center-to-center distance of the corrole macrocycles: 9.199 Å for the computed structure compared to 8.304 Å for the solid-state structure. The molecular orbitals of **3** are similar to those of the monomer **2** (Supporting Information, Figure S22), although there are two dimer orbitals per monomer orbital owing to the presence of two distinct π systems in the dimer. As a result, there are eight frontier orbitals that are analogous to the four orbitals for monomeric corroles. The two nearly degenerate orbitals only differ by the nature of the lobe along the 3−3′ bond that forms the dimer (see Supporting Information, Figures S23 and S24). For example, the only difference between HOMO−3 and HOMO−2 of **3** is the nature of the lobe along the 3−3′ bond: the HOMO−3 has a continuous lobe, whereas the HOMO−2 has a node along the bond. This phenomenon is observed for each pair of molecular orbitals in the dimer **3**.

TD-DFT calculations were performed using the B3LYP functional to interrogate the nature of the excited states of these compounds and correlate the electronic structure to the absorption spectra. Single-point excited-state energy calculations determined the 10 lowest-energy singlet and triplet states for compounds **2**, **4**−**6** using the 6-311++G** basis set and a CPCM solvation model in toluene. Simulated UV−vis spectra of these compounds are presented in Supporting Information, Figures S25−S28. The energy of these singlet and triplet excited states, as well as the orbital contributions to each transition, are presented in Supporting Information, Tables S9−S16. The four lowest-energy singlet excited states give rise to two Q-like transitions and two Soret-like transitions. These states (S_1−S_4) for compounds **2**, **4**−**6** exclusively involve the four frontier orbitals (with the exception of S_4 for **6**, which has an 18% contribution of HOMO−2 → LUMO). The deviation between the calculated and experimental optical transitions range from 0.05 to 0.28 eV and is in range with TD-DFT benchmark studies on test sets of organic molecules, which demonstrate an absolute mean error of 0.3−0.5 eV.[95−97] Although the exact energies of the calculated transitions do not align precisely with experiment, the predicted UV−vis spectra (Supporting Information, Figures S25−S28) qualitatively reflect experimental observations. The Soret region broadens and subsequently splits with increasing bromination. As observed experimentally, the Soret bands of **2** and **4** look like a single, broad transition, while **5** displays a prominent shoulder, and **6** exhibits two resolved transitions. Additionally, the oscillator strength of the lower-energy Q-band increases with increasing bromination, as observed experimentally. Moreover, the two Q states (S_1 and S_2) and two Soret states (S_3 and S_4) are orthogonally polarized (see Supporting Information, Tables S17−S20 for the components of the electronic dipole moment vectors for states S_1−S_4). This implies that both the Q and B bands are split into x and y polarizations due to the low symmetry of the corrole. Thus, the split Soret band is due to the energetic separation of the B_x and B_y transitions. Calculated triplet states are qualitatively similar to absorbance bands observed experimentally by TA spectroscopy (see Supporting Information, Figure S8), although the exact wavelength maxima are slightly shifted.

To interrogate the nature of the excited states of **3**, TD-DFT calculations were performed. Single-point excited-state energy calculations were performed to determine the 15 lowest-energy singlet and triplet states using the same methods as those used with compounds **2** and **4**−**6**. The simulated UV−vis spectrum is presented in Supporting Information, Figure S29 and the results of these calculations are summarized in Supporting Information, Tables S21−S23. Since the dimer has twice the number of molecular orbitals and they come in nearly degenerate pairs, there are many more states calculated for this compound. For example, 15 singlet states appear in the 630 to 390 nm range, whereas there are only four for the monomeric compounds **2** and **4**−**6**. Thus, it is not surprising that there are several nearly degenerate states calculated for the dimer. This phenomenon is particularly prevalent for the triplet states. Despite the preponderance of states, there are only four Q-like states and four Soret-like states that have substantial (>0.05) oscillator strengths, giving a qualitative correspondence to experimental observations.

DISCUSSION

Since the introduction of one-pot corrole synthetic methodologies,[18−21] there has been a renewed interest in corrole chemistry with regard to the coordination chemistry, reactivity, and applications of these molecules. Given the diverse and numerous reports of corroles, H_3TPFC has become the archetypical corrole, just as 5,10,15,20-tetraphenylporphyrin (H_2TPP) is the prototypical porphyrin. The corrole core is inherently more electron-rich than porphyrin[98] and, hence, is particularly prone to decomposition by prolonged exposure to light and oxygen. In this regard, H_3TPFC has three electron-

DOI: 10.1021/ic502860g
Inorg. Chem. 2015, 54, 2713−2725

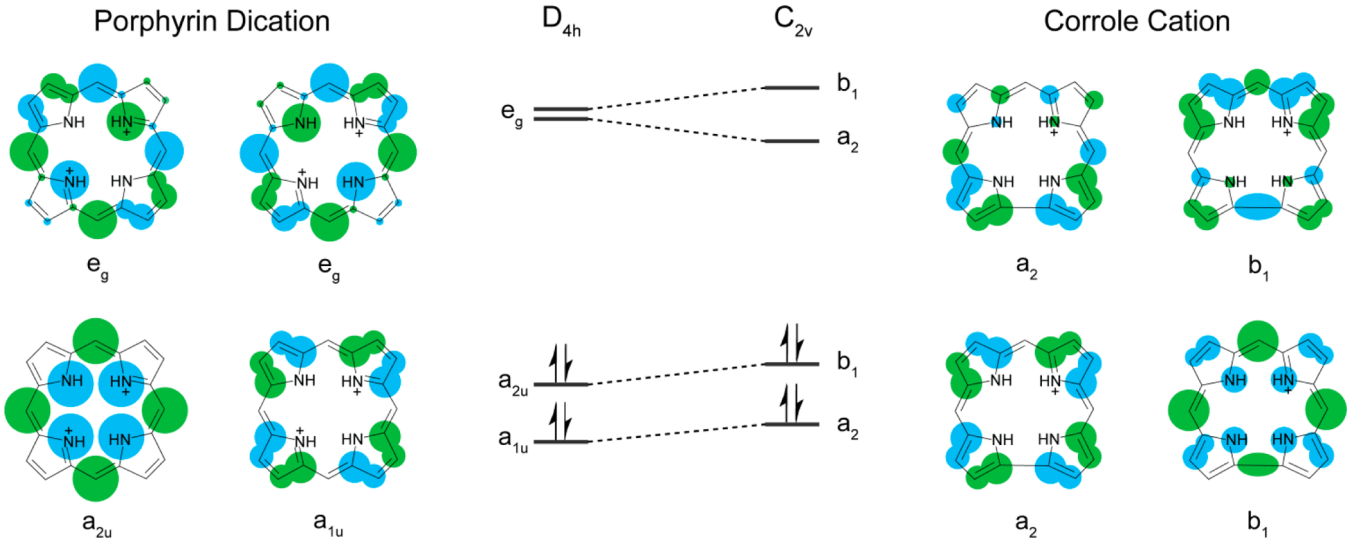

Figure 10. The four frontier orbitals for a porphyrin with D_{4h} symmetry, adapted from ref 94. With a descent in symmetry from porphyrin with D_{4h} symmetry to corrole with C_{2v} symmetry, the degeneracy of the LUMOs is lifted. The schematics for the corrole frontier orbitals are adapted from DFT calculations reported in refs 103 and 104; the orbital ordering is based on the calculations shown in Figure 9 and ref 105.

withdrawing pentafluorophenyl groups to reduce the electron density of the tetrapyrrole core, rendering this molecule one of the most stable (i.e., resistant to decomposition) corroles.[99] To harness the stability of H_3TPFC while still featuring a synthetic handle for further derivatization or conjugation, we targeted the preparation of corrole **2** and its brominated analogues. This molecule features two pentafluorophenyl groups for stability as well as a methyl ester that may be hydrolyzed to a carboxylic acid, which may subsequently react with a free amine to furnish more elaborate molecular architectures via amide bond formation.

β-Substitution on the pyrrole units of the corrole ring significantly perturbs the electronic structure by modulating the relative energies of the HOMO and LUMO levels. A convenient benchmark for the corrole electronic structure is the four orbital model of porphyrins shown in Figure 10.[94,100−102] The two HOMOs (a_{1u} and a_{2u}) and the two LUMOs (e_g) of π symmetry are energetically well-separated from all other molecular orbitals. Transitions associated with the ($a_{2u}e_g$) and ($a_{1u}e_g$) electron configurations, which are $\pi-\pi^*$ in nature, lead to the characteristic Soret and Q bands. Ghosh and co-workers have demonstrated that this four orbital model holds for corroles as well.[103,104] With a descent in symmetry from D_{4h} for a metalloporphyrin to C_{2v} for a metallocorrole, the x and y axes of the molecule are inequivalent, resulting in splitting of both the Q and B bands into x and y components. Symmetry is further lowered for free-base corroles with their three interior N−H protons. The four lowest-energy transitions (in C_{2v} symmetry) are (b_1b_1) and (a_2a_2) of A_1 symmetry, as well as (b_1a_2) and (a_2b_1) configurations of B_2 symmetry;[103] they configurationally mix to result in intense B bands and weak Q bands, analogous to those observed for porphyrins. Orbital calculations of an unsubstituted gallium(III) corrole[103] and diboron corrole[104] indicate that all four frontier orbitals possess some electron density at the *β*-positions. The order of the orbitals is consistent with the DFT calculations of Figure 9, as well as the experimental electron paramagnetic resonance spectrum of an oxidized Ga(III) corrole. This species displays hyperfine coupling to the nitrogen atoms, demonstrating that the unpaired electron resides in an orbital with density on the nitrogen atoms, thus supporting the assignment of the HOMO as the orbital of b_1 symmetry (Figure 10) and the HOMO−1 of a_2 symmetry.[105]

The series of compounds **2** and **4**−**6** provides insight into the correlation of the absorption spectra with the molecular orbital picture of Figure 10. A unique feature of corroles is the observance of the splitting of the Soret into two bands under various experimental conditions. Deprotonation of a pyrrole nitrogen has been implicated as the origin of this phenomenon in polar solvents.[18,20,43,92,106] However, there are several counterexamples in which a split Soret band is observed in nonpolar solvents such as toluene or dichloromethane.[40,107] In the case of **2**, two bands do resolve with increasing polarity of the solvent (Figure 5b). However, a very strong acid would be formed if solvent were to deprotonate the macrocycle (e.g., $pK_a(PhCNH^+) = -10$).[108] Alternatively, unique Soret transitions have been ascribed to the presence of two tautomers in solution.[47,92,107] While tautomerization is fast at room temperature on the NMR time scale,[109] the energy difference between tautomers is too small (E_{S0} = 33 cm^{-1}) to account for the 970 cm^{-1} observed splitting.[47] Moreover, DFT calculations have demonstrated that each tautomer displays several Soret-like transitions.[107] Finally, it has been postulated that the split Soret may be ascribed to nonplanarity of the macrocycle, engendered by sterically demanding meso substituents,[40,110] though corroles with unhindered substituents also exhibit a split Soret band.[107] Supporting Information, Table S24 provides structural metrics to assess the planarity of meso substituted free-base corroles without *β* substituents. The example with mesityl substituents, which has the smallest deviation from the 23-atom plane and the smallest dihedral angles of Table S24, displays a split Soret band in toluene.[111] Conversely, corroles with pentafluorophenyl groups do not exhibit split Soret bands although they display a greater degree of nonplanarity.[112,113] As a result, there is no strong correlation between the degree of nonplanarity and splitting of the Soret band. A better correlation is the asymmetry induced along the x and y axes of the corrole macrocycle. Differentiation of the x and y axes, either by structural distortion of the macrocyclic ring, or more directly by chemical substituents, leads to an energetic

DOI: 10.1021/ic502860g
Inorg. Chem. 2015, 54, 2713−2725

separation of the x and y polarized transitions, manifesting in a resolved split of the Soret band. In the cases of **2** and **4**–**6**, this differentiation is afforded by the bromination of one edge of the corrole. More subtle effects can also influence the polarization as well. As shown by the crystal structures of **2** and **6**, polar solvents may interact with the pyrroles of the corrole to lower the overall symmetry of the system, thus also engendering differences in the transition dipoles along the molecular x and y axes.

The differentiation of the (x, y) transition dipole moments is also reflected in the Q transitions. The lowest-energy Q(0,0) band is the most perturbed by bromination, exhibiting a significant red shift (358 cm^{-1} in going from **2** to **6**) with a concomitant increase in oscillator strength. This is contrasted with the higher-energy Q(0,0) band, which has similar energy and oscillator strength for **2**, **4**, and **5**, with significant changes only observed for **6**. If the brominated edge of the macrocycle is taken as the x axis (2, 3, 17, 18 positions), then the low-energy Q-band (~650 nm) is consistent with a $Q_x(0,0)$ assignment, as it is most affected by bromination, whereas the higher-energy Q-band (~565 nm) is less affected and is assigned as $Q_y(0,0)$. Similarly, the higher-energy band in the Soret manifold is less perturbed, whereas the lower-energy band shifts to lower energy with increasing bromination. These results are consistent with a y-polarized higher-energy band and an x-polarized lower-energy band. These band assignments are consistent with the results of magnetic circular dichroism spectroscopy.[107]

Calculated orbital energies are in accordance with the contentions deduced from spectroscopic trends. TD-DFT calculations corroborate that the visible absorbance bands arise from transitions among the four frontier orbitals of Figure 9; the calculated singlet states for **3** constitute transitions among the analogous eight frontier molecular orbitals of the dimer. Although the predicted spectra are qualitatively similar to experiment, the calculations do not accurately predict the low-energy Q bands. A single reference method thus does not account for the significant configuration interaction among the frontier MO set, and as a result, multireference methods[114] are needed to capture the excited states more accurately.

Using the calculated molecular orbitals, one may attempt to correlate electron density with the observed product distribution. Bromination by NBS may proceed by either an electrophilic aromatic substitution (EAS) or radical mechanism. If the EAS mechanism is operative, then the corrole HOMO is likely to participate in the reaction. Conversely, the corrole LUMO may be more prominent in a radical mechanism. This orbital has similar density at the 2 and 3 positions (Figure 9) and may explain the observance of both 2-bromo-**2** and 3-bromo-**2**. The radical mechanism is consistent with the observance of a distribution of products when less than 4 equiv of NBS is used. While this correlation is satisfying, no experiments were performed to determine which mechanism (or if both) is operative in the bromination reaction, and thus a correlation between molecular orbital density and reactivity is tenuous at best.

Emission spectral features red shift with increasing bromination. Calculations clearly establish that the primary orbital contribution in the fluorescence emission is LUMO → HOMO. The difference in the HOMO/LUMO gap between compounds **2** and **6** (640 cm^{-1}) is quite similar to the observed energy difference (600 cm^{-1}) of the $Q_x(0,0)$ emission feature for **2** and **6**. Of greater significance is the substantial decrease in fluorescence quantum yield with bromination. On the basis of lifetime data and the natural lifetimes per eq 3, k_r is relatively constant across the series (~4×10^7 s^{-1}) for **2** and **4**–**6**, whereas there is a drastic increase in k_{nr} from 2×10^8 s^{-1} for **2** to 1×10^{10} s^{-1} for **6**. Analysis of $\ln(k_{nr})$ versus ΔE reveals that that the nonradiative rate deviates positively from the linear prediction of the energy gap law (Supporting Information, Figure S30).[115,116] The energy gap law underestimates k_{nr} by a factor of ~10 per bromine atom. Thus, the perturbation of the energy of the frontier molecular orbital manifold by β-substitution is insufficient to rationalize the significant increase in k_{nr} with bromination. The enhanced k_{nr} is ascribed to a bromine heavy atom effect; increased spin–orbit coupling with increased bromination promotes intersystem crossing and thus results in a shorter emission lifetimes and lower quantum yields. In the absence of bromination, k_{nr} is well-behaved. These results are in accordance with those of Gross and co-workers[54] who observe a serial red shift of spectral features and a decrease in fluorescence lifetime with increasing β-iodination of aluminum and gallium corroles. Dimer **3** has approximately the same nonradiative rate constant k_{nr} as monomer **2**. The higher fluorescence quantum yield of **3** is in line with an increase in the radiative rate constant ($\tau_o = 1/k_r + k_{nr}$), as reflected by the increased oscillator strength of the dimer.

The photophysical properties of these free-base corroles form a reference for the properties of the corresponding metal complexes. By examining the molecular orbitals of Figure 9, it is likely that the HOMO will be most affected by the presence of a metal, as this orbital does not have a node at the center. The extent of perturbation of the absorption properties will depend of the eletronegativity of the metal and the conformation it imposes on the macrocycle. As with porphyrins, the emission properties will be governed by the nature of the metal to render complexes fluorescent, phosphorescent, or nonemissive. The DFT calculations of this study indicate that the LUMO and HOMO−1 are most affected by bromination, and hence serial bromination of a metallocorrole should lead to a red shift of all spectral features and an increase in the oscillator strength of the lowest-energy absorption features, as observed for the free-base corroles in this study. The precise extent of the perturbation of bromination on the metallocorroles is under investigation.

CONCLUSIONS

The combined experimental and computational examination of compounds **2**–**6** has provided insight into the basic photophysics of free-base β-substituted corroles. Serial bromination of the corrole periphery at the β positions greatly perturbs the four frontier molecular orbital manifold of N_4 macrocycles. TD-DFT calculations corroborate spectral assignments, which are governed by two Q states and two B (Soret) states with orthogonal polarization. The Soret band splits upon increasing bromination as a result of the asymmetry along the x- and y-axes of the corrole core. This study has helped to contextualize previous observations of a split Soret band. We contend that there are always two Soret transitions, as dictated by the symmetry of the corrole framework. The ability to resolve the bands depends on the electronic nature of the substituents and the polarity of the solvent in which the spectrum is obtained.

In addition to the red shift of observed spectral features, the inclusion of bromine atoms produces a pronounced heavy atom effect, which is the primary determinant of the photophysical properties of the free-base corrole. Bromination decreases the fluorescence quantum yield and lifetime by promoting

DOI: 10.1021/ic502860g
Inorg. Chem. 2015, 54, 2713–2725

enhanced intersystem crossing, as evidenced by a dramatic increase in k_{nr} with bromine substitution. A nonbrominated dimer exhibits absorption and emission features comparable to the tetrabrominated derivative, suggesting that oligomerization is a means of red-shifting the spectral properties akin to bromination but without decreasing the fluorescence quantum yield. With this understanding of the photophysical properties of free-base corroles, we are currently exploring applications of these platforms as energy-transfer acceptors within quantum dot−corrole conjugates for optical chemosensing applications.

■ ASSOCIATED CONTENT

Supporting Information

Synthetic procedures for the synthesis of compound **1** in addition to ^{1}H and ^{19}F NMR spectra for all compounds. Summaries of crystallographic data, TA spectral data, and results of DFT calculations (including optimized geometries, molecular orbital illustrations, simulated UV−vis spectra, tables of Cartesian coordinates, and tables of TD-DFT results). This material is available free of charge via the Internet at http://pubs.acs.org.

■ AUTHOR INFORMATION

Corresponding Author

*E-mail: dnocera@fas.harvard.edu.

Funding

This material is based upon work supported by the U.S. Department of Energy Office of Science, Office of Basic Energy Sciences under Award No. DE-SC0009758.

Notes

The authors declare no competing financial interest.

■ ACKNOWLEDGMENTS

C.M.L. acknowledges the National Science Foundation's Graduate Research Fellowship Program. We thank Bryce Anderson and Andrew Maher for assistance with experiments using the Libra-F-HE laser system as well as Casandra Cox and Bon Jun . Koo for the images used in the TOC graphic. Calculations were performed using the Odyssey cluster supported by FAS Research Computing.

■ REFERENCES

(1) Mody, T. D.; Sessler, J. L. In *Perspectives Supramolecular Chemistry;* Reinhoudt, D. N., Ed.; John Wiley & Sons: Chichester, U.K., 1999; pp 245−294.
(2) Vicente, M. G. H. *Curr. Med. Chem. Anti-Cancer Agents* **2001**, *1*, 175−194.
(3) Berg, K.; Selbo, P. K.; Weyergang, A.; Dietze, A.; Prasmickaite, L.; Bonsted, A.; Engesaeter, B. Ø.; Angell-Petersen, E.; Warloe, T.; Frandsen, N.; Høgset, A. *J. Microsc.* **2005**, *218*, 133−147.
(4) Ethirajan, M.; Chen, Y.; Joshi, P.; Pandey, R. K. *Chem. Soc. Rev.* **2011**, *40*, 340−362.
(5) Bonnett, R. *Chem. Soc. Rev.* **1995**, 19−33.
(6) Sternberg, E. D.; Dolphin, D.; Brückner, C. *Tetrahedron* **1998**, *54*, 4151−4202.
(7) O'Connor, A. E.; Gallagher, W. M.; Byrne, A. T. *Photochem. Photobiol.* **2009**, *85*, 1053−1074.
(8) Kim, D.; Osuka, A. *Acc. Chem. Res.* **2004**, *37*, 735−745.
(9) Imahori, H. *J. Phys. Chem. B* **2004**, *108*, 6130−6143.
(10) Imahori, H.; Umeyama, T.; Ito, S. *Acc. Chem. Res.* **2009**, *42*, 1809−1818.
(11) Martínez-Díaz, M. V.; de la Torre, G.; Torres, T. *Chem. Commun.* **2010**, *46*, 7090−7108.
(12) Papkovsky, D. B. *Sens. Actuators, B* **1993**, *11*, 293−300.
(13) Papkovsky, D. B.; Ponomarev, G. V.; Trettnak, W.; O'Leary, P. *Anal. Chem.* **1995**, *67*, 4112−4117.
(14) Papkovsky, D. B.; O'Riordan, T.; Soini, A. *Biochem. Soc. Trans.* **2000**, *28*, 74−77.
(15) Zhang, X. B.; Guo, C. C.; Li, Z. Z.; Shen, G. L.; Yu, R. Q. *Anal. Chem.* **2002**, *74*, 821−825.
(16) Johnson, A. W.; Kay, I. T. *Proc. Chem. Soc.* **1964**, 89−90.
(17) Johnson, A. W.; Kay, I. T. *J. Chem. Soc.* **1965**, 1620−1629.
(18) Gross, Z.; Galili, N.; Saltsman, I. *Angew. Chem., Int. Ed.* **1999**, *38*, 1427−1429.
(19) Gross, Z.; Galili, N.; Simkhovich, L.; Saltsman, I.; Botoshansky, M.; Bläser, D.; Boese, R.; Goldberg, I. *Org. Lett.* **1999**, *1*, 599−602.
(20) Paolesse, R.; Jaquinod, L.; Nurco, D. J.; Mini, S.; Sagone, F.; Boschi, T.; Smith, K. M. *Chem. Commun.* **1999**, 1307−1308.
(21) Paolesse, R.; Nardis, S.; Sagone, F.; Khoury, R. G. *J. Org. Chem.* **2001**, *66*, 550−556.
(22) Paolesse, R. In *The Porphyrin Handbook;* Kadish, K. M., Smith, K. M., Guilard, R., Eds.; Academic Press: San Diego, CA, 2000; Vol. 2; pp 201−232.
(23) Nardis, S.; Monti, D.; Paolesse, R. *Mini-Rev. Org. Chem.* **2005**, *2*, 355−374.
(24) Paolesse, R. *Synlett* **2008**, 2215−2230.
(25) Gryko, D. T. *J. Porphyrins Phthalocyanines* **2008**, *12*, 906−917.
(26) Lemon, C. M.; Brothers, P. J. *J. Porphyrins Phthalocyanines* **2011**, *15*, 809−834.
(27) Barata, J. F. B.; Santos, C. I. M.; Neves, M. G. P. M. S.; Faustino, M. A. F.; Cavaleiro, J. A. S. *Top. Heterocycl. Chem.* **2014**, *33*, 79−142.
(28) Aviv, I.; Gross, Z. *Chem. Commun.* **2007**, 1987−1999.
(29) Aviv-Harel, I.; Gross, Z. *Chem.—Eur. J.* **2009**, *15*, 8382−8394.
(30) Aviv-Harel, I.; Gross, Z. *Coord. Chem. Rev.* **2011**, *255*, 717−736.
(31) Gross, Z.; Golubkov, G.; Simkhovich, L. *Angew. Chem., Int. Ed.* **2000**, *39*, 4045−4047.
(32) Mahammed, A.; Gray, H. B.; Meier-Callahan, A. E.; Gross, Z. *J. Am. Chem. Soc.* **2003**, *125*, 1162−1163.
(33) Gross, Z.; Gray, H. B. *Adv. Synth. Catal.* **2004**, *364*, 165−170.
(34) Dogutan, D. K.; Stoian, S. A.; McGuire, R.; Schwalbe, M.; Teets, T. S.; Nocera, D. G. *J. Am. Chem. Soc.* **2011**, *133*, 131−140.
(35) Dogutan, D. K.; McGuire, R.; Nocera, D. G. *J. Am. Chem. Soc.* **2011**, *133*, 9178−9180.
(36) Lemon, C. M.; Dogutan, D. K.; Nocera, D. G. In *Handbook of Porphyrin Science;* Kadish, K. M., Smith, K. M., Guilard, R., Eds.; World Scientific Publishing: Singapore, 2012; Vol. *21*; pp 1−143.
(37) Luobeznova, I.; Raizman, M.; Goldberg, I.; Gross, Z. *Inorg. Chem.* **2006**, *45*, 386−394.
(38) Wagnert, L.; Berg, A.; Stavitski, E.; Luobeznova, I.; Gross, Z.; Levanon, H. *J. Porphyrins Phthalocyanines* **2007**, *11*, 645−651.
(39) Agadjanian, H.; Ma, J.; Rentsendorj, A.; Valluripalli, V.; Hwang, J. Y.; Mahammed, A.; Farkas, D. L.; Gray, H. B.; Gross, Z.; Medina-Kauwe, L. K. *Proc. Natl. Acad. Sci. U.S.A.* **2009**, *106*, 6105−6110.
(40) Ventura, B.; Esposti, A. D.; Koszarna, B.; Gryko, D. T.; Flamigni, L. *New J. Chem.* **2005**, *29*, 1559−1566.
(41) Shao, W.; Wang, H.; He, S.; Shi, L.; Peng, K.; Lin, Y.; Zhang, L.; Ji, L.; Liu, H. *J. Phys. Chem. B* **2012**, *116*, 14228−14234.
(42) Hwang, J. Y.; Gross, Z.; Gray, H. B.; Medina-Kauwe, L. K.; Farkas, D. L. *J. Biomed. Opt.* **2011**, *16*, 066007/1−6.
(43) Ding, T.; Alemán, E. A.; Modarelli, D. A.; Ziegler, C. J. *J. Phys. Chem. A* **2005**, *109*, 7411−7417.
(44) Shi, L.; Liu, H. Y.; Shen, H.; Hu, J.; Zhang, G. L.; Wang, H.; Ji, L. N.; Chang, C. K.; Jiang, H. F. *J. Porphyrins Phthalocyanines* **2009**, *13*, 1221−1226.
(45) Zhan, H. Y.; Liu, H. Y.; Lu, J.; Wang, A. Z.; You, L. L.; Wang, H.; Ji, L. N.; Jiang, H. F. *J. Porphyrins Phthalocyanines* **2010**, *14*, 150−157.
(46) Ngo, T. H.; Puntoriero, F.; Nastasi, F.; Robeyns, K.; Van Meervelt, L.; Campagna, S.; Dehaen, W.; Maes, W. *Chem.—Eur. J.* **2010**, *16*, 5691−5705.
(47) Ivanova, Y. B.; Savva, V. A.; Mamardashvili, N. Z.; Starukhin, A. S.; Ngo, T. H.; Dehaen, W.; Maes, W.; Kruk, M. M. *J. Phys. Chem. A* **2012**, *116*, 10683−10694.

DOI: 10.1021/ic502860g
Inorg. Chem. 2015, 54, 2713−2725

(48) Kruk, M.; Ngo, T. H.; Verstappen, P.; Starukhin, A.; Hofkens, J.; Dehaen, W.; Maes, W. *J. Phys. Chem. A* **2012**, *116*, 10695−10703.
(49) Kruk, M.; Ngo, T. H.; Savva, V.; Starukhin, A.; Dehaen, W.; Maes, W. *J. Phys. Chem. A* **2012**, *116*, 10704−10711.
(50) Beenken, W.; Pressely, M.; Ngo, T. H.; Dehaen, W.; Maes, W.; Kruk, M. *J. Phys. Chem. A* **2014**, *118*, 862−871.
(51) Flamigni, L.; Ventura, B.; Tasior, M.; Gryko, D. T. *Inorg. Chim. Acta* **2007**, *360*, 803−813.
(52) Tasior, M.; Gryko, D. T.; Cembor, M.; Jaworski, J. S.; Ventura, V.; Flamigni, L. *New J. Chem.* **2007**, *31*, 247−259.
(53) Tasior, M.; Gryko, D. T.; Pielacinska, D. J.; Zanelli, A.; Flamigni, L. *Chem.—Asian J.* **2010**, *5*, 130−140.
(54) Vestfrid, J.; Goldberg, I.; Gross, Z. *Inorg. Chem.* **2014**, *53*, 10536−10542.
(55) Laha, J. K.; Dhanalekshmi, S.; Taniguchi, M.; Ambroise, A.; Lindsey, J. S. *Org. Process Res. Dev.* **2003**, *7*, 799−812.
(56) Zaidi, S. H. H.; Loewe, R. S.; Clark, B. A.; Jacob, M. J.; Lindsey, J. S. *Org. Process Res. Dev.* **2006**, *10*, 304−314.
(57) Lemon, C. M. M.S. Thesis, Massachusetts Institute of Technology: Cambridge, MA, U.S.A., 2013.
(58) Fulmer, G. R.; Miller, A. J. M.; Sherden, N. H.; Gottlieb, H. E.; Nudelman, A.; Stoltz, B. M.; Bercaw, J. E.; Goldberg, K. I. *Organometallics* **2010**, *29*, 2176−2179.
(59) *CRC Handbook of Chemistry and Physics,* 73rd ed.; CRC Press: Boca Raton, FL, 1992.
(60) Seybold, P. G.; Gouterman, M. *J. Mol. Spectrosc.* **1969**, *31*, 1−13.
(61) Lemon, C. M.; Karnas, E.; Bawendi, M. G.; Nocera, D. G. *Inorg. Chem.* **2013**, *52*, 10394−10406.
(62) Loh, Z. H.; Miller, S. E.; Chang, C. J.; Carpenter, S. D.; Nocera, D. G. *J. Phys. Chem. A* **2002**, *106*, 11700−11708.
(63) Pizano, A. A.; Lutterman, D. A.; Holder, P. G.; Teets, T. S.; Stubbe, J.; Nocera, D. G. *Proc. Natl. Acad. Sci. U.S.A.* **2012**, *109*, 39−43.
(64) Holder, P. G.; Pizano, A. A.; Anderson, B. L.; Stubbe, J.; Nocera, D. G. *J. Am. Chem. Soc.* **2012**, *134*, 1172−1180.
(65) Becke, A. D. *Phys. Rev. A* **1988**, *38*, 3098−3100.
(66) Becke, A. D. *J. Chem. Phys.* **1993**, *98*, 1372−1377.
(67) Becke, A. D. *J. Chem. Phys.* **1993**, *98*, 5648−5652.
(68) Lee, C.; Yang, W.; Parr, R. G. *Phys. Rev. B* **1988**, *37*, 785−789.
(69) Frisch, M. J.; et al. *Gaussian 09,* Revision D.01; Gaussian, Inc.: Wallingford, CT, 2009.
(70) Wadt, W. R.; Hay, P. J. *J. Chem. Phys.* **1985**, *82*, 284−298.
(71) Hay, P. J.; Wadt, W. R. *J. Chem. Phys.* **1985**, *82*, 299−310.
(72) Barone, V.; Cossi, M. *J. Phys. Chem. A* **1998**, *102*, 1995−2001.
(73) Cossi, M.; Rega, N.; Scalmani, G.; Barone, V. *J. Comput. Chem.* **2003**, *24*, 669−681.
(74) Bauernschmitt, R.; Ahlrichs, R. *Chem. Phys. Lett.* **1996**, *256*, 454−464.
(75) Casida, M. E.; Jamorski, C.; Casida, K. C.; Salahub, D. R. *J. Chem. Phys.* **1998**, *108*, 4439−4449.
(76) Stratmann, R. E.; Scuseria, G. E.; Frisch, M. J. *J. Chem. Phys.* **1998**, *109*, 8218−8224.
(77) Van Caillie, C.; Amos, R. D. *Chem. Phys. Lett.* **1999**, *308*, 249−255.
(78) Scalmani, G.; Frisch, M. J.; Mennucci, B.; Tomasi, J.; Cammi, R.; Barone, V. *J. Chem. Phys.* **2006**, *124*, 094107/1−15.
(79) Hanwell, M. D.; Curtis, D. E.; Lonie, D. C.; Vandermeersch, T.; Zurek, E.; Hutchison, G. R. *J. Cheminf.* **2012**, *4*, 17/1−17.
(80) Sheldrick, G. M. *Acta Crystallogr., Sect. A: Found. Crystallogr.* **2008**, *A64*, 112−122.
(81) Golubkov, G.; Bendix, J.; Gray, H. B.; Mahammed, A.; Goldberg, I.; DiBilio, A. J.; Gross, Z. *Angew. Chem., Int. Ed.* **2001**, *40*, 2132−2134.
(82) Wasbotten, I. H.; Wondimagegn, T.; Ghosh, A. *J. Am. Chem. Soc.* **2002**, *124*, 8104−8116.
(83) Palmer, J. H.; Day, M. W.; Wilson, A. D.; Henling, L. M.; Gross, Z.; Gray, H. B. *J. Am. Chem. Soc.* **2008**, *130*, 7786−7787.
(84) Nardis, S.; Mandoj, F.; Paolesse, R.; Fronczek, F. R.; Smith, K. M.; Prodi, L.; Montalti, M.; Battistini, G. *Eur. J. Inorg. Chem.* **2007**, 2345−2352.
(85) Du, R. B.; Liu, C.; Shen, D. M.; Chen, Q. Y. *Synlett* **2009**, 2701−2705.
(86) Tortora, L.; Nardis, S.; Fronczek, F. R.; Smith, K. M.; Paolesse, R. *Chem. Commun.* **2011**, *47*, 4243−4245.
(87) Scrivanti, A.; Beghetto, V.; Matteoli, U.; Antonaroli, S.; Marini, A.; Mandoj, F.; Paolesse, R.; Crociani, B. *Tetrahedron Lett.* **2004**, *45*, 5861−5864.
(88) Koszarna, B.; Gryko, D. T. *J. Org. Chem.* **2006**, *71*, 3707−3717.
(89) Barata, J. F. B.; Silva, A. M. G.; Neves, M. G. P. M. S.; Tomé, A. C.; Silva, A. M. S.; Cavaleiro, J. A. S. *Tetrahedron Lett.* **2006**, *47*, 8171−8174.
(90) Hiroto, S.; Furukawa, K.; Shinokubo, H.; Osuka, A. *J. Am. Chem. Soc.* **2006**, *128*, 12380−12381.
(91) Hirabayshi, S.; Omote, M.; Aratani, N.; Osuka, A. *Bull. Chem. Soc. Jpn.* **2012**, *85*, 558−562.
(92) Ding, T.; Harvey, J. D.; Ziegler, C. J. *J. Porphyrins Phthalocyanines* **2005**, *9*, 22−27.
(93) Reith, L. M.; Stiftinger, M.; Monkowius, U.; Knör, G.; Schoefberger, W. *Inorg. Chem.* **2011**, *50*, 6788−6797.
(94) Gouterman, M. In *The Porphyrins;* Dolphin, D., Ed.; Academic Press: New York, 1978; Vol. 3; pp 1−165.
(95) Dreuw, Z.; Head-Gordon, M. *Chem. Rev.* **2005**, *105*, 4009−4037.
(96) Jacquemin, D.; Wathelet, V.; Perpète, E. A.; Adamo, C. *J. Chem. Theory Comput.* **2009**, *5*, 2420−2435.
(97) Jacquemin, D.; Mennucci, B.; Adamo, C. *Phys. Chem. Chem. Phys.* **2011**, *13*, 16987−16998.
(98) Gross, Z.; Gray, H. B. *Comments Inorg. Chem.* **2006**, *27*, 61−72.
(99) Geier, G. R.; Chick, J. F. B.; Callinan, J. B.; Reid, C. G.; Auguscinski, W. P. *J. Org. Chem.* **2004**, *69*, 4159−4169.
(100) Gouterman, M. *J. Chem. Phys.* **1959**, *30*, 1139−1161.
(101) Gouterman, M. *J. Mol. Spectrosc.* **1961**, *6*, 138−163.
(102) Gouterman, M.; Wagnière, G. H.; Snyder, L. C. *J. Mol. Spectrosc.* **1963**, *11*, 108−127.
(103) Ghosh, A.; Wondimagegn, T.; Parusel, A. B. J. *J. Am. Chem. Soc.* **2000**, *122*, 5100−5104.
(104) Albrett, A. M.; Conradie, J.; Ghosh, A.; Brothers, P. J. *Dalton Trans.* **2008**, 4464−4473.
(105) Bendix, J.; Dmochowski, I. J.; Gray, H. B.; Mahammed, A.; Simkhovich, L.; Gross, Z. *Angew. Chem., Int. Ed.* **2000**, *39*, 4048−4051.
(106) Simkhovich, L.; Goldberg, I.; Gross, Z. *J. Inorg. Biochem.* **2000**, *80*, 235−238.
(107) Ziegler, C. J.; Sabin, J. R.; Geier, G. R.; Nemykin, V. N. *Chem. Commun.* **2012**, *48*, 4743−4745.
(108) Ripin, D. H.; Evans, D. A. *Evans pK_a Table.* http://evans.harvard.edu/pdf/evans_pka_table.pdf.
(109) Balazs, Y. S.; Saltsman, I.; Mahammed, A.; Tkachenko, E.; Golubkov, G.; Levine, J.; Gross, Z. *Magn. Reson. Chem.* **2004**, *42*, 624−635.
(110) Koszarna, B.; Gryko, D. T. *Chem. Commun.* **2007**, 2994−2996.
(111) Gryko, D. T.; Jadach, K. *J. Org. Chem.* **2001**, *66*, 4267−4275.
(112) Egorova, O. A.; Tsay, O. G.; Khatua, S.; Meka, B.; Maiti, N.; Kim, M. K.; Kwon, S. J.; Huh, J. O.; Bucella, D.; Kang, S. O.; Kwak, J.; Churchill, D. G. *Inorg. Chem.* **2010**, *49*, 502−512.
(113) Gryko, D. T.; Koszarna, B. *Synthesis* **2004**, 2205−2209.
(114) Rohrdanz, M. A.; Herbert, J. M. *J. Chem. Phys.* **2008**, *129*, 034107/1−9.
(115) Siebrand, W. *J. Chem. Phys.* **1967**, *46*, 440−447.
(116) Siebrand, W. *J. Chem. Phys.* **1967**, *47*, 2411−2422.

DOI: 10.1021/ic502860g
Inorg. Chem. 2015, 54, 2713−2725

JACS
JOURNAL OF THE AMERICAN CHEMICAL SOCIETY

Article

pubs.acs.org/JACS

Micelle-Encapsulated Quantum Dot-Porphyrin Assemblies as *in Vivo* Two-Photon Oxygen Sensors

Christopher M. Lemon,[†,‡] Elizabeth Karnas,[‡] Xiaoxing Han,[§] Oliver T. Bruns,[‡] Thomas J. Kempa,[†] Dai Fukumura,[*,§] Moungi G. Bawendi,[*,‡] Rakesh K. Jain,[*,§] Dan G. Duda,[*,§] and Daniel G. Nocera[*,†]

[†]Department of Chemistry and Chemical Biology, Harvard University, 12 Oxford Street, Cambridge, Massachusetts 02138, United States

[‡]Department of Chemistry, Massachusetts Institute of Technology, 77 Massachusetts Avenue, Cambridge, Massachusetts 02139, United States

[§]Edwin L. Steele Laboratory for Tumor Biology, Department of Radiation Oncology, Massachusetts General Hospital and Harvard Medical School, 100 Blossom Street, Cox-7, Boston, Massachusetts 02114, United States

Supporting Information

ABSTRACT: Micelles have been employed to encapsulate the supramolecular assembly of quantum dots with palladium(II) porphyrins for the quantification of O_2 levels in aqueous media and *in vivo*. Förster resonance energy transfer from the quantum dot (QD) to the palladium porphyrin provides a means for signal transduction under both one- and two-photon excitation. The palladium porphyrins are sensitive to O_2 concentrations in the range of 0−160 Torr. The micelle-encapsulated QD-porphyrin assemblies have been employed for *in vivo* multiphoton imaging and lifetime-based oxygen measurements in mice with chronic dorsal skinfold chambers or cranial windows. Our results establish the utility of the QD-micelle approach for *in vivo* biological sensing applications.

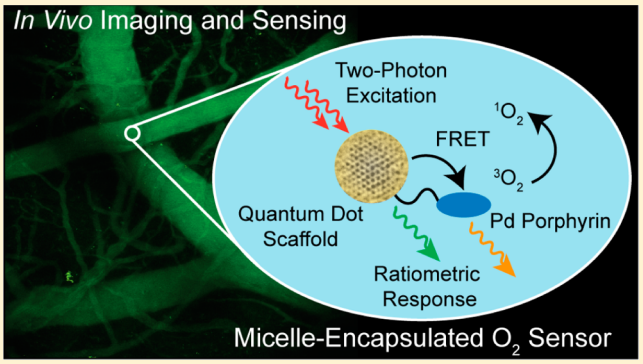

INTRODUCTION

Metabolic profiles of tumors may provide a spatiotemporal map of key markers for the growth of tumors and for their response to therapy. Three key parameters that represent the metabolic status of a tumor are glucose, pH, and oxygen, as these serve as direct measures of tumor consumption, metabolism, and respiration, respectively.[1,2] Since tumors primarily exploit glycolysis for energy needs, the tumor microenvironment is characterized by low extracellular pH arising from both lactic acid and carbonic acid; the latter is derived from dissolved CO_2 as a product of aerobic respiration.[2] These species tend to accumulate in the tumor due to inefficient removal pathways, resulting in a further decrease in pH (6.6−6.8).[3] Additionally, tumor vasculature exhibits abnormal structure and function, resulting in leaky vessels and heterogeneous blood flow.[4] Vascular hyperpermeability and the lack of functional lymphatic vessels induce an elevation of interstitial fluid pressure in solid tumors. This forms physiological barriers to the delivery of therapeutics.[5] Moreover, the vascular abnormalities result in characteristically low oxygenation (hypoxia) in tumors. Hypoxia is a master regulator of tumor progression, through stimulation of angiogenesis (the formation of new blood vessels), metastasis, stem-like cell phenotype, reduced tumor cell apoptosis (programmed cell death), and immune suppression.[5−8] It induces the production and activation of growth factors, cytokines, and enzymes that promote these cell phenotypes. This hostile microenvironment, characterized by acidosis and hypoxia, also reduces the effectiveness of chemotherapy and radiation therapy, which depend on oxygen for cytotoxicity.[4,9] Both pH and pO_2 affect tumor cell metabolism, tumor cell proliferation and viability, and glucose and oxygen consumption rates.[2] Together, tumor acidosis and hypoxia incapacitate immune cells, render tumor cells invasive and metastatic, and induce the expression of angiogeneic factors, which trigger and stimulate tumor growth.[10−12]

A new therapeutic strategy—established over the past decade—is to target angiogenesis, as tumors require blood vessels for growth and metastasis.[5,13−18] Certain antiangiogenic therapies can transiently "normalize" the abnormal tumor vasculature, thereby increasing the flow of both oxygen and therapeutics as well as removal of wastes and metabolites.[19] The "vascular normalization" hypothesis posits that restoring the balance between pro- and antiangiogenic factors in the tumors by using antiangiogenic drugs can result in a time window in which tumor vasculature resembles normal vessels. It has been demonstrated that such therapies can engender normalization of the leaky, distended, and tortuous tumor

Received: March 2, 2015
Published: July 7, 2015

DOI: 10.1021/jacs.5b04765
J. Am. Chem. Soc. 2015, 137, 9832−9842

vasculature.[20] Upon normalization, blood flow, and thus oxygen and drug distribution, is increased; this represents an opportunity to treat the tumor with a substantial dose of chemotherapeutics to have a superior impact on tumor progression.[21] However, in order to optimize it, the normalization process must be efficiently monitored, and the drug doses must be high enough to induce normalization, but not excessive to prune the vasculature.[22]

Although measurements of gene expression, drug delivery, and physiological parameters have yielded valuable insights into tumor angiogenesis and other pathophysiological processes, these techniques are either destructive or have poor spatial resolution. More desirable are nondestructive and noninvasive techniques that are able to monitor dynamic processes within a tumor. The spatial resolution of the technique should be on the order of 1−10 μm to monitor events at the cellular and subcellular level. Intravital microscopy (i.e., imaging of living organisms) allows dynamic processes to be observed and physiological functions to be determined quantitatively.[4,9] Specifically, multiphoton laser scanning microscopy (MPLSM) enables noninvasive 3-D optical imaging with significant depth penetration and ∼1 μm spatial resolution.[23−26] Although much research has focused on imaging tumor angiogenesis and microenvironment, there have been few studies that monitor dynamic changes in the functional parameters of pH and pO_2.[4,9] Understanding how pH and O_2 levels change as a function of disease progression or therapy is critical to develop novel targeted therapeutics. For MPLSM imaging to be realized, new noninvasive sensors, with sufficiently high quantum yields to generate sufficient signal for deep tissue imaging, must be developed that are small enough to penetrate into the tumor and monitor dynamic changes with high resolution.[19]

To this end, we have developed optical chemosensors that exploit a quantum dot (QD) scaffold. The QD serves both as a photon antenna for multiphoton absorption as well as an internal emission intensity standard for ratiometric sensing.[27] Quantum dots have been used as two-photon donors in Förster resonance energy transfer (FRET)-based donor−acceptor dyad configurations,[28−30] complementing biological FRET sensing schemes that employ organic fluorophores as two photon antenna.[31−33] Self-referencing pH sensors[34−36] and a higher-pressure (160−760 Torr) oxygen sensor[37] have also been developed to probe biological microenvironments. Recently, we developed supramolecular QD/palladium(II) porphyrin (**1**, Chart 1) assemblies for lower-pressure (0−160 Torr) oxygen sensing under one- and two-photon excitation.[38] Herein, we report the water solubilization of these assemblies by encapsulating a preassembled QD-porphyrin construct within a phospholipid micelle. Encapsulation of QDs in lipid or amphiphilic polymer micelles is an established method of solubilizing them in aqueous buffer.[39−52] Whereas micelles have been used for biological imaging, micelle-encapsulated QDs have been only used to sense nitric oxide.[53] We now exploit the micelle approach to sense oxygen ratiometrically under two-photon excitation. Using the sensing scheme outlined in Figure 1, we have established the utility of the micelle approach for *in vivo* imaging and sensing for the first time.

Chart 1

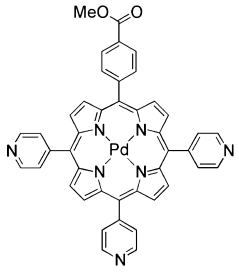

1

EXPERIMENTAL SECTION

Materials. The following chemicals were used as received: propionic acid, chloroform ($CHCl_3$), dichloromethane (CH_2Cl_2), toluene, methanol (MeOH), ethanol (EtOH), ethyl acetate (EtOAc), acetonitrile (MeCN), pyrrole, 4-pyridinecarboxaldehyde, methyl 4-formylbenzoate, 2′,7′-dichlorofluorescein (fluorescein 27), 1,3-diphenylisobenzofuran (DPBF), and tris(2,2′-bipyridyl)dichlororuthenium(II) hexahydrate ($[Ru(bpy)_3]Cl_2$) from Sigma-Aldrich; sodium bicarbonate ($NaHCO_3$), sodium hydroxide (NaOH), and sodium sulfate (Na_2SO_4) from Mallinckrodt; palladium(II) acetylacetonate ($Pd(acac)_2$) from Strem; pyridine from EMD; silica gel 60 Å 230−400 mesh ASTM from Whatman; 1,2-dioleoyl-*sn*-glycero-3-phosphoethanolamine-*N*-[methoxy(polyethylene glycol)-2000] ammonium salt, 25 mg/mL solution in chloroform from Avanti Polar Lipids Inc.; Dulbecco's phosphate-buffered saline (PBS) without calcium and magnesium from Mediatech Inc.; chloroform-*d* ($CDCl_3$) from Cambridge Isotope Laboratories; and argon from Airgas. Cadmium selenide core−shell QDs obtained from QD Vision were twice precipitated from toluene using EtOH and redissolved in toluene prior to use. Compound **1** was prepared as previously reported.[38]

5-(4-Methoxycarbonylphenyl)-10,15,20-tris(4-pyridyl) porphyrin (1-H_2). The free-base porphyrin was prepared with a variation to the Adler−Longo porphyrin synthesis.[54,55] The modification affords usable (>350 mg) amounts of porphyrin with minimal chromatography. In a three-neck round-bottom flask, 100 mL propionic acid and 100 mL toluene were brought to reflux. An aldehyde solution was prepared by dissolving 1.62 g methyl 4-formyl-benzoate (9.87 mmol) and 2.7 mL 4-pyridinecarboxaldehyde (3.1 g, 29 mmol) in 7 mL toluene. A pyrrole solution was prepared by dissolving 2.6 mL pyrrole (2.5 g, 37 mmol) in 7 mL toluene. These two solutions were simultaneously added to the refluxing solvent dropwise via syringe. After the addition was complete, the solution was refluxed for 1.5 h. The reaction mixture was then cooled to room temperature, and solvents were removed by rotary evaporation. The crude residue was dissolved in 100 mL $CHCl_3$, and a saturated solution of $NaHCO_3$ was carefully added; the biphasic mixture was stirred until bubbling had subsided. The organic layer was washed with water, dried over Na_2SO_4, and brought to dryness. The crude reaction mixture was purified on a silica gel column using CH_2Cl_2 to elute all of the fast-moving porphyrin isomers (B_4, AB_3, and *cis*-/*trans*-A_2B_2 isomers). After these four products eluted, the solvent was changed to 100% EtOAc and then 10% MeOH in EtOAc to elute the desired A_3B porphyrin. A second silica gel column, using EtOAc as the sole eluent, was necessary to fully purify the desired product, affording 387 mg (5.8% yield, based on the amount of B aldehyde) of the title compound. ^1H NMR (500 MHz, $CDCl_3$, 25 °C) δ = −2.90 (bs, 2H), 4.12 (s, 3H), 8.16 (m, 6H), 8.30 (m, 2H), 8.47 (m, 2H), 8.82−8.89 (bm, 8H), 9.06 (m, 6H) (Figure S1).

Preparation of Sensors. Toluene stock solutions of **1** (∼100 μM) and **QD** (∼10 μM) were prepared. The concentration of the QD stock solution was calculated using $\varepsilon_{350} = 4.34 \times 10^5\ M^{-1}\ cm^{-1}$, as estimated using an empirical formula based on the first absorbance feature (λ = 501 nm).[56] To prepare the sensor **QD1-MC**, an aliquot of the QD stock (typically containing ∼10 nmol of QDs) was dissolved in 4 mL of chloroform, and an appropriate volume of the porphyrin stock was then added to give 10 mol equiv of porphyrin per QD. The resultant mixture was stirred overnight at room temperature in a 20 mL scintillation vial to allow equilibration of the porphyrin on the QD surface. Solvent was removed by rotary evaporation, and the residue

DOI: 10.1021/jacs.5b04765
J. Am. Chem. Soc. 2015, 137, 9832−9842

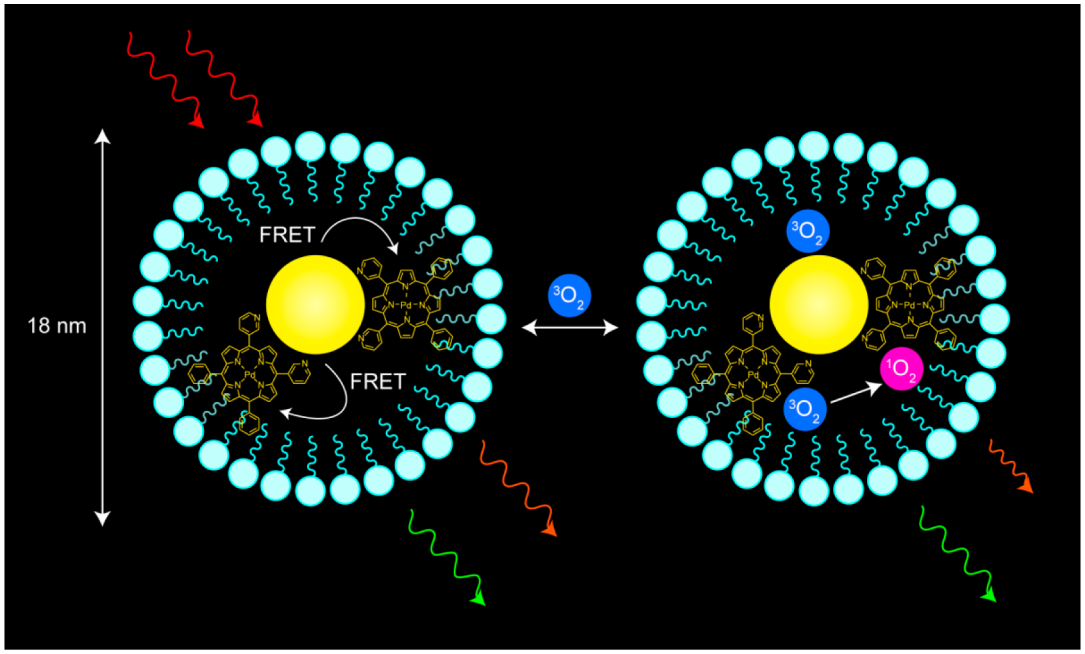

Figure 1. Schematic representation of the oxygen sensing method developed in this study. The quantum dot-porphyrin assembly encapsulated in a lipid micelle is irradiated under two-photon excitation using NIR (700−1000 nm) light. Through FRET, the porphyrin is promoted to an excited electronic state. Oxygen can freely diffuse into the micelle and reversibly quench porphyrin emission; the lifetime and intensity of the emission are a quantitative measure of O_2 concentration.

was dissolved in 750 μL of the lipid solution (1,2-dioleoyl-*sn*-glycero-3-phosphoethanolamine-*N*-[methoxy(polyethylene glycol)-2000] ammonium salt 25 mg/mL solution in chloroform). Solvent was removed by rotary evaporation and 4 mL PBS were added. The mixture was then sonicated for 5 min using a Microson XL 2000 ultrasonic liquid processor (Qsonica LLC) with an output power of 2 W to give an orange, nonturbid solution. Aggregates were removed by filtering the solution through a 0.45 μm and then 0.22 μm syringe filter (Millipore). Solutions for *in vivo* imaging were prepared by combining four independent batches and concentrating the solution using 50,000 MW centrifuge filters to a final volume of 500−700 μL. The porphyrin-free construct **QD-MC** was prepared using the same micelle formation protocol outlined above for **QD1-MC**.

Physical Measurements. ^{1}H NMR spectra were recorded on a Varian Inova-500 spectrometer at the MIT Department of Chemistry Instrumentation Facility (DCIF) and internally referenced to the residual solvent signal (δ = 7.26 for $CHCl_3$ in $CDCl_3$).[57] UV−vis absorption spectra were acquired using a Cary 5000 spectrometer (Agilent). Steady-state emission and excitation spectra were recorded on a SPEX FluoroMax-3 spectrofluorimeter. Porphyrin emission quantum yields were referenced relative to a freeze−pumped−thawed sample of $[Ru(bpy)_3]Cl_2$ in MeCN (Φ = 0.094).[58] The quantum yield of **QD** was determined using fluorescein 27 in 0.1 M NaOH (Φ = 0.87, η = 1.335)[59] as the standard. Samples for phosphorescence quantum yield measurements, vacuum lifetime (τ_o) measurements, and nonquenched steady-state emission spectra were prepared by subjecting solutions to three cycles of freeze−pump−thaw to pressures below 10^{-5} Torr. Gel filtration chromatography (GFC) was performed on an Akta Prime system (GE) with a Superose 6 cross-linked dextran column, using PBS as the eluent; the UV absorbance at 280 nm was monitored over the course of the column. Dynamic light scattering (DLS) measurements were made using a Zetasizer Nano S90 (Malvern). Bright-field transmission electron micrographs (TEM) were recorded using a JEOL 2100 transmission electron microscope. Dark-field scanning transmission electron micrographs (STEM) were recorded on a JEOL 2010 TEM/STEM. For spectroscopic measurements conducted at 37 °C, a TC 125 temperature controller (Quantum Northwest) equipped with a circulating water bath was used to maintain the sample temperature. Samples were equilibrated at 37 °C for 1 h before any measurements were made.

Solution oxygen measurements were made using an Ocean Optics NeoFox Phase Measurement system equipped with a FOXY-HPT-1-PNA fiber optic probe. The sensor was calibrated using a two-point calibration: an air-equilibrated PBS solution and a PBS solution purged with argon for 1 h. The probe was recalibrated before each set of data was collected; the measured lifetime of the sensor was used to determine the amount of dissolved oxygen in the sample. For these calibration measurements, the solubility of oxygen (20.94%) from 1 atm of air in pure water as a function of temperature was calculated using the empirical equation[60] as advocated by the National Institute of Standards and Technology (NIST):[61]

$$\ln c = -52.16764 + \frac{84.59929}{\tau} + 23.41230 \ln \tau \quad (1)$$

where c is in units of mL of gas at STP per liter of solution and $\tau = T/100$, where T is the temperature in K. A variation of this equation assumes 1 atm of O_2.[62] At 25 and 37 °C, c = 5.951 and 4.999, respectively. Using the ideal gas law, the solubility of oxygen in pure water was calculated to be 265 and 223 μM at 25 and 37 °C, respectively. For PBS buffer, the concentration of oxygen was adjusted by[60]

$$k_{sc\alpha} = \left(\frac{1}{c_2}\right) \log\left(\frac{c^0}{c}\right) \quad (2)$$

where $k_{sc\alpha}$ is the salt effect parameter, c_2 is the concentration of solute, c° is the solubility of oxygen in pure water, and c is the solubility of oxygen in the electrolyte solution. Since the primary component of this buffer is NaCl, the concentration of the salt, c_2 = 137 mM in the buffer[63] and $k_{sc\alpha}$ = 0.145 L mol^{-1} for NaCl[60] was used in eq 2 to furnish the solubility of oxygen in PBS to be 255 and 213 μM at 25 and 37 °C, respectively. For the solubility of oxygen in blood, the molar concentration of oxygen was converted to a partial pressure using $c = \alpha P$, where c is the concentration of dissolved oxygen, P the partial pressure of oxygen, and α is the solubility parameter, taken to be 0.031 mL L^{-1} Torr^{-1} or 122 μmol L^{-1} Torr^{-1} for blood at 37 °C.[64]

DOI: 10.1021/jacs.5b04765
J. Am. Chem. Soc. 2015, 137, 9832−9842

The presence of singlet oxygen was determined by monitoring the decrease in absorbance of DPBF at 410 nm upon steady-state photolysis as a function of time. White light, produced using a Newport 67005 xenon lamp operating at 200 W, was passed though a Newport 74100 monochromator, to furnish 414 nm light with a photovoltage of ~60 mV, as measured using a silicon amplified detector (DET-L-SIVU-R-C, Newport) connected to a Newport Merlin radiometry system. Samples were irradiated for a total of 60 min; absorption spectra were recorded every 5 min using a CCD array UV−vis spectrophotomer (SI Photonics, Inc.). A solution of the sensitizer (~4 mL) was prepared such that the absorbance at the irradiation wavelength was matched (A_{414} = 0.195): **QD1-MC** in PBS and $Ru(bpy)_3Cl_2$ in MeOH as a reference. A stock solution of DPBF was prepared (5.7 mg in 12 mL MeOH, 1.8 mM). An aliquot (100 μL, 0.18 μmol) of the DPBF solution was added to the sensitizer solution. Control samples were prepared by adding 100 μL DPBF solution to ~4 mL of solvent (MeOH or PBS).

Nanosecond time-resolved emission measurements of porphyrin lifetimes were acquired using a previously reported system.[65,66] Pump light was provided by the third harmonic (355 nm) of a Quanta-Ray Nd:YAG laser (Spectra-Physics) operating at 10 Hz. The pump light was passed through a BBO crystal in an optical parametric oscillator (OPO) yielding a visible frequency that was tuned to 450 nm. Excitation light was attenuated to 1−3 mJ per pulse for all experiments using neutral density filters. Emitted light was first passed through a series of long pass filters to remove excitation light then to a Triax 320 monochromator (Jobin Yvon Horiba) and dispersed by a blazed grating (500 nm, 300 grooves/mm) centered at 685 nm. The entrance and exit slits of the monochromator were set to 0.36 mm in all experiments herein, corresponding to a spectral resolution of 4.5 nm. The signal was amplified by a photomultiplier tube (R928, Hamamatsu) and collected on a 1 GHz digital oscilloscope (9384CM, LeCroy); acquisition was triggered using a photodiode to collect scattered laser excitation light.

Femtosecond time-resolved emission measurements of QD lifetimes were acquired using a Libra-F-HE (Coherent) chirped-pulse amplified Ti:sapphire laser system, as previously described.[38] Excitation pulses of 450 nm were produced via fourth harmonic generation of the idler using a BBO crystal; the pulse power was attenuated to 0.4−1 mW at the sample. Emission lifetimes were measured on a Hamamatsu C4334 Streak Scope streak camera, which has been described elsewhere.[67] The emission signal was collected over a 140 nm window centered at 480 nm using 100 and 2 ns time windows; delays for these time windows were generated using a Hamamatsu C1097−04 delay unit. A 495 nm long pass filter was used to remove laser excitation light. Two-photon emission spectra were generated using this Libra-F-HE (Coherent) laser system. Excitation pulses of 800 nm were used directly from the Libra output; the pulse power was attenuated to 5−8 mW using neutral density filters, and the beam was focused onto the sample using a 200 mm focal length lens. The emission spectrum was collected using a Hamamatsu C4334 Streak Scope streak camera in a 140 nm window centered at 480 nm.

Two-photon lifetime measurements were made using a custom-built MPLSM in the Edwin L. Steele Laboratory, Department of Radiation Oncology at Massachusetts General Hospital, as previously described.[68] Additions to the MPLSM system[69] were made such that lifetime measurements could be performed; these modifications have been previously described.[38] The 850 nm laser output was adjusted using a 10RP52-2 zero-order half-wave plate (Newport) and a 10GL08AR.16 Glan-Laser polarizer (Newport) to attenuate the power to 700 mW for air samples and 400 mW for freeze−pumped−thawed samples. The beam was passed through a 350−50 KD*P Pockel cell (Conoptics) that switched the triggering pulses from a DG535 digital delay generator (Stanford Research Systems); the output of the Pockel cell was ~10% of the incident power during the "off" cycle. The excitation cycle was 1.60 μs in duration for air samples and 15.36 μs in duration for freeze−pumped−thawed samples. A 750DCXR short pass dichroic mirror (Chroma Technology), a HQ690/90m-2p bandpass filter (Chroma Technology), and a focusing lens were used in front of the GaAs H7421-50 photomultiplier tube (Hamamatsu) to collect phosphorescent emission. Photon counting was performed using a SR430 multichannel scaler (Stanford Research Systems) to histogram the counts in 1024 or 2048 bins of 40 ns for air samples or 2.56 μs for freeze−pumped−thawed samples.

***In Vivo* Experiments.** The MPLSM system described above was used to collect two-photon *in vivo* images of severe combined immunodeficient (SCID) mice with surgically implanted dorsal skinfold chambers (DSC)[70] or cranial windows (CW).[71] Prior to imaging, mice were anesthetized with Ketamine/Xylazine (10/1 mg/mL) and subsequently treated with 150−200 μL of the concentrated sensor solution via retro-orbital injection. This sensor dosage was determined empirically, balancing the desire to inject a minimal amount of sensor while dosing a sufficient quantity to view blood vessels upon systemic injection. At this dosage, the sensor remained in circulation long enough to perform continuous imaging for several hours without the need to inject additional sensor. For imaging, 850 nm excitation light was used at a power of 400 mW. Collected light was split into three channels: green for QD emission using either a 565 or 570 nm long pass dichroic mirror and a HQ535/40m-2p bandpass filter (40 nm bandwidth centered at 535 nm), yellow using a 585 nm long pass dichroic mirror alone, and red for porphyrin emission using a HQ690/90m-2p bandpass filter. For *in vivo* porphyrin emission lifetimes, the excitation cycle was 15.36 μs in duration, and photon counts were collected in 1024 bins of 2.56 μs.

Energy-Transfer Analysis. The efficiency of energy transfer from the QD to the porphyrin was evaluated using Förster analysis:[72,73]

$$E = \frac{mk_{D\to A}}{mk_{D\to A} + \tau_D^{-1}} = \frac{mR_0^6}{mR_0^6 + r^6} \quad (3)$$

where $k_{D\to A}$ is the rate of energy transfer, r is the distance between the donor and acceptor, R_0 is the Förster distance, or the distance at which the energy transfer efficiency is 50%, and m is the number of acceptor molecules per donor. This quantity (E) can be measured experimentally:

$$E = 1 - \frac{\tau_{D\to A}}{\tau_D} \quad (4)$$

where τ_D is the lifetime of the QD alone and $\tau_{D\to A}$ is the lifetime of the QD with surface-bound porphyrin. R_0 is determined from the spectral overlap integral:

$$R_0^6 = \frac{9000(\ln 10)\kappa^2\Phi}{128\pi^5 N n^4}\int_0^\infty F_D(\lambda)\varepsilon_A(\lambda)\lambda^4 d\lambda \quad (5)$$

where κ^2 is the relative orientation factor of the dipoles, taken to be 0.476 for static donor−acceptor orientations,[73,74] Φ_D is the quantum efficiency of the donor, N is Avogadro's number, n is the index of refraction of the medium, which is taken to be 1.334 for PBS,[75] $F_D(\lambda)$ is the normalized intensity of the donor, and $\varepsilon_A(\lambda)$ is the extinction coefficient of the acceptor at wavelength λ. The average number of porphyrins attached to the QD, m, was determined from the optical cross sections of the spectra of QD, the porphyrin, and the corresponding assembly. The absorption spectrum of the assemblies was taken as the sum of the individual absorbance spectra of the donor and acceptor, as previously demonstrated.[38] The value for m and the concentration of the assemblies was calculated using the individual donor and acceptor absorption spectra, their known ε values, and Beer's law.

RESULTS AND DISCUSSION

Sensor Preparation. Micelle encapsulation represents a scalable method of synthesizing water-soluble QD nanosensors and circumvents laborious multistep polymer syntheses required for coating QDs for covalent conjugation to a chemosensor. Figure 1 shows the porphyrin-QD micelle construct used in this study. A lipid functionalized with a PEG-2000 chain for water solubility was used to prepare these micelles. This particular phosphoethanolamine lipid was

DOI: 10.1021/jacs.5b04765
J. Am. Chem. Soc. 2015, 137, 9832−9842

selected based on the studies of Dubertret, Norris, and co-workers, who demonstrated that single QDs may be encapsulated within the micelle when the QD is sufficiently large (diameter >3 nm).[39] TEM images revealed that the QDs used in this study are ∼3.5 nm in diameter (Figure S2), suggesting that the volume of the micelle can accommodate a single QD donor in the presence of multiple porphyrin acceptors, analogous to the organic-soluble constructs.[38]

Whereas the vast majority of synthetic procedures for micelle formation involve heating and evaporation of an organic solvent[39,41,43,44,50] or dissolution of an organic film in aqueous media or a similar method of phase transfer,[40,42,45,46,49,51,52] sonication offers an alternative method to assemble micelles. In contrast to other protocols,[47] we were able to rapidly (∼5 min) and facilely produce micelle nanosensors of a consistent size by conducting sonication at room temperature. The lower sonication temperatures for micelle formation are afforded by the QD, which serves as a template for micelle formation as evidenced by the inability to form micelles in the absence of QD. Additionally, when a porphyrin solution in the absence of QD was treated in an identical manner, the solution remained turbid and inhomogeneous. Gel filtration chromatography (GFC) (Figure S3) and DLS (Figure S4) establish a Gaussian distribution of particles. In order to determine the size of these constructs, micelles containing the QD alone (**QD-MC**) were imaged using dark-field STEM and bright-field TEM (Figure 2); additional images are provided in Figures S5 and S6. The STEM images demonstrate that the micelles are largely well dispersed and the particles are 4.69 ± 0.81 nm, measuring 46 independent QDs over 10 different images. This is corroborated by the bright-field data, which show that the QDs are 3.80 ± 0.64 nm in diameter, measuring 39 independent QDs over 10 different images. In instances of aggregation, the bright-field data confirm that the QDs are individual particles (Figures 2b and S6). Both imaging techniques give the same size particles within error, confirming that single QDs are encapsulated in the majority of micelles. Based on DLS, the average particle size (i.e., hydrodynamic diameter) for a typical **QD-MC** is 16.8 ± 0.7 nm, and micelles with the porphyrin (**QD1-MC**) are slightly larger at 18.2 ± 0.7 nm. The size of **QD-MC** is consistent with micelles containing single QDs reported by Dubertret, Norris, and co-workers (10−15 nm), as measured by TEM using phosphotungstic acid to stain the phospholipid layer.[39] Our observation of slightly larger particles is likely due to the radial extension of the PEG-2000 chains in solution, rather than the incorporation of multiple QDs within a single micelle. Presumably, the appended porphyrins on the surface of the QD increase the radius of the assembly relative to the QD alone, resulting in a larger micelle size. These QD-micelle constructs are only a few nanometers larger than our previously reported polymeric conjugates with dihydrolipoic acid-polyethylene glycol (DHLA-PEG)[76] or poly imidazole ligands (PIL),[77] both of which exhibit particle sizes of ∼11.5 nm by DLS.

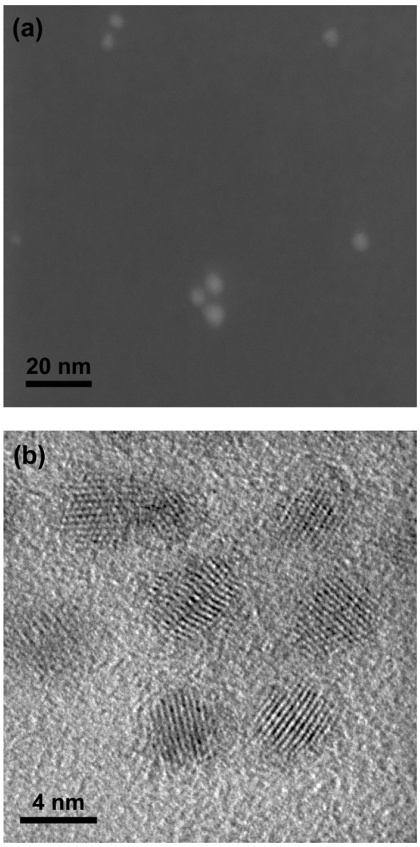

Figure 2. (a) Dark-field STEM and (b) bright-field TEM images of **QD-MC**, demonstrating that the individual QDs are observed. While the micelles may aggregate, the TEM grid is clearly visible between individual particles, indicating that the vast majority of micelles contain a single QD.

The QD-micelle constructs are stable for over 2.5 years when stored at 4 °C. Both dilute and concentrated (i.e., those used for *in vivo* imaging) samples of **QD-MC** remained nonturbid, green solutions that are highly fluorescent, as observed using a hand-held UV lamp as the excitation source. Concentrated samples of **QD1-MC** developed a fine orange precipitate over time. The supernatant from this sample has an absorption spectrum that is identical to that of a freshly prepared sample (Figure S7). If the entire sample and pellet were resuspended in PBS buffer and filtered through 0.2 μm syringe filter, the absorption spectrum showed a decrease in porphyrin absorption relative to QD absorption (λ < 375 nm). Moreover, the sample shows green QD fluorescence when excited with a hand-held UV lamp. This phenomenon is not observed for freshly prepared samples of **QD1-MC**, where QD emission is not visible by eye. These observations suggest that the pellet is largely free porphyrin that has been released from degraded micelles. The QDs, however, remain in solution, accounting for the green fluorescence of the sample and increased absorption at λ < 375 nm. Although dilute solutions of **QD1-MC** did not have a visible precipitate after 2.5 years, an increase of QD absorption and visible green fluorescence were observed.

Photophysical Properties. The absorption spectrum of **QD1-MC**, shown in Figure 3, is dominated by the Soret and two Q bands of porphyrin **1**, which is superimposed onto the absorption spectrum of the QD. These spectral features are comparable to those of **QD1** in toluene (Table S1). The emission spectrum of **QD1-MC** exhibits the luminescence features of the QD ($\lambda_{em,max}$ = 527 nm) as well as the triplet ($\lambda_{em,max}$ = 682 and 754 nm) and singlet ($\lambda_{em,max}$ = 608 nm) transitions of **1**.[38,78,79]

The emission quantum yield of the QD is perturbed by the micelle, decreasing from Φ = 0.72 for the QD in toluene[38] to Φ = 0.42 for **QD-MC** in PBS (Figure S8). However, **QD-MC** has a superior quantum yield relative to micelles assembled from the same lipid with heating (Φ = 0.24),[39] suggesting that

DOI: 10.1021/jacs.5b04765
J. Am. Chem. Soc. 2015, 137, 9832−9842

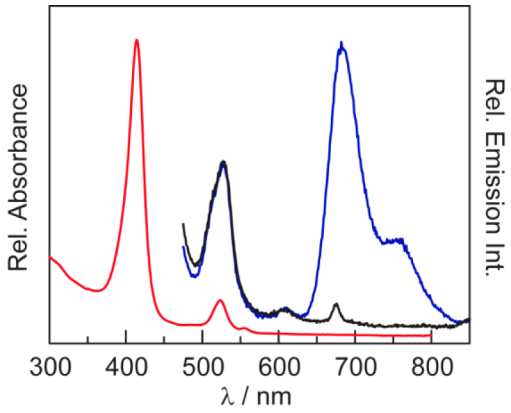

Figure 3. Steady-state absorption (red line) and emission spectra of **QD1-MC** (λ_{exc} = 450 nm) in PBS buffer. Whereas the emission intensity of the phosphor is almost completely quenched in the presence of air (~160 Torr O_2) (black line), it is pronounced under vacuum (blue line). The emission of the QD in **QD1-MC** ($\lambda_{em,max}$ = 523 nm) is unchanged in air and vacuum, thereby establishing a ratiometric sensor.

synthesis of the micelle using sonication as opposed to heating may be beneficial to furnish higher QD quantum yields. The high emission quantum yields, together with the high two-photon absorption cross sections of QDs,[80−82] enable emission spectra to be obtained under two-photon excitation in toluene.[38] Similar spectra are difficult to obtain in PBS, which was found to effectively generate white light under excitation by the tightly focused femtosecond laser beam (5−8 mW of focused 800 nm light). As a result, two-photon emission could be detected easily only for **QD-MC** owing to its high quantum yield (Figure S9), where the green emission of the sample exceeded the generated white light. Owing to FRET, the two-photon emission spectrum of **QD1-MC** is obscured by the generated white light continuum. However, two-photon emission from all samples could be detected using MPLSM (*vide infra*).

The energy-transfer efficiency and QD quenching of **QD1-MC** were compared to the toluene soluble construct **QD1**. At 10 equiv of porphyrin **1**, a 97% decrease in QD emission intensity, relative to the QD alone, was observed. This is consistent with the 94% FRET efficiency determined from QD lifetime measurements.[38] A summary of the FRET parameters is presented in Table S2. The emission spectrum of **QD1** shows that the QD and porphyrin emission features have approximately equal intensity. For convenience, these data have been reproduced in Figure S10. Upon micelle encapsulation, QD emission is further attenuated, as demonstrated in Figure 3 for equal porphyrin loadings. Indeed, the QD emission intensity of **QD1-MC** is reduced by 98% relative to **QD-MC** at equivalent QD loadings (Figure S11). The lifetime of the QD similarly reflects very efficient energy transfer. Whereas the lifetime of the QD in the micelle (13 ns) increases relative to toluene (Table S3), likely due to a modulation of the surface states of the QD,[38,83] the QD lifetime in **QD1-MC** is dramatically diminished (~80 ps). This is a direct result of energy transfer. Using eq 4, we calculate the FRET efficiency to be 99% (Table S2), which is consistent with the observed decrease in emission intensity. The increased quenching efficiency in **QD1-MC** relative to **QD1** is attributed to the increased spectral overlap (Figure S12) in the micelle construct as a result of the 10 nm red shift of QD emission in the micelle (see Tables S1 and S2). Additionally, the excitation spectrum of **QD1-MC** (Figure S13) exhibits increased emission relative to **1** in the 300−400 nm region, where QD absorbance dominates, indicating that the QD is the donor in the FRET process.

From this value of efficiency, eq 3 yields an average QD-porphyrin distance of 2.67 nm. Based on the bright-field TEM data presented in Figure S6, the radius of the QD is 1.90 nm. Using the crystal structure of an analogous A_3B porphyrin with a single 4-pyridyl substituent,[38] the distance between the pyridyl nitrogen and the palladium center is 0.77 nm. Thus, the QD to porphyrin center-to-center distance based on structural metrics is 2.67 nm, which matches the average donor−acceptor distance (r) determined by FRET analysis.

Using the absorption spectrum of **QD1-MC**, we measure an average of eight porphyrins per QD. This value is lower than the 10 equiv excess of porphyrin to QD, but it is consistent with our photophysical studies of **QD1** (10 equiv **1**) in toluene, which showed that the phosphorescence lifetime exhibited biexponential kinetics attributed to bound and free porphyrin in a 75:25 ratio.[38] This demonstrates that ~8 equiv of porphyrin are encapsulated within the micelle. Presumably, the rest of the hydrophobic porphyrin intercalates in the excess lipid used to prepare the micelles. This porphyrin population, associated with excess lipid, is subsequently washed away from the micelles.

The excited-state lifetimes of porphyrin in **QD1-MC** under both one- and two-photon (λ_{exc} = 450 and 850 nm, respectively) excitation were measured, and the results are presented in Table 1. Under one-photon excitation, the

Table 1. Porphyrin Lifetimes for QD1-MC under One- and Two-Photon Excitation

sample[a]	λ_{exc}/nm	τ_1 (μs)[b]	A_1 (%)[c]	τ_2 (μs)[b]	A_2 (%)[c]
QD1-MC	450 (1-hν)	411 ± 27	48	29 ± 5	52
QD1-MC	850 (2-hν)	233 ± 18	100	–	–

[a]Freeze−pumped−thawed (<10^{-5} Torr) solutions of PBS at 25 °C. [b]95% confidence interval. [c]Relative contribution to the biexponential fit.

porphyrin excited-state decay is biexponential. Relative to the lifetime of free porphyrin **1** (τ(**1**) = 154 μs),[38] a longer and shorter lifetime component is observed for porphyrin in the micelle. This behavior has been observed previously for **QD1**, which exhibits a long lifetime component of τ(**QD1**) = 590 μs and a short lifetime component of (τ(**QD1**) = 149 μs (Table S4).[38] This biexponential decay has been attributed to the porphyrin under dynamic equilibrium with the QD surface. The longer component is due to porphyrin associated with the QD, residing within the passivating ligand that coats the QD surface. The shorter lifetime component is due to the free porphyrin, which is under dynamic equilibrium with the surface-bound porphyrins. Similarly, in **QD1-MC**, biexponential decays are obtained with lifetimes on the order of **QD1**. Figure S14 shows a representative decay trace for a freeze−pump−thawed sample of **QD1-MC** and demonstrates that the biexponential fit is superior to the monoexponential one. The long lifetime is ascribed to porphyrin associated with the QD surface within the micelle and the short lifetime is consistent with free porphyrin residing within the oleate groups of the micelle. Consistent with this behavior is the observation of a monoexponential decay of **QD1-MC** under two-photon excitation. The observed difference in one- and two-photon

DOI: 10.1021/jacs.5b04765
J. Am. Chem. Soc. 2015, 137, 9832−9842

lifetimes is typically ascribed to differences in vibronic coupling between one- and two-photon excitation.[84,85] A signature for differences in vibronic coupling is a small shift in the emission maximum owing to varying Franck−Condon factors, which will affect both the radiative and nonradiative decay pathways and, hence, lifetimes. Linear polyenes exhibit a shift of 50−80 cm^{-1} in emission energy under one- and two-photon excitation and an attendant difference in lifetime.[86] Noting that the earliest descriptions of porphyrin electronic structure were successfully based on a cyclic polyene model,[87] we observe a 64 cm^{-1} energy difference in the porphyrin emission maximum in **QD1** under one- and two-photon excitation. On this basis, we ascribe the difference in one- and two-photon lifetimes in Table 1 as the difference in oscillator strength arising from vibronic coupling. Because the QD is the two photon antenna, only porphyrins at the surface of the QD can be excited via FRET. The free porphyrin within the micelle cannot be excited, and hence emission decay from this population is absent under two-photon excitation conditions. In this regard, the two-photon experiment is ideal for *in vivo* sensing for self-assembled chemosensors, as the experiment naturally selects for a single population of chemosensors which are associated with the QD. Background signal from unassociated chemosensors is absent, since this population cannot directly be excited under two photon conditions.

Oxygen Sensing. The porphyrin luminescence is significantly quenched by oxygen, as shown in Figure 3. Under 450 nm excitation, where the QD is the primary photon absorber, there is a 10-fold diminishment in the intensity of the T(0,0) transition of the aerated sample relative to the same sample in fpt solutions. A similar trend is observed in the lifetime of **QD1-MC** in aerated PBS buffer owing to oxygen quenching. We note that the quenched lifetime of **QD1-MC** is 10× greater than that of **QD1** in aerated toluene (see Table S4), suggesting that the micelle provides a modest barrier of O_2 versus that observed for freely diffusing O_2 in solution. This phenomenon has also been previously observed for Pd porphyrins in asolectin vesicles.[88] Under MPLSM excitation with 850 nm light, the sensitivity of the porphyrin emission to oxygen in **QD1** and **QD1-MC** is similar. This suggests that two-photon excitation mechanism of the porphyrin via FRET from the QD is the same for both sensor constructs.

Emission spectra of **QD1-MC** were recorded after exposure to dissolved oxygen at different concentrations (Figure 4a). The nominal O_2 dependence of the QD emission at 528 nm arises as a consequence of only freeze−pump−thawing the sample (Figure S15) and is not observed for typical samples. This phenomenon has also been observed with the organic soluble construct **QD1** (see Figure S10b). Since the sensor contains two fluorophores, ratiometric oxygen sensing may be realized by using the porphyrin to QD emission intensity ratio. An *in vitro* ratiometric calibration curve (Figure 4b) was constructed by plotting the 682 to 528 nm intensity ratio as a function of $[O_2]$. The data exhibit an exponential relation; this has also been observed for a ratiometric O_2 sensor consisting of a platinum porphyrin as the oxygen-sensitive phosphor and a QD as an intensity reference embedded in a polymer hydrogel.[89]

The rate constant for oxygen quenching of porphyrin emission in **QD1-MC** was determined by Stern−Volmer analysis of the lifetime variance with the concentration of oxygen. A representative example of the decay traces as a function of oxygen concentration in the range of biological sensing (*vide infra*) is presented in Figure S16. Decay traces are

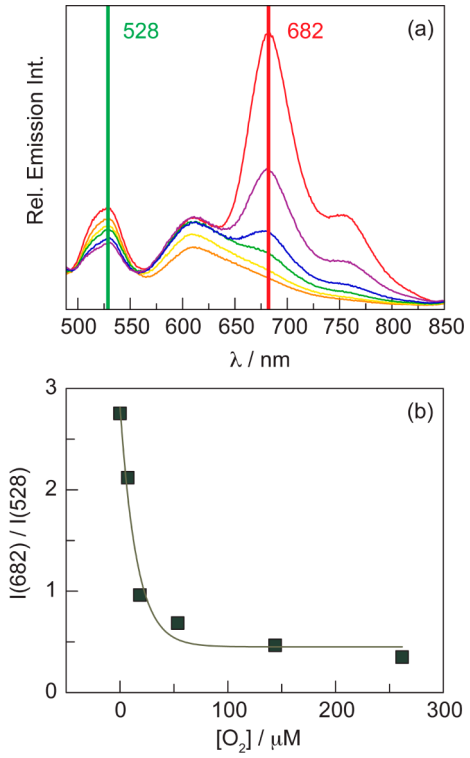

Figure 4. (a) Steady-state emission spectra of **QD1-MC** (λ_{exc} = 450 nm) in PBS buffer with various oxygen concentrations: 0 (red line), 5 (purple line), 20 (blue line), 55 (green line), 145 (yellow line), and 260 (orange line) μM O_2. (b) *In vitro* ratiometric intensity calibration curve constructed from data obtained in (a). The data were fit to an exponential function: $y = 0.45 + 2.36\exp(-0.065x)$, where x is the oxygen concentration in μM and y is the 682 nm/528 nm intensity ratio.

fit to a biexponential decay (Table 1). The long and short lifetime components each obey Stern−Volmer behavior:

$$\frac{\tau_o}{\tau} = 1 + k_q\tau_0[O_2] \quad (6)$$

where τ_o is the natural radiative lifetime of the phosphor in the absence of quencher, τ is the lifetime of the phosphor at a given oxygen concentration $[O_2]$, and k_q is the bimolecular quenching rate constant. Figure 5 illustrates representative examples of the long lifetime component at 25 and 37 °C. Values of the Stern−Volmer constant of K_{SV} (= $k_q\,\tau_o$) = 0.371 ± 0.099 μM^{-1} and 0.370 ± 0.169 μM^{-1}, for the long and short decay components, respectively, were obtained from five independent samples at 25 °C (Table S5). Similar results are obtained for measurements at 37 °C, which were performed for the purposes of calibrating *in vivo* lifetimes. At 37 °C, five independent samples (Table S6) furnished an average K_{SV} = 0.588 ± 0.064 μM^{-1} and 1.065 ± 0.473 for the long and short components, respectively. As mentioned above, the long lifetime component is attributed to porphyrins associated with the QD. Using the natural lifetime of this population, an oxygen quenching rate constants of $k_q = 9.02 \pm 2.41 \times 10^8$ M^{-1} s^{-1} at 25 °C and $k_q = 1.36 \pm 0.15 \times 10^9$ M^{-1} s^{-1} at 37 °C are obtained. This increase in k_q at higher temperatures agrees with previously devised empirical relationships for the temperature dependence of k_q for Pd(II) porphyrins $k_q = (6.4 + 0.21T)^2$.[90] The rate constants at 37 °C should be faster than that at 25 °C

DOI: 10.1021/jacs.5b04765
J. Am. Chem. Soc. 2015, 137, 9832−9842

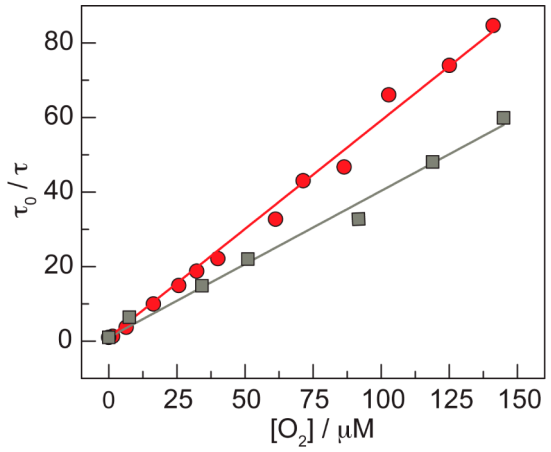

Figure 5. A representative Stern–Volmer plot of the long component of the biexponential decay for **QD1-MC** at 25 °C (gray square) and 37 °C (red circle) under 450 nm excitation. These two data sets yield k_q values of 9.57×10^8 M^{-1} s^{-1} at 25 °C and 1.35×10^9 M^{-1} s^{-1} at 37 °C.

by a factor of 1.5, which is exactly what we observe for both the long and short components.

In addition to collisional quenching, the formation of singlet oxygen ($^1O_2$) may also deactivate the excited triplet state of the porphyrin in **QD1-MC**. There have been several reports of FRET-based QD-photosensitizer conjugates that produce $^1O_2$.[91−93] To test this possibility, a DPBF assay[94] was performed, monitoring the disappearance of the 410 nm absorption feature of this molecule as a function of time (Figure S17). It was found that the slope of this plot for **QD1-MC** is identical to the DPBF control in PBS, indicating that a negligible amount of $^1O_2$ is formed. Singlet oxygen will decay back to the ground state before diffusing out of the micelle: $\tau(^1O_2)$ = 20 μs in toluene[95] (similar dielectric to the hydrophobic interior of the micelle) and 2 μs in H_2O.[96] If $^1O_2$ were to form, it is likely to react before diffusing out of the micelle as $^1O_2$ is known to react with electron-rich olefins, such as those found in the oleate groups of the micelle phospholipid, to form the corresponding ketone.[97]

***In Vivo* Oxygen Sensing.** Having established that **QD1-MC** exhibits oxygen sensitivity at 0−160 Torr, which completely covers the biologically relevant range, *in vivo* oxygen concentration profiles were constructed from two-photon lifetime measurements of **QD1-MC**. Experiments were conducted on SCID mice with a surgically implanted DSC or CW. Collected light was separated into three optical channels: green for QD emission using a 565 or 570 nm long pass dichroic mirror and a HQ535/40m-2p bandpass filter, yellow for Q(0,0) fluorescence of **1** using a 585 nm long pass dichroic mirror, and red for T(0,0) phosphorescence of **1** using a HQ690/90m-2p bandpass filter. Figure S18 provides a schematic of the optical detection configuration as well as an illustration of the spectral ranges captured by each channel. Under typical imaging conditions (400 mW of 850 nm excitation light), significant signal intensity was observed after systemic injection of the sensor; minimal background signal was observed prior to injection (Figure S19). We observed that **QD1-MC** remains in circulation for several hours, obviating the need for additional injection of the sensor. A post-mortem examination of a mouse injected with **QD-MC** by fluorescence imaging showed that the micelles were distributed throughout the body, but were particularly concentrated in the liver.

QD emission in the green channel served as a suitable means of tracking the sensor. Figure 6 shows 3-D depth projections of the brain vasculature, constructed from a series of images taken at 10 μm steps over a depth of 200 μm. As evidenced by the green channel, the sensor is evenly distributed throughout the vessels. Conversely, the intensity of the red channel is variable, illustrating differences in oxygen levels of arteries and veins. Figure 7 shows composite images of a DSC at a depth of 70 μm (a) and a CW at a depth of 115 μm (b). Lifetime measurements were made at the indicated points (1−10). Using the lifetime from the monoexponential fit, oxygen levels at these points were determined using eq 6 with τ_o = 233 μs (Table 1) and k_q = 1.36×10^9 M^{-1} s^{-1}. These data are summarized in Table 2.

In addition to lifetime measurements, we examined the red to green intensity ratios at each of these points in an effort to exploit the ratiometric nature of **QD1-MC**. Many of the points exhibit red/green ratios that fall outside of the *in vitro*

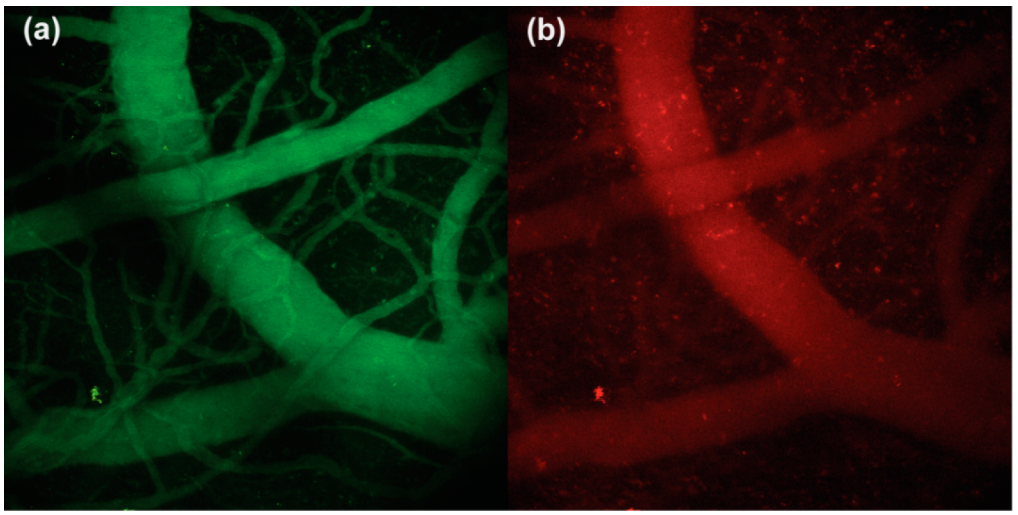

Figure 6. Three-dimensional projections of brain vasculature under two-photon excitation of a SCID mouse with a CW. Images were collected over a depth of 200 μm in 10 μm increments and combined into a projection using the ImageJ software package.

DOI: 10.1021/jacs.5b04765
J. Am. Chem. Soc. 2015, 137, 9832−9842

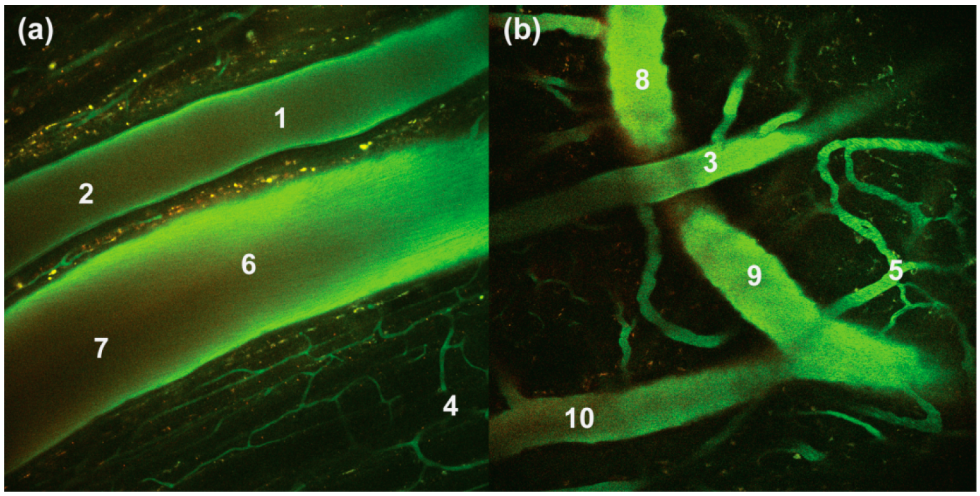

Figure 7. Composite two-photon images of a SCID mouse with either (a) a DSC at a depth of 70 μm or (b) a CW at a depth of 115 μm. These images are an overlay of three optical channels. The indicated points (1−10) represent locations at which *in vivo* lifetimes were measured: arteries (1−3), capillaries (4 and 5), and veins (6−10).

Table 2. *In vivo* Lifetime Measurements

point	τ (μs)[a]	[O_2] (μM)[b,c]	pO_2 (Torr)[c,d]
1	11.1 ± 0.4	63.3 ± 2.4	51.9 ± 2.0
2	8.0 ± 0.4	88.3 ± 4.6	72.3 ± 3.8
3	11.2 ± 0.5	62.5 ± 3.0	51.3 ± 2.5
4	24.9 ± 2.1	26.3 ± 2.5	21.6 ± 2.1
5	19.3 ± 1.0	34.9 ± 2.0	28.6 ± 1.7
6	26.4 ± 0.6	24.7 ± 0.6	20.2 ± 0.5
7	21.0 ± 1.5	31.8 ± 2.6	26.1 ± 2.2
8	18.3 ± 0.6	37.1 ± 1.4	30.4 ± 1.2
9	24.0 ± 0.1	27.4 ± 0.2	22.5 ± 0.2
10	27.0 ± 0.5	24.1 ± 0.5	19.7 ± 0.4

[a]Standard deviation of three measurements at the same point. [b]Calculated using $k_q = 1.36 \times 10^9$ M^{-1} s^{-1} and $\tau_o = 233$ μs in eq 6. [c]Error estimated based on error of lifetime measurement. [d]Partial pressure of O_2 determined from O_2 concentration, see Experimental section.

calibration curve (Figure 4b). For points that fall on the curve, the intensity-based O_2 measurements deviate from the lifetime measurements. We have encountered similar problems when analyzing *in vivo* intensity data using a QD-SNARF-5F pH sensor in a colorectal adenocarcinoma model.[27] The primary reason for the disparity of *in vivo* data and the *in vitro* calibration is the difference in the scatter and absorption of photons as a function of wavelength,[98−100] thereby skewing the measured red:green ratio. As a result, the observed ratio will depend on both the depth at which the image was acquired as well as the optical properties of the tissue above the imaging plane. For these reasons, we preferred lifetime measurements for the quantification of oxygen.

Based on the size of the vessels in Figure 7a, the top vessel bearing points 1 and 2 is an artery, whereas the lower vessel with points 6 and 7 is a vein; the measured lifetimes and corresponding oxygen levels are consistent with this observation. Specifically, the artery (points 1 and 2) in Figure 7a has a diameter of 120 μm and exhibits O_2 pressures that fall within observed ranges for small mammals (50−70 Torr for ∼100 μm arteries).[101,102] Owing to the lower O_2 levels in veins, the average intensity of red signal (see Figure S19f) in the vein is 1.25 times greater than it is in the artery. The vein (points 6 and 7) has a diameter of 185 μm, and the measured O_2 levels are consistent with those observed for veins (20−30 Torr for ∼200 μm veins).[102] It is further noteworthy that the partial pressure of oxygen increases by about 3 Torr when the smaller vein bearing point 10 joins the larger one with point 9; the observed increase is consistent with previously reported values for small veins flowing to larger ones.[102] The capillaries (points 4 and 5) exhibit oxygen pressures that are consistent with literature reports (20−30 Torr).[102,103] Overall, the partial oxygen pressures in the CW and DSC models are similar for each vessel type, demonstrating that the sensor gives consistent oxygen readings, irrespective of the window model and the tissue that is imaged. Together, these results establish the viability of **QD1-MC** as an oxygen sensor *in vivo* and more generally the utility of the micelle approach for *in vivo* sensing.

CONCLUSIONS

We report the development of a micelle-encapsulated construct **QD1-MC** for *in vivo* oxygen sensing by microscopy. The synthesis of the sensors is rapid and scalable. Within the micelle, the porphyrin associates with the QD surface with a significant equilibrium constant such that cumbersome methods to conjugate the porphyrin covalently to the QD surface are circumvented. Moreover, sonication processing provides consistently sized particles without the need for chromatography. The porphyrin may be excited via FRET from the QD. Under one-photon excitation, the porphyrin may be directly excited, whether it is associated with the QD or free within the micelle. However, under two-photon excitation, only the porphyrin bound to the QD surface is selectively excited owing to the large two-photon absorption cross-section of QDs as compared to the porphyrin. The porphyrin excited state is quenched by molecular oxygen, and a quantitative measure of oxygen levels is provided by measurements of porphyrin lifetime, which fit a biexponential decay. The long component is attributed to the porphyrin bound to the surface of the QD, while the short component is due to free porphyrin dispersed in the lipids of the micelle. Stern−Volmer analysis indicates that the oxygen sensitivity of the porphyrin within the micelle occurs in a biologically relevant (0−160 Torr) range. Under two-photon excitation, the QD-bound porphyrin population is

DOI: 10.1021/jacs.5b04765
J. Am. Chem. Soc. 2015, 137, 9832−9842

selectively excited via FRET, thereby eliminating background signal from free porphyrin. This is supported by the observation of monoexponential decay kinetics for oxygen quenching under two-photon irradiation both *in vitro* and *in vivo*. QD emission is unaffected by O_2, thereby serving as an intensity standard for ratiometric sensing.

The small size of the micelle permits the use of **QD1-MC** as a probe of biological microenvironments. **QD1-MC** provides sufficient signal to collect *in vivo* images and lifetime-based oxygen measurements that are consistent with known values. The cranial window image of Figure 5b demonstrates a known feature of oxygen levels in the vasculature: arteries exhibit higher levels of oxygen than veins, and moreover the partial pressure of oxygen decreases as the diameter of the vessel decreases.[101−103] Current work is directed to exploiting the ratiometric nature of this sensor by performing tissue phantom experiments to calibrate the red:green ratio as a function of depth. These experiments are performed in conjunction with Monte Carlo simulations and *ex vivo* tissue calibrations so that *in vivo* intensity data may be used quantitatively. This will enable faster data acquisition, thus affording greater fidelity in rapidly detecting real time changes in oxygen levels within living organisms.

■ ASSOCIATED CONTENT

Supporting Information

Characterization data for the micelles, including GFC, DLS, and TEM data, are provided. Additional spectroscopic and analytical data are included. Tables comparing spectral data, QD lifetimes, and FRET parameters are also provided. Supplemental *in vivo* images are also included. The Supporting Information is available free of charge on the ACS Publications website at DOI: 10.1021/jacs.5b04765.

■ AUTHOR INFORMATION

Corresponding Authors

*dai@steele.mgh.harvard.edu
*mgb@mit.edu
*jain@steele.mgh.harvard.edu
*dan@steele.mgh.harvard.edu
*dnocera@fas.harvad.edu

Notes

The authors declare no competing financial interest.

■ ACKNOWLEDGMENTS

We thank Dr. Dilek Dogutan for helpful synthetic discussions and Andrew Maher for assistance with experiments using the Libra-F-HE laser system. This research was supported by the U.S. National Cancer Institute grant R01-CA126642, the ISN ARO W911NF-07-D-0004, and the U.S. Department of Energy Office of Science, Office of Basic Energy Sciences under award no. DE-SC0009758. C.M.L. acknowledges the National Science Foundation (NSF) for a Graduate Research Fellowship Program (GRFP) Fellowship.

■ REFERENCES

(1) Vaupel, P.; Kallinowski, F.; Okunieff, P. *Cancer Res.* **1989**, *49*, 6449−6465.
(2) Helmlinger, G.; Yuan, F.; Dellian, M.; Jain, R. K. *Nat. Med.* **1997**, *3*, 177−182.
(3) Helmlinger, G.; Sckell, A.; Dellian, M.; Forbes, N. S.; Jain, R. K. *Clin. Cancer Res.* **2002**, *8*, 1284−1291.
(4) Fukumura, D.; Jain, R. K. *APMIS* **2008**, *116*, 695−715.
(5) Chauhan, V. P.; Stylianopoulos, T.; Boucher, Y.; Jain, R. K. *Annu. Rev. Chem. Biomol. Eng.* **2011**, *2*, 281−298.
(6) Fukumura, D.; Jain, R. K. *Microvasc. Res.* **2007**, *74*, 72−84.
(7) Fukumura, D.; Jain, R. K. *J. Cell. Biochem.* **2007**, *101*, 937−949.
(8) Jain, R. K. *Cancer Cell* **2104**, *26*, 605−622.
(9) Fukumura, D.; Duda, D. G.; Munn, L. L.; Jain, R. K. *Microcirculation* **2010**, *17*, 206−225.
(10) Erler, J. T.; Bennewith, K. L.; Nicolau, M.; Dornhoefer, N.; Kong, C.; Le, Q. T.; Chi, J. T.; Jeffrey, S. S.; Giaccia, A. J. *Nature* **2006**, *440*, 1222−1226.
(11) Pennacchietti, S.; Michieli, P.; Galluzzo, M.; Mazzone, M.; Giordano, S.; Comoglio, P. M. *Cancer Cell* **2003**, *3*, 347−361.
(12) Rofstad, E. K.; Mathiesen, B.; Kindem, K.; Galappathi, K. *Cancer Res.* **2006**, *66*, 6699−6707.
(13) Folkman, J. *N. Engl. J. Med.* **1971**, *285*, 404−405.
(14) Carmeliet, R.; Jain, R. K. *Nature* **2000**, *407*, 249−257.
(15) Jain, R. K. *Nat. Med.* **2001**, *7*, 987−989.
(16) Folkman, J. *Nat. Rev. Drug Discovery* **2007**, *6*, 273−286.
(17) Carmeliet, P.; Jain, R. K. *Nat. Rev. Drug Discovery* **2011**, *10*, 417−427.
(18) Jain, R. K. *J. Clin. Oncol.* **2013**, *31*, 2205−2210.
(19) Jain, R. K. *Science* **2005**, *307*, 58−62.
(20) Chauhan, V. P.; Stylianopoulos, T.; Boucher, Y.; Jain, R. K. *Annu. Rev. Chem. Biomol. Eng.* **2011**, *2*, 281−298.
(21) Folkman, J. *Nat. Rev. Drug Discovery* **2007**, *6*, 273−286.
(22) Huang, Y.; Yuan, J.; Righi, E.; Kamoun, W. S.; Ancukiewicz, M.; Nezivar, J.; Santosuosso, M.; Martin, J. D.; Martin, M. R.; Vianello, F.; Leblanc, P.; Munn, L. L.; Huang, P.; Duda, D. G.; Fukumura, D.; Jain, R. K.; Pozansky, M. C. *Proc. Natl. Acad. Sci. U. S. A.* **2012**, *109*, 17561−17566.
(23) Xu, C.; Zipfel, W.; Shear, J. B.; Williams, R. M.; Webb, W. W. *Proc. Natl. Acad. Sci. U. S. A.* **1996**, *93*, 10763−10768.
(24) Jain, R. K.; Booth, M. F.; Padera, T. P.; Munn, L. L.; Fukumura, D.; Brown, E. Applications of Nonlinear Intravital Microscopy in Tumor Biology. In *Handbook of Biomedical Nonlinear Optical Microscopy*; Masters, B. R., So, P. T. C., Eds.; Oxford University Press: New York, 2008; pp 735−756.
(25) Zipfel, W. R.; Williams, R. M.; Webb, W. W. *Nat. Biotechnol.* **2003**, *21*, 1369−1377.
(26) Helmchen, F.; Denk, W. *Nat. Methods* **2005**, *2*, 932−940.
(27) Lemon, C. M.; Curtin, P. N.; Somers, R. C.; Greytak, A. B.; Lanning, R. M.; Jain, R. K.; Bawendi, M. G.; Nocera, D. G. *Inorg. Chem.* **2014**, *53*, 1900−1915.
(28) Clapp, A. R.; Pons, T.; Medintz, I. L.; Delehanty, J. B.; Melinger, J. S.; Tiefenbrunn, T.; Dawson, P. E.; Fisher, B. R.; O'Rourke, B.; Mattoussi, H. *Adv. Mater.* **2007**, *19*, 1921−1926.
(29) Fowley, C.; Nomikou, N.; McHale, A. P.; McCarron, P. A.; McCaughan, B.; Callan, J. F. *J. Mater. Chem.* **2012**, *22*, 6456−6462.
(30) Liu, L.; Li, H.; Qiu, T.; Zhou, G.; Wong, K. Y.; He, Z.; Liu, Z. *Chem. Commun.* **2011**, *47*, 2622−2624.
(31) Finikova, O. S.; Lebedev, A. Y.; Aprelev, A.; Troxler, T.; Gao, F.; Garnacho, C.; Muri, S.; Hochstrasser, R. M.; Vinogradov, S. A. *ChemPhysChem* **2008**, *9*, 1673−1679.
(32) Sakadžić, S.; Roussakis, E.; Yaseen, M. A.; Mandeville, E. T.; Srinivasan, V. J.; Arai, K.; Ruvinskaya, S.; Devor, A.; Lo, E. H.; Vinogradov, S. A.; Boas, D. A. *Nat. Methods* **2010**, *7*, 755−759.
(33) Lecoq, J.; Parpaleix, A.; Roussakis, E. M.; Ducros, M.; Houssen, Y. G.; Vinogradov, S. A.; Charpak, S. *Nat. Med.* **2011**, *17*, 893−898.
(34) Snee, P. T.; Somers, R. C.; Nair, G.; Zimmer, J. P.; Bawendi, M. G.; Nocera, D. G. *J. Am. Chem. Soc.* **2006**, *128*, 13320−13321.
(35) Somers, R. C.; Lanning, R. M.; Snee, P. T.; Greytak, A. B.; Jain, R. K.; Bawendi, M. G.; Nocera, D. G. *Chem. Sci.* **2012**, *3*, 2980−2985.
(36) Kay, E. R.; Lee, J.; Nocera, D. G.; Bawendi, M. G. *Angew. Chem., Int. Ed.* **2013**, *52*, 1165−1169.
(37) McLaurin, E. J.; Greytak, A. B.; Bawendi, M. G.; Nocera, D. G. *J. Am. Chem. Soc.* **2009**, *131*, 12994−13001.
(38) Lemon, C. M.; Karnas, E.; Bawendi, M. G.; Nocera, D. G. *Inorg. Chem.* **2013**, *52*, 10394−10406.

DOI: 10.1021/jacs.5b04765
J. Am. Chem. Soc. 2015, 137, 9832−9842

(39) Dubertret, B.; Skourides, P.; Norris, D. J.; Noireaux, V.; Brivanlou, A. H.; Libchaber, A. *Science* **2002**, *298*, 1759−1762.
(40) Fan, H.; Leve, E. W.; Scullin, C.; Gabaldon, J.; Tallant, D.; Bunge, S.; Boyle, T.; Wilson, M. C.; Brinker, C. J. *Nano Lett.* **2005**, *5*, 645−648.
(41) Carion, O.; Mahler, B.; Pons, T.; Dubertret, B. *Nat. Protoc.* **2007**, *2*, 2383−2390.
(42) Lee, Y. K.; Hong, S. M.; Kim, J. S.; Im, J. H.; Min, H. S.; Subramanyam, E.; Huh, K. M.; Park, S. W. *Macromol. Res.* **2007**, *15*, 330−336.
(43) Ducongé, F.; Pons, T.; Pestourie, C.; Hérin, L.; Thézé, B.; Gombert, K.; Mahler, B.; Hinnen, F.; Kühnast, B.; Dollé, F.; Dubertret, B.; Tavitian, B. *Bioconjugate Chem.* **2008**, *19*, 1921−1926.
(44) Cormode, D. P.; Skajaa, T.; an Schooneveld, M. M.; Koole, R.; Jarzyna, P.; Lobatto, M. E.; Calcagno, C.; Barazza, A.; Gordon, R. E.; Zanzonico, P.; Fisher, E. A.; Fayad, Z. A.; Mulder, W. J. M. *Nano Lett.* **2008**, *8*, 3715−3723.
(45) Papagiannaros, A.; Levchenko, T.; Hartner, W.; Mongayt, D.; Torchilin, V. *Nanomedicine* **2009**, *5*, 216−224.
(46) Yong, K. T.; Roy, I.; Law, W. C.; Hu, R. *Chem. Commun.* **2010**, *46*, 7136−7138.
(47) Liu, J.; Yang, X.; Wang, K.; He, Y.; Zhang, P.; Ji, H.; Jian, L.; Liu, W. *Langmuir* **2012**, *28*, 10602−10609.
(48) Mai, Y.; Eisenberg, A. *Acc. Chem. Res.* **2012**, *45*, 1657−1666.
(49) Khatun, Z.; Nurunnabi, M.; Cho, K. J.; Lee, Y. *ACS Appl. Mater. Interfaces* **2012**, *4*, 3880−3887.
(50) Liu, L.; Hu, R.; Law, W. C.; Roy, I.; Zhu, J.; Ye, L.; Hu, S.; Zhang, X.; Yong, K. Y. *Analyst* **2013**, *138*, 6144−6153.
(51) Aimé, A.; Beztsinna, N.; Patwa, A.; Pokolenko, A.; Bestel, I.; Barthélémy, P. *Bioconjugate Chem.* **2013**, *24*, 1345−1355.
(52) Ostermann, J.; Merkl, J. P.; Flessau, S.; Wolter, C.; Kornowski, A.; Schmidtke, C.; Pietsch, A.; Kloust, H.; Feld, A.; Weller, H. *ACS Nano* **2013**, *7*, 9156−9167.
(53) Wang, S.; Han, M. Y.; Huang, D. *J. Am. Chem. Soc.* **2009**, *131*, 11692−11694.
(54) Adler, A. D.; Longo, F. R.; Shergalis, W. *J. Am. Chem. Soc.* **1964**, *86*, 3145−3149.
(55) Adler, A. D.; Longo, F. R.; Finarelli, J. D.; Goldmacher, J.; Assour, J.; Korsakoff, L. *J. Org. Chem.* **1967**, *32*, 476.
(56) Leatherdale, C. A.; Woo, W. K.; Mikulec, F. V.; Bawendi, M. G. *J. Phys. Chem. B* **2002**, *106*, 7619−7622.
(57) Fulmer, G. R.; Miller, A. J. M.; Sherden, N. H.; Gottlieb, H. E.; Nudelman, A.; Stoltz, B. M.; Bercaw, J. E.; Goldberg, K. I. *Organometallics* **2010**, *29*, 2176−2179.
(58) Suzuki, K.; Kobayashi, A.; Kaneko, S.; Takehira, K.; Yoshihara, T.; Ishida, H.; Shiina, Y.; Oishi, S.; Tobita, S. *Phys. Chem. Chem. Phys.* **2009**, *11*, 9850−9860.
(59) Grabolle, M.; Spieles, M.; Lesnyak, V.; Gaponik, N.; Eychmüller, A.; Resch-Genger, U. *Anal. Chem.* **2009**, *81*, 6285−6294.
(60) Battino, R.; Rettich, T. R.; Tominaga, T. *J. Phys. Chem. Ref. Data* **1983**, *12*, 163−178.
(61) A full-text version of ref 60 is provided on the NIST website: http://www.nist.gov/data/PDFfiles/jpcrd219.pdf.
(62) *CRC Handbook of Chemistry and Physics*, 84th ed.; CRC Press: Boca Raton, FL, 2003.
(63) Dulbecco, R.; Vogt, M. *J. Exp. Med.* **1954**, *99*, 167−182.
(64) Saltzman, H. A.; Brown, I. W. *Annu. Rev. Med.* **1965**, *16*, 253−262.
(65) Pizano, A. A.; Lutterman, D. A.; Holder, P. G.; Teets, T. S.; Stubbe, J.; Nocera, D. G. *Proc. Natl. Acad. Sci. U. S. A.* **2012**, *109*, 39−43.
(66) Holder, P. G.; Pizano, A. A.; Anderson, B. L.; Stubbe, J.; Nocera, D. G. *J. Am. Chem. Soc.* **2012**, *134*, 1172−1180.
(67) Loh, Z. H.; Miller, S. E.; Chang, C. J.; Carpenter, S. D.; Nocera, D. G. *J. Phys. Chem. A* **2002**, *106*, 11700−11708.
(68) Brown, E. B.; Campbell, R. B.; Tsuzuki, Y.; Xu, L.; Carmeliet, P.; Fukumura, D.; Jain, R. K. *Nat. Med.* **2001**, *7*, 864−868.
(69) Lanning, R. M. Ph.D. Thesis, Massachusetts Institute of Technology, Cambridge, MA, 2009.
(70) Leunig, M.; Yuan, F.; Menger, M. D.; Boucher, Y.; Goetz, A. E.; Messmer, K.; Jain, R. K. *Cancer Res.* **1992**, *52*, 6553−6560.
(71) Yuan, F.; Salehi, H. A.; Boucher, Y.; Vasthare, U. S.; Tuma, R. F.; Jain, R. K. *Cancer Res.* **1994**, *54*, 4564−4568.
(72) Förster, T. *Ann. Phys.* **1948**, *437*, 55−75.
(73) Lakowicz, J. R. *Principles of Fluorescence Spectroscopy*, 3rd ed.; Springer: New York, 2006.
(74) Steinberg, I. Z. *Annu. Rev. Biochem.* **1971**, *40*, 83−114.
(75) Chen, F. C.; Chen, S. J. *Opt. Lett.* **2006**, *31*, 187−189.
(76) Liu, W.; Howarth, M.; Greytak, A. B.; Zheng, Y.; Nocera, D. G.; Ting, A. Y.; Bawendi, M. G. *J. Am. Chem. Soc.* **2008**, *130*, 1274−1284.
(77) Liu, W.; Greytak, A. B.; Lee, M.; Wong, C. R.; Park, J.; Marshall, L. F.; Jiang, W.; Curtin, P. N.; Ting, A. Y.; Nocera, D. G.; Fukumura, D.; Jain, R. K.; Bawendi, M. G. *J. Am. Chem. Soc.* **2010**, *132*, 472−483.
(78) Eastwood, D.; Gouterman, M. *J. Mol. Spectrosc.* **1970**, *35*, 359−375.
(79) Callis, J. B.; Gouterman, M.; Jones, Y. M.; Henderson, B. H. *J. Mol. Spectrosc.* **1971**, *39*, 410−420.
(80) Blanton, S. A.; Dehestani, A.; Lin, P. C.; Guyot-Sionnest, P. *Chem. Phys. Lett.* **1994**, *229*, 317−322.
(81) Larson, D. R.; Zipfel, W. R.; Williams, R. M.; Clark, S. W.; Bruchez, M. P.; Wise, F. W.; Webb, W. W. *Science* **2003**, *300*, 1434−1436.
(82) Pu, S. C.; Yang, M. J.; Hsu, C. C.; Lai, C. W.; Hsieh, C. C.; Lin, S. H.; Cheng, Y. M.; Chou, P. T. *Small* **2006**, *2*, 1308−1313.
(83) Javier, A.; Magana, D.; Jennings, T.; Strouse, G. F. *Appl. Phys. Lett.* **2003**, *83*, 1423−1425.
(84) Bonin, K. D.; McIlrath, T. J. *J. Opt. Soc. Am. B* **1984**, *1*, 52−55.
(85) Horwitz, J. S.; Kohler, B. E.; Spiglanin, T. A. *J. Chem. Phys.* **1985**, *83*, 2186−2190.
(86) Petek, H.; Bell, A. J.; Choi, Y. S.; Yoshihara, K.; Tounge, B. A.; Christensen, R. L. *J. Chem. Phys.* **1995**, *102*, 4726−4739.
(87) Gouterman, M. In *The Porphyrins*; Dolphin, D., Ed.; Academic Press: New York, 1978; Vol 3, pp 1−163.
(88) Losev, A. P.; Aghion, J. *J. Photochem. Photobiol., B* **1990**, *7*, 181−187.
(89) Collier, B. B.; Singh, S.; McShane, M. *Analyst* **2011**, *136*, 962−967.
(90) Sinaasappel, M.; Ince, C. *J. Appl. Physiol.* **1996**, *81*, 2297−2303.
(91) Samia, A. C. S.; Chen, X.; Burda, C. *J. Am. Chem. Soc.* **2003**, *125*, 15736−15737.
(92) Tsay, J. M.; Trzoss, M.; Shi, L.; Kong, X.; Selke, M.; Jung, M. E.; Weiss, S. *J. Am. Chem. Soc.* **2007**, *129*, 6865−6871.
(93) Fowley, C.; Nomikou, N.; McHale, A. P.; McCarron, P. A.; McCaughan, B.; Callan, J. F. *J. Mater. Chem.* **2012**, *22*, 6456−6462.
(94) Wilkinson, F.; Helman, W. P.; Ross, A. B. *J. Phys. Chem. Ref. Data* **1993**, *22*, 113−262.
(95) Nowakowska, M. *J. Chem. Soc., Faraday Trans. 1* **1984**, *80*, 2119−2126.
(96) Merkel, P. B.; Kearns, D. R. *J. Am. Chem. Soc.* **1972**, *94*, 1029−1030.
(97) Turro, N. J. *Modern Molecular Photochemistry*; University Science Books: Sausalito, CA, 1991.
(98) Beaurepaire, E.; Mertz, J. *Appl. Opt.* **2002**, *41*, 5376−5382.
(99) Bashkatov, A. N.; Genina, E. A.; Kochubey, V. I.; Tuchin, V. V. *J. Phys. D: Appl. Phys.* **2005**, *38*, 2543−2555.
(100) Jacques, S. L. *Phys. Med. Biol.* **2013**, *58*, R37−R61.
(101) Filho, I. P. T.; Kerger, H.; Intaglietta, M. *Microvasc. Res.* **1996**, *51*, 202−212.
(102) Tsai, A. G.; Johnson, P. C.; Intaglietta, M. *Physiol. Rev.* **2003**, *83*, 933−963.
(103) Intaglietta, M.; Johnson, P. C.; Winslow, R. M. *Cardiovasc. Res.* **1996**, *32*, 632−643.

DOI: 10.1021/jacs.5b04765
J. Am. Chem. Soc. 2015, 137, 9832−9842

THE JOURNAL OF PHYSICAL CHEMISTRY B

Article

pubs.acs.org/JPCB

Ultrafast Photoinduced Electron Transfer from Peroxide Dianion

Bryce L. Anderson,[†,§] Andrew G. Maher,[†,‡,§] Matthew Nava,[‡] Nazario Lopez,[‡] Christopher C. Cummins,*[,‡] and Daniel G. Nocera*[,†]

[†]Department of Chemistry and Chemical Biology, Harvard University, 12 Oxford Street, Cambridge, Massachusetts 02138-2902, United States

[‡]Department of Chemistry, Massachusetts Institute of Technology, 77 Massachusetts Avenue, Cambridge, Massachusetts 02139-4307, United States

Supporting Information

ABSTRACT: The encapsulation of peroxide dianion by hexacarboxamide cryptand provides a platform for the study of electron transfer of isolated peroxide anion. Photoinitiated electron transfer (ET) between freely diffusing $Ru(bpy)_3^{2+}$ and the peroxide dianion occurs with a rate constant of 2.0×10^{10} M^{-1} s^{-1}. A competing electron transfer quenching pathway is observed within an ion pair. Picosecond transient spectroscopy furnishes a rate constant of 1.1×10^{10} s^{-1} for this first-order process. A driving force dependence for the ET rate within the ion pair using a series of $Ru(bpy)_3^{2+}$ derivatives allows for the electronic coupling and reorganization energies to be assessed. The ET reaction is nonadiabatic and dominated by a large inner-sphere reorganization energy, in accordance with that expected for the change in bond distance accompanying the conversion of peroxide dianion to superoxide anion.

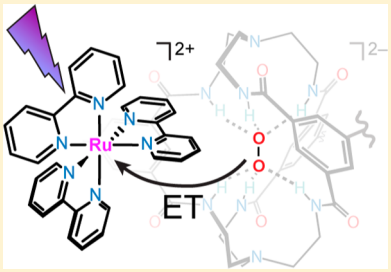

INTRODUCTION

The redox chemistry of peroxide (O_2^{2-}) anion is fundamental to aerobic life processes,[1] valuable industrial feedstock conversions,[2] and energy storage as pertaining to rechargeable metal−air batteries.[3,4] Whereas the superoxide (O_2/O_2^-) redox couple has been studied extensively,[5−8] the electron transfer (ET) properties of the peroxide dianion as an isolated species have remained largely undefined because the dianion is not readily available as a solvent soluble entity. Typically, peroxide is stable in the form of hydrogen peroxide or when it is bound to a metal ion. The availability of isolated peroxide anion is unusual having been only identified as an inclusion complex within a layered complex salt of maltose[9] and within the extensive hydrogen bonding network of a channel leading to the metal active site of class Ib ribonucleotide reductase.[10] The isolation of a soluble peroxide dianion has only recently been accomplished by its encapsulation within the cleft of a hydrogen-bond-donating hexacarboxamide cryptand ligand (*m*BDCA-5t-H_6).[11] This occlusion compound permits, for the first time, detailed electrochemical, chemical, and photochemical studies of the oxidation−reduction properties of peroxide dianion to be undertaken, unencumbered by the presence of protons or metal ions.

Knowledge of the ET behavior of discrete O_2^{2-} is useful not only for the design of metal−air batteries capable of recharging at lower overpotentials but also for the informed use of cryptand-encapsulated O_2^{2-} as an oxidant and/or atom transfer reagent in chemical transformations. To date, we have examined the ET kinetics of the peroxide dianion by the stopped-flow technique, which is limited to millisecond response times of diffusion controlled bimolecular reactions with chemical oxidants.[12] We now report the ET kinetics of peroxide ion, free of diffusion, by employing picosecond time-resolved spectroscopy to probe photoinitiated ET within an ion-paired complex shown in Chart 1. By varying the driving force of the Ru(II) polypyridyl photosensitizer, a Marcus analysis of the first-order ET rate constant establishes electronic coupling in the nonadiabatic regime, and a charge transfer reaction that is dominated by an inner sphere reorganization energy accompanying the change in bond length upon oxidation of peroxide to superoxide ion, consistent with the

Chart 1

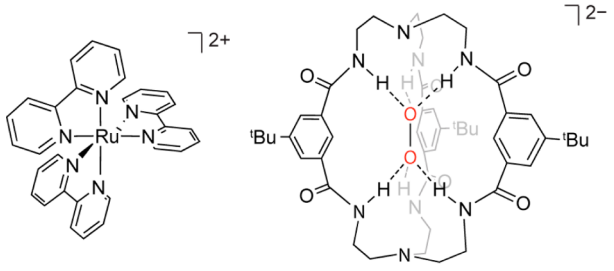

$Ru(bpy)_3^{2+}$ $[(O_2)\subset mBDCA\text{-}5t\text{-}H_6]^{2-}$

Special Issue: John R. Miller and Marshall D. Newton Festschrift

Received: November 4, 2014
Revised: January 29, 2015
Published: January 30, 2015

DOI: 10.1021/jp5110505
J. Phys. Chem. B 2015, 119, 7422−7429

results of a DFT treatment of the energetics of the peroxide and superoxide anions.

EXPERIMENTAL SECTION

General Methods. All reagents, unless otherwise indicated, were purchased from Aldrich. Solvents were purified on a Glass Contour Solvent Purification System manufactured by SG Water USA, LLC. NMR solvents were obtained from Cambridge Isotope Laboratories. ^{1}H NMR spectra were obtained at the MIT Department of Chemistry Instrumentation Facility on a Bruker 400 MHz spectrometer. Elemental analysis was performed by Robertson Microlit Labratories. Microwave-assisted synthesis was accomplished using a CEM Discover microwave reactor. UV−vis spectra were recorded on a Varian Cary 5000 UV−vis−NIR spectrophotometer. Steady-state emission spectra were obtained on a PTI QM 4 Fluorometer, with a 150 W Xe arc lamp for excitation and a Hamamatsu R928 photomultiplier tube for detection. All samples for the room temperature optical spectroscopy experiments were prepared using DMF stored over activated 3 Å molecular sieves in a N_2-atmosphere glovebox. Samples were prepared in 1.0 cm path length quartz cuvettes (Starna, Inc.) with Teflon screw-caps for room temperature emission spectroscopy; 1.0 mm path length quartz cuvettes (Starna, Inc.) for UV vis spectroscopy; custom 2.0 mm path length high-vacuum cells for nanosecond and picosecond transient absorption (TA) spectroscopy; and quartz EPR tubes, which were brought to 77 K using liquid nitrogen for low temperature emission spectroscopy. Electrochemical measurements were made in a N_2-atmosphere glovebox using a CH Instruments 760D Electrochemical Workstation using CHI Version 10.03 software. Thin-layer UV−vis spectroelectrochemistry experiments were performed using a 0.5 mm path length quartz cell with an Ocean Optics USB4000 spectrophotometer and a DT-Mini-2GS UV−vis−NIR light source in conjunction with the CH electrochemical workstation.

Synthesis of $[Ru(dmbpy)_3][PF_6]_2$. The previously reported synthesis[13] of $Ru(dmbpy)_3^{2+}$ was modified by isolating the PF_6^- salt. $RuCl_3{\cdot}xH_2O$ (88 mg) and 4,4′-dimethyl-2,2′-bipyridine (324 mg) were loaded into a 100 mL round-bottom flask along with 11.4 mL of deionized H_2O. To the flask was added 3 mL of 0.1 M HCl, and the mixture was brought to reflux. After 90 min, 1.7 mL of 30% neutralized hypophosphoric acid was added to the flask. The mixture continued to reflux for 1 h, at which point it was allowed to cool. After filtration, the solution was concentrated and excess sodium hexafluorophosphate was added, resulting in the formation of an orange precipitate. The precipitate was collected by vacuum filtration and washed ×3 with THF. The solid was dried at 80 °C under a vacuum overnight. The ^{1}H NMR spectrum of the product was consistent with literature reports of the compound.[14]

Synthesis of $[Ru(bpy)_2(dmbpy)]Cl_2$. The previously reported synthesis[15] of $Ru(bpy)_2(dmbpy)^{2+}$ was adapted for the microwave technique. $Ru(bpy)_2Cl_2$ (104 mg) and 4,4′-dimethyl-2,2′-bipyridine (278 mg) were dissolved in 15 mL of ethanol contained within a 35 mL microwave reactor tube. The reaction mixture was subjected to microwave irradiation for 1.75 h at a reaction condition of 120 °C. Upon completion of the reaction, the solution was filtered while still warm and the filtrate was brought to dryness. H_2O (40 mL) was added to the remaining solid, and the solution was washed ×4 with $CHCl_3$. The aqueous fraction was again brought to dryness to furnish the product. The product was dried at 80 °C under a vacuum overnight. The ^{1}H NMR spectrum of the product was consistent with literature reports of the compound.[14]

Synthesis of $[Ru(bpy)_2(dOMebpy)]Cl_2$. The title compound was prepared as described above for $[Ru(bpy)_2(dmbpy)]Cl_2$, but a stoichiometric amount of 4,4′-dimethoxy-2,2′-bipyridine was used rather than an excess.

Preparation of Ru-bpy|Peroxide Salt. $[K_2(DMF)_5][(O_2)\subset m\text{BDCA-5t-H}_6]$ (1 equiv), which was prepared by previously published procedures,[12] and the corresponding ruthenium(II) bipyridyl chloride or hexafluorophosphate salt (1 equiv) were placed as solids into a 20 mL scintillation vial equipped with a Teflon stir bar. The solids were dissolved in DMF (2 mL). This dark red solution was allowed to stir at room temperature for ∼5 min, after which it was passed through a 200 nm Teflon membrane syringe filter to remove KCl. To the filtrate, diethyl ether (15 mL) was added to induce precipitation of solids. The resulting slurry was allowed to stir at room temperature for 10 min to ensure complete precipitation of the product. The resulting dark red solid was collected on a medium sintered glass frit, washed with diethyl ether (3 × 5 mL), and dried under a dynamic vacuum for 3 h. The ^{1}H NMR spectrum indicates a 1:1 integration of the Ru complex cation to peroxide adduct dianion.

$[Ru(bpy)_3][(O_2)\subset m\text{BDCA-5t-H}_6]$. $[K_2(DMF)_5][(O_2)\subset m\text{BDCA-5t-H}_6]$ (260 mg, 0.196 mmol) and $[Ru(bpy)_3]Cl_2$ (126 mg, 0.196 mmol) were employed in the aforementioned procedure to furnish 270 mg (95%) of product. ^{1}H NMR (400 MHz, DMSO-d_6, δ): $[(O_2)\subset m\text{BDCA-5t-H}_6]^{2-}$: 14.62 (s, 6 H), 10.14 (s, 3 H), 8.13 (s, 6 H), 3.37 (br, 6 H), 2.59 (br d, 6 H), 2.34 (br d, 12 H), 1.29 (s, 27 H). $Ru(bpy)_3^{2+}$: 8.76 (d, 6 H), 8.06 (t, 6 H), 7.71 (d, 6 H), 7.50 (t, 6 H). ^{13}C NMR (100 MHz, DMSO-d_6, δ): $[(O_2)\subset m\text{BDCA-5t-H}_6]^{2-}$: 165.58, 148.99, 135.00, 126.74, 124.21, 59.93, 40.83, 34.38, 31.16. $[Ru(bpy)_3]^{2+}$: 156.44, 151.17, 137.81, 127.83, 124.37. Anal. Calcd (Found) for $[Ru(bpy)_3][(O_2))\subset m\text{BDCA-5t-H}_6]\cdot 6\text{DMF}$, $C_{96}H_{136}N_{20}O_{14}Ru_1$: C, 60.97 (60.44); H, 7.03 (7.01); N, 14.81 (14.44).

$[Ru(bpy)_2(dmbpy)][(O_2)\subset m\text{BDCA-5t-H}_6]$. $[K_2(DMF)_5][(O_2)\subset m\text{BDCA-5t-H}_6]$ (164 mg, 0.124 mmol) and $[Ru(bpy)_2(dmbpy)]Cl_2$ (85 mg, 0.127 mmol) were employed in the aforementioned procedure to furnish 162 mg (89%) of product. ^{1}H NMR (400 MHz, DMSO-d_6, δ): $[(O_2)\subset m\text{BDCA-5t-H}_6]^{2-}$: 14.59 (s, 6 H), 10.10 (s, 3 H), 8.14 (s, 6 H), 3.37 (br, 6 H), 2.59 (br d, 6 H), 2.33 (br d, 12 H), 1.30 (s, 27 H). $[Ru(bpy)_2(dmbpy)]^{2+}$: 8.80 (d, 4 H), 8.71 (s, 2 H), 8.10 (t, 4 H), 7.73 (t, 4 H), 7.53 (q, 6 H), 7.36 (d, 2H), 2.52 (s, 6H).

$[Ru(bpy)_2(dOMebpy)][(O_2)\subset m\text{BDCA-5t-H}_6]$. $[K_2(DMF)_5][(O_2)\subset m\text{BDCA-5t-H}_6]$ (112 mg, 0.084 mmol) and $[Ru(bpy)_2(dOMebpy)]Cl_2$ (60.6 mg, 0.086 mmol) were employed in the aforementioned procedure to furnish 110 mg (86%) of product. ^{1}H NMR (400 MHz, DMSO-d_6, δ): $[(O_2)\subset m\text{BDCA-5t-H}_6]^{2-}$: 14.59 (s, 6 H), 10.10 (s, 3 H), 8.15 (s, 6 H), 3.37 (br, 6 H), 2.59 (br d, 6 H), 2.33 (br d, 12 H), 1.30 (s, 27 H). $Ru(bpy)_2(dmbpy)^{2+}$: 8.78 (d, 4 H), 8.48 (s, 2 H), 8.10 (q, 4 H), 7.82 (d, 2 H), 7.72 (d, 2 H), 7.51 (m, 4H), 7.41 (d, 2H), 7.15 (d, 2H), 3.98 (s, 6H).

$[Ru(dmbpy)_3][(O_2)\subset m\text{BDCA-5t-H}_6]$. $[K_2(DMF)_5][(O_2)\subset m\text{BDCA-5t-H}_6]$ (111 mg, 0.084 mmol) and $[Ru(dmbpy)_3]PF_6$ (79 mg, 0.084 mmol) were employed in the aforementioned procedure to furnish 123 mg (95%) of product. ^{1}H NMR (400 MHz, DMSO-d_6, δ): $[(O_2)\subset m\text{BDCA-5t-H}_6]^{2-}$: 14.60 (s, 6 H), 10.09 (s, 3 H), 8.14 (s, 6 H), 3.37 (br, 6 H), 2.59 (br d, 6 H), 2.31 (br d, 12 H), 1.29 (s, 27 H).

DOI: 10.1021/jp5110505
J. Phys. Chem. B 2015, 119, 7422−7429

$[Ru(dmbpy)_3]^{2+}$: 8.68 (s, 6 H), 7.49 (d, 6 H), 7.32 (d, 6 H), 2.49 (s, 18 H).

Crystallography. Structural data were collected as a series of φ scans using 0.41328 Å radiation at a temperature of 15 K (Oxford Diffraction Helijet) on a vertical mounted Bruker D8 three-circle platform goniometer equipped with an Apex II CCD at ChemMatCARS located at Advances Photon Source (APS), Argonne National Laboratory (ANL). Crystals were mounted on a glass fiber using Paratone N oil. Data were integrated using SAINT[16] and scaled with a multiscan absorption correction using SADABS. The structures were solved by direct methods using SHELXS-97 and refined against F^2 on all data by full matrix least-squares with SHELXL-97.[17] All non-hydrogen atoms were refined anisotropically. Hydrogen atoms were placed at idealized positions and refined using a riding model.

Spectroscopic Experiments. Nanosecond and picosecond TA experiments were performed using previously reported home-built Nd:YAG[18] and Ti:sapphire[19] laser systems, respectively. Full details of the TA experiments are provided in the Supporting Information.

For the steady-state emission quenching experiments, samples were excited with 400 nm light. Each sample comprised 0.1 mM $[Ru(bpy)_3]Cl_2$ and a different concentration of $[K(18\text{-crown-}6)]_2[(O_2)\subset m\text{BDCA-5t-H}_6]$ ranging from 0.0 to 0.7 mM. The emission spectrum of $[Ru(bpy)_3]Cl_2$ was recorded and integrated three times, and the average integrated emission intensity was used for Stern−Volmer analysis.

For the time-resolved emission quenching experiments, the excitation source was the same Ti:sapphire laser system used for TA experiments. Emission data was collected using a Hamamatsu C4334 Streak Scope camera that has been described previously.[20] The laser excitation source was tuned to 400 nm, and the power was attenuated to 2.5 mW using a neutral density filter in front of the sample. A 1 or 5 μs time window was used, and 5000 exposures were captured for each sample. The same samples were used for both the steady-state and time-resolved emission quenching experiments. The emission decay traces were fit with monoexponential functions to afford the lifetime of excited $[Ru(bpy)_3]Cl_2$ in each sample. The lifetimes were then used for Stern−Volmer analysis.

Computational Methods. Density functional theory (DFT) calculations were performed using ORCA version 3.0.[21] Structure optimizations were performed using the BP[22] functional and polarized Ahlrichs TZV basis sets (H, TZV(p); main-group, TZV(2d)).[23,24] Single point energies were computed using the B3LYP hybrid functional and foregoing basis sets as implemented in ORCA 3.0.[25−27]

RESULTS AND DISCUSSION

Tris(bipyridyl) ruthenium(II) complex, $Ru(bpy)_3^{2+}$, and its derivatives were chosen as photo-oxidants due to their complementary charge with the $[(O_2)\subset m\text{BDCA-5t-H}_6]^{2-}$ anion and their tunable ^{3}MLCT excited state reduction potentials. Salts of each Ru(II) polypyridyl complex with the $[(O_2)\subset m\text{BDCA-5t-H}_6]^{2-}$ anion were obtained in high yield by treatment of $[K_2(DMF)_5][(O_2)\subset m\text{BDCA-5t-H}_6]$ with 1 equiv of the chloride or hexafluorophosphate salt of the Ru(II) complex in DMF. The salt metathesis reaction proceeded as indicated by a 1:1 [Ru complex]:[O_2-adduct] ratio of the respective ^{1}H NMR signals (Figures S1−S4, Supporting Information). $[Ru(bpy)_3][(O_2)\subset m\text{BDCA-5t-H}_6]$ was obtained in crystalline form by diffusion of Et_2O into a DMF solution of the salt. The solid state structure shown in Figure 1

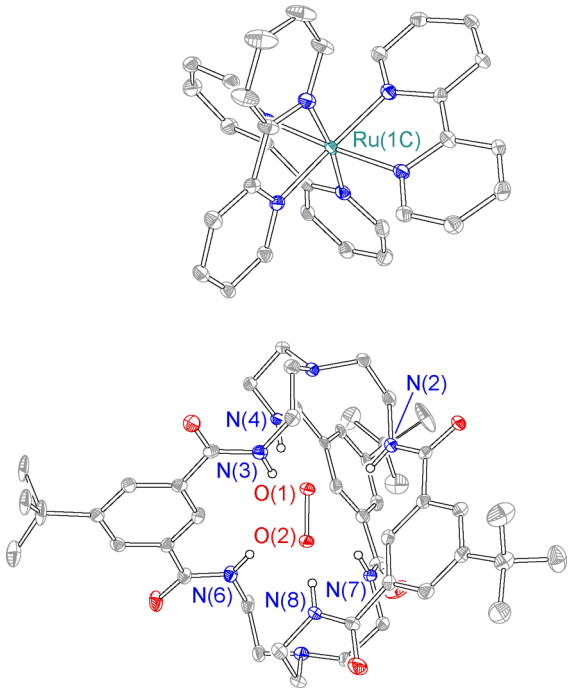

Figure 1. Thermal ellipsoid plot of $[Ru(bpy)_3][(O_2)\subset m\text{BDCA-5t-H}_6]$ drawn at the 50% probability level. Solvents of crystallization and H atoms not participating in hydrogen bonds are omitted for clarity. C, gray; N, blue; O, red; Ru, teal. The ions shown in the plot are in the same asymmetric unit cell. The center-to-center distance between the Ru metal and peroxide is 16.005 Å. A $Ru(bpy)_3^{2+}$ ion in a neighboring unit cell is at a closer distance to the $[(O_2)\subset m\text{BDCA-5t-H}_6]^{2-}$ ion than that pictured. The center-to-center distance between this Ru metal and peroxide is 8.47 Å.

corroborates 1:1 complex formation. The $O-O_{peroxide}$ bond length (1.497 Å) is in the range of the bond length observed for peroxide bound to metal centers.[28] The distance between the Ru center of the metal complex and the center of the peroxide moiety is 8.47(1) Å.

Nanosecond TA of $[Ru(bpy)_3][(O_2)\subset m\text{BDCA-5t-H}_6]$ in DMF under a nitrogen atmosphere demonstrates the growth of an absorption feature at 505 nm (Figure S5, Supporting Information) that is indicative of the $Ru(bpy)_3^+$ reduction product according to the difference spectrum obtained from thin layer spectroelectrochemistry (Figure S6, Supporting Information); the maximum in the TA spectrum is also consistent with the electronic absorption spectrum reported for prepared samples of $Ru(bpy)_3^+$.[29−31] TA spectra of $[Ru(bpy)_3]Cl_2$ and free mBDCA-5t-H_6 ligand (no encapsulated peroxide) showed a negligible signal at 505 nm (Figure S7, Supporting Information), indicating that the production of $Ru(bpy)_3^+$ is due to the presence of the peroxide dianion as the predominant electron donor. The single wavelength kinetics for the formation of $Ru(bpy)_3^+$ was measured with increasing concentration of $[Ru(bpy)_3][(O_2)\subset m\text{BDCA-5t-H}_6]$ (Figure S8, Supporting Information). With increasing concentration of the $[Ru(bpy)_3][(O_2)\subset m\text{BDCA-5t-H}_6]$, the intensity of the TA signal and rate of formation of $Ru(bpy)_3^+$ increase. Monoexponential fits of the growth curves in Figure S8 (Supporting Information) yield the pseudo-first-order rate constants plotted

DOI: 10.1021/jp5110505
J. Phys. Chem. B 2015, 119, 7422−7429

in Figure S9 (Supporting Information), the slope of which furnishes a second-order rate constant of 2.0×10^{10} M^{-1} s^{-1}, which is consistent with diffusion-limited kinetics. On the microsecond time scale, the $Ru(bpy)_3^+$ feature observed at 505 nm decays toward the baseline with nonexponential kinetics (Figure S10, Supporting Information). The loss of $Ru(bpy)_3^+$ can be attributed to the bimolecular back electron transfer with the superoxide adduct, $[(O_2)\subset m\text{BDCA-5t-H}_6]^-$, as well as reacting with any O_2, which may be formed by disproportionation of $[(O_2)\subset m\text{BDCA-5t-H}_6]^-$.[12] Due to the complexity of the mechanism, interpretation of the kinetics of the back reaction will require more detailed studies.

Steady-state and time-resolved photoluminescence experiments are consistent with the TA rate constant measurement. The steady-state emission intensity and time-resolved lifetime quenching of $Ru(bpy)_3^{2+*}$ was examined as a function of the concentration of $[K(18\text{-crown-6})]_2[(O_2)\subset m\text{BDCA-5t-H}_6]$. A Stern–Volmer analysis (Figure S11, Supporting Information) of emission intensity and lifetime data yield diffusion-limited rate constants of 1.7×10^{10} and 1.2×10^{10} M^{-1} s^{-1}, respectively, in agreement with the nanosecond TA result. The TA and quenching experiments together establish that the peroxide dianion engages in a photoinduced, diffusion-controlled electron transfer with the Ru(II) polypyridyl excited state.

Picosecond TA of solutions of $[Ru(bpy)_3][(O_2)\subset m\text{BDCA-5t-H}_6]$ prepared at concentrations approaching 1 mM also revealed production of $Ru(bpy)_3^+$ but at time scales faster than diffusion. Figure 2a shows the temporal growth of the $Ru(bpy)_3^+$ signal over 400 ps. The wavelength maximum of the TA signal is 525 nm, which is 20 nm red-shifted from that observed in nanosecond TA experiments (Figure S5, Supporting Information). We attribute this red-shift to the superposition of the TA spectrum of $Ru(bpy)_3^+$ (Figure S6b, Supporting Information) with that of the $Ru(bpy)_3^{2+*}$ excited state. The $Ru(bpy)_3^{2+*}$ difference spectrum features a large bleach of the MLCT band centered at ~450 nm. This bleach tails into the region where the $Ru(bpy)_3^+$ signal at 505 nm is located, causing a red-shift in the wavelength maximum. This effect manifests itself in the picosecond TA, and not the nanosecond TA, because a vast majority of the excited $Ru(bpy)_3^{2+*}$ species do not participate in ET with the peroxide at this time scale (*vide infra*), leaving the large bleach intact. Conversely, on the nanosecond time scale, all of the $Ru(bpy)_3^{2+*}$ signal is depleted by either relaxation to the ground state or reaction with the peroxide dianion and hence the red-shift is not evident. In the absence of encapsulated peroxide, no $Ru(bpy)_3^+$ is formed, as established by the lack of a TA signal at 525 nm in the control experiments (black squares, $Ru(bpy)_3^{2+}$ alone; red circles, $Ru(bpy)_3^{2+}$, cryptand, no peroxide) in Figure 2b. Single-wavelength kinetics monitored at 525 nm exhibits monoexponential growth kinetics of $Ru(bpy)_3^+$ with a time constant of 90 ± 8 ps (blue triangles, Figure 2b), corresponding to a first-order rate constant of 1.1×10^{10} s^{-1}. Picosecond single wavelength kinetics experiments on samples containing different concentrations of $[Ru(bpy)_3][(O_2)\subset m\text{BDCA-5t-H}_6]$ show $Ru(bpy)_3^+$ signal intensities that are concentration-dependent but rates of growth that are concentration-independent (Figure S12, Supporting Information). This result is consistent with a unimolecular process.

The unimolecular rate constant is consistent with an ET reaction occurring within ion pairs formed between the oppositely charged $[Ru(bpy)_3]^{2+}$ and $[(O_2)\subset m\text{BDCA-5t-H}_6]^{2-}$ ions. In order to verify ion pairing, picosecond TA experiments were repeated in DMF solutions at the elevated ionic strength supplied by 0.1 M tetrabutylammonium hexafluorophosphate. Picosecond TA of these high ionic strength solutions of the complex showed no growth of a signal at 525 nm (Figure S13, Supporting Information), which is consistent with the disruption of the ion pair. Conversely, the $Ru(bpy)_3^+$ signal in the nanosecond TA experiments is preserved under high ionic strength conditions though suppressed (Figure S14, Supporting Information), consistent with an attenuated diffusion rate constant due to the kinetic salt effect.[32] The observation that ET is maintained on the nanosecond time scale under these conditions implies that the lack of signal in the picosecond TA is not due to deleterious reactivity between the electrolyte and the components of the $[Ru(bpy)_3][(O_2)\subset m\text{BDCA-5t-H}_6]$ salt but rather is a result of the increased ionic strength of the solution. With ion paring established, the yield of $Ru(bpy)_3^+$, as measured by the picosecond TA experiments, was used to estimate the ion-pair equilibrium constant K_{IP}. Values of 100 and 68 M^{-1} for samples containing 250 and 500 μM $[Ru(bpy)_3][(O_2)\subset m\text{BDCA-5t-H}_6]$, respectively, were estimated as detailed in the Supporting Information.

In principle, ion-pairing should be manifested in the Stern–Volmer analysis. For a system in which both dynamic and static

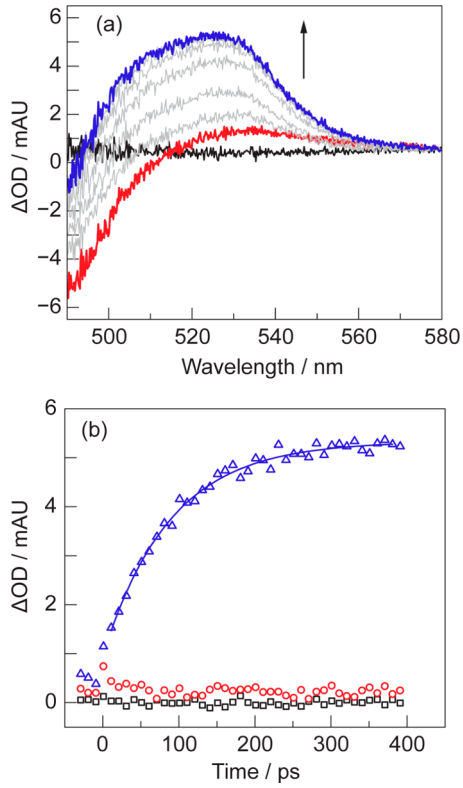

Figure 2. (a) Picosecond TA spectrum of a 0.76 mM solution of $[Ru(bpy)_3][(O_2)\subset m\text{BDCA-5t-H}_6]$. The growth of the $Ru(bpy)_3^+$ spectral feature at 525 nm is shown over the time window of 1 ps (red) to 400 ps (blue) (λ_{exc} = 325 nm). (b) Single wavelength kinetics monitored at 525 nm of 0.68 mM $[Ru(bpy)_3]Cl_2$ (black squares), 1.0 mM $[Ru(bpy)_3]Cl_2$ and 1.0 mM *m*BDCA-5t-H_6 (red circles), and 0.76 mM $[Ru(bpy)_3][(O_2)\subset m\text{BDCA-5t-H}_6]$ (blue triangles). The growth curve of $Ru(bpy)_3^+$ indicated by the blue triangles fits to a monoexponetial with a time constant of 90 ± 8 ps.

DOI: 10.1021/jp5110505
J. Phys. Chem. B 2015, 119, 7422–7429

quenching mechanisms operate, the steady-state emission intensity quenching may be expressed as follows:[33]

$$\frac{I_0}{I} = (1 + k_q\tau_0[Q])(1 + K_{IP}[Q]) \quad (1)$$

where I is the emission intensity, I_0 is the emission intensity in the absence of quencher Q, k_q is the dynamic quenching rate, τ_0 is the emission lifetime in the absence of quencher, and K_{IP} is the equilibrium constant for ion pair formation. K_{IP} under the emission quenching conditions may be estimated using Debye–Huckel theory, as shown in eq S9 in the Supporting Information. The quadratic nature of eq 1 implies a deviation from linearity of the Stern–Volmer plots when static quenching is present. However, under the conditions of our emission quenching experiments (Figure S11, Supporting Information), K_{IP} is estimated to be small (~60–90 M^{-1} depending on the ionic strength), consistent with the estimates of K_{IP} obtained from transient data. At the millimolar concentrations of $[(O_2)\subset m\text{BDCA-5t-H}_6]^{2-}$ used for quenching experiments, $K_{IP}[Q]$ is $\ll 1$, and thus, the emission intensity quenching is dominated by dynamic quenching, resulting in a linear Stern–Volmer curve.

The combined nanosecond and picosecond TA results suggest competitive ET mechanisms for the photoinduced reduction of $Ru(bpy)_3^{2+*}$ by encapsulated peroxide dianion: a bimolecular route that is limited by the rate of diffusion, and a unimolecular pathway in which $Ru(bpy)_3^{2+}$ is photoexcited within the ion pair, where the rate limiting step is activated electron transfer, k_{ET} (Scheme 1). Such competitive ET

Scheme 1. Parallel Pathways for Oxidation of $[(O_2)\subset m\text{BDCA-5t-H}_6]^{2-}$ by $Ru(bpy)_3^{2+*}$

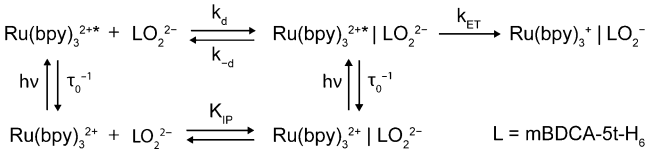

channels for the reaction of $Ru(bpy)_3^{2+*}$ with anionic quenchers have been observed previously for persulfate[34,35] and anionic coordination compounds such as $Mo(CN)_8^{4-}$ and $PtCl_4^{2-}$.[36]

The ability to perform ET within the ion pair permits the ET reactivity of peroxide ion to be isolated from diffusion-limiting kinetics. Accordingly, salts of the encapsulated peroxide with other Ru polypyridyl complexes, listed in Table 1, were investigated by picosecond TA. The difference spectra, as determined by spectroelectrochemistry (Figures S17–S19, Supporting Information), were similar to that of $Ru(bpy)_3^{+}$. As with the $Ru(bpy)_3^{2+}$ salt of $[(O_2)\subset m\text{BDCA-5t-H}_6]^{2-}$, a prompt growth of the singly reduced Ru(I) complex is observed upon excitation. The single wavelength traces shown in Figures S20–S22 (Supporting Information) for each system obey monoexponential growth kinetics; the ET rate constants listed in Table 1 increase monotonically with driving force. The observed ET rate constants are in accordance with the Marcus theory of electron transfer at the classical limit[37]

$$k_{ET} = \frac{2\pi}{\hbar}|V|^2\frac{1}{\sqrt{4\pi\lambda k_B T}}e^{-(\Delta G^{\circ\prime}+\lambda)^2/4\lambda k_B T} \quad (2)$$

where k_{ET} is related to $\Delta G^{\circ\prime}$ and the total reorganization energy, λ. The reactants and products in the ET reaction are charged, and therefore, the $\Delta G^{\circ\prime}$ in eq 2 and the values listed in Table 1 are corrected with Coulombic work terms, as detailed in the Supporting Information. Figure 3 shows the Marcus plot

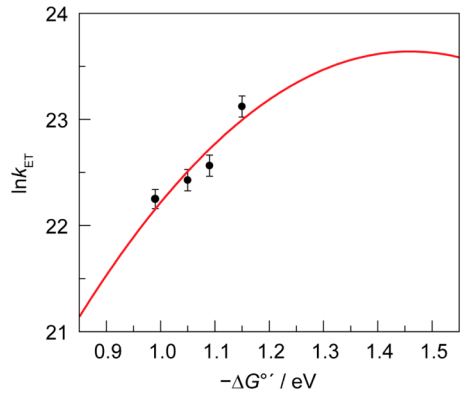

Figure 3. Semilog plot of k_{ET} vs the free energy driving force for [Ru(II) complex]$[(O_2)\subset m\text{BDCA-5t-H}_6]$ salt in DMF. The calculated fit of eq 2 is illustrated (red).

for the four complexes. The choice of the Ru(II) polypyridyl complex was limited owing to the reactivity of the encapsulated peroxide with ligands possessing strong electron withdrawing groups (thus limiting the overall span of $-\Delta G^{\circ\prime}$). For instance, *tris*(4,4′-dichloro-2,2′-bipyridyl) ruthenium(II) and *tris*(-*bis*(4,4′-trifluoromethyl)-2,2′-bipyridyl) ruthenium(II) were unstable in the presence of $[(O_2)\subset m\text{BDCA-5t-H}_6]^{2-}$ and decomposition reactions ultimately led to the production of chloride and fluoride cryptand adducts, respectively. Accordingly, the Marcus inverted region[37,38] was not accessible and our measurements were confined to the Marcus normal region.

The least-squares fit of eq 2 to the data of Figure 3 provides an estimate of the electronic coupling term, $|V|$,[41] between the excited Ru(II) polypyridyl complexes and the encapsulated peroxide anion, as well as λ, yielding values of $|V| = 9 \pm 3$ cm^{-1} and $\lambda = 1.5 \pm 0.1$ eV. These values for $|V|$ and λ obtained in the

Table 1. Electrochemical and Photophysical Data of Ruthenium Polypyridyl Complexes

Ru^{II} complex	E°(II/I) (V)	E_{00}[a] (eV)	E(II*/I) (V)	$-\Delta G^{\circ\prime}$[b] (eV)	k_{ET} (s^{-1})
$Ru(bpy)_3^{2+}$	−1.73	2.11	0.39	1.15	1.1×10^{10}
$Ru(bpy)_2(dmbpy)^{2+}$	−1.76[c]	2.08	0.33	1.09	6.3×10^{9}
$Ru(bpy)_2(dOMebpy)^{2+}$	−1.77	2.05	0.29	1.05	5.5×10^{9}
$Ru(dmbpy)_3^{2+}$	−1.84[c]	2.06	0.22	0.99	4.6×10^{9}

[a] E_{00} determined from fitting of 77 K emission spectra (Figure S16, Supporting Information) using the method in refs 39 and 40 and detailed in the Supporting Information. [b] Using $E^\circ([(O_2^-)\subset m\text{BDCA-5t-H}_6]/[(O_2^{2-})\subset m\text{BDCA-5t-H}_6]) = -0.85$ V vs Fc^+/Fc, ref 12. [c] Redox potential adjusted to the Fc^+/Fc reference couple, ref 15.

DOI: 10.1021/jp5110505
J. Phys. Chem. B 2015, 119, 7422–7429

classical limit neglect nuclear tunneling effects, which can be significant when high frequency vibrations ($\hbar\omega \geq 4k_BT$) contribute to the inner sphere reorganization energy (λ_i).[37,42] To address the suitability of the classical limit for this system, a quantum mechanical treatment was also performed as detailed in the Supporting Information (eq S5) to yield $|V|$ and λ_i of 17 ± 10 cm^{-1} and 1.2 ± 0.3 eV, respectively. A total reorganization energy in the quantum treatment can be estimated by adding the outer sphere contribution λ_o = 0.60 eV, obtained by treating the solvent with a dielectric continuum model (*vide infra*), to λ_i to obtain a value of λ = 1.8 ± 0.3 eV.

The classical and quantum models yield values of $|V|$ and λ that are within error, suggesting the effects of nuclear tunneling are not resolvable in the data. Due to the large uncertainty of $|V|$, the only conclusion we draw is that $|V|$ is small, consistent with nonadiabatic electron transfer. In principal, UV−vis spectroscopy can be employed to detect optical charge transfer transitions in the ion pairs.[43] Assuming weak coupling, we would expect a charge transfer band to be observed in the 500−800 nm region (see the Supporting Information, eq S6). However, a charge transfer band was not observed above the detection limit (Figure S23, Supporting Information), which is unsurprising in light of the weak absorptivity expected for such bands ($\varepsilon \sim 10^2$ M^{-1} cm^{-1})[44] and the limited concentrations achievable for ion pairs in DMF (~100 μM).

The inner sphere contribution (λ_i) is approximated in the classical limit by[37]

$$\lambda_i = \sum_j \frac{f_j^r f_j^p}{f_j^r + f_j^p}(\Delta q_j)^2 \quad (3)$$

where f_j^r and f_j^p are the force constants for the jth vibrational mode of the reactants and products, respectively, and Δq_j is the change in the equilibrium value of the bond length. Whereas the contribution of ruthenium polypyridyl complexes to the inner sphere reorganization energy is negligible,[45] that of peroxide within *m*BDCA-5t-H_6 is significant. The contribution to the inner sphere reorganization, λ_i, due to the shortening of the O−O bond upon oxidation of the peroxide dianion to superoxide can be estimated using eq 3. Substitution of the known force constants and bond distances for peroxide (1.497 Å, 2.8 N/cm force constant)[46] and superoxide (1.28 Å, 6.17 N/cm force constant)[47] in eq 3 yields λ_i = 0.90 eV for an *isolated* peroxide/superoxide moiety. However, $\lambda_i(O_2^{2-}/O_2^-)$ will be perturbed by the presence of the cryptand environment. To incorporate the effect of the cryptand ligand on $\lambda_i(O_2^{2-}/O_2^-)$ as well as conformational changes of the ligand itself upon ET, density functional theory (DFT) was applied to calculate λ_i in the classical limit for the complete $[(O_2)\subset m\text{BDCA-5t-H}_6]^{2-}$ ion. In this case, λ_i is determined by the difference in energy between the peroxide−cryptand adduct at its equilibrium nuclear configuration and the nuclear configuration of peroxide within the cryptand at the equilibrium geometry of the superoxide−cryptand adduct, i.e., $\lambda_i[(O_2^{2-}/O_2^-)\subset m\text{BDCA-5t-H}_6] = E[(O_2^{2-})\subset m\text{BDCA-5t-H}_6]_{\text{supereroxide-equil-geom}} - E[(O_2^{2-})\subset m\text{BDCA-5t-H}_6]_{\text{peroxide-equil-geom}}$, where E is the single point energy as determined by DFT calculations. This approach has been implemented successfully for the calculation of λ_i for blue copper proteins.[48] It should be noted that this method, as is typically done, assumes identical free energy surface shapes for the reactant and product, which is a fundamental assumption for a linear Marcus theory model of ET.[37,49,50] Moreover, even when departing from a linear model, Marcus showed that the effect of any differences in force constants with respect to oxidation state is generally negligible.[51] Geometry optimizations were first performed for the peroxide−cryptand adduct and the superoxide−cryptand adduct using the crystal structure coordinates of the $[(O_2)\subset m\text{BDCA-5t-H}_6]^{2-}$ anion as a starting point for geometry optimization. Tables S3 and S4 (Supporting Information) list the atomic coordinates for the optimized structures. The computed peroxide O−O bond distance (1.506 Å) and the average computed amide nitrogen to peroxide oxygen bond distances (2.728 Å) are in good agreement with distances measured in the crystal structure (1.497 and 2.685 Å, respectively), supporting the validity of the computations. Although the superoxide adduct cannot be isolated, let alone crystallized owing to its proclivity to disproportionate in the presence of the cryptand,[11] the computed O−O bond distance (1.36 Å) is also in good agreement with that measured in crystalline potassium superoxide (1.28 Å).[52] We next performed the single point energy calculations of the peroxide−cryptand in its optimized geometry as well as in the optimized geometry of the superoxide adduct. The total energies for the peroxide−cryptand adduct in the peroxide and superoxide equilibrium geometries are provided in Table S7 (Supporting Information). The energy difference between these two geometries is λ_i = 0.89 eV. In order to assess the agreement between inner sphere reorganization energies calculated using eq 3 and those calculated with the computational approach described above, we also applied the computational method for a free peroxide dianion. This afforded a value of λ_i = 0.74 eV, consistent with a minor deviation from the harmonic oscillator approximation used in eq 3. Notwithstanding the slight deviation between the DFT method and calculation of λ_i from eq 3, the similar values obtained for $\lambda_i(O_2^{2-}/O_2^-)$ from eq 3 and for $\lambda_i[(O_2^{2-}/O_2^-)\subset m\text{BDCA-5t-H}_6]$ from the DFT calculations lead us to conclude that the contribution of the peroxide dianion itself dominates the inner sphere reorganization energy for the oxidation of $[(O_2)\subset m\text{BDCA-5t-H}_6]^{2-}$ and the cryptand contribution is minor.

The total reorganization energy for the ET reaction is the sum of inner and outer sphere reorganization energies, $\lambda = \lambda_o + \lambda_i$. The λ_o for the $[Ru(bpy)_3][(O_2)\subset m\text{BDCA-5t-H}_6]$ system in DMF was estimated using the dielectric continuum model.[37] The molecular radius of the $[(O_2)\subset m\text{BDCA-5t-H}_6]^{2-}$ anion (r_{avg} = 5.0 Å) was taken as the geometric mean of the radii along the three axes of the crystal structure (Figure S24, Supporting Information); we prefer to use this metric versus the closest distance of the ions from the crystal structure, as this specific distance is unlikely to be sampled on average in solution. Together with the r_{avg} = 6.5 Å for the ruthenium complex,[53] we calculate an outer sphere reorganization energy of 0.60 eV for the ET reaction in DMF (ε_{op} = 2.05, ε_s = 36.7). A total reorganization energy of λ = 1.49 eV obtained from calculation is in excellent agreement with the value of λ = 1.5 ± 0.1 eV obtained from the classical Marcus fit of the experimental data shown in Figure 3.

CONCLUSION

Electron transfer reactions of peroxide are a cornerstone of dioxygen reactivity in chemistry and biology. The intrinsic reactivity of this diatomic dianion is difficult to establish because it does not typically exist in a soluble form. To this end, the cavity of hexacarboxamide cryptand (*m*BDCA-5t-H_6) offers a site for the molecular recognition of peroxide and a platform

DOI: 10.1021/jp5110505
J. Phys. Chem. B 2015, 119, 7422−7429

from which to investigate the dianion's electron transfer chemistry. By forming complex salts of the $[(O_2)\subset m\text{BDCA-5t-H}_6]^{2-}$ with Ru(II) polypyridyl dications, a photoinduced ET reaction chemistry of peroxide may be established. Whereas a bimolecular ET reaction is diffusion-limited, photoinduced charge transfer within an ion pair of the complex ion permits the intrinsic ET kinetics to be isolated. Picosecond TA spectroscopy allows for the direct measurement of the activated electron transfer rate constant, k_{ET}, which is on the order of 10^{10} s^{-1}. The driving-force dependence of k_{ET} using a homologous series of Ru(II) polypryridyl cations allows for the determination of the Marcus parameters of the system. The modest electronic coupling for the $[Ru(bpy)_3][(O_2)\subset m\text{BDCA-5t-H}_6]$ ion-paired complex is consistent with a nonadiabatic ET, attributable to the sterically shielding environment of the cryptand ligand. An experimental reorganization energy of 1.5 ± 0.1 eV is obtained using the classical Marcus model of electron transfer, in good agreement with estimates from calculations. Evaluation of λ_i shows that the contraction of the peroxide O−O bond prior to ET dominates the reorganization energy of the system with little contribution from the cryptand ligand. This suggests that the encapsulated peroxide provides a faithful model system with which to study the ET kinetics of free peroxide dianion with limited structural influence from the cryptand.

■ ASSOCIATED CONTENT

Supporting Information

Additional experimental details, an explanation of the Marcus theory analysis, K_{IP} estimations, emission spectral fitting, NMR and UV−vis spectra, X-ray crystallographic data in CIF format, additional nanosecond and picosecond TA data, emission data, spectroelectrochemical data, calculation of the molecular radius of $[(O_2)\subset m\text{BDCA-5t-H}_6]^{2-}$, and optimized geometries from DFT. This material is available free of charge via the Internet at http://pubs.acs.org. Complete crystallographic data were deposited in the Cambridge Crystallographic Database Centre (CCDC 1030626).

■ AUTHOR INFORMATION

Corresponding Authors

*E-mail: ccummins@mit.edu.

*E-mail: dnocera@fas.harvard.edu.

Author Contributions

§These authors contributed equally to this work.

Notes

The authors declare no competing financial interest.

■ ACKNOWLEDGMENTS

We thank Marshall D. Newton, Andrew M. Ullman, and Ryan G. Hadt for helpful discussions, Charles Margarit for providing *m*BDCA-5t-H_6 ligand, and David C. Powers for assistance in X-ray structure determination. We acknowledge Dr. Yu-Sheng Chen for assistance with X-ray crystallography at ChemMatCARS, APS. ChemMatCARS Sector 15 is principally supported by the NSF/DOE under grant number NSF/CHE-1346572. Use of APS was supported by the U.S. DOE, Office of Science, Office of Basic Energy Sciences, under Contract No. DE-AC02-06CH11357. C.C.C. acknowledges the support of NSF-CCI (CHE-0802907). D.G.N. acknowledges support by the U.S. Department of Energy Office of Science, Office of Basic Energy Sciences program, under Award Number DE-SC0009758. Grants from the NSF also provided instrument support to the DCIF at MIT (Grants CHE-9809061 and DBI-9729592).

■ REFERENCES

(1) Sawyer, D. T. *Oxygen Chemistry*; Oxford University Press: New York, 1991.

(2) Jones, C. W. *Applications of Hydrogen Peroxide and Derivatives*; Royal Society of Chemistry: Cambridge, U.K., 1999.

(3) Kwabi, D. G.; Ortiz-Vitoriano, N.; Freunberger, S. A.; Chen, Y.; Imanishi, N.; Bruce, P. G.; Shao-Horn, Y. Materials Challenges in Rechargeable Lithium-Air Batteries. *MRS Bull.* **2014**, *39*, 443−452.

(4) Girishkumar, G.; McCloskey, B.; Luntz, A. C.; Swanson, S.; Wilcke, W. Lithium-Air Battery: Promise and challenges. *J. Phys. Chem. Lett.* **2010**, *1*, 2193−2203.

(5) Stanbury, D. M.; Mulac, W. A.; Sullivan, J. C.; Taube, H. Superoxide Reactions with (Isonicotinamide)pentaammineruthenium-(II) and -(III). *Inorg. Chem.* **1980**, *19*, 3735−3740.

(6) Sawyer, D. T.; Valentine, J. S. How Super is Superoxide? *Acc. Chem. Res.* **1981**, *14*, 393−400.

(7) Sawyer, D. T.; Chiericato, G.; Angelis, C. T.; Nanni, E. J.; Tsuchiya, T. Effects of Media and Electrode Materials on the Electrochemical Reduction of dioxygen. *Anal. Chem.* **1982**, *54*, 1720−1724.

(8) Wood, P. M. The potential Diagram for Oxygen at pH 7. *Biochem. J.* **1988**, *253*, 278−289.

(9) Kato, T.; Fujimoto, T.; Tsutsui, A.; Tashiro, M.; Mitsutsuka, Y.; Machinami, T. Identification of a Discrete Peroxide Dianion, O_2^{2-}, in a Two Sodium-(1,6-Anhydro-β-maltose)$_2$-Peroxide Complex. *Chem. Lett.* **2010**, *39*, 136−137.

(10) Boal, A. K.; Cotruvo, J. A., Jr.; Stubbe, J.; Rosenzweig, A. C. Structural Basis for Activation of Class Ib Ribonucleotide Reductase. *Science* **2010**, *329*, 1526−1530.

(11) Lopez, N.; Graham, D. J.; McGuire, R.; Alliger, G. E.; Shao-Horn, Y.; Cummins, C. C.; Nocera, D. G. Reversible Reduction of Oxygen to Peroxide Facilitated by Molecular Recognition. *Science* **2012**, *335*, 450−453.

(12) Ullman, A. M.; Sun, X.; Graham, D. J.; Lopez, N.; Nava, M.; De Las Cuevas, R.; Müller, P.; Rybak-Akimova, E. V.; Cummins, C. C.; Nocera, D. G. Electron-Transfer Studies of a Peroxide Dianion. *Inorg. Chem.* **2014**, *53*, 5384−5391.

(13) Segers, D. P.; DeArmond, M. K. Emission Studies of Transition-Metal Complexes of 2,2′-dipyridylamine. 2. Tris Complexes of Ruthenium(II). *J. Phys. Chem.* **1982**, *86*, 3768−3776.

(14) McClanahan, S. F.; Dallinger, R. F.; Holler, F. J.; Kincaid, J. R. Mixed-Ligand Poly(pyridine) Complexes of ruthenium(II). Resonance Raman Spectroscopic Evidence for Selective Population of Ligand-Localized ^{3}MLCT Excited States. *J. Am. Chem. Soc.* **1985**, *107*, 4853−4860.

(15) Mabrouk, P.; Wrighton, M. Resonance Raman Spectroscopy of the Lowest Excited State of Derivatives of Tris(2,2′-bipyridine)-ruthenium(II): Substituent Effects on Electron Localization in Mixed-Ligand Complexes. *Inorg. Chem.* **1986**, *25*, 526−531.

(16) Bruker AXS (2009). Apex II. Bruker AXS: Madison, WI.

(17) Sheldrick, G. M. Experimental Phasing with SHELXC/D/E: Combining Chain Tracing with Density Modification. *Acta Crystallogr.* **2010**, *66*, 479−485.

(18) Holder, P. G.; Pizano, A. A.; Anderson, B. L.; Stubbe, J.; Nocera, D. G. Deciphering Radical Transport in the Large Subunit of Class I Ribonucleotide Reductase. *J. Am. Chem. Soc.* **2011**, *134*, 1172−1180.

(19) Powers, D. C.; Anderson, B. L.; Nocera, D. G. Two-Electron HCl to H_2 Promoted by Ni(II) Polypyridyl Halide Complexes. *J. Am. Chem. Soc.* **2013**.

(20) Loh, Z.-H.; Miller, S. E.; Chang, C. J.; Carpenter, S. D.; Nocera, D. G. Excited-State Dynamics of Cofacial Pacman Porphyrins. *J. Phys. Chem. A* **2002**, *106*, 11700−11708.

(21) Neese, F. The ORCA Program System. *Comput. Mol. Sci.* **2012**, *2*, 73−78.

DOI: 10.1021/jp5110505
J. Phys. Chem. B 2015, 119, 7422−7429

(22) Becke, A. D. Density-Functional Exchange-Energy Approximation with Correct Asymptotic Behavior. *Phys. Rev. A* **1988**, *38*, 3098−3100.
(23) Schäfer, A.; Horn, H.; Ahlrichs, R. Fully Optimized Contracted Gaussian Basis Sets for atoms Li to Kr. *J. Chem. Phys.* **1992**, *97*, 2571−2577.
(24) Weigend, F.; Ahlrichs, R. Balanced Basis Sets of Split Valence Triple Zeta Valence and Quadruple Zeta Valence Quality for H to Rn: Design and Assessment of Accuracy. *Phys. Chem. Chem. Phys.* **2005**, *7*, 3297−3305.
(25) Lee, C.; Yang, W.; Parr, R. G. Development of the Colle-Salvetti Correlation-Energy Formula into a Functional of the Electron Density. *Phys. Rev. B* **1988**, *37*, 785−789.
(26) Becke, A. D. A New Mixing of Hartree−Fock and Local Density-functional Theories. *J. Chem. Phys.* **1993**, *98*, 1372−1377.
(27) Becke, A. D. Density-Functional Thermochemistry. III. The Role of Exact Exchange. *J. Chem. Phys.* **1993**, *98*, 5648−5652.
(28) Jones, R. D.; Summerville, D. A.; Basolo, F. Synthetic Oxygen Carriers Related to Biological Systems. *Chem. Rev.* **1979**, *79*, 139−179.
(29) Creutz, C.; Sutin, N. Electron-Transfer Reactions of Excited-States − Direct Evidence of Charge-Transfer Excited Tris(2,2′-Bipyridine)ruthenium(II). *J. Am. Chem. Soc.* **1976**, *98*, 6384−6385.
(30) Anderson, C. P.; Salmon, D. J.; Meyer, T. J.; Young, R. C. Photochemical Generation of $Ru(bpy)_3^+$ and O_2^-. *J. Am. Chem. Soc.* **1977**, *99*, 1980−1982.
(31) Heath, G. A.; Yellowlees, L. J.; Braterman, P. S. Spectroelectrochemical Studies on Tris-bipyridyl Ruthenium Copmlexes; Ultra-violet, Visible, and Near-Infrared Spectra of the Series $[Ru(bipyridyl)_3]^{2+/1+/0/1-}$. *J. Chem. Soc., Chem. Commun.* **1981**, 287−289.
(32) Atkins, P.; de Paula, J. *Physical Chemistry for the Life Sciences*; Macmillan: New York, 2011.
(33) Lakowicz, J. R. *Principles of Fluorescence Spectroscopy*, 3rd ed.; Springer: New York, 2006.
(34) White, H. S.; Becker, W. G.; Bard, A. J. Photochemistry of the Tris(2,2′-bipyridine)ruthenium(II)-Peroxysulfate System in Aqueous and Mixed Acetonitrile-Water Solutions. Evidence for a Long-lived Photoexcited Ion Pair. *J. Phys. Chem.* **1984**, *88*, 1840−1846.
(35) Lewandowska-Andralojc, A.; Polyansky, D. E. Mechanism of the Quenching of the Tris(bipyridine)ruthenium(II) Emission by Persulfate: Implications for Photoinduced Oxidation Reactions. *J. Phys. Chem. A* **2013**, *117*, 10311−10319.
(36) Bolletta, F.; Maestri, M.; Moggi, L.; Balzani, V. Dynamic and Static Quenching of the tris(2,2′-dipyridyl)ruthenium(II) Phosphorescence by Anionic Coordination Compounds in Various Solvents. *J. Phys. Chem.* **1974**, *78*, 1374−1377.
(37) Marcus, R. A.; Sutin, N. Electron Transfers in Chemistry and Biology. *Biochim. Biophys. Acta, Rev. Bioenerg.* **1985**, *811*, 265−322.
(38) Closs, G. L.; Miller, J. R. Intramolecular Long-Distance Electron Transfer in Organic Molecules. *Science* **1988**, *240*, 440−447.
(39) Kober, E. M.; Caspar, J. V.; Lumpkin, R. S.; Meyer, T. J. Application of the Energy Gap Law to Excited-State Decay of osmium(II)-Polypyridine Complexes: Calculation of Relative Nonradiative Decay Rates from Emission Spectral Profiles. *J. Phys. Chem.* **1986**, *90*, 3722−3734.
(40) Striplin, D. R.; Reece, S. Y.; McCafferty, D. G.; Wall, C. G.; Friesen, D. A.; Erickson, B. W.; Meyer, T. J. Solvent Dependence of Intramolecular Electron Transfer in a Helical Oligoproline Assembly. *J. Am. Chem. Soc.* **2004**, *126*, 5282−5291.
(41) Newton, M. D. Quantum Chemical Probes of Electron-Transfer Kinetics: The Nature of Donor-Acceptor Interactions. *Chem. Rev.* **1991**, *91*, 767−792.
(42) Marcus, R. A. The Second R. A. Robinson Memorial Lecture. Electron, Proton and Related Transfers. *Faraday Discuss. Chem. Soc.* **1982**, *74*, 7−15.
(43) Hush, N. S. Intervalence-Transfer Absorption. Part 2. Theoretical Consideration and Spectroscopic Data. In *Progress in Inorganic Chemistry*; Cotton, F. A., Ed.; John Wiley & Sons, Inc.: Hoboken, NJ, 1967; Vol. *8*, pp 391−444.
(44) Curtis, J. C.; Meyer, T. J. Outer-Sphere Charge Transfer in Mixed-Metal Ion Pairs. *Inorg. Chem.* **1982**, *21*, 1562−1571.
(45) Creutz, C.; Keller, A. D.; Sutin, N.; Zipp, A. P. Poly(pyridine)-ruthenium(II)-Photoinduced Redox Reactions of Bipyridinium Cations, Poly(pyridine)rhodium Complexes, and Osmium Ammines. *J. Am. Chem. Soc.* **1982**, *104*, 3618−3627.
(46) Wiberg, E.; Wiberg, N.; Holleman, A. F. *Inorganic Chemistry*; Academic Press: San Diego, CA, 2001.
(47) Creighton, J. A.; Lippincott, E. R. Vibrational Frequency and Dissociation Energy of the Superoxide Ion. *J. Chem. Phys.* **1964**, *40*, 1779−1780.
(48) Olsson, M. H. M.; Ryde, U.; Roos, B. O. Quantum Chemical Calculations of the Reorganization Energy of Blue-Copper Proteins. *Protein Sci.* **1998**, *7*, 2659−2668.
(49) Warshel, A. Dynamics of Reactions in Polar Solvents. Semiclassical Trajectory Studies of Electron-Transfer and Proton-Transfer Reactions. *J. Phys. Chem.* **1982**, *86*, 2218−2224.
(50) King, G.; Warshel, A. Investigation of the Free Energy Functions for Electron Transfer Reactions. *J. Chem. Phys.* **1990**, *93*, 8682−8692.
(51) Marcus, R. A. On the Theory of Electron-Transfer Reactions. VI. Unified Treatment for Homogeneous and Electrode Reactions. *J. Chem. Phys.* **1965**, *43*, 679−701.
(52) Abrahams, S. C.; Kalnajs, J. The Crystal Structure of α-Potassium Superoxide. *Acta Crystallogr.* **1955**, *8*, 503−506.
(53) Brown, G. M.; Sutin, N. A Comparison of the Rates of Electron Exchange Reactions of Ammine Complexes of Ruthenium(II) and -(III) with the Predictions of Adiabatic, Outer-sphere Electron Transfer Models. *J. Am. Chem. Soc.* **1979**, *101*, 883−892.

DOI: 10.1021/jp5110505
J. Phys. Chem. B 2015, 119, 7422−7429

Ligand Non-Innocence

International Edition: DOI: 10.1002/anie.201509099
German Edition: DOI: 10.1002/ange.201509099

Electronic Structure of Copper Corroles

*Christopher M. Lemon, Michael Huynh, Andrew G. Maher, Bryce L. Anderson, Eric D. Bloch, David C. Powers, and Daniel G. Nocera**

Abstract: *The ground state electronic structure of copper corroles has been a topic of debate and revision since the advent of corrole chemistry. Computational studies formulate neutral Cu corroles with an antiferromagnetically coupled Cu^{II} corrole radical cation ground state. X-ray photoelectron spectroscopy, EPR, and magnetometry support this assignment. For comparison, Cu^{II} isocorrole and [TBA][$Cu(CF_3)_4$] were studied as authentic Cu^{II} and Cu^{III} samples, respectively. In addition, the one-electron reduction and one-electron oxidation processes are both ligand-based, demonstrating that the Cu^{II} centre is retained in these derivatives. These observations underscore ligand non-innocence in copper corrole complexes.*

Since the original synthesis of copper corroles,[1] the electronic structure and oxidation state of the copper centre in these compounds has been a topic of debate. The corrole was initially formulated as a Cu^{II} metal centre in a dianionic ligand, where one of the pyrrole nitrogen atoms retains a proton.[1–4] The electronic structure was later revised as a fully deprotonated corrole ligand containing a Cu^{III} centre[5] due to the lack of an *N*-pyrrole proton by IR spectroscopy and crystallography, and the diamagnetic nature of the compound. Subsequent structural[6–10] and computational[11,12] studies of copper corroles with a wide variety of *meso* and β-substituents have suggested the ground state to be best described as an antiferromagnetically coupled Cu^{II} corrole radical cation. These studies have shown that saddling distortions are *inherent* to copper corroles as a consequence of significant overlap between the Cu $d_{x^2-y^2}$ orbital and the corrole π HOMO.[6] However, the electronic structure of copper corroles remains an unresolved issue as a recent report of a one-electron-oxidized Cu corrole derivative was assigned as the first example of a discrete Cu^{IV} species.[13] This conclusion was derived from the assumption that the neutral corrole complex contains a Cu^{III} centre. In this study, we provide comparative spectroscopic and magnetic data of Cu corroles, the corresponding cation and anion, and a Cu isocorrole that establish the presence of Cu^{II} across the series of complexes with the redox load borne by the macrocyclic ligand.

[*] C. M. Lemon, M. Huynh, A. G. Maher, B. L. Anderson, Dr. E. D. Bloch, Prof. Dr. D. G. Nocera
Department of Chemistry and Chemical Biology, Harvard University
12 Oxford Street, Cambridge MA 02138 (USA)
E-mail: dnocera@fas.harvard.edu
Prof. Dr. D. C. Powers
Department of Chemistry, Texas A&M University
College Station, TX 77843-3255 (USA)

Supporting information for this article is available on the WWW under http://dx.doi.org/10.1002/anie.201509099.

The copper complex of corrole **1** (Scheme 1) was prepared following literature methods using $Cu(OAc)_2$ in pyridine[14,15] with an isolated yield comparable to those obtained for other Cu corrole complexes.[6] Brown crystals of **Cu-1** suitable for X-ray diffraction were grown from a toluene solution of the compound. A summary of the crystallographic data is provided in Table S1 in the Supporting Information (SI). Figure 1 shows the crystal structure of one of the two corroles in the asymmetric unit. The metal centre displays a distorted square planar geometry, with d(Cu–N) = 1.883–1.899 Å bond lengths, which is consistent with other Cu corrole structures.[15,16] The corrole adopts the typical nonplanar, saddled geometry,[6,9,10] where alternating pyrrole units point above and below the plane of the macrocycle.

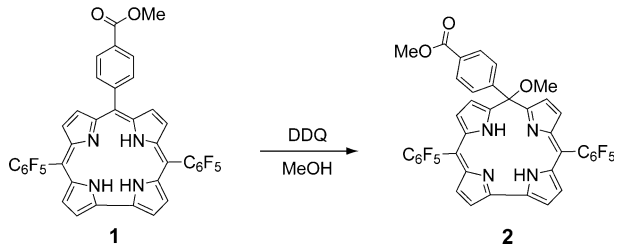

Scheme 1. Conversion of corrole **1** to isocorrole **2**.

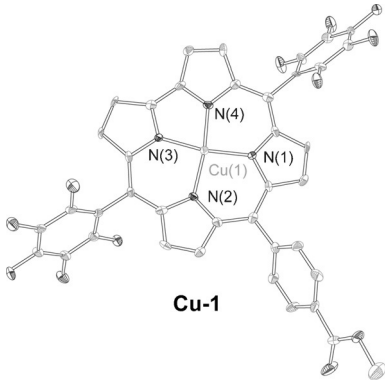

Figure 1. Solid state structure of **Cu-1**. Thermal ellipsoids are drawn at the 50% probability level.

An authentic Cu^{II} reference compound of the corrole in a nearly identical ligand field is obtained by oxidation of **1** followed by attack of methanol[17,18] to furnish the analogous isocorrole **2** (Scheme 1). In the isocorrole, one of the *meso* carbons is sp^3 hybridized, rendering it a non-aromatic dianionic ligand. Metallation of **2** with copper acetate and

mild heating gave **Cu-2** in high yield. The absorption spectra of **2** and **Cu-2** (Figure S1) are consistent with other reports.[17,18] As expected for a Cu^{II} complex, the χT versus T plot (Figure S2) of **Cu-2** is indicative of a typical paramagnet, with magnetic ordering observed at $T < 15$ K.

Cu-1 displays an apparent diamagnetic ^{1}H NMR spectrum at room temperature in $CDCl_3$ and [D_8]toluene (Figure 2 and S3). However, unlike other diamagnetic metallocorroles, only the *meso* aryl protons are well-resolved doublets (at 7.38 and 8.19 ppm). The four β-pyrrole protons (at 7.74, 7.18, 7.13, and 7.10) appear in the 7.1–7.8 ppm region as broad signals. This is in contrast to **Au-1**, a true diamagnetic M^{III} compound, where all of the signals are resolved into clear doublets[19] and display resonances that are similar to those of the free-base **1** (8.6–9.2 ppm).[20] The large spectral shift and the broad signals of **Cu-1** suggest the presence of a paramagnetic species at room temperature. The singlet–triplet equilibrium that gives rise to this paramagnetism may be quantified from VT ^{1}H NMR of **Cu-1** (Figure 2a). Noting that the β-proton signal at 7.74 ppm clearly shifts without interference from other signals over the 25–100 °C range, a fit of the shift of this signal (δ) with temperature (T) to the following equation yields the energy difference ($\Delta E_{T\text{-}S}$) between the triplet and singlet states:[21–23]

$$\delta(\text{ppm}) = \delta_{\text{singlet}} + 10^6 \frac{g\beta_e}{g_N\beta_N}\frac{aS(S+1)}{kT}\left[3 + \exp\left(\frac{\Delta E_{T\text{-}S}}{RT}\right)\right]^{-1} \quad (1)$$

where g and g_N are the electronic and nuclear g-values, respectively, β_e and β_N are the Bohr and nuclear magnetons, respectively, a is the isotropic hyperfine coupling constant, S is the spin of the system ($S = 1$ for a triplet), k is the Boltzmann constant, and R is the gas constant. The fit of the data in Figure 2b to Equation (1) yields $\delta_{\text{singlet}} = 7.42 \pm 0.04$ ppm, $a = 0.152 \pm 0.027$ G, and $\Delta E_{T\text{-}S} = 13.9 \pm 0.7$ kJ mol^{-1} (0.144 ± 0.007 eV); details of the fitting procedure are provided in the Supporting Information. As a means of validating the results of this experiment, **Cu-1** was examined by SQUID magnetometry (Figure 2c) and the data was fit to the following Hamiltonian:

$$\hat{H} = -J\hat{S}_A\cdot\hat{S}_B + \beta\left(\hat{S}_A\cdot g_A + \hat{S}_B\cdot g_B\right)\cdot B \quad (2)$$

where J is the exchange coupling constant, $\hat{S}$ is the spin angular momentum operator, β is the Bohr magneton of the electron, g is the electron g-factor, and B is the applied field; the subscripts A and B refer to the two spin components (metal and ligand) that are coupled. This Hamiltonian accounts for both magnetic exchange (first term) and Zeeman splitting (second term). The plot of χT versus T is indicative of an antiferromagnetically coupled complex with a coupling ($-2J$) of 1236 ± 40 cm^{-1} or 14.8 ± 0.5 kJ mol^{-1} (see SI). We note that this coupling represents the energy difference between the antiferromagnetic (singlet) and ferromagnetic (triplet) states and is identical to $\Delta E_{T\text{-}S}$ of Equation (1). Thus the energy difference between the singlet and triplet states of **Cu-1** as determined from Figure 2b and c are in excellent agreement. Our experimental value of $\Delta E_{T\text{-}S}$ for **Cu-1** shows good agreement with the energy gap predicted by DFT calculations.[11] Using the value of $\Delta E_{T\text{-}S} = 13.9 \pm 0.7$ kJ mol^{-1}, the relative population of the two states can be determined at a given temperature by the Boltzmann factor:

$$\frac{N_T}{N_S} = 3\exp\left(\frac{-\Delta E_{T\text{-}S}}{kT}\right) \quad (3)$$

where N_T and N_S are the populations of the triplet and singlet states, respectively and the factor of 3 accounts for the degeneracy of the triplet state. At 23 °C, only 1.05 % of the **Cu-1** molecules in the sample are in the triplet state; this value increases to 3.29 % at 100 °C. The low population of the triplet state accounts for the seemingly diamagnetic nature of the compound, as well as the broad signals of the β-pyrrole protons due to their proximity to the copper centre.

Figure 3a shows the cyclic voltammogram of **Cu-1**. Two reversible reductions at −0.28 V and −2.15 V versus Fc^+/Fc are observed, as well as a reversible oxidation at + 0.55 V and a quasi-reversible oxidation around + 1.27 V. The accessibility of the oxidized and reduced species at reasonable potentials allowed for their preparation with mild reagents. Reduced **Cu-1** was obtained using zinc metal in pyridine to give Zn[**Cu-1**]$_2$ as a dark green solution. The oxidized derivative [**Cu-1**][PF_6] was produced by treating **Cu-1** with $AgPF_6$ in CH_2Cl_2 to give a light yellow-brown solution. The reduced corrole exhibits a significant red shift of the Soret band with a concomitant growth of the Q bands. Conversely, the intensity of the Soret band decreases and the Q bands have virtually no intensity for the oxidized corrole (Figure 3b). The reduced corrole is stable in solution on the bench top for several months, while the oxidized corrole has limited stability. Whereas the UV-vis spectrum of a dilute sample of [**Cu-1**][PF_6] in CH_2Cl_2 remains virtually unchanged after 2 hours (Figure S4a), the stock solution turns green over this period of time (Figure S4b) to give a diamagnetic compound

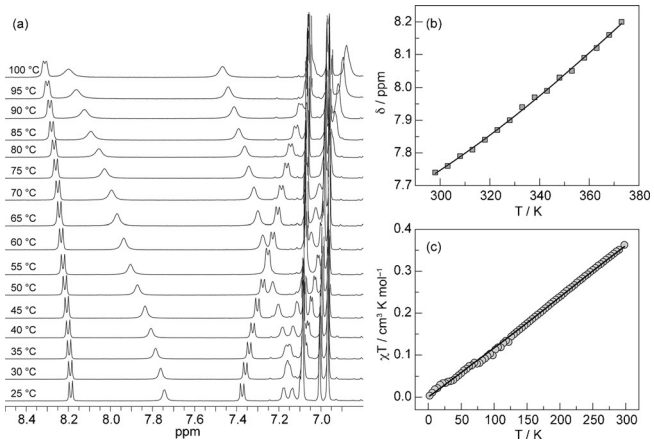

Figure 2. a) Variable temperature ^{1}H NMR spectra of **Cu-1** in [D_8]toluene showing the aromatic region of the spectrum. The large peaks between 6.9 and 7.1 ppm are from toluene. b) Plot of the data from (a), analysing the β pyrrole proton that shifts from 7.74 at 25 °C to 8.20 at 100 °C. c) SQUID magnetometry data for a solid sample of **Cu-1**. The data was fit to Equation (2) and shows that this compound is antiferromagnetic with a coupling ($-2J$) of 1236 cm^{-1}.

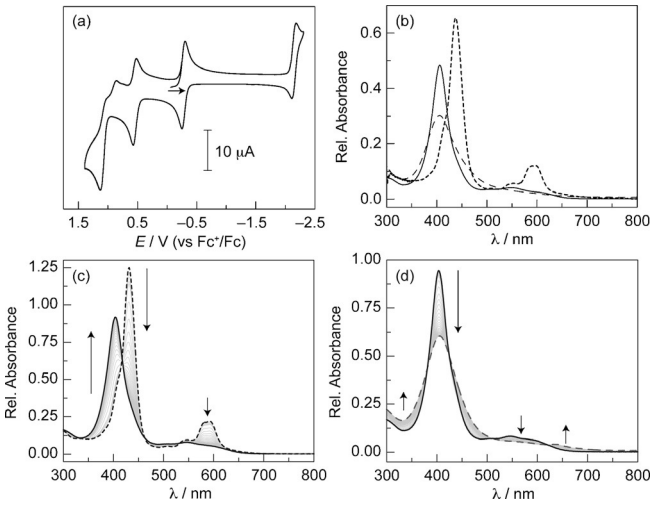

Figure 3. a) Cyclic voltammogram of **Cu-1** in MeCN with 0.1 M [TBA][PF_6] recorded at 100 mV s^{-1}. b) Comparative absorption spectra of **Cu-1** (——), [**Cu-1**][PF_6] (– – –), and Zn[**Cu-1**]$_2$ (-----). c) Spectroelectrochemistry of **Cu-1** showing the conversion of [**Cu-1**]$^-$ (-----) to **Cu-1** (——) using bulk electrolysis at 0 V. d) Spectroelectrochemistry of **Cu-1** showing the conversion of **Cu-1** (——) to [**Cu-1**]$^+$ (– – –) using bulk electrolysis at 0.8 V.

(Figure S5) and, presumably, free copper in solution. Thin-layer spectroelectrochemical experiments (Figure 3c,d) are consistent with the absorption spectra of Zn[**Cu-1**]$_2$ and [**Cu-1**][PF_6].

EPR spectra of **Cu-1** and **Cu-2** provide information regarding the formal oxidation state of the metal centre. As a benchmark, Figure 4a shows the EPR spectrum of **Cu-2.** As expected for a Cu^{II} sample, the spectrum is characteristic of an axial doublet for a single unpaired electron ($S = 1/2$) with

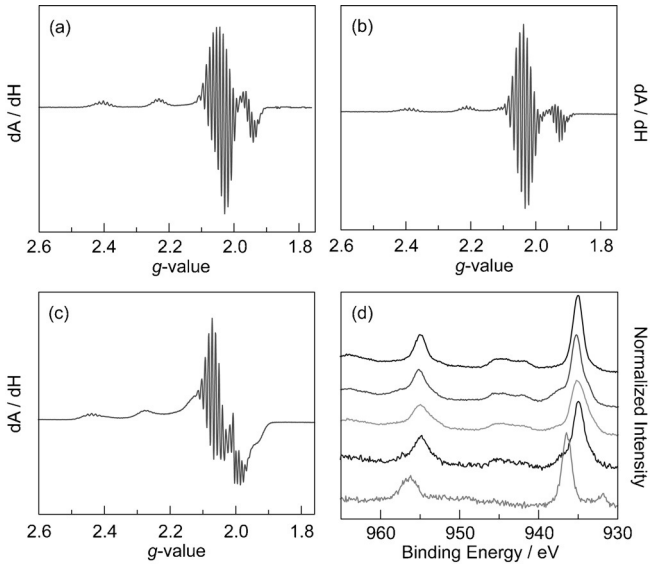

Figure 4. X-band EPR spectra of a) **Cu-2** in 2-Me-THF, b) Zn[**Cu-1**]$_2$ in 2-Me-THF/pyridine, and c) [**Cu-1**][PF_6] in 2-Me-THF/DCM. All spectra were recorded at 77 K. d) The Cu 2p region of the XPS spectra of the compounds and derivatives studied herein, from top to bottom: **Cu-2**, **Cu-1**, Zn[**Cu-1**]$_2$, [**Cu-1**][PF_6], and [TBA][$Cu(CF_3)_4$].

hyperfine coupling to the $^{65}Cu/^{63}Cu$ nucleus ($I = 3/2$) to give a four-line pattern; this signal is further split by ligand superhyperfine coupling to the four ^{14}N nuclei ($I = 1$) of the corrole to give a nine-line pattern. This type of spectrum has been previously observed for the copper complex of a 10-oxacorrole.[6] As expected from the magnetic data, a sample of **Cu-1** in 2-Me-THF is EPR silent. The EPR spectra for Zn[**Cu-1**]$_2$ in pyridine/2-Me-THF (Figure 4b) and [**Cu-1**][PF_6] in DCM/2-Me-THF (Figure 4c) are very similar to **Cu-2**, establishing the presence of a Cu^{II} centre in these compounds. Simulations for these spectra are presented in Figure S6 and the parameters are summarised in Table S2.

X-ray photoelectron spectroscopy (XPS) is particularly diagnostic of the oxidation state in copper complexes, as shake-up satellite peaks are observed in the Cu 2p region of the spectrum for Cu^{II} species, but are absent for Cu^{III} derivatives.[24,25] Figure 4d shows the XPS spectra of the Cu corroles as compared to **Cu-2** and [TBA][$Cu(CF_3)_4$],[26] which were studied as authentic Cu^{II} and Cu^{III} samples, respectively. With the caveat that ligand field inversion for the [$Cu(CF_3)_4$]$^-$ anion leads to a Cu^{I} complex,[27] the XPS data suggests that the metal is in a highly oxidized state, exhibiting Cu 2p binding energies greater than Cu^{II} samples. The derivatives of **Cu-1** and **Cu-2** exhibit broad shake-up satellites between 940.2 and 947.4 eV while [TBA][$Cu(CF_3)_4$] does not. Moreover, the Cu $2p_{3/2}$ peak appears at 935.0 eV for **Cu-2** and all the **Cu-1** corrole derivatives are within 0.1 eV of this peak. This feature is shifted to 936.4 eV for [TBA][$Cu(CF_3)_4$], consistent with a more oxidized Cu centre in this compound. These results further support the presence of Cu^{II} in **Cu-1** and its oxidized and reduced derivatives.

To complement spectroscopic experiments, DFT calculations (B3LYP/6-311G(d,p) with toluene CPCM solvation) were performed for **Cu-1** as a closed shell ^{1}Cu(III) singlet, a ferromagnetically coupled ^{3}Cu(II) corrole radical cation, and an antiferromagnetically coupled, broken symmetry ^{1}Cu(II) corrole radical cation (Tables S3–S5, Figure S7 and S8). The B3LYP functional has been used to study a wide variety of copper complexes[28] and it has been shown for copper corroles to give the most accurate values of $\Delta E_{T\text{-}S}$ when benchmarked against pure functionals or multiconfigurational methods.[11] As a benchmark, energies were also computed for optimized structures using Complete Active Space Multiconfiguration SCF (CASSCF). Both methods predict the broken symmetry singlet ^{1}Cu(II) as the ground state, consistent with experiment, and bound the triplet state +0.0167–0.415 eV higher in energy. This energy range corresponds to the calculated magnetic coupling for **Cu-1**, which is known to be highly dependent on the choice of functional.[11] In addition, comparison of computed geometries to the solid-state structure of **Cu-1** (Figure S9) shows that singlet state calculations match best (i.e., lowest RMS deviation) with the saddled experimental structure, while the calculated triplet state geometry is planar. Doublet and quartet states were calculated for both [**Cu-1**]$^+$ and [**Cu-1**]$^-$ and it was found that the quartet states are higher in energy for both species by 0.132 eV and 1.381 eV, respectively (Tables S6–S9 and Figure S10 and S11). TD-DFT calculations of **Cu-1**, [**Cu-1**]$^-$, and [**Cu-1**]$^+$ (Tables S10–S12 and Fig-

ure S12–S14) provide simulated UV-vis spectra that have qualitative similarities to the experimental spectra (Figure S15) inasmuch as the reduced corrole has red-shifted Q bands relative to **Cu-1** and the oxidized corrole has a less intense Soret band.

The electronic structure of each compound examined in this study is summarised in Figure 5, which presents the calculated spin density plots and a qualitative molecular orbital diagram with canonical a_2 and b_1 ligand orbitals for reference (Figure 5a). First, **Cu-1** is best described as an antiferromagnetically coupled Cu^{II} corrole radical cation. The strong coupling (1236 cm^{-1}) between the Cu^{II} and the ligand radical accounts for the diamagnetic nature of the compound. The presence of a Cu^{II} centre is demonstrated by XPS, and is corroborated by the spin density plot (Figure 5b) that shows one α electron (black) in $d_{x^2-y^2}$ and one β electron (gray) in the corrole b_1 orbital.

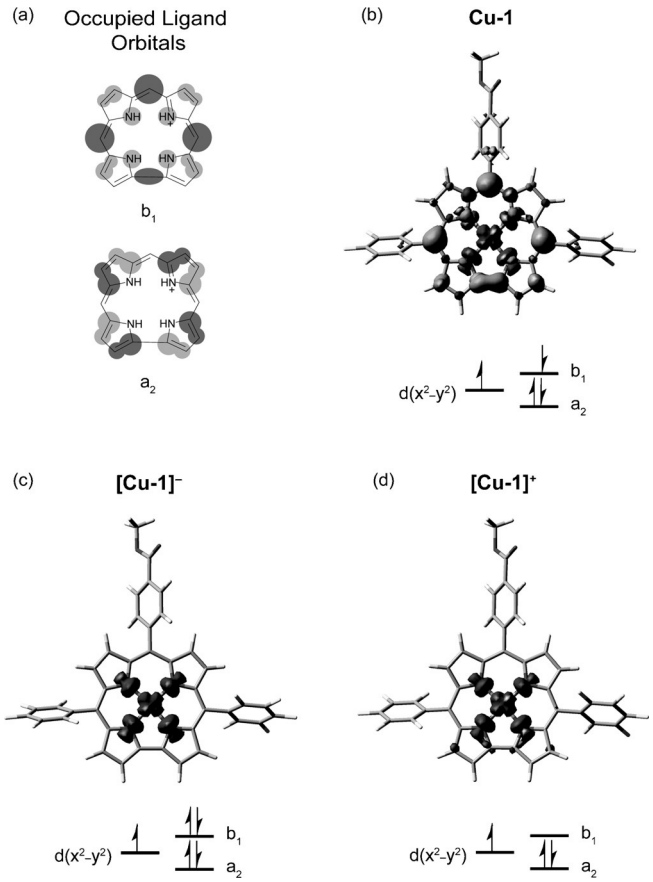

Figure 5. a) Canonical occupied corrole ligand orbitals: HOMO (b_1) and HOMO−1 (a_2), adapted from Ref. [20]. To illustrate the electronic structure of each derivative examined in this study, the calculated spin density plot and orbital occupancy is provided: b) singlet **Cu-1**, c) doublet $[\mathbf{Cu\text{-}1}]^-$, and d) doublet $[\mathbf{Cu\text{-}1}]^+$.

Both $[\mathbf{Cu\text{-}1}]^-$ and $[\mathbf{Cu\text{-}1}]^+$ have a single unpaired electron in $d_{x^2-y^2}$, as demonstrated by EPR, XPS, and corroborated by the spin density plots in Figure 5c and d. Thus, $[\mathbf{Cu\text{-}1}]^-$ is best described as a Cu^{II} $corrole^{3-}$ (closed shell, trianionic ligand), while $[\mathbf{Cu\text{-}1}]^+$ is a Cu^{II} $corrole^-$. The latter is a more satisfying electronic structure description than the recently proposed Cu^{IV} corrole complex;[13] our data for $[\mathbf{Cu\text{-}1}]^+$ is nearly identical to that reported for the proposed Cu^{IV} corrole. Our electronic structure formulations are consistent with those proposed by Ghosh on the basis of computational studies.[29] As a result, the reversible one electron reduction and oxidation are both ligand-based. It has been previously demonstrated that both of these processes are dependent on the identity of the *meso* substituents. The half-wave potential of the reduction shifts 160 mV, while that of the oxidation shifts 240 mV upon varying the substituent at the 4-position of the *meso* aryl ring from methoxy to trifluoromethyl.[14] In that study, Ghosh concluded that the electron was removed from a corrole orbital with substantial density at the *meso* positions (i.e., the b_1 orbital). For comparison, the metal-centred Mn^{III}/Mn^{II} reduction wave shifts only 50 mV by changing the 4-position of the *meso* aryl rings on the porphyrin ligand from methoxy to fluoro.[30]

We have presented a series of complementary spectroscopic experiments in order to assign the electronic structure of Cu corroles. We find that the ground state of Cu corroles is best described as an antiferromagnetically coupled Cu^{II} corrole radical cation, consistent with computational predictions. Strikingly, we demonstrate that the Cu^{II} oxidation state is maintained upon oxidation and reduction of the complex, with the macrocycle bearing the oxidizing and reducing equivalents. The Cu^{II} centre is preserved in each of these derivatives, underscoring the non-innocence of the corrole ligand in these complexes.

Acknowledgements

This work is supported by the U.S. Department of Energy Office of Science, Office of Basic Energy Sciences under Award No. DE-SC0009758. Funds were also provided by the TomKat Foundation. C.M.L. acknowledges the National Science Foundation's Graduate Research Fellowship Program and D.C.P. acknowledges a Ruth L. Kirchenstein National Research Service award (F32GM103211). We thank Dr. Kwabena Bediako for helpful discussions of the electrochemical data and Dr. Ryan Hadt for assistance with DFT calculations. We thank Dr. Yu-Sheng Chen for assistance with X-ray crystallography at ChemMatCARS, APS. ChemMatCARS Sector 15 is principally supported by the NSF/DOE under grant number NSF/CHE-1346572 and under Contract No. DE-AC02-06CH11357.

Keywords: computational chemistry · copper corroles · electronic structure · ligand non-innocence · redox chemistry

How to cite: *Angew. Chem. Int. Ed.* **2016**, *55*, 2176–2180
Angew. Chem. **2016**, *128*, 2216–2220

[1] A. W. Johnson, I. T. Kay, *J. Chem. Soc.* **1965**, 1620–1629.
[2] A. W. Johnson, *Pure Appl. Chem.* **1971**, *28*, 195–217.
[3] N. S. Hush, J. M. Dyke, *J. Inorg. Nucl. Chem.* **1973**, *35*, 4341–4347.
[4] N. S. Hush, J. M. Dyke, *J. Chem. Soc. Dalton Trans.* **1974**, 395–399.

[5] S. Will, J. Lex, E. Vogel, H. Schmickler, J. P. Gisselbrecht, C. Haubtmann, M. Bernard, M. Gross, *Angew. Chem. Int. Ed. Engl.* **1997**, *36*, 357 – 361; *Angew. Chem.* **1997**, *109*, 367 – 371.
[6] M. Bröring, F. Brégier, E. C. Tejero, C. Hell, M. C. Holthausen, *Angew. Chem. Int. Ed.* **2007**, *46*, 445 – 448; *Angew. Chem.* **2007**, *119*, 449 – 452.
[7] A. B. Alemayehu, E. Gonzalez, L. K. Hansen, A. Ghosh, *Inorg. Chem.* **2009**, *48*, 7794 – 7799.
[8] K. E. Thomas, J. Conradie, L. K. Hansen, A. Ghosh, *Eur. J. Inorg. Chem.* **2011**, 1865 – 1870.
[9] K. E. Thomas, A. B. Alemayehu, J. Conradie, C. M. Beavers, A. Ghosh, *Acc. Chem. Res.* **2012**, *45*, 1203 – 1214.
[10] A. B. Alemayehu, L. K. Hansen, A. Ghosh, *Inorg. Chem.* **2010**, *49*, 7608 – 7610.
[11] K. Pierloot, H. Zhao, S. Vancoillie, *Inorg. Chem.* **2010**, *49*, 10316 – 10329.
[12] A. Alemayehu, J. Conradie, A. Ghosh, *Eur. J. Inorg. Chem.* **2011**, 1857 – 1864.
[13] W. Sinha, M. G. Sommer, N. Deibel, F. Ehret, M. Bauer, B. Sarkar, S. Kar, *Angew. Chem. Int. Ed.* **2015**, *54*, 13769 – 13774; *Angew. Chem.* **2015**, *127*, 13973 – 13978.
[14] I. H. Wasbotten, T. Wondimagegn, A. Ghosh, *J. Am. Chem. Soc.* **2002**, *124*, 8104 – 8116.
[15] I. Luobeznova, L. Simkhovich, I. Goldberg, Z. Gross, *Eur. J. Inorg. Chem.* **2004**, 1724 – 1732.
[16] C. Brückner, R. P. Briñas, J. A. K. Bauer, *Inorg. Chem.* **2003**, *42*, 4495 – 4497.
[17] S. Nardis, G. Pomarico, F. R. Fronczek, M. G. H. Vicente, R. Paolesse, *Tetrahedron Lett.* **2007**, *48*, 8643 – 8646.
[18] G. Pomarico, X. Xiao, S. Nardis, R. Paolesse, F. R. Fronczek, K. M. Smith, Y. Fang, Z. Ou, K. M. Kadish, *Inorg. Chem.* **2010**, *49*, 5766 – 5774.
[19] C. M. Lemon, D. G. Nocera, *Faraday Discuss.* **2015**, *185*, 249 – 266.
[20] C. M. Lemon, R. L. Halbach, M. Huynh, D. G. Nocera, *Inorg. Chem.* **2015**, *54*, 2713 – 2725.
[21] B. Le Guennic, T. Floyd, R. B. Galan, J. Autschbach, J. B. Keister, *Inorg. Chem.* **2009**, *48*, 5504 – 5511.
[22] F. A. Cotton, J. L. Eglin, C. A. James, R. L. Luck, *Inorg. Chem.* **1992**, *31*, 5308 – 5315.
[23] F. A. Cotton, J. L. Eglin, B. Hong, C. A. James, *Inorg. Chem.* **1993**, *32*, 2104 – 2106.
[24] W. E. Keyes, W. E. Swartz, T. M. Loehr, *Inorg. Chem.* **1978**, *17*, 3316.
[25] P. C. Healy, S. Myhra, A. M. Stewart, *Jpn. J. Appl. Phys.* **1987**, *26*, L1884 – L1887.
[26] A. M. Romine, N. Nebra, A. I. Konovalov, E. Martin, J. Benet-Buchholz, V. V. Grushin, *Angew. Chem. Int. Ed.* **2015**, *54*, 2745 – 2749; *Angew. Chem.* **2015**, *127*, 2783 – 2787.
[27] J. P. Snyder, *Angew. Chem. Int. Ed. Engl.* **1995**, *34*, 80 – 81; *Angew. Chem.* **1995**, *107*, 112 – 113.
[28] A. C. Tsipis, *RSC Adv.* **2014**, *4*, 32504 – 32529.
[29] K. E. Thomas, H. Vazquez-Lima, Y. Fang, Y. Song, K. J. Gagnon, C. M. Beavers, K. M. Kadish, A. Ghosh, *Chem. Eur. J.* **2015**, *21*, 16839 – 16847.
[30] K. M. Kadish, M. M. Morrison, *Bioelectrochem. Bioenerg.* **1976**, *3*, 480 – 490.

Received: September 30, 2015
Revised: November 10, 2015
Published online: January 6, 2016

ORGANOMETALLICS

Article

pubs.acs.org/Organometallics

Electrocatalytic H_2 Evolution by Proton-Gated Hangman Iron Porphyrins

Daniel J. Graham and Daniel G. Nocera*

Department of Chemistry and Chemical Biology, Harvard University, 12 Oxford Street, Cambridge, Massachusetts 02138, United States

Supporting Information

ABSTRACT: The ability to control proton translocation is essential for optimizing electrocatalytic reductions in acidic solutions. We have synthesized a series of new hangman iron porphyrins with hanging groups of differing proton-donating abilities and evaluated their electrocatalytic hydrogen-evolving ability using foot-of-the-wave analysis. In the presence of excess triphenylphosphine, iron porphyrins initiate proton reduction electrocatalysis upon reduction to Fe^{I}. By changing the proton-donating ability of the hanging group, we can affect the rate of catalysis by nearly 3 orders of magnitude. The presence of an acid/base moiety in the second coordination sphere results in a marked increase in turnover frequency when extrapolated to zero overpotential.

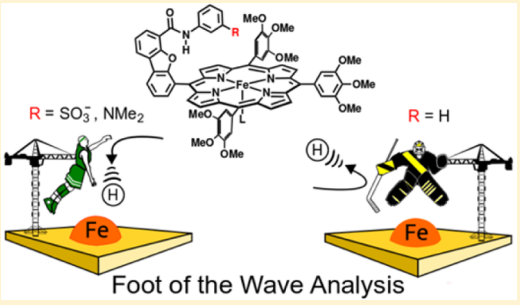

INTRODUCTION

The potential utility of hydrogen (H_2) as a form of renewable energy storage continues to drive the development of catalysts to promote its catalytic generation from acidic solutions. Complexes comprising earth-abundant transition-metals have been studied extensively as electrocatalysts for H_2 evolution and are of particular interest due to their noncriticality.[1−4] The placement of an acid/base moiety in the second coordination sphere of metal redox platforms has been shown by our group[5−16] and others[17−27] to facilitate proton-coupled electron transfer (PCET) at the metal-bound substrate, especially in the context of electrocatalytic H_2 production.

Iron porphyrins are competent and efficient electrocatalysts for the reduction of protons[28] and CO_2.[29−31] We have recently synthesized a series of iron complexes based on hanging dibenzofuran porphyrins (HPDs).[32] These new HPDs, shown in Scheme 1, allow for the modular installation of a wide range of pendant acid/base moieties, which are sterically imposing. In combination with a phosphine to occupy the "non-hangman" face of the reduced porphyrin, these hangman porphyrins channel protons from solution to the catalyst active site via the pendant acid/base group. In our study of the catalytic efficacy of these new hangman porphyrins, we have employed foot-of-the-wave analysis (FOWA), developed by Costentin and Savéant.[33] FOWA is a useful tool for evaluating the activity of a molecular, homogeneous electrocatalyst even when it is obscured by substrate consumption, catalyst decomposition, or product inhibition. As of yet, FOWA has only been used in a few cases to analyze the electrocatalytic reduction of CO_2 to CO[33−39] and the reduction of protons to H_2.[40] Herein, we apply FOWA to electrocatalytic proton reduction on iron hangman porphyrins in order to evaluate the turnover frequency (TOF) and the effect of a pendant proton donor.

EXPERIMENTAL SECTION

General Considerations. Acetonitrile (CH_3CN) was purified by passage through alumina[41] and was stored over activated 3 Å molecular sieves under nitrogen. Tetraethylammonium *p*-toluenesulfonate ($[TEA^+][TsO^-]$) and tetraethylammonium tetrafluoroborate ($[TEA^+][BF_4^-]$) were purchased from Alfa Aesar and recrystallized prior to use. $[TEA^+][BF_4^-]$ was purified by dissolving in CH_3CN, adding ethanol until saturation was achieved, and placing in the refrigerator for recrystallization. The crystals were washed with cold ethanol, dried at 100 °C in vacuo overnight, and stored under nitrogen. $[TEA^+][TsO^-]$ was purified by dissolving in minimal ethanol, adding ethyl acetate until saturation was achieved, and placing in the refrigerator for recrystallization. The crystals were washed with cold ethyl acetate, dried at 100 °C in vacuo overnight, and stored under nitrogen. Tetrafluoroboric acid etherate was purchased from Alfa Aesar and used as received. Triethylamine (NEt_3), methanol, benzene, ethanol, ethyl acetate, $FeBr_2$ (98%), and anhydrous $FeCl_2$ beads (99.99%) were purchased from Sigma-Aldrich and were used as received. Triphenylphosphine (PPh_3) was purchased from Strem, recrystallized from hexanes, and dried in vacuo prior to use. All porphyrins were synthesized according to published procedures.[32] The microwave-assisted reactions were performed inside the cavity of a CEM Discover microwave synthesis system equipped with infrared, pressure, and temperature sensors for monitoring the synthesis. The reaction vessels were 35 mL crimp-sealed thick-walled glass tubes. The contents of each vessel were stirred with a magnetic stirrer. Absorption spectral measurements were made on 5 μM solutions of each iron porphyrin in acetonitrile using a Cary 5000 UV−vis−NIR spectrometer from Varian employing the software Cary WinUV. Quartz cells with a 10 mm path length were used. Electrospray ionization mass spectra (ESI-MS) were obtained using a Bruker

Special Issue: Organometallic Electrochemistry

Received: March 23, 2014
Published: August 4, 2014

   dx.doi.org/10.1021/om500300e | *Organometallics* 2014, 33, 4994−5001

Scheme 1. Method for Iron Insertion To Furnish Iron Porphyrins

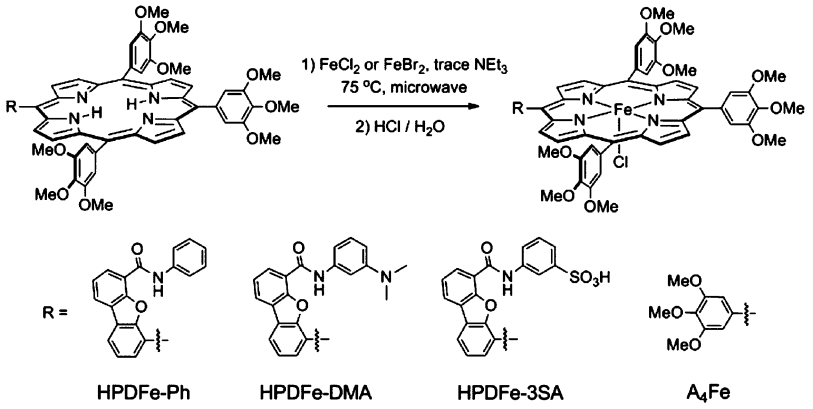

micrOTOF-QII instrument. Mass spectra were generated using mMass.[42] Elemental analyses were not collected, as they provide little insight into the purity of hangman porphyrins (see the Supporting Information).

Preparation of [5-(6-(Dibenzofuran-4-*N*-(phenyl)-carboxamide))-10,15,20-tris(3,4,5-trimethoxyphenyl)-porphyrinato]iron(III) Chloride (HPDFe-Ph). Free base hangman porphyrin (5-(6-(dibenzofuran-4-*N*-(phenyl)carboxamide))-10,15,20-tris(3,4,5-trimethoxyphenyl)porphyrin), 75 mg, 69 μmol) and freshly ground $FeCl_2$ (173 mg, 1.37 mmol, 20.0 equiv) were dissolved in 15 mL of CH_3CN and transferred to a 35 mL microwave reactor tube. A small amount of NEt_3 (0.05 mL) was added to the solution, the tube was capped, and microwave irradiation proceeded for 1 h at 70 °C. The solution was analyzed by TLC, and no red fluorescence (indicative of free base porphyrin) was detected. The solution was transferred to a separatory funnel containing 100 mL of EtOAc. The organic layer was washed with 1 M HCl/H_2O (2 × 100 mL), H_2O (1 × 100 mL), and brine (1 × 100 mL), dried over Na_2SO_4, and dried in vacuo. The solids were dissolved in dichloromethane (DCM) (2% MeOH), loaded onto a silica column packed with DCM (2% MeOH), and eluted with DCM (2% MeOH). The major brown band was collected. The volatiles were removed, the solids were dissolved in DCM which was covered in 1 M HCl/H_2O, and the solution was stirred thoroughly for 4 h. The organic layer was dried over Na_2SO_4, and the volatiles were removed. The solids were dissolved in benzene and filtered through filter paper. The volatiles were removed, and the solids were sonicated in pentane (3 × 5 mL) then dried at 80 °C in vacuo. Yield: 45.6 mg (83.5%). ESI-MS (m/z): $[M - Cl^-]^+$ calcd (found) 1147.31 (1147.3013). $\lambda_{max,abs}$/nm (ε/M^{-1} cm^{-1}) (MeCN): 380 (5.7×10^4), 423 (1.1×10^5), 577 (5.4×10^3).

Preparation of [5-(6-(Dibenzofuran-4-*N*-(3-dimethylaminophenyl)carboxamide))-10,15,20-tris(3,4,5-trimethoxyphenyl)porphyrinato]iron(III) Chloride (HPDFe-DMA). Free base hangman porphyrin (5-(6-(dibenzofuran-4-*N*-(3-dimethylaminophenyl)carboxamide))-10,15,20-tris(3,4,5-trimethoxyphenyl)porphyrin), 50.0 mg, 44.0 μmol) and freshly ground $FeCl_2$ (111 mg, 0.880 mmol, 20 equiv) were dissolved in 15 mL of CH_3CN and transferred to a 35 mL microwave reactor tube. A small amount of NEt_3 (0.05 mL) was added to the solution, the tube was capped, and microwave irradiation proceeded for 1 h at 70 °C. The solution was analyzed by TLC, and no red fluorescence (indicative of free base porphyrin) was detected. The solution was transferred to a separatory funnel containing 100 mL of EtOAc. The organic layer was washed with 1 M HCl/H_2O (2 × 100 mL), H_2O (1 × 100 mL), and brine (1 × 100 mL), dried over Na_2SO_4, and dried in vacuo. The solids were dissolved in DCM (2% MeOH, 2% NEt_3), loaded onto a silica column packed with DCM (2% MeOH, 2% NEt_3), and eluted with DCM (2% MeOH, 2% NEt_3). The major brown band was collected. The volatiles were removed, the solids were dissolved in DCM which was covered in 1 M HCl/H_2O, and and the solution was stirred thoroughly for 4 h. The organic layer was dried over Na_2SO_4, and the volatiles were removed. The solids were dissolved in benzene and filtered through filter paper. The volatiles were removed, and the solids were sonicated in pentane (3 × 5 mL) then dried at 80 °C in vacuo. Yield: 35.6 mg (66%). ESI-MS (m/z): $[M + H^+]^+$ calcd (found) 1226.33 (1226.3250); $[M - Cl^-]^+$ calcd (found) 1190.35 (1190.3503). $\lambda_{max,abs}$/nm (ε/M^{-1} cm^{-1}) (MeCN): 422 (1.5×10^5), 573 (7.1×10^3).

Preparation of [5-(6-(Dibenzofuran-4-(3-*N*-carboxamido)-benzenesulfonic acid))-10,15,20-tris(3,4,5-trimethoxyphenyl)-porphyrinato]iron(III) Chloride (HPDFe-3SA). Free base hangman porphyrin (5-(6-(dibenzofuran-4-(3-*N*-carboxamido)benzenesulfonic acid))-10,15,20-tris(3,4,5-trimethoxyphenyl)porphyrin), 36.0 mg, 30.6 μmol) and freshly ground $FeCl_2$ (77.4 mg, 0.614 mmol, 20.0 equiv) were dissolved in 15 mL of CH_3CN and transferred to a 35 mL microwave reactor tube. A small amount of NEt_3 (0.05 mL) was added to the solution, the tube was capped, and microwave irradiation proceeded for 1 h at 70 °C. The solution was analyzed by TLC, and no red fluorescence (indicative of free base porphyrin) was detected. The solution was transferred to a separatory funnel containing 100 mL of EtOAc. The organic layer was washed with 1 M HCl/H_2O (2 × 100 mL) and H_2O (2 × 100 mL) and dried in vacuo. The solids were dissolved in DCM (10% MeOH), loaded onto a silica column packed with DCM (10% MeOH), and eluted with DCM (15% MeOH). The major brown band was collected. The volatiles were removed, the solids were dissolved in DCM which was covered in 1 M HCl/H_2O, and the solution was stirred thoroughly for 4 h. The organic layer was filtered through filter paper, the volatiles were removed, and the solids were sonicated in pentane (3 × 5 mL) then dried at 80 °C in vacuo. Yield: 30.7 mg (79.3%). ESI-MS (m/z): $[M - Cl^-]^+$ calcd (found): 1227.27 (1227.2618). $\lambda_{max,abs}$/nm (ε/M^{-1} cm^{-1}) (MeCN): 381 (7.4×10^4), 423 (1.4×10^5), 579 (6.8×10^3).

Preparation of [Tetrakis(3,4,5-trimethoxyphenyl)-porphyrinato]iron(III) Chloride (A_4Fe). Free base A_4 porphyrin (123 mg, 126 μmol) and $FeBr_2$ (318 mg, 2.52 mmol, 20.0 equiv) were dissolved in 15 mL of CH_3CN and transferred to a 35 mL microwave reactor tube. A small amount of NEt_3 (0.05 mL) was added to the solution, the tube was capped, and microwave irradiation proceeded for 1 h at 70 °C. The solution was analyzed by TLC, and no red fluorescence (indicative of free base porphyrin) was detected. The solution was transferred to a separatory funnel containing 100 mL of EtOAc. The organic layer was washed with 1 M HCl/H_2O (2 × 100 mL), H_2O (1 × 100 mL), and brine (1 × 100 mL), dried over Na_2SO_4, and dried in vacuo. The solids were dissolved in DCM (2% MeOH), loaded onto a silica column packed with DCM (2% MeOH), and eluted with DCM (2% MeOH). The major brown band was collected. The volatiles were removed, the solids were dissolved in DCM which was covered in 1 M HCl/H_2O, and the solution was stirred thoroughly for 4 h. The organic layer was dried over Na_2SO_4, and the volatiles were removed. The solids were dissolved in benzene and filtered through filter paper. The volatiles were removed, and the solids were sonicated in pentane (3 × 5 mL) then dried at 80 °C in vacuo. Yield: 112 mg (83.5%). ESI-MS (m/z): $[M - Cl^-]^+$ calcd (found) 1028.29

dx.doi.org/10.1021/om500300e | *Organometallics* 2014, 33, 4994−5001

(1028.2819). $\lambda_{max,abs}$/nm (ε /M^{-1} cm^{-1})) (MeCN): 379 (6.3 × 10^4), 422 (1.2 × 10^5), 577 (4.8 × 10^3).

Cyclic Voltammetry. All studies were conducted under a nitrogen atmosphere using a CHInstruments 730C potentiostat. All CV measurements were performed in an oven-dried conical glass cell purchased from BASi. Working solutions were prepared from 1 mL of a 1 mM iron porphyrin stock solution in CH_3CN (0.1 M electrolyte) combined with 0.4 mL of 0.2 M stock solution of PPh_3 in CH_3CN (0.1 M electrolyte) and 0.6 mL of CH_3CN (0.1 M electrolyte) to make the 0.5 mM iron porphyrin solution. HBF_4 was added from a 0.2 M stock solution in CH_3CN (0.1 M electrolyte). The working electrode for cyclic voltammetry was a 0.7 cm^2 glassy-carbon disk, which was polished before each series of CVs with 50 nm alumina, sonicated in 18 MΩ water, and rinsed with methanol before being dried with compressed air. The pseudoreference electrode was a polished Ag wire encased in a glass container immersed in CH_3CN containing a 0.1 M solution of the supporting electrolyte; the reference and working electrode compartments were separated by a Vycor frit. The counter electrode was a Pt wire. All potentials were referenced to Fc^+/Fc. In [TEA^+][TsO^-] solutions, acid titrations were carried out with the addition of HBF_4·OEt_2, exploiting the large difference in pK_as of TsOH (8.6) and HBF_4 (0.1) in CH_3CN to generate TsOH and its homoconjugate in situ.

Bulk Electrolysis. Four milliliters of CH_3CN (0.1 M [TEA^+][TsO^-]) containing 20 mM PPh_3 and 10 mM [H^+] (added in the form of HBF_4) was placed in the auxiliary compartment of a small H-cell consisting of ca. 10 mL compartments separated by porous glass, which were custom-made by James Glass (www.jamesglass.com). A Pt-mesh counter electrode and Ag-wire pseudoreference electrode (in a glass compartment containing CH_3CN (0.1 M [TEA^+][TsO^-]) separated from the auxiliary solution by a Vycor frit) were placed in the auxiliary compartment. Four milliliters of CH_3CN (0.1 M [TEA^+][TsO^-]) containing 0.25 mM iron porphyrin, 20 mM PPh_3, and 10 mM [H^+] (added in the form of HBF_4) was placed in the working compartment. A glassy-carbon rod (connected to Cu wire which was inserted through a silicone 14/20 septum) and a stirbar were inserted into the working compartment. The working compartment was sealed with a silicone septum. The solution resistance was countered with *iR* compensation. A CV was collected, and controlled-potential electrolysis was performed at the foot of the catalytic wave with vigorous stirring. After sufficient current was passed (2−4 C), the electrolysis was halted, and 50 μL of the headspace of the working electrode was injected into a gas chromatograph to detect the presence of H_2. The Faradaic efficiency was calculated using a calibration curve constructed using multiple injections of 1%, 3%, and 5% H_2 in N_2. The percentage of H_2 in the headspace of the working compartment after each bulk electrolysis was determined, and the total amount of H_2 in the headspace of the working compartment was calculated. The headspace volume was calculated by subtracting the volume of the working solution from the volume of the working compartment containing the glassy-carbon-disk electrode.

Foot-of-the-Wave Analysis. Data from the CVs of each iron porphyrin were analyzed by the methods developed by Costentin et al.[33] Observed currents from the catalytic waves were baseline corrected by subtracting the diffusion-limited current after the $Fe^{III/II}$ reduction (between −1.1 and −1.2 V vs Fc^+/Fc) and then divided by the peak current of the iron porphyrins in the absence of H^+ (i_p°), which was baseline corrected in the same manner. Slopes at the foot of the wave were obtained from linear fits of all data $1 < (i/i_p^\circ) < 3$ for HPDFe-Ph and HPDFe-DMA, whereas slopes for HPDFe-3SA and A_4Fe were obtained from linear fits of all data $1 < (i/i_p^\circ) < 5$. The normalized current for catalytic enhancement was plotted vs $[1 + \exp((F/RT)(E - E^\circ)]^{-1}$, where E° is the half-wave potential for the $Fe^{II/I}$ reduction determined for each iron porphyrin in the absence of acid and E is the applied potential.

RESULTS AND DISCUSSION

Hangman porphyrins were synthesized from 3,4,5-trimethoxybenzaldehyde and dibenzofuran aldehyde.[32] Iron insertion into free base porphyrins was accomplished with microwave-assisted metalation (Scheme 1). In contrast to standard methods that use *N*,*N*-dimethylformamide (DMF) as the reaction solvent,[43,44] acetonitrile (CH_3CN) containing a trace amount of triethylamine (NEt_3) was an equally competent solvent system that delivered the desired product after 1 h of microwave irradiation (Scheme 1). Column chromatography, extensive washing with aqueous HCl, and rigorous drying at elevated temperatures in vacuo furnished the Fe^{III}Cl porphyrins in moderate yields as brown powders.

Cyclic voltammograms (CVs) of the Fe^{III}Cl porphyrins employed in this study display a quasi-reversible wave corresponding to $Fe^{III/II}$ reduction and loss of Cl^-, and two reversible waves attributed to the $Fe^{II/I}$ reduction and the $Fe^{I/"0"}$ reduction (Figure 1). A fourth reversible reduction is apparent

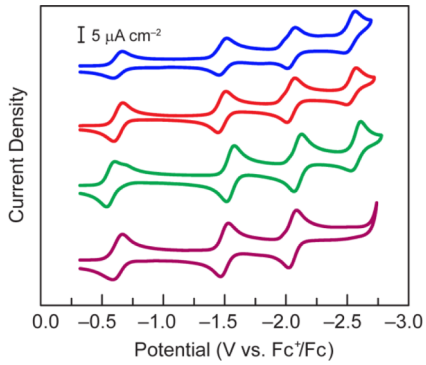

Figure 1. Cyclic voltammograms of 0.5 mM solutions of HPDFe-Ph (blue), HPDFe-DMA (red), HPDFe-3SA (green), and A_4Fe (purple) in CH_3CN (0.1 M [TEA^+][TsO^-]) with 40 mM PPh_3 at 50 mV/s.

for the hangman porphyrins and is most likely ligand based. All of the respective reduction potentials for the hangman iron porphyrin are within 120 mV of each other, which is expected for a homologous series of molecules that have similar redox centers (Table 1). Moreover, the reduction potentials of the

Table 1. $E_{1/2}$ Values for All Fe Porphyrins in the Absence of H^+

	$E_{1/2}$ (V vs Fc^+/Fc)			
compd	$Fe^{III/II}$	$Fe^{II/I}$	$Fe^{I/"0"}$	L/L^-
HPDFe-Ph	−0.629	−1.431	−2.046	−2.522
HPDFe-DMA	−0.632	−1.466	−2.040	−2.532
HPDFe-3SA	−0.567	−1.551	−2.098	−2.569
A_4Fe	−0.627	−1.499	−2.055	N/A

non-hangman A_4Fe are very similar to those of the hangman porphyrins, suggesting that dibenzofuran and 3,4,5-trimethoxyphenyl meso substitutions have similar electronic influences on the porphyrin.

Catalysis. Electrochemical experiments were conducted using CH_3CN as the solvent because the pK_a values of many common acids are known in CH_3CN.[45,46] Initial studies utilized tetraethylammonium tetrafluoroborate ([TEA^+][BF_4^-]) as the supporting electrolyte and *p*-toluenesulfonic acid (TsOH) as the proton source, but it was found that the onset potential for direct reduction of TsOH at a glassy-carbon electrode occurred at potentials significantly positive of the $Fe^{II/I}$ reduction potential (Figure S1, Supporting Information). Replacing the BF_4^- supporting anion by *p*-toluenesulfonate (TsO^-) dramat-

dx.doi.org/10.1021/om500300e | *Organometallics* 2014, 33, 4994−5001

ically reduced the proton discharge current (Figure S2, Supporting Information). The presence of 0.1 M TsO^- in solution suppresses the direct reduction of TsOH, presumably through its ability to form a hydrogen-bonded homoconjugate with an equilibrium constant of 790 M^{-1} (eq 1).[47−49] This

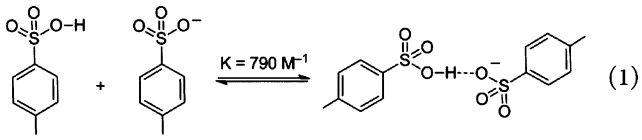

(1)

equilibrium essentially transforms the proton source into a negatively charged entity ($TsOH{\cdot}OTs^-$) and reduces the concentration of "free" TsOH to at most 2% of the total H^+ concentration for these studies (see SI). The effective pK_a of the homoconjugate may be obtained by adding the free energy of homoconjugate formation to the free energy of acid dissociation of TsOH, both of which can be determined from their respective equilibrium constants, resulting in a pK_a of 11.5, nearly 3 pK_a units higher than that of TsOH.

The addition of excess triphenylphosphine (PPh_3) was found to prevent additional, unwanted reduction events under acidic conditions and thus was present in excess at all times (Figure S3, Supporting Information). We note that protonated PPh_3 is not expected to be present in any meaningful concentrations, due to its pK_a in CH_3CN (7.6)[46] being 1 pK_a unit lower than that of TsOH, competing homoconjugate formation, and the abundance of TsO^- in solution. With acid concentrations higher than 20 mM, unwanted features in CVs of iron porphyrins were observed, even in the presence of 40 mM PPh_3, putting an upper limit on the acid concentration for this study. This upper limit is far below that needed to observe an S-shaped catalytic wave in the CV, which permits the most straightforward determination of the pseudo-first-order rate constant for the catalysts. In the absence of the S-shaped CV, FOWA permits the rate of catalysis at low concentrations of acid to be ascertained.

CVs of iron porphyrins in CH_3CN under these conditions display a catalytic wave that grows from the $Fe^{II/I}$ reduction wave upon addition of H^+ to solution (Figure 2). As the acid concentration increases, the catalytic wave slightly shifts to more positive potential as a consequence of facilitating protonation of the iron center upon reduction. Such shifts with acid concentration are well established from previous investigations.[16,49] Gas chromatographic analysis confirmed the presence of H_2 in the headspace of a two-compartment cell following controlled-potential electrolysis (Figures S5−S8, Supporting Information). Faradaic efficiencies were notably similar among working solutions utilizing HPDFe-Ph (66%), HPDFe-DMA (65%), HPDFe-3SA (65%), and A_4Fe (67%). The FOWA analysis allows for insight into the catalytic H_2-evolving activity of these systems, despite these nonideal Faradaic efficiencies.

The beneficial role of excess PPh_3 is thought to be 3-fold: (1) inducing a low-spin d^6 configuration of the Fe^{II}, thus preventing any side reactions that may occur between H^+ and intermediate- or high-spin Fe^{II} porphyrin, (2) physically blocking the "non-hangman" porphyrin face from acidic species in solution, and (3) providing a strong trans influence to increase the reactivity of Fe^I and any resulting Fe hydride. Given the ability of Fe^{II} porphyrins to bind two axial phosphines,[50] one would expect excess PPh_3 to hinder further

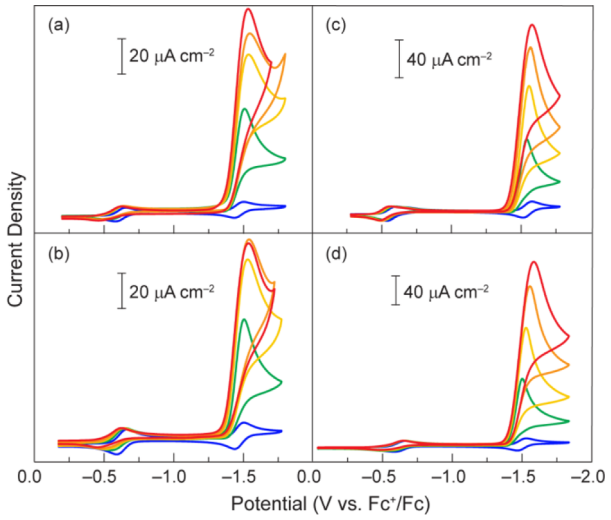

Figure 2. Cyclic voltammograms of 0.5 mM solutions of (a) HPDFe-Ph, (b) HPDFe-DMA, (c)HPDFe-3SA, and (d) A_4Fe in the presence of 0 mM (blue), 5 mM (green), 10 mM (yellow), 15 mM (orange), and 20 mM (red) of H^+ (from added HBF_4). Conditions: 40 mM PPh_3 in CH_3CN (0.1 M $[TEA^+][TsO^-]$) at 50 mV/s.

reduction to five-coordinate Fe^I, since it would require an additional chemical step (PPh_3 dissociation). CVs of A_4Fe in the presence of various concentrations of PPh_3 indicate that both the $Fe^{III/II}$ and $Fe^{II/I}$ half-wave potentials are hardly affected by increasing concentrations of phosphine and remain electrochemically reversible, even when there is no obstruction to inhibit axial ligand binding (Figure S4, Supporting Information). The probable explanation for this behavior is the existence of a fast equilibrium between five- and six-coordinate Fe^{II}. We posit that the presence of an imposing hanging group is likely to shift the equilibrium toward five-coordinate Fe^{II}, with one PPh_3 on the non-hangman face of the porphyrin, consistent with previous observations of low-spin, five-coordinate Fe^{II} porphyrin where binding is disfavored on one porphyrin face.[51]

In previous studies of the reduction of weak acids by iron porphyrins, catalysis was reported to occur upon reduction of the iron porphyrin unit to a formal "Fe^0" oxidation state.[28] The nature of "Fe^0" has been studied by crystallography[52] and by NMR techniques;[53] the commonly accepted electronic configuration is a d^7 Fe^I ion ligated by a porphyrin-based radical anion (Fe^IPorph^{-1}). This ligand-based radical anion can act as a nucleophile, resulting in decomposition or deactivation of the catalyst.[54,55] Using strong acids that react with the iron porphyrin at the Fe^I oxidation state, our iron porphyrins generate H_2 at more positive potentials while bypassing deleterious porphyrin-based radicals.

The catalytic current at the Fe^{II}/Fe^I reduction potential suggests that Fe^I is the species that undergoes protonation. However, the question remains as to whether the Fe^I species reacts via the metal center or the porphyrin ligand, as the electronic configuration of reduced metalloporphyrins is sensitive to a number of factors. Fe^I porphyrins may have ligand-based radical character in the solid state,[52] but solution EPR studies suggest that axially ligated Fe^I porphyrins are d^7 species containing an unpaired electron in the Fe d_{z^2} orbital with no observed radical character on the porphyrin ring (provided there are only meso substituents on the porphyrin periphery).[56,57] The fact that extended controlled-potential

dx.doi.org/10.1021/om500300e | Organometallics 2014, 33, 4994−5001

electrolysis did not result in a green solution (indicative of porphyrin ring reduction) leads us to believe that ligand-based reactions do not occur and direct protonation of Fe^{I} is the first chemical step during catalysis, as indicated in Scheme 2. The

Scheme 2. Proposed Catalytic Mechanism

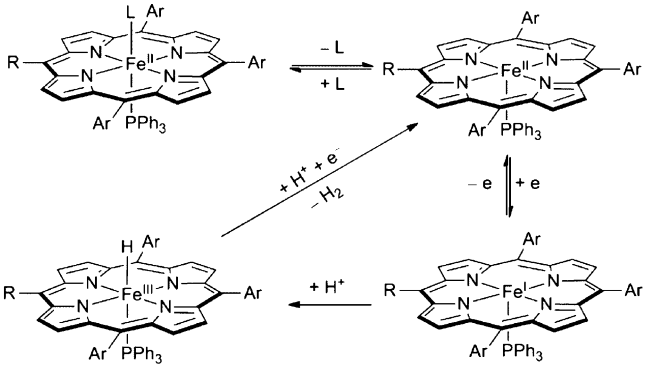

appearance of catalysis at the Fe^{II}/Fe^{I} suggests that $Fe^{III}H$ may be hydridic enough to react with H^+. Studies to measure the hydricity of a $Fe^{III}H$ porphyrin are currently underway.

Foot-of-the-Wave Analysis. All iron porphyrins in this study are catalytically active for the reduction of $TsOH{\cdot}OTs^-$ at the $Fe^{II/I}$ reduction potential, but differences in catalytic behavior are not immediately apparent from CVs. FOWA allows one to quantify catalytic activity in the absence of any catalyst decomposition or extensive substrate consumption that may occur.[33] FOWA can be applied to electrocatalytic proton reduction by iron porphyrin if it is assumed that the process begins with a fast electron transfer (eq 2), followed by a combination of chemical steps (eq 3) and regeneration of Fe^{II} porphyrin by electron transfer from an Fe^{I} porphyrin in solution (eq 4). Reduction of Fe^{III} by Fe^{I} in solution, rather than the electrode, is more likely when catalysis is relatively slow in comparison to electron transfer.

$$Fe^{II} \rightleftharpoons Fe^{I} \tag{2}$$

$$Fe^{I} + 2H^{+} \rightarrow Fe^{III} + H_2 \tag{3}$$

$$Fe^{I} + Fe^{III} \rightarrow 2Fe^{II} \tag{4}$$

Since the $Fe^{II/I}$ reduction is reversible and $E_{1/2}(Fe^{II}/Fe^{I})$ is known, the concentration of active catalyst (Fe^{I}) for every potential is given by the Nernst equation; additional current observed at potentials near $E_{1/2}(Fe^{II}/Fe^{I})$ is due to catalysis. The concentration of substrate at the electrode decreases as catalysis progresses, thereby affecting the observed rate of catalysis. By analyzing the beginning (foot) of the catalytic wave, the activity of the catalyst may be ascertained before significant substrate consumption occurs. In order to analyze the foot of the wave, a plot of the catalytic enhancement (current (i) as a fraction of the $Fe^{II/I}$ reduction wave peak current in the absence of substrate (i_p°)) as a function of $[1 + \exp((F/RT)(E - E^\circ)]^{-1}$ (where $E^\circ = E_{1/2}(Fe^{II}/Fe^{I})$) allows us to classify catalyst behavior (Figure 3). Invoking the steady-state approximation for the catalytic intermediates allows us to use eq 5 to determine the apparent rate constant, k, representing the combination of the steps corresponding to eq 3.

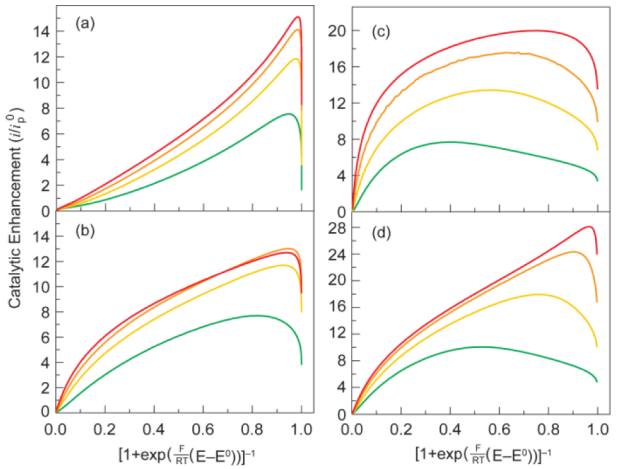

Figure 3. Foot-of-the-wave analyses of (a) HPDFe-Ph, (b) HPDFe-DMA, (c) HPDFe-3SA, and (d) A_4Fe using the CVs displayed in Figure 1. Concentrations of H^+ (from added HBF_4) are 5 mM (green), 10 mM (yellow), 15 mM (orange), and 20 mM (red).

$$\frac{i}{i_p^\circ} = \frac{2.24\sqrt{\frac{RT}{F\nu}2kC_{H^+}}}{1 + \exp\left[\frac{F}{RT}(E - E^\circ)\right]} \tag{5}$$

In the cases of HPDFe-DMA, HPDFe-3SA, and A_4Fe, FOWA shows a curve that deviates from the initial trajectory. This behavior is consistent with modeled examples of rapid substrate consumption near the electrode, which limits the catalytic current.[33] FOWA of HPDFe-Ph results in nearly linear plots, suggesting that this catalyst consumes H^+ much more slowly than the other catalysts in this study.

Values of k are obtained from linearizing the curves in Figure 2 at early points on the graph, which have slopes of $2.24((RT/F\nu)2kC_{H^+})^{1/2}$ (Table 2). These values of k show little to no

Table 2. Values of log k for All Catalysts at Different H^+ Concentrations[a]

	log k (M^{-1} s^{-1})			
compd	5 mM[b]	10 mM[b]	15 mM[b]	20 mM[b]
HPDFe-Ph	3.74	3.72	3.69	3.66
HPDFe-DMA	4.25	4.43	4.48	4.53
HPDFe-3SA	5.06	5.44	5.81	6.12
A_4Fe	4.96	5.02	5.08	5.17

[a]Values were obtained from the foot-of-the-wave slope per eq 5. All experiments were conducted under an atmosphere of N_2 in CH_3CN (0.1 M $[TEA^+][TsO^-]$) containing 0.5 mM iron porphyrin. All scans were performed at 50 mV/s. [b]H^+ concentration from added HBF_4 (to generate TsOH and its homoconjugate in situ).

variation over a range of scan rates (Figure S17, Supporting Information). When comparing the activity of the iron porphyrins in the presence of a 40-fold excess of H^+, we see a clear trend between the proton-donating ability and k. While no direct measurements of the hanging group pK_as were made, we can approximate them from the pK_a of related acids in CH_3CN. With their N-bound carboxamide, the sulfonic acid in HPDFe-3SA and *N,N*-dimethylanilinium in HPDFe-DMA should have pK_as slightly higher than that of TsOH and *N,N*-dimethylanilinium ($pK_a(CH_3CN)$ = 8.6 and 11.5, respectively).[45] The apparent rate of catalysis is higher for hangman

dx.doi.org/10.1021/om500300e | *Organometallics* 2014, 33, 4994–5001

porphyrins that are able to transfer a proton to the metal center in an intramolecular fashion.

HPDFe-3SA is by far the highest performing catalyst, most likely due to its ability to undergo intramolecular, rather than intermolecular, H^+ transfer from a sulfonic acid, a phenomenon which has been studied computationally and shows that a reduced energetic barrier to proton transfer results when the proton is delivered intramolecularly.[58] In accordance with this result, the hangman effect results in a high local proton concentration that effectively requires an effective intermolecular concentration that is 10^3 greater than that needed for the proton-assisted intramolecular concentration.[16] When intramolecular proton transfer is retarded by increasing the hanging group pK_a, as in the case of HPDFe-DMA, we observe a large decrease in k in comparison to HPDFe-3SA. It is noteworthy that the hanging group of HPDFe-DMA is more often protonated under our conditions, whereas the hanging group in HPDFe-3SA has a lower pK_a and is less likely to be a protonated at any given time, yet HPDFe-3SA still operates more quickly than HPDFe-DMA and A_4Fe. HPDFe-Ph is the slowest of the catalysts and is much slower than A_4Fe, which also lacks a hanging acid/base moiety. This is expected only if direct protonation of HPDFe-Ph by H^+ in solution is inhibited by both PPh_3 on one face and the hanging group on the other.

Turnover Frequency. An accurate picture of a catalyst TOF is furnished from FOWA. The TOF varies with overpotential (η) according to eq 6. This equation accounts for the slight differences in $Fe^{II/I}$ reduction potentials and driving forces. By extrapolating the potential dependent TOF back to the standard reduction potential of the acid (E°_{HA/H_2}) (Figures S9–S16, Supporting Information), we can determine the TOF at zero overpotential ($TOF_0^{(2)}$) for each electrocatalyst at different acid concentrations (Table 3). $TOF_0^{(2)}$ can be thought of as the molecular catalyst's exchange current and can therefore be used to directly compare different electrocatalysts. $TOF_0^{(2)}$ can also be calculated by dropping the last term of eq 6 (since $\eta = 0$) and rearranging to get eq 7. $E_{HA/H_2}{}^\circ$ in our study has to be slightly modified from the standard reduction potential of TsOH, since the acid source in this study is primarily a homoconjugate. Taking into account the free energy of $TsOH{\cdot}OTs^-$ formation gives us an E_{HA/H_2} value of −0.71 V vs Fc^+/Fc (derived in the Supporting Information), which results in the values aggregated in Table 3. Using this calculated E_{HA/H_2} value, the iron porphyrins display an onset of catalytic current around 0.7 V overpotential.

Table 3. Values for $\log(TOF_0^{(2)})$ at Different H^+ Concentrations[a]

	$\log(TOF_0^{(2)})$ (M^{-1} s^{-1})			
compd	5 mM[b]	10 mM[b]	15 mM[b]	20 mM[b]
HPDFe-Ph	−8.41	−8.45	−8.50	−8.55
HPDFe-DMA	−8.52	−8.35	−8.29	−8.24
HPDFe-3SA	−9.17	−8.77	−8.41	−8.10
A_4Fe	−8.34	−8.31	−8.30	−8.32

[a]Values were obtained from eq 7. All experiments were conducted under an atmosphere of N_2 in CH_3CN (0.1 M $[TEA^+][TsO^-]$) containing 0.5 mM iron porphyrin. All scans were performed at 50 mV/s. [b]H^+ concentration from added HBF_4 (to generate TsOH and its homoconjugate in situ).

$$\log TOF^{(2)} = \log k - \frac{F}{RT \ln 10}(E^\circ_{HA/H_2} - E^\circ_{Fe^{II}/Fe^{I}}) - \frac{\eta F}{RT \ln 10} \quad (6)$$

$$TOF_0^{(2)} = \frac{k}{1 + \exp\left[\frac{F}{RT}(E^\circ_{HA/H_2} - E^\circ_{Fe^{II}/Fe^{I}})\right]} \quad (7)$$

The $TOF_0^{(2)}$ value of HPDFe-3SA changes drastically as the acid concentration is increased from 5 mM, where it has the lowest $TOF_0^{(2)}$ value, to 20 mM, where it outperforms all other catalysts. We attribute this behavior to the acid/base equilibrium between the hanging sulfonic acid on HPDFe-3SA and $TsOH{\cdot}OTs^-$. Even though the hanging *N,N*-dimethylanilinium in **HDFe-DMA** is a weaker proton donor than the hanging sulfonate in HPDFe-3SA, it has an advantage at lower H^+ concentrations because it effectively increases the local concentration of H^+ near the iron center, giving it a $TOF_0^{(2)}$ value higher than that for HPDFe-3SA. As the concentration of H^+ increases, the hanging sulfonate on HPDFe-3SA is more likely to be protonated and $TOF_0^{(2)}$ increases.

In the presence of 5 mM H^+, A_4Fe displays the highest $TOF_0^{(2)}$ value but shows little variation with increasing acid concentration. At 15 and 20 mM concentrations of acid, both HPDFe-DMA and HPDFe-3SA have higher values of $TOF_0^{(2)}$, suggesting that when the hanging group is more likely to be protonated, it outperforms non-hangman porphyrins. Additionally, the ability of the hanging phenyl group in HPDFe-Ph to impede the approach of H^+ sources may be discerned from its $TOF_0^{(2)}$ values at every acid concentration, which are consistently lower than those of A_4Fe. The $TOF_0^{(2)}$ value of HPDFe-Ph shows very little variation with increasing acid concentration, suggesting that the combination of excess PPh_3 and the steric profile of the hanging phenyl group is effective at shielding the iron center from $TsOH{\cdot}OTs^-$ or TsOH in solution.

FOWA analysis of electrocatalytic H_2 evolution using the hydrogenase models $[Fe_2(\mu\text{-bdt})(CO)_6]$ and $[Fe_2(\mu\text{-bdt})P(OMe)_3(CO)_5]$ (bdt = 1,2-benzenedithiolate) in CH_3CN[40] yields rates of catalysis lower than those observed here for the hangman iron porphyrins of this study. However, we note that $[Fe_2(\mu\text{-bdt})(CO)_6]$ operates at a ∼200 mV lower overpotential, which yields a higher intrinsic activity ($\log(TOF_0^{(2)}) = -7.03$) upon extrapolation back to the standard potential of the substrate. These results highlight the interplay between activity and overpotential and the importance of using FOWA to compare catalysts.

CONCLUSION

We have quantified the enhancement of catalytic activity toward hydrogen evolution that accompanies the placement of a proton donor in the second coordination sphere of iron porphyrins during electrocatalysis. In the presence of excess PPh_3, the hanging dibenzofuran porphyrins limit the exposure of the iron center to solution to such an extent that it modulates the rate of electrocatalytic hydrogen evolution by gating the flow of protons to the catalyst active site. The presence of an acid/base group in the second coordination sphere increases the rate of catalysis, with stronger pendant proton donors resulting in consistently faster proton reduction. On correction for differences in $Fe^{II/I}$ reduction potentials by

dx.doi.org/10.1021/om500300e | *Organometallics* 2014, 33, 4994–5001

determining the $TOF_0^{(2)}$ value, the higher performance as a result of the hangman effect is apparent at high concentrations of acid. Future studies will use recently reported methods[59] to determine the mechanism of proton reduction on iron porphyrins and exploit our ability to modulate the effective rate of proton transfer to the catalyst's active site. For instance, in cases where H_2 evolution represents a parasitic side reaction, such as carbon dioxide reduction,[60,61] nitrite reduction,[62−64] and olefin reduction[65] in the acidic solutions, we wish to tailor the rate of proton transfer to the catalyst active site in order to minimize parasitic evolution of H_2.

■ ASSOCIATED CONTENT

Supporting Information

Text, figures, and a table giving experimental procedures, cyclic voltammograms, mass spectra, gas chromatographs, UV−vis spectra, derivation of $E_{TsOH\cdot TsO^-/H_2}$, calculation of percent free TsOH, and the utility of elemental analysis for hangman porphyrins. This material is available free of charge via the Internet at http://pubs.acs.org.

■ AUTHOR INFORMATION

Corresponding Author

*E-mail for D.G.N.: dnocera@fas.harvard.edu.

Notes

The authors declare no competing financial interest.

■ ACKNOWLEDGMENTS

D.J.G. is grateful for funding from the NSF Graduate Research Fellowship Program and for productive discussions with Andrew Ullman and is deeply indebted to Dr. Cyrille Costentin for guidance. We are also grateful for funding from the DOE award number DE-SC0009758.

■ REFERENCES

(1) Thoi, V. S.; Sun, Y.; Long, J. R.; Chang, C. J. *Chem. Soc. Rev.* **2013**, *42*, 2388.
(2) McKone, J. M.; Marinescu, S. C.; Brunschwig, B. S.; Winkler, J. R.; Gray, H. B. *Chem. Sci.* **2014**, *5*, 865.
(3) Wang, M.; Chen, L.; Sun, L. *Energy Environ. Sci.* **2012**, *5*, 6763.
(4) Dempsey, J. L.; Brunschwig, B. S.; Winkler, J. R.; Gray, H. B. *Acc. Chem. Res.* **2009**, *12*, 1995.
(5) Rosenthal, J.; Nocera, D. G. *Acc. Chem. Res.* **2007**, *40*, 543.
(6) McGuire, R., Jr.; Dogutan, D. K.; Teets, T. S.; Suntivich, J.; Shao-Horn, Y.; Nocera, D. G. *Chem. Sci.* **2010**, *1*, 411.
(7) Dogutan, D. K.; Stoian, S. A.; McGuire, R., Jr.; Schwalbe, M.; Teets, T. S.; Nocera, D. G. *J. Am. Chem. Soc.* **2011**, *133*, 131.
(8) McGuire, R., Jr.; Dogutan, D. K.; Shao-Horn, Y.; Nocera, D. G. *J. Am. Chem. Soc.* **2011**, *133*, 9178.
(9) Soper, J. D.; Kryatov, S. V.; Rybak-Akimova, E. V.; Nocera, D. G. *J. Am. Chem. Soc.* **2007**, *129*, 5069.
(10) Chang, C. J.; Chng, L. L.; Nocera, D. G. *J. Am. Chem. Soc.* **2003**, *125*, 1866.
(11) Rosenthal, J.; Chng, L. L.; Fried, S. D.; Nocera, D. G. *Chem. Commun.* **2007**, 2642.
(12) Liu, S.-Y.; Nocera, D. G. *J. Am. Chem. Soc.* **2005**, *127*, 5278.
(13) Chng, L. L.; Chang, C. J.; Nocera, D. G. *Org. Lett.* **2003**, *5*, 2421.
(14) Schwalbe, M.; Dogutan, D. K.; Stoian, S. A.; Teets, T. S.; Nocera, D. G. *Inorg. Chem.* **2011**, *50*, 1368.
(15) Graham, D. J.; Dogutan, D. K.; Schwalbe, M.; Nocera, D. G. *Chem. Commun.* **2012**, *48*, 4175.
(16) Roubelakis, M. M.; Bediako, D. K.; Dogutan, D. K.; Nocera, D. G. *Energy Environ. Sci.* **2012**, *5*, 7737.
(17) Lee, C. H.; Dogutan, D. K.; Nocera, D. G. *J. Am. Chem. Soc.* **2011**, *133*, 8775.
(18) Appel, A. M.; Pool, D. H.; O'Hagan, M. J.; Shaw, W. J.; Yang, J. Y.; DuBois, M. R.; DuBois, D. L.; Bullock, R. M. *ACS Catal.* **2011**, *1*, 777.
(19) O'Hagan, M.; Ho, M.-H.; Yang, J. Y.; Appel, A. M.; DuBois, M. R.; Raugei, S.; Shaw, W. J.; DuBois, D. L.; Bullock, R. M. *J. Am. Chem. Soc.* **2012**, *134*, 19409.
(20) Monte, L.; Helm, M. L.; Stewart, M. P.; Bullock, R. M.; DuBois, M. R.; DuBois, D. L. *Science* **2011**, *333*, 863.
(21) DuBois, D. L.; Bullock, R. M. *Eur. J. Inorg. Chem.* **2011**, 1017.
(22) Yang, J. Y.; Bullock, R. M.; DuBois, M. R.; DuBois, D. L. *MRS Bull.* **2011**, *36*, 39.
(23) Baran, J. D.; Gronbeck, H.; Hellman, A. *J. Am. Chem. Soc.* **2014**, *136*, 1320.
(24) Zyska, B.; Schwalbe, M. *Chem. Commun.* **2013**, *49*, 3799.
(25) Lai, W. Z.; Cao, R.; Dong, G.; Shaik, S.; Yao, J.; Chen, H. *J. Phys. Chem. Lett.* **2012**, *3*, 2315.
(26) Mahammed, A.; Gross, Z. *Catal. Sci. Technol.* **2011**, *1*, 535.
(27) Natale, D.; Mareque-Rivas, J. C. *Chem. Commun.* **2008**, 425.
(28) Bhugun, I.; Lexa, D.; Savéant, J.-M. *J. Am. Chem. Soc.* **1996**, *118*, 3982.
(29) Hammouche, M.; Lexa, D.; Savéant, J.-M. *J. Electroanal. Chem.* **1988**, *249*, 347.
(30) Bhugun, I.; Lexa, D.; Savéant, J.-M. *J. Am. Chem. Soc.* **1994**, *116*, 5015.
(31) Bhugun, I.; Lexa, D.; Savéant, J.-M. *J. Phys. Chem.* **1996**, *100*, 19981.
(32) Graham, D. J.; Zheng, S.-L.; Nocera, D. G. *ChemSusChem* **2014**, DOI: 10.1002/cssc.201402242.
(33) Costentin, C.; Drouet, S.; Robert, M.; Savéant, J.-M. *J. Am. Chem. Soc.* **2012**, *134*, 19949.
(34) Costentin, C.; Drouet, S.; Robert, M.; Savéant, J.-M. *J. Am. Chem. Soc.* **2012**, *134*, 11235.
(35) Costentin, C.; Drouet, S.; Robert, M.; Savéant, J.-M. *Science* **2012**, *338*, 91.
(36) Costentin, C.; Robert, M.; Savéant, J.-M. *Chem. Soc. Rev.* **2013**, *42*, 2423.
(37) Costentin, C.; Drouet, S.; Passard, G.; Robert, M.; Savéant, J.-M. *J. Am. Chem. Soc.* **2013**, *135*, 9023.
(38) Elgrishi, N.; Chambers, M. B.; Artero, V.; Fontecave, M. *Phys. Chem. Chem. Phys.* **2014**, *16*, 13635.
(39) Teesdale, J. J.; Pistner, A. J.; Yap, G. P. A.; Ma, Y.-A.; Lutterman, D. A.; Rosenthal, J. *Catal. Today* **2014**, *225*, 149.
(40) Quentel, F.; Gloaguen, F. *Electrochim. Acta* **2013**, *110*, 641.
(41) Pangborn, A. B.; Giardello, M. A.; Grubbs, R. H.; Rosen, R. K.; Timmers, F. J. *Organometallics* **1996**, *15*, 1518.
(42) Strohalm, M.; Hassman, M.; Košata, B.; Kodíček, M. *Rapid Commun. Mass Spectrom.* **2008**, *22*, 905.
(43) Schwalbe, M.; Dogutan, D. K.; Stoian, S. A.; Teets, T. S.; Nocera, D. G. *Inorg. Chem.* **2011**, *50*, 1368.
(44) Graham, D. J.; Dogutan, D. K.; Schwalbe, M.; Nocera, D. G. *Chem. Commun.* **2012**, *48*, 4175.
(45) Kütt, A.; Leito, I.; Kaljurand, I.; Sooväli, L.; Vlasov, V. M.; Yagupolskii, L. M.; Koppel, I. A. *J. Org. Chem.* **2006**, *71*, 2829.
(46) Haav, K.; Saame, J.; Kütt, A.; Leito, I. *Eur. J. Org. Chem.* **2012**, 2167.
(47) Mecke, R. *Discuss. Faraday Soc.* **1950**, *9*, 161.
(48) French, C. M.; Roe, I. G. *Trans. Faraday Soc.* **1953**, *49*, 314.
(49) Fourmond, V.; Jacques, P.-A.; Fontecave, M.; Artero, V. *Inorg. Chem.* **2010**, *49*, 10338.
(50) Stynes, D. V.; Fletcher, D.; Chen, X. *Inorg. Chem.* **1986**, *25*, 3483.
(51) Ellis, P. E., Jr.; Jones, R. D.; Basolo, F. *J. Chem. Soc. Chem. Commun.* **1980**, *2*, 54.
(52) Mashiko, T.; Reed, C. A.; Haller, K. J.; Scheidt, W. R. *Inorg. Chem.* **1984**, *23*, 3192.
(53) Hickman, D. L.; Shirazi, A.; Goff, H. M. *Inorg. Chem.* **1985**, *24*, 563.
(54) Dhanasekaran, T.; Grodkowski, J.; Neta, P.; Hambright, P.; Fujita, E. *J. Phys. Chem. A* **1999**, *103*, 7742.

(55) Grodkowski, J.; Behar, D.; Neta, P. *J. Phys. Chem. A* **1997**, *101*, 248.
(56) Srivatsa, G. S.; Sawyer, D. T.; Boldt, N. J.; Bocian, D. F. *Inorg. Chem.* **1985**, *24*, 2123.
(57) Donohoe, R. J.; Atamian, M.; Bocian, D. F. *J. Am. Chem. Soc.* **1987**, *109*, 5593.
(58) Wang, Y.; Wang, M.; Sun, L.; Ahlquist, M. S. G. *Chem. Commun.* **2012**, *48*, 4450.
(59) Costentin, C.; Savéant, J.-M. *ChemElectroChem* **2014**, *1*, 1226.
(60) Rail, M. D.; Berben, L. A. *J. Am. Chem. Soc.* **2011**, *133*, 18577.
(61) Kang, P.; Cheng, C.; Chen, Z.; Schauer, C. K.; Meyer, T. J.; Brookhart, M. *J. Am. Chem. Soc.* **2012**, *134*, 5500.
(62) Toth, J. E.; Anson, F. C. *J. Am. Chem. Soc.* **1989**, *111*, 2451.
(63) Bryleva, O.; Sarrazina, M.; Rouéb, L.; Bélanger, D. *Electrochim. Acta* **2007**, *52*, 6237.
(64) Uyeda, C.; Peters, J. C. *J. Am. Chem. Soc.* **2013**, *135*, 12023.
(65) Rasnoshika, H.; Masarwaa, A.; Cohenab, H.; Zilbermann, I.; Maimon, E.; Meyerstein, D. *Dalton Trans.* **2010**, *39*, 823.

Role of pendant proton relays and proton-coupled electron transfer on the hydrogen evolution reaction by nickel hangman porphyrins

D. Kwabena Bediako[a], Brian H. Solis[b], Dilek K. Dogutan[a], Manolis M. Roubelakis[a], Andrew G. Maher[a], Chang Hoon Lee[a], Matthew B. Chambers[a], Sharon Hammes-Schiffer[b], and Daniel G. Nocera[a,1]

[a]Department of Chemistry and Chemical Biology, Harvard University, Cambridge, MA 02138-2902; and [b]Department of Chemistry, University of Illinois at Urbana–Champaign, Urbana, IL 61801

Contributed by Daniel G. Nocera, August 10, 2014 (sent for review June 24, 2014)

The hangman motif provides mechanistic insights into the role of pendant proton relays in governing proton-coupled electron transfer (PCET) involved in the hydrogen evolution reaction (HER). We now show improved HER activity of Ni compared with Co hangman porphyrins. Cyclic voltammogram data and simulations, together with computational studies using density functional theory, implicate a shift in electrokinetic zone between Co and Ni hangman porphyrins due to a change in the PCET mechanism. Unlike the Co hangman porphyrin, the Ni hangman porphyrin does not require reduction to the formally metal(0) species before protonation by weak acids in acetonitrile. We conclude that protonation likely occurs at the Ni(I) state followed by reduction, in a stepwise proton transfer–electron transfer pathway. Spectroelectrochemical and computational studies reveal that upon reduction of the Ni(II) compound, the first electron is transferred to a metal-based orbital, whereas the second electron is transferred to a molecular orbital on the porphyrin ring.

renewable | solar fuels | electrocatalysis

Solar-to-fuels conversions provide a path to harnessing the ubiquitous albeit intermittent renewable energy resource offered by the sun (1–6). Efficient catalysis of transformations of energy consequence (7–13) mandates the coupling of electron transfer (ET) to proton transfer (PT) in proton-coupled electron transfer (PCET) reactions (14–20). In the absence of PCET, intermediates possessing equilibrium potentials that are prohibitively large depreciate the storage capacity offered by the solar-to-fuels conversion process. The coupling of protons to changes in electron equivalency offers the possibility of restricting the equilibrium potentials of the redox steps to a more narrow potential range, thereby minimizing the overpotential required to sustain catalysis at a desired turnover rate. Thus, the exploitation of PCET pathways to permit potential-leveling effects is a crucial prerequisite for the efficient catalytic conversion reactions of energy relevant molecules.

PCET reactions may be classified into stepwise and concerted pathways (14, 16, 20, 21). Stepwise PCET may involve ET first followed by PT (ETPT), or PT followed by ET (PTET). In concerted proton–electron transfers (CPET), the proton and electron traverse a common transition state. Whereas concerted pathways avoid the formation of thermodynamically costly intermediates, CPET reactions may incur kinetic penalties associated with the requirements for proton tunneling (19, 20, 22). The competition between these dynamics during catalysis determines the most efficient route of reaction. Studies that explore the interplay between these factors are crucial to designing catalytic reactions of high efficiency. Along these lines, the incorporation of proton relays in the second coordination sphere of molecular catalysts has emerged as a useful tool in optimizing PCET transformations (23–29). We have focused on the synthesis and mechanistic investigation of a class of metalloporphyrin molecules attached to a xanthene backbone bearing a carboxylic acid functional group—"hangman" porphyrins (**1-M**, Scheme 1) (23, 30, 31). These hangman porphyrins have been especially useful for examining the PCET reactions of O_2 (25, 32, 33), H_2O (34), and H_2 (35). Recently, we established quantitatively the value of the hangman effect for hydrogen evolution reaction (HER) by cobalt hangman porphyrin **1-Co** (Scheme 1) (35). Mechanistic studies (36) unveiled a stepwise ETPT generation of a formal Co^{II} hydride intermediate from the Co^{I} resting state. Comparison of the catalysis of **1-Co** with its nonhangman cobalt porphyrin congener showed that a significant catalytic enhancement of the HER was manifested in a rapid intramolecular rate-limiting PT ($k_{PT} = 8.5 \times 10^6$ s^{-1}) from the pendant acid. In contrast, the corresponding second-order rate constant for proton transfer of the nonhangman was 10^3 $M^{-1}{\cdot}s^{-1}$.

The intramolecular PT should be mediated by the pK_a of the metal. Indeed, the basicity of the metal center relative to a given acidity of the proton relay may be a critical determinant in the HER (37). We now show that the nickel hangman porphyrin **1-Ni** (Scheme 1) offers an improvement in catalytic activity over its cobalt analog owing to a change in the PCET mechanism. By comparing HER activity of the Ni hangman catalyst with the Co hangman catalyst, a unified HER mechanism begins to emerge for complexes that use a secondary coordination sphere to manage PCET.

Results and Discussion

Free-base porphyrins **1** and **2** were synthesized in good yields in relatively short synthesis times using a two-step statistical

Significance

The conversion of solar energy into fuels involves coupled multiproton–multielectron reactions. Because of different length scales for electron transfer and proton transfer, efficient catalysts must couple proton hops to redox events. We have developed a hangman motif where placing a pendant acid–base group over the face of a redox macrocycle ensures coupling of the electron to the proton. We now show that the presence of the pendant acid relay of a Ni hangman porphyrin facilitates proton-coupled electron transfer (PCET) during turnover of the hydrogen evolution reaction (HER). By comparing HER activity of the Ni hangman catalyst to its Co analog, a unified HER mechanism begins to emerge for complexes that use a secondary coordination sphere to manage PCET.

Author contributions: D.K.B., B.H.S., D.K.D., S.H.-S., and D.G.N. designed research; D.K.B., B.H.S., D.K.D., M.M.R., A.G.M., and M.B.C. performed research; D.K.B. and B.H.S. contributed new reagents/analytic tools; D.K.B., B.H.S., D.K.D., C.H.L., M.B.C., and D.G.N. analyzed data; and D.K.B., B.H.S., S.H.-S., and D.G.N. wrote the paper.

The authors declare no conflict of interest.

Freely available online through the PNAS open access option.

Data deposition: The atomic coordinates and structure factors have been deposited in the Cambridge Crystallographic Data Centre database, www.ccdc.cam.ac.uk (accession no. CCDC 1017950-1017951).

[1]To whom correspondence should be addressed. Email: dnocera@fas.harvard.edu.

This article contains supporting information online at www.pnas.org/lookup/suppl/doi:10.1073/pnas.1414908111/-/DCSupplemental.

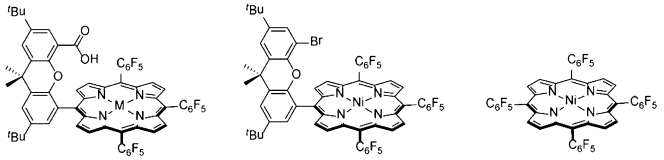

Scheme 1. Cobalt and nickel hangman complexes.

method to construct the hangman porphyrin (31). Insertion of nickel into the free-base porphyrin to generate **1-Ni** was performed by 8–10-h microwave irradiation of **1** and excess $NiBr_2$ in a chloroform:methanol solvent mixture (4:1) at 65 °C. Purification was accomplished by column chromatography. Full synthetic procedures and characterization data including ^1H NMR spectra (*SI Appendix*, Figs. S2–S4), electrospray ionization-mass spectrometry (ESI-MS) and laser desorption-mass spectrometry (LD-MS) (*SI Appendix*, Figs. S5–S7), electronic absorption spectra (*SI Appendix*, Figs. S8–S10), and cyclic voltammogram (CV) data (*SI Appendix*, Figs. S11–S18) are provided in *SI Appendix*.

Compound **1-Ni** was crystallized by slow evaporation of a dichloromethane–hexane solution; the crystal structure is shown in Fig. 1. The distance between the oxygen center of the hangman group and the metal center is 4.510 Å in the solid state. Other structural metrics are similar to those of a similar Co(II) hangman porphyrin possessing mesityl *meso*-substituents (32). One notable difference in the crystallographic structures of these two molecules is the presence of an apical ligand bound to cobalt. The absence of an apical ligand in the Ni complex is a result of the d^8 electron count of the nickel; consequently the d_z^2 orbital is fully populated and thus unavailable for interaction with an apical ligand. The distance of the proton of the hanging group to the metal is 4.46 Å (Co) and 4.25 Å (Ni). This 0.21-Å difference in M–H distance is a result of a larger tilt angle of the xanthene relative to the porphyrin ring for the cobalt porphyrin (13.9° for Co, 7.1° for Ni), which positions the hanging group farther from the Co center. We believe this difference is likely due to packing effects in the solid state and thus of little consequence of the molecule's behavior in solution. Thus, differences in subsequent HER chemistry between the Co and Ni complexes are attributed to electronic effects and not to an underlying structural difference between the two complexes.

CVs of **1-Ni** and **2-Ni** in acetonitrile are shown in Fig. 2*A*. The CV of **2-Ni** (Fig. 2*A*, – –, blue) simply displays two reversible waves centered at –1.39 and –1.96 V (all potentials are referenced to the standard reduction potential of the ferrocenium ion, Fc^+/Fc); we ascribe these waves to the formal $Ni^{II/I}$ (**2-Ni**/[**2-Ni**]$^-$) and $Ni^{I/0}$ ([**2-Ni**]$^-$/[**2-Ni**]$^{2-}$) redox couples, respectively. As shown in *SI Appendix*, Fig. S12, electrochemically reversible behavior is also observed for the A_4 porphyrin **3-Ni** (Scheme 1); the reduction potentials are shifted positively as a result of the additional electron-withdrawing C_6F_5 substituent. The CV of **1-Ni** (Fig. 2*A*,—, red) displays two reversible waves possessing midpoint potentials of –1.37 and –2.01 V that flank an irreversible wave with a peak potential of –1.76 V. By analogy to **2-Ni**, we assign the first reversible wave observed in the case of **1-Ni** to the formal $Ni^{II/I}$ redox couple (e.g., **1-Ni**/[**1-Ni**]$^-$) and the second reversible wave to the [**1-Ni**]$^-$/[**1-Ni**]$^{2-}$ couple. The irreversible wave is associated with H_2 catalysis, and a detailed discussion of the processes associated with this wave is presented below.

Variable scan rate voltammetry permits isolation of the standard heterogeneous ET rate constants (k_{ET}°) associated with the electrochemically reversible processes of all complexes. Increasing separation between cathodic and anodic peak potentials as the scan rate is increased is indicative of deviation away from strict Nernstian behavior toward electrochemical irreversibility. Accordingly, the degree of separation for a given scan rate relies on k_{ET}° (38). CV simulation software (39) provides a reliable means of determining k_{ET}° from the "trumpet plot" generated by

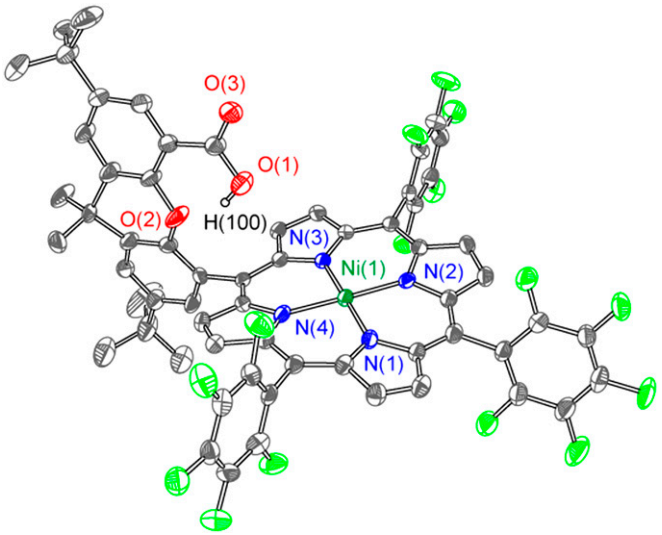

Fig. 1. Crystal structure of **1-Ni** with thermal ellipsoids set at 50% probability. Selected internuclear distances (Å) and angles (°): Ni(1)–N(1) 1.951(3), Ni(1)–N(2) 1.940(3), Ni(1)–N(3) 1.951(3), Ni(1)–N(4) 1.951(3), Ni(1)–O(1) 4.510(6), N(1)–Ni(1)–N2 89.83(12), N(1)–Ni(1)–N(4) 90.31(12), N(2)–Ni(1)–N(3) 90.06(12), N(3)–Ni(1)–N(4) 89.87(13).

simulating CVs over a range of scan rates (40). Trumpet plots of the **1-Ni**/[**1-Ni**]$^-$ peak potentials (blue circles) as a function of the logarithm of the scan rate, shown in Fig. 2*B*, furnish a k_{ET}° value of 0.025 cm/s. Owing to the influence of the irreversible wave on the peak potential of the second reversible wave, the k_{ET}° value for the [**1-Ni**]$^-$/[**1-Ni**]$^{2-}$ couple was determined at a later stage from fits to the entire CV (*vide infra*). Similarly, k_{ET}° values were obtained for the **2-Ni**/[**2-Ni**]$^-$ and [**2-Ni**]$^-$/[**2-Ni**]$^{2-}$ reversible redox couples

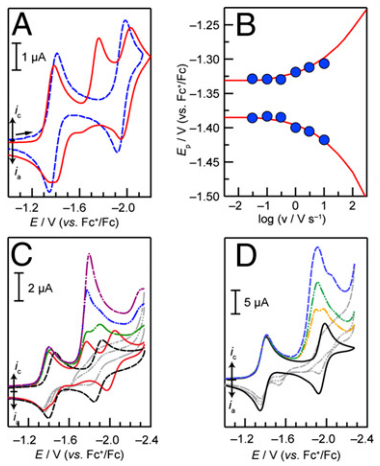

Fig. 2. CV of **1-Ni** and **2-Ni** in 0.1 M $TBAPF_6$–acetonitrile electrolyte at a glassy carbon electrode. (*A*) CVs of 0.4 mM **1-Ni** (red —) and 0.4 mM **2-Ni** (– –, blue) at a scan rate of 30 mV/s. (*B*) Anodic (upper circles) and cathodic (lower circles) peak potentials (E_p) of the formal Ni(II/I) wave as a function of the logarithm of scan rate (v). The solid red line represents the simulation of the trumpet plot to a standard heterogeneous rate constant k_{ET}° of 0.025 cm/s. The diffusion coefficient D of **1-Ni** was determined to be 4.5×10^{-6} cm^2/s from the peak current density as described in ref. 38. (*C*) CVs of 0.25 mM **1-Ni** before (—, red) and after (– –, black) treatment with K_2CO_3 followed by addition of 0.6 (— • —, green), 1.2 (— ••, blue), and 1.8 (— - •, purple) molar equivalents of benzoic acid (scan rate: 30 mV/s). (*D*) CVs of 0.5 mM **2-Ni** (—) upon titration with 0.5 (— • —, orange) 1.0 (— ••, green), and 2.0 (– –, blue) molar equivalents of benzoic acid (scan rate: 30 mV/s).

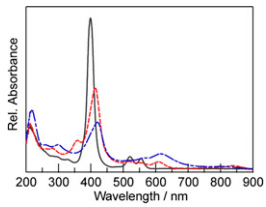

Fig. 3. UV-vis absorption spectra of **3-Ni** (dark gray —), $[\mathbf{3\text{-}Ni}]^{-}$ (red – –), and $[\mathbf{3\text{-}Ni}]^{2-}$ (royal blue — - —) in 0.1 M $TBAPF_6$ in acetonitrile obtained using thin-layer spectroelectrochemistry.

(both found to be about 0.06 cm/s, *SI Appendix*, Figs. S14 and S15) and the **3-Ni**/$[\mathbf{3\text{-}Ni}]^{-}$ and $[\mathbf{3\text{-}Ni}]^{-}$/$[\mathbf{3\text{-}Ni}]^{2-}$ couples (0.05 and 0.03 cm/s, respectively), *SI Appendix*, Figs. S16 and S17. The greater kinetic facility of the $Ni^{II/I}$ reduction relative to the $Co^{II/I}$ reduction is attributed to the requisite dissociation of a solvent [$k^{\circ}_{ET} = 0.01$ cm/s (36)] ligand that is axially coordinated to the low-spin d^7 Co^{II} molecule as observed in the solid-state (32). No axial ligand is expected from our theoretical computations nor observed in the solid-state structure (Fig. 1) of the low-spin d^8 Ni^{II} species.

Titration of **1-Ni** with benzoic acid results in the growth of the irreversible wave centered at –1.76 V (*SI Appendix*, Fig. S18), indicative of an electrocatalytic reaction. Treatment of **1-Ni** with solid potassium carbonate to deprotonate the pendant acid group results in the elimination of the central irreversible feature (Fig. 2*C*, – –) as well as an ~60-mV negative shift in the midpoint potential of the first reversible wave to –1.43 V. The midpoint potential of the second reversible wave shifts in the positive direction to *ca*. –1.88 V following treatment with K_2CO_3. These data confirm that the middle, irreversible peak is associated with an electrocatalytic reaction involving an acid species along with proton transfer from the hangman group. The observed negative shift in the first equilibrium potential is consistent with deprotonation of the pendant carboxylic acid group leading to an increase in the charge on the molecule as a whole, which disfavors reduction. Titration of the deprotonated **1-Ni** with increasing amounts of benzoic acid leads to the return of the irreversible wave (Fig. 2*C*, – • –, green, blue, and purple traces), and subsequent growth with increasing benzoic acid concentration is also in agreement with the occurrence of an electrocatalytic reaction involving an acid source. Indeed, chronocoulometry of a 0.4-mM solution of **1-Ni** in the presence of 15 mM benzoic acid at –1.77 V leads to the generation of H_2 with a faradaic efficiency of 92% over the course of an electrolysis that passed a total of 20.0 C.

Titration of **2-Ni** with benzoic acid also results in the emergence and growth of an irreversible catalytic wave as shown in Fig. 2*D*. However, this catalytic feature is offset toward more negative potentials relative to what is observed in **1-Ni**. The presence of the pendant proton relay is therefore integral to the observance of a catalytic wave that is markedly shifted toward more positive potentials (i.e., the hangman effect).

The CV characteristics displayed in Fig. 2 *A* and *C*—specifically the irreversible catalytic wave and subsequent reversible wave—are reminiscent of what Savéant classifies as "total catalysis." (41, 42) This term denotes a mechanistic regime wherein, owing to a high catalytic rate and/or a dearth of reactant, the rate of reactant consumption is very rapid, leading to control of the electrocatalytic response by diffusion of the reactant from the bulk electrolyte. This behavior results in the presence of two waves: (*i*) an irreversible wave involving the reactant-diffusion-controlled catalytic process, followed by (*ii*) a reversible wave associated with the molecular catalyst, centered at the potential where it appears in the absence of reactant. The catalytic rate constant influences the peak potential of the irreversible wave, but not the peak current (41, 42). In the case of **1-Ni**, notwithstanding the absence of exogenous benzoic acid, one equivalent of acid from each hangman porphyrin is available. These acid functional groups should permit H_2 production, and catalytic turnover would regenerate the $[\mathbf{1\text{-}Ni}]^{-}$ state. Hence, we infer that the second reversible wave involves the formal $Ni^{I/0}$ reduction of the molecule in its deprotonated (hanging carboxylate group) state. We ascribe the positive shift in the second reduction potential upon addition of potassium carbonate to the greater stabilizing effect of the smaller and possibly ion-paired K^+ countercations present in this case, compared with tetrabutylammonium cations that serve to provide charge balance upon electrochemical reduction. The effect of the more charge-dense potassium ions would be pronounced particularly in the reduction to the highly charged deprotonated and doubly reduced state.

Thin-layer spectroelectrochemical analysis of **3-Ni** was undertaken to provide insight into the electronic structure of the Ni(II), Ni(I), and formally Ni(0) states of the porphyrin molecules. The UV-vis absorption spectra of the three species are shown in Fig. 3. Controlled potential electrolysis of **3-Ni** in acetonitrile at –1.3 V cleanly generates the spectrum of $[\mathbf{3\text{-}Ni}]^{-}$ with good isosbestic points (*SI Appendix*, Fig. S19*A*). The bathochromic shift and concomitant loss of intensity of the Soret band along with the growth of new bands at 358 and 608 nm are consistent with spectra obtained by Savéant and coworkers for the one-electron reduction products of similar Ni porphyrins that were assigned as formal Ni(I) species based on UV-vis absorption and ESR data (43). These data therefore support the contention that the first reduction of **3-Ni** to $[\mathbf{3\text{-}Ni}]^{-}$ is metal-centered. Electrolysis at –1.9 V generates the spectrum of the two-electron reduced species $[\mathbf{3\text{-}Ni}]^{2-}$. The growth of a broad absorption band at 615 nm that extends into the near-infrared region (*SI Appendix*, Fig. S19*B*) is consistent with a ligand-centered second reduction (44). The absorption spectrum of **3-Ni** is quantitatively recovered upon electrolysis at 0.0 V following the generation of $[\mathbf{3\text{-}Ni}]^{2-}$ (*SI Appendix*, Fig. S19*C*), supporting the CV data that indicate that the reduction processes are reversible.

Density functional theory (DFT) calculations (see *SI Appendix* for full details on the computational method) were used to probe the electronic structure of the compounds in the different oxidation states. For computational tractability, the *tert*-butyl groups on the xanthene backbone and pentafluorophenyl *meso*-substituents of the porphyrin ring were truncated to methyl groups and chlorine atoms, respectively. These truncations were chosen based on Hammett constants (45) of similar values (*SI Appendix*), and we have exploited this protocol successfully in recent studies to compute the equilibrium potentials of intermediates involved in homogeneous hydrogen evolution (46).

We find that the Ni(II) closed-shell singlet of the **3-Ni** resting state is 8.5 kcal/mol lower in energy than the triplet. In addition, upon reduction to $[\mathbf{3\text{-}Ni}]^{-}$, the results of calculations using five different functionals (*SI Appendix*, Table S1) all agree that the spin density on Ni is near unity, suggesting that the unpaired electron is localized on the nickel center. DFT calculations on the doubly reduced molecule $[\mathbf{3\text{-}Ni}]^{2-}$ with seven different functionals (*SI Appendix*, Table S2) all show that only one electron is localized on Ni, and the triplet state is lower in energy than the closed-shell singlet. Fig. 4 displays the singly occupied molecular orbitals (SOMOs) calculated for $[\mathbf{3\text{-}Ni}]^{-}$ (Fig. 4*A*) and $[\mathbf{3\text{-}Ni}]^{2-}$ (Fig. 4 *B*

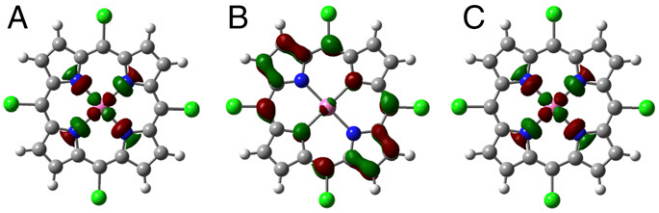

Fig. 4. Calculated (B3P86 solvated phase; IsoValue: 0.05): (*A*) SOMO of $[\mathbf{3\text{-}Ni}]^{-}$ showing electron density localized on the nickel center. (*B*) SOMO and (*C*) SOMO–1 of $[\mathbf{3\text{-}Ni}]^{2-}$ showing that the second electron is localized primarily on the ligands.

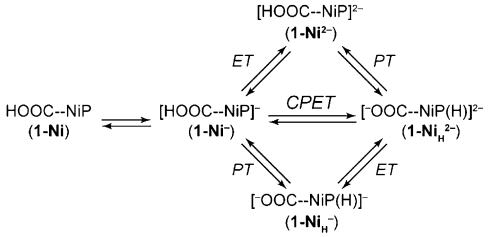

Scheme 2. Stepwise (ETPT and PTET) and concerted (CPET) PCET from $[\mathbf{1\text{-}Ni}]^-$ leading to the generation of a formally Ni(II) hydride, $[\mathbf{1\text{-}Ni_H}]^{2-}$. HOOC–NiP is synonymous with **1-Ni**, indicating the presence of a proton on the carboxylate group in the second coordination sphere of the Ni^{2+} metal center.

and *C*), showing that in the case of the monoanion (S = 1/2), the electron is localized primarily on the $\sigma^*(d_{x^2-y^2})$ orbital of the Ni center. Subsequent reduction to the dianion (S = 1) leads to the highest energy SOMO possessing electron density primarily localized on the porphyrin ligand, whereas the SOMO–1 resembles the SOMO for $[\mathbf{3\text{-}Ni}]^{2-}$. Spin density plots of the mono- and dianion are displayed in *SI Appendix*, Fig. S20.

The electrocatalytic generation of hydrogen from the $[\mathbf{1\text{-}Ni}]^-$ resting state must proceed through an initial step consisting of either one of two stepwise PCET pathways or a concerted one. The stepwise (ETPT and PTET) and concerted (CPET) pathways from $[\mathbf{1\text{-}Ni}]^-$ leading to the generation of a formally Ni(II) hydride, $[\mathbf{1\text{-}Ni_H}]^{2-}$, are shown in Scheme 2 (where HOOC–NiP is synonymous with **1-Ni**). Insight into the operative PCET pathway comes from modeling the CV responses in concert with using the insights garnered from DFT computations as a guide. We computed the equilibrium potentials E_{eq} of plausible intermediates using the experimentally determined $Ni^{II/I}$ reduction potential of **1-Ni** (–1.37 V) as a reference value (Table 1). The correspondence between experimental and computed equilibrium potentials of nonhangman porphyrins **2-Ni** and **3-Ni** is very satisfying, and gives us confidence in the relevance of the computational results. Moreover, the computed reduction potential for a putative $Ni^{II}H$ intermediate (calculated as –1.84 V) is found to lie between the reduction potentials of **1-Ni** and $[\mathbf{1\text{-}Ni}]^-$, within our voltage sweep window. As such, a subsequent reduction of this $Ni^{II}H$ to $Ni^{I}H$ could be favored. Theoretical studies on the mechanism of hydrogen production by cobaloximes have revealed that the equilibrium potential of the $Co^{II}H$–$Co^{I}H$ couple in those systems may also lie between that of $Co^{II/I}$ and $Co^{I/0}$ (47).

Table 1. Computed reduction potentials of nickel hangman porphyrins

Oxidized species	S_{ox}	Reduced species	S_{red}	E^0/V vs. Fc^+/Fc^*
HOOC–NiP	0	$[HOOC–NiP]^-$	1/2	–1.37 (–1.37)[†]
$[HOOC–NiP]^-$	1/2	$[HOOC–NiP]^{2-}$	1	–1.85
$[OOC–NiP]^-$	0	$[OOC–NiP]^{2-}$	1/2	–1.40 (–1.43)
$[OOC–NiP]^{2-}$	1/2	$[OOC–NiP]^{3-}$	1	–2.01 (–1.99)
$[OOC–Ni(H)P]^-$	1/2	$[OOC–Ni(H)P]^{2-}$	1	–0.81
$[OOC–Ni(H)P]^{2-}$	1	$[OOC–Ni(H)P]^{3-}$[‡]	3/2	–1.84
2-Ni	0	$[\mathbf{2\text{-}Ni}]^-$	1/2	–1.34 (–1.39)
$[\mathbf{2\text{-}Ni}]^-$	1/2	$[\mathbf{2\text{-}Ni}]^{2-}$	1	–1.91 (–1.96)
3-Ni	0	$[\mathbf{3\text{-}Ni}]^-$	1/2	–1.32 (–1.27)
$[\mathbf{3\text{-}Ni}]^-$	1/2	$[\mathbf{3\text{-}Ni}]^{2-}$	1	–1.76 (–1.82)

Calculations were performed with DFT using the B3P86 functional, 6–31+G(d), and 6–31+G(d,p) basis sets, and conductor-like polarizable continuum model (C-PCM) solvation. Geometries were optimized in solution.
*Experimental midpoint potential ($E_{1/2}$) values are given in parentheses.
[†]These experimental and computational values are the same by construction because this is the reference reaction used in computation.
[‡]This reduced species refers to the formally Ni(I) hydride; the spin density on nickel remains ~2 (*SI Appendix*), indicating that the reduction is ligand-based.

We first set out to determine whether the ETPT framework that is operative in the case of **1-Co** could account for the electrocatalytic behavior manifest in Fig. 2 *A* and *C*. In the context of such an ETPT mechanism (top route of Scheme 2), three critical parameters that control the electrochemical response are (*i*) the reduction potential of $[\mathbf{1\text{-}Ni}]^-$, (*ii*) the associated standard heterogeneous ET rate constant, and (*iii*) the rate of the subsequent intramolecular PT. The experimentally measured equilibrium potential and standard ET rate constant of the nonhangman analog (i.e., the $[\mathbf{2\text{-}Ni}]^-/[\mathbf{2\text{-}Ni}]^{2-}$ couple, which possesses $E^\circ = -1.96$ V and $k^\circ_{ET} = 0.06$ cm/s) provide an estimate for (*i*) and (*ii*). However, this still leaves the intramolecular PT rate constant (*iii*) as well any equilibrium–rate constant and reduction potential values associated with follow-up reactions (such as the protonation of a hydride to evolve H_2) as unknowns. If these are fast and post–rate-limiting they will not influence the electrokinetic response.

As in the case for the one-electron ET reactions, CV simulation is a powerful tool for gaining mechanistic insight into homogeneous electrocatalytic reactions, especially in cases where substrate limitation cannot be avoided. CV simulations of an ETPT pathway using the aforementioned parameters are shown in *SI Appendix*, Fig. S21. In these simulations, we also assumed that all bimolecular reactions proceed at the diffusion limit with a rate constant on the order of 10^{10} $M^{-1}\cdot s^{-1}$. Moreover, the intramolecular rate constant k_{PT}^{intra} is set to 10^{13} s^{-1}, such that it is many orders of magnitude faster than the bimolecular reactions (i.e., we ensure that the product of the diffusion-limited rate constant, 10^{10} $M^{-1}\cdot s^{-1}$, and the concentration of the catalyst–substrate (<1 mM) will be much less than k_{PT}^{intra}). We also set the reduction potential of the $Ni^{II}H$ that is formed by protonation of the formally Ni^0 species to be equal to –1.4 V, close to that of the $Ni^{II/I}$ reduction potential. This value is considerably more positive than the potential at which catalysis is observed (~–1.76 V) and also more positive than that computed by DFT (–1.84 V). These parameters (tabulated in Table S3) were specifically chosen to be representative of a best-case scenario for the ETPT mechanism. These governing factors will lead to the most positive peak potentials possible for an ETPT process, which proceeds through the $[\mathbf{1\text{-}Ni}]^{2-}$ intermediate: in a reaction scheme governed by these parameters the most negative reduction potential is that of $[\mathbf{1\text{-}Ni}]^-/[\mathbf{1\text{-}Ni}]^{2-}$ and all bimolecular reactions proceed at the diffusion limit. Even though the resulting simulation reveals a voltammogram that displays the general total catalysis behavior, the ETPT model leads to voltammetric features that are not fully coincident with the experimental results (*SI Appendix*, Fig. S21*A*); anticipated peak potentials are too negative and peak current

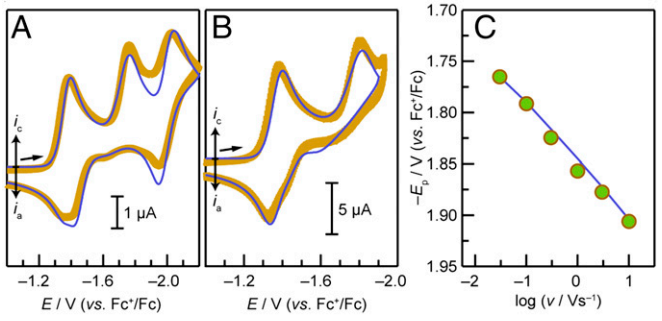

Fig. 5. Experimental (thick light-brown curves) and simulated (thin blue curves) CVs of a 0.4-mM solution of **1-Ni** at a scan rate of (*A*) 30 mV/s and (*B*) 300 mV/s. Voltammograms were simulated according to a mechanistic framework consisting of a PTET pathway (Scheme 2) from $\mathbf{1\text{-}Ni}^-$ to $\mathbf{1\text{-}Ni_H}^{2-}$, followed by reduction to $\mathbf{1\text{-}Ni_H}^{3-}$, which is subsequently protonated by the pendant acid group of another porphyrin molecule to liberate H_2. Parameters used in simulation are tabulated in Tables 2 and 3. (*C*) Variation of the experimental peak potential of the irreversible catalytic wave of **1-Ni** as a function of scan rate (green circles) compared with the variation observed from simulated CVs (blue trace).

Table 2. Parameters of heterogeneous/electrochemical reactions used in simulating PTET-based pathway

Oxidized species	Reduced species	E^{o}_{sim}*	k^{o}_{ET}/cm s^{-1}
HOOC–NiP	$[HOOC–NiP]^{-}$	−1.37	0.025†
$[HOOC–NiP]^{-}$	$[HOOC–NiP]^{2-}$	−1.96‡	0.06‡
$[OOC–NiP]^{-}$	$[OOC–NiP]^{2-}$	−1.45§	0.025¶
$[OOC–NiP]^{2-}$	$[OOC–NiP]^{3-}$	−1.99	0.002†
$[OOC–Ni(H)P]^{-}$	$[OOC–Ni(H)P]^{2-}$	−1.57†	0.01†
$[OOC–Ni(H)P]^{2-}$	$[OOC–Ni(H)P]^{3-}$	−1.95†	0.05†

*Reduction potentials are relative to the reduction potential of Fc^{+}/Fc.
†Obtained from simulating experimental CV data.
‡Values estimated from that of nonhangman compound **2-Ni**.
§Value determined from treatment of **1-Ni** with potassium carbonate, and further refined by simulating shoulder near anodic return peak of **1-Ni**/$[$**1-Ni**$]^{-}$ wave.
¶Value set equal to that obtained from trumpet plots of the corresponding protonated species.

values remain too low to account for the experimental result. These observations are conserved over a scan rate range of two orders of magnitude (*SI Appendix*, Fig. S21*B*).

To explore the possibility of this ETPT mechanism further, we also simulated CVs using the computed $[$**1-Ni**$]^{-}$/$[$**1-Ni**$]^{2-}$ and $[$**1-Ni$_H$**$]^{2-}$/$[$**1-Ni$_H$**$]^{3-}$ $E°$ values (−1.85 and −1.84 V, respectively; Table 1) as opposed to using that of the nonhangman analog. The resulting simulated voltammogram is shown in *SI Appendix*, Fig. S22. Using these computed parameters, a much slower intramolecular PT rate constant of 2,000 s^{-1} is needed to replicate the peak potential of the irreversible catalytic wave (*SI Appendix*, Table S4). However, the simulations show that prominent peaks expected at 30 mV in the return sweep are inconsistent with experimental data. Thus, simulations of the ETPT pathway under any reasonable fitting condition do not match the experimental CVs of **1-Ni**. We therefore turned our attention to the interrogation of the PTET and CPET mechanisms displayed in Scheme 2.

To assist in differentiating between the PTET and CPET mechanisms, we set out to measure the H–D isotope effect. In the case of the PTET mechanism, no significant isotope effect is expected because the proton transfer exists in a rapid preequilibrium, and any equilibrium isotope effect is expected to be too small to lead to a detectable change in peak position. In contrast, any change in the standard CPET rate constant k_{CPET} associated with H–D isotopic substitution would lead to a shift in peak position if that reaction were to be the rate-determining step. Indeed, as shown by CV simulations (*SI Appendix*, Fig. S23) a CPET-based framework accommodates the voltammetric behavior of **1-Ni**, but the catalytic peak potential is very sensitive to k_{CPET}. Following treatment of **1-Ni** with K_2CO_3 to deprotonate the pendant acid as described above, a batch of this deprotonated hangman porphyrin was titrated with C_6H_5COOH and an identical batch was titrated with C_6H_5COOD. The difference in catalytic peak potential in the case of the two isotopes is plotted as a function of the number of equivalents of acid titrated in *SI Appendix*, Fig. S24. Because we do not observe a significant isotope effect, we consider a rate-limiting concerted pathway to be unlikely. Instead, these data are consistent with the occurrence of a stepwise PTET from $[$**1-Ni**$]^{-}$ to form the formally Ni(II)H intermediate. We note that we cannot entirely rule out the possibility of a rapid, reversible non–rate-limiting CPET at this time. In this case, isotopic substitution and consequent alteration of the heterogeneous rate constant would not give rise to a change in peak potential at these relatively slow scan rates. Additional computational studies are required to explore this possibility while considering the various potential proton-acceptor sites of the molecule.

Simulations of the PTET pathway are successful in replicating the experimental data with good fidelity as shown in Fig. 5. Simulation parameters are provided in Tables 2 and 3, and these values provide estimates of the thermodynamic and kinetic parameters that govern catalysis. According to these CV simulations, an intramolecular PT from the Ni^{I} resting state leads to a formal $Ni^{III}H$ species, which exists in minor equilibrium. Subsequent ET furnishes $Ni^{II}H$, followed by another reduction to $Ni^{I}H$. Protonation of the hydride by an acid source produces H_2 in a facile step. This contrasts the HER mechanism for the analogous **1-Co** system and benzoic acid, which displays an ETPT mechanism for HER (35). The Co^{I} state is not protonated and only after Co^{0} is formed does the proton transfer to produce $Co^{II}H$. A PTET pathway for **1-Co** may be realized but only when strong acids such as *p*-toluenesulfonic (tosic) acid are used. The only ET step for which there is poor agreement between the computed equilibrium potential (–0.81 V) and experiment/simulation (*ca*. –1.57 V) is for the formally $Ni^{III}H$ to $Ni^{II}H$ reduction (Table 2). The DFT calculations only considered cases where the proton is transferred to the metal center; the disparity between CV simulation (Table 2) and computation (Table 1) in this single reduction potential value thus suggests that the proton may not transfer directly to the metal center but rather to the macrocycle. Efforts to explore alternative proton accepting sites are underway. Nevertheless, the CV data and simulation provide compelling evidence for an operative PTET pathway.

The discrepancy in mechanistic pathway between **1-Co** and **1-Ni** could arise from a difference in basicity of the metal centers. It is interesting that for both **1-Co** and **1-Ni**, it is the d^9 electronic configuration that is protonated (Co^{0} for **1-Co** and Ni^{I} for **1-Ni**). The presence of an electron in the in-plane metal-based orbital might provide a more favorable electrostatic environment that induces proton transfer. The contributions of electrostatic versus covalent factors in the HER mechanism have not yet been computationally disentangled. The results here suggest this may be a fruitful line of inquiry.

Conclusions

The effect of a pendant proton relay (hangman group) proximate to the catalytic center in nickel hangman porphyrins leads to an improvement in catalytic activity over analogous nonhangman molecules. The hangman effect is associated with the facilitation of a stepwise PTET mechanism, which is favored over the ETPT pathway that is observed in the case of the cobalt catalyst. Indeed, because Ni-based catalysis avoids generation of the

Table 3. Parameters of homogeneous/chemical reactions used in simulating PTET pathway

Reactants	Products	K_{eq}	$k_{forward}$
$[HOOC–NiP]^{-}$	$[OOC–NiP(H)]^{-}$	9×10^{-3}*	$>10^{5}$*
$[OOC–NiP(H)]^{-}$ + $[OOC–NiP]^{3-}$	$[OOC–NiP(H)]^{2-}$ + $[OOC–NiP]^{2-}$	1.25×10^{7}†	k_{diff}‡
$[OOC–NiP(H)]^{2-}$ + $[OOC–NiP]^{3-}$	$[OOC–NiP(H)]^{3-}$ + $[OOC–NiP]^{2-}$	4.74†	k_{diff}‡
$[OOC–NiP(H)]^{3-}$ + acid§	H_2 + $[OOC–NiP]^{2-}$conjugate base	$>10^{5}$	k_{diff}‡

*Obtained from simulating experimental CV data.
†These equilibrium constants are governed by the difference in reduction potentials of the two sets of species.
‡The forward rate constants of these downhill reactions are assumed to be the diffusion-limited rate constant: 10^{10} $M^{-1}·s^{-1}$.
§All nickel porphyrins with protonated hanging groups are permitted as acid sources in the mechanism.

formally metal(0) species, the nickel porphyrin offers an improvement in catalytic activity over the cobalt analog, which proceeds through a stepwise ETPT route via Co^0. Computational and spectroelectrochemical results are consistent with the reduction of Ni(I) involving porphyrin ligand-based orbitals, such that the Ni(0) species is truly a Ni(I) porphyrin radical. Studies to shed more light on the nature of the hydrides formed during these PCET reactions as well as the stabilization of proposed intermediates by appropriate ligand design are underway. Such studies could shed more light on the requirements for facile H_2 evolution through PCET.

Materials and Methods

^{1}H NMR spectra (500 MHz) were recorded on samples in $CDCl_3$ at room temperature unless noted otherwise. Silica gel (60-μm average particle size) was used for column chromatography. THF (anhydrous), methanol (anhydrous), CH_2Cl_2 (anhydrous), benzoic acid (≥99.5%), and tetrabutylammonium hexafluorophosphate ($TBAPF_6$, ≥99.0%), and all other chemicals were used as received.

Electrochemical measurements were performed on a CH Instruments 760D Electrochemical Workstation using CHI Version 10.03 software. CV experiments were conducted in a nitrogen-filled glovebox, a glassy carbon button working electrode (area = 0.071 cm^2), BASi $Ag/AgNO_3$ (0.1 M) reference electrode in 0.1 M $TBAPF_6$ acetonitrile solution at room temperature, and Pt mesh counterelectrode. All CVs were recorded with compensation for solution resistance. Bulk electrolysis was performed using a glassy carbon rod (7 mm × 5 cm) working electrode and a platinum mesh auxiliary electrode in a gas-tight electrochemical cell. The amount of H_2 gas produced in the headspace was analyzed by an Agilent 7890A GC.

UV-vis spectra were recorded at room temperature in quartz cuvettes in CH_2Cl_2 on a Varian Cary 5000 UV-vis-near-infrared (NIR) spectrophotometer. UV-vis spectroelectrochemical measurements were made using a quartz thin-layer cell (0.5-mm path length) at room temperature in a N_2-filled glovebox with an Ocean Optics USB4000 spectrophotometer and DT-Mini-2GS UV-vis-NIR light source.

Computed structures were optimized with DFT using a variety of exchange-correlation functionals. For computation tractability, the *tert*-butyl groups on the xanthene backbone and pentafluorophenyl *meso*-substituents of the porphyrin ring were truncated to methyl groups and chlorine atoms, respectively.

All simulated CVs were calculated using DigiElch 7 software (39). Symmetry factors–transfer coefficients were set to 0.5 for all ET steps. Additional experimental details are available in *SI Appendix*.

ACKNOWLEDGMENTS. D.G.N. acknowledges that this material is based on work supported by the US Department of Energy Office of Science, Office of Basic Energy Sciences Energy Frontier Research Centers program under Award DE-SC0009758. B.H.S. and S.H.-S. acknowledge support for the computational work by the Center for Chemical Innovation of the National Science Foundation (Solar Fuels, Grant CHE-1305124).

1. Hoffert MI, et al. (1998) Energy implications of future stabilization of atmospheric CO_2 content. *Nature* 395:881–884.
2. Lewis NS, Nocera DG (2006) Powering the planet: Chemical challenges in solar energy utilization. *Proc Natl Acad Sci USA* 103(43):15729–15735.
3. Abbott D (2010) Keeping the energy debate clean: How do we supply the world's energy needs? *Proc IEEE* 98:42–66.
4. Chu S, Majumdar A (2012) Opportunities and challenges for a sustainable energy future. *Nature* 488(7411):294–303.
5. Cook TR, et al. (2010) Solar energy supply and storage for the legacy and nonlegacy worlds. *Chem Rev* 110(11):6474–6502.
6. Barber J (2009) Photosynthetic energy conversion: Natural and artificial. *Chem Soc Rev* 38(1):185–196.
7. Nocera DG (2009) Chemistry of personalized solar energy. *Inorg Chem* 48(21):10001–10017.
8. Liu F, et al. (2008) Mechanisms of water oxidation from the blue dimer to photosystem II. *Inorg Chem* 47(6):1727–1752.
9. Schneider J, Jia H, Muckerman JT, Fujita E (2012) Thermodynamics and kinetics of CO_2, CO, and H^+ binding to the metal centre of CO_2 reduction catalysts. *Chem Soc Rev* 41(6):2036–2051.
10. Costentin C, Robert M, Savéant JM (2013) Catalysis of the electrochemical reduction of carbon dioxide. *Chem Soc Rev* 42(6):2423–2436.
11. Medina-Ramos J, DiMeglio JL, Rosenthal J (2014) Efficient reduction of CO_2 to CO with high current density using in situ or ex situ prepared Bi-based materials. *J Am Chem Soc* 136(23):8361–8367.
12. Li CW, Ciston J, Kanan MW (2014) Electroreduction of carbon monoxide to liquid fuel on oxide-derived nanocrystalline copper. *Nature* 508(7497):504–507.
13. Smieja JM, et al. (2013) Manganese as a substitute for rhenium in CO_2 reduction catalysts: The importance of acids. *Inorg Chem* 52(5):2484–2491.
14. Cukier RI, Nocera DG (1998) Proton-coupled electron transfer. *Annu Rev Phys Chem* 49:337–369.
15. Mayer JM (2004) Proton-coupled electron transfer: A reaction chemist's view. *Annu Rev Phys Chem* 55:363–390.
16. Huynh MH, Meyer TJ (2007) Proton-coupled electron transfer. *Chem Rev* 107(11): 5004–5064.
17. Costentin C (2008) Electrochemical approach to the mechanistic study of proton-coupled electron transfer. *Chem Rev* 108(7):2145–2179.
18. Hammarström L, Styring S (2008) Coupled electron transfers in artificial photosynthesis. *Philos Trans R Soc, B* 363:1283–1291.
19. Reece SY, Nocera DG (2009) Proton-coupled electron transfer in biology: Results from synergistic studies in natural and model systems. *Annu Rev Biochem* 78:673–699.
20. Hammes-Schiffer S, Stuchebrukhov AA (2010) Theory of coupled electron and proton transfer reactions. *Chem Rev* 110(12):6939–6960.
21. Hammes-Schiffer S (2012) Proton-coupled electron transfer: Classification scheme and guide to theoretical methods. *Energy Environ Sci* 5:7696–7703.
22. Bonin J, Costentin C, Robert M, Savéant JM, Tard C (2012) Hydrogen-bond relays in concerted proton-electron transfers. *Acc Chem Res* 45(3):372–381.
23. Chang CJ, Chng LL, Nocera DG (2003) Proton-coupled O-O activation on a redox platform bearing a hydrogen-bonding scaffold. *J Am Chem Soc* 125(7):1866–1876.
24. Soper JD, Kryatov SV, Rybak-Akimova EV, Nocera DG (2007) Proton-directed redox control of O-O bond activation by heme hydroperoxidase models. *J Am Chem Soc* 129(16):5069–5075.
25. Rosenthal J, Nocera DG (2007) Role of proton-coupled electron transfer in O-O bond activation. *Acc Chem Res* 40(7):543–553.
26. Helm ML, Stewart MP, Bullock RM, DuBois MR, DuBois DL (2011) A synthetic nickel electrocatalyst with a turnover frequency above 100,000 s^{-1} for H_2 production. *Science* 333(6044):863–866.
27. Smith SE, Yang JY, DuBois DL, Bullock RM (2012) Reversible electrocatalytic production and oxidation of hydrogen at low overpotentials by a functional hydrogenase mimic. *Angew Chem Int Ed Engl* 51(13):3152–3155.
28. Yang JY, et al. (2013) Two pathways for electrocatalytic oxidation of hydrogen by a nickel bis(diphosphine) complex with pendant amines in the second coordination sphere. *J Am Chem Soc* 135(26):9700–9712.
29. Carver CT, Matson BD, Mayer JM (2012) Electrocatalytic oxygen reduction by iron tetra-arylporphyrins bearing pendant proton relays. *J Am Chem Soc* 134(12):5444–5447.
30. Chang CJ, Yeh CY, Nocera DG (2002) Porphyrin architectures bearing functionalized xanthene spacers. *J Org Chem* 67(4):1403–1406.
31. Dogutan DK, Bediako DK, Teets TS, Schwalbe M, Nocera DG (2010) Efficient synthesis of hangman porphyrins. *Org Lett* 12(5):1036–1039.
32. McGuire R, Jr, et al. (2010) Oxygen reduction reactivity of cobalt(II) hangman porphyrins. *Chem Sci* 1:411–414.
33. Rosenthal J, Nocera DG (2007) Oxygen activation chemistry of pacman and hangman porphyrin architectures based on xanthene and dibenzofuran spacers. *Prog Inorg Chem* 55:483–544.
34. Dogutan DK, McGuire R, Jr, Nocera DG (2011) Electocatalytic water oxidation by cobalt(III) hangman β-octafluoro corroles. *J Am Chem Soc* 133(24):9178–9180.
35. Lee CH, Dogutan DK, Nocera DG (2011) Hydrogen generation by hangman metalloporphyrins. *J Am Chem Soc* 133(23):8775–8777.
36. Roubelakis MM, Bediako DK, Dogutan DK, Nocera DG (2012) Proton-coupled electron transfer kinetics for the hydrogen evolution reaction of hangman porphyrins. *Energy Environ Sci* 5:7737–7740.
37. Small YA, Dubois DL, Fujita E, Muckerman JT (2011) Proton management as a design principle for hydrogenase-inspired catalysts *Energy. Environ Sci* 4:3008–3020.
38. Savéant JM (2006) Single electron transfer at an electrode. *Elements of Molecular and Biomolecular Electrochemistry: An Electrochemical Approach to Electron Transfer Chemistry* (Wiley, New York).
39. Rudolf M (2003) Digital simulations on unequally spaced grids. Part 2. Using the box method by discretisation on a transformed equally spaced grid. *J Electroanal Chem* 543:23–39.
40. Costentin C, Robert M, Savéant JM, Teillout AL (2009) Concerted proton-coupled electron transfers in aquo/hydroxo/oxo metal complexes: Electrochemistry of $[Os^{II}(bpy)_2py(OH_2)]_2+$ in water. *Proc Natl Acad Sci USA* 106(29):11829–11836.
41. Savéant JM (2006) Coupling of electrode electron transfers with homogeneous chemical reactions. *Elements of Molecular and Biomolecular Electrochemistry: An Electrochemical Approach to Electron Transfer Chemistry* (Wiley, New York), p 109.
42. Savéant JM (2008) Molecular catalysis of electrochemical reactions. Mechanistic aspects. *Chem Rev* 108(7):2348–2378.
43. Lexa D, Momenteau M, Mispelter J, Savéant JM (1989) Does one-electron transfer to nickel(II) porphyrins involve the metal or the porphyrin ligand? *Inorg Chem* 28:30–35.
44. Kadish KM, Franzen MM, Han BC, Araullo-McAdams C, Sazou D (1991) Factors determining the site of electroreduction in nickel metalloporphyrins. Spectral characterization of nickel(I) porphyrins, nickel(II) porphyrin pi-anion radicals, and nickel(II) porphyrin pi-anion radicals with some nickel(I) character. *J Am Chem Soc* 113:512–517.
45. Hansch C, Leo A, Taft RW (1991) A survey of Hammett substituent constants and resonance and field parameters. *Chem Rev* 91:165–195.
46. Solis BH, Hammes-Schiffer S (2011) Substituent effects on cobalt diglyoxime catalysts for hydrogen evolution. *J Am Chem Soc* 133(47):19036–19039.
47. Muckerman JT, Fujita E (2011) Theoretical studies of the mechanism of catalytic hydrogen production by a cobaloxime. *Chem Commun (Camb)* 47(46):12456–12458.

Nickel phlorin intermediate formed by proton-coupled electron transfer in hydrogen evolution mechanism

Brian H. Solis[a,1], Andrew G. Maher[b], Dilek K. Dogutan[b], Daniel G. Nocera[b], and Sharon Hammes-Schiffer[a,2]

[a]Department of Chemistry, University of Illinois at Urbana–Champaign, Urbana, IL 61801; and [b]Department of Chemistry and Chemical Biology, Harvard University, Cambridge, MA 02138

This contribution is part of the special series of Inaugural Articles by members of the National Academy of Sciences elected in 2013.

Contributed by Sharon Hammes-Schiffer, November 5, 2015 (sent for review October 1, 2015; reviewed by Jillian L. Dempsey and James T. Muckerman)

The development of more effective energy conversion processes is critical for global energy sustainability. The design of molecular electrocatalysts for the hydrogen evolution reaction is an important component of these efforts. Proton-coupled electron transfer (PCET) reactions, in which electron transfer is coupled to proton transfer, play an important role in these processes and can be enhanced by incorporating proton relays into the molecular electrocatalysts. Herein nickel porphyrin electrocatalysts with and without an internal proton relay are investigated to elucidate the hydrogen evolution mechanisms and thereby enable the design of more effective catalysts. Density functional theory calculations indicate that electrochemical reduction leads to dearomatization of the porphyrin conjugated system, thereby favoring protonation at the *meso* carbon of the porphyrin ring to produce a phlorin intermediate. A key step in the proposed mechanisms is a thermodynamically favorable PCET reaction composed of intramolecular electron transfer from the nickel to the porphyrin and proton transfer from a carboxylic acid hanging group or an external acid to the *meso* carbon of the porphyrin. The C–H bond of the active phlorin acts similarly to the more traditional metal-hydride by reacting with acid to produce H_2. Support for the theoretically predicted mechanism is provided by the agreement between simulated and experimental cyclic voltammograms in weak and strong acid and by the detection of a phlorin intermediate through spectroelectrochemical measurements. These results suggest that phlorin species have the potential to perform unique chemistry that could prove useful in designing more effective electrocatalysts.

electrocatalysis | metalloporphyrin | proton transfer | dearomatization

Direct solar-to-fuel processes are important components of global energy sustainability efforts (1, 2). Such processes include the hydrogen evolution reaction (HER), oxidation of water to oxygen, and reduction of CO_2 to hydrocarbons (3, 4). Proton-coupled electron transfer (PCET), which is generally defined in terms of coupling between electron transfer (ET) and proton transfer (PT) reactions, is essential to all of these processes. PCET can be classified as occurring via either a sequential or a concerted mechanism (5, 6). The mechanism is determined to be sequential rather than concerted if a stable intermediate associated with initial ET or PT can be identified. This distinction is not rigorous, however, because the identification of a stable intermediate may depend on the experimental approach or the level of theory, as well as the lifetime of the intermediate. Regardless of the specific mechanism, the coupling of ET and PT plays a significant role in a wide range of energy conversion processes (7–11). Moreover, the coupling of ET and PT can be enhanced by incorporating proton relays into molecular catalysts, exploiting the proximal positioning of the proton donor and acceptor (12–16). Recognition and characterization of successful PCET motifs within molecular electrocatalysts provides insight into the design of efficient catalytic processes (17–19).

Cobalt and nickel metalloporphyrins, depicted in Fig. 1, have been investigated as HER electrocatalysts (20, 21). Experimental (22) and theoretical (23) examination of the key PCET step within the HER mechanism of the cobalt "hangman" complex (the cobalt analog of **[1-H]** in Fig. 1) revealed a sequential ET–PT mechanism, with an experimentally measured PT rate constant $k_{PT} = 8.5 \times 10^6\ s^{-1}$ (22). In the proposed mechanism, the formally Co(I) is reduced to a Co("0.5") complex in which the unpaired electron is shared between the metal and the ligands, breaking the aromaticity of the porphyrin ring. Subsequent PT from the carboxylic acid proton of the hangman moiety to the porphyrin *meso* carbon, forming a cobalt phlorin intermediate, was hypothesized on the basis of a theoretical study (23). In particular, the calculations indicated that this PT to the porphyrin is structurally and thermodynamically favored over PT to the metal center, and the calculated PT rate constant $k_{PT} = 1.4 \times 10^6\ s^{-1}$ is consistent with the experimental value. Upon protonation of the hangman carboxylate by benzoic acid and additional electrochemical reduction, H_2 is thermodynamically favored to self-eliminate from the complex (23). With strong acid, H_2 is evolved through the more traditional protonation of the metal to generate a metal-hydride, which is more thermodynamically favorable than phlorin formation. For the nickel hangman complex (**[1-H]** in Fig. 1), previous computational results suggested that the PT step involves a proton acceptor other than the nickel center (21), as was the case for the cobalt analog (23), but the specific mechanism was not determined.

Significance

Global energy sustainability requires the development of effective energy conversion processes. In the hydrogen evolution reaction, electrons and protons are combined to generate molecular hydrogen, which stores energy in its chemical bond. Molecular electrocatalysts have been designed to facilitate this reaction by making it occur faster with lower energy input, often utilizing proton-coupled electron transfer (PCET), which couples the motions of electrons and protons to avoid high-energy intermediates. Examination of a nickel porphyrin electrocatalyst indicates that the active intermediate stores electrons in the C–H bond of the modified porphyrin generated by PCET, rather than in the traditional metal-hydride bond. The ability to store electrons in the ligand rather than in the metal has significant implications for the design of electrocatalysts.

Author contributions: B.H.S., A.G.M., D.K.D., D.G.N., and S.H.-S. designed research; B.H.S., A.G.M., and D.K.D. performed research; B.H.S., A.G.M., and D.K.D. contributed new reagents/analytic tools; B.H.S., A.G.M., D.K.D., D.G.N., and S.H.-S. analyzed data; and B.H.S., A.G.M., and S.H.-S. wrote the paper.

Reviewers: J.L.D., University of North Carolina at Chapel Hill; and J.T.M., Brookhaven National Laboratory.

The authors declare no conflict of interest.

See Commentary on page 478.

[1]Present address: Institut für Chemie, Humboldt Universität zu Berlin, 10099 Berlin, Germany.

[2]To whom correspondence should be addressed. Email: shs3@illinois.edu.

This article contains supporting information online at www.pnas.org/lookup/suppl/doi:10.1073/pnas.1521834112/-/DCSupplemental.

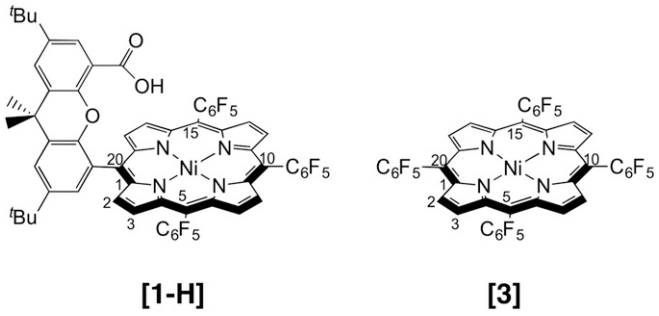

Fig. 1. Structures of nickel porphyrins **[1-H]** and **[3]**. Select carbon atoms of the porphyrin ring are labeled according to position, including *meso* carbons 5, 10, 15, and 20. Complex **[2]** is the analog of **[1-H]**, where a bromine atom replaces the carboxylic acid substituent.

In this paper, we use computational and experimental methods to elucidate the full catalytic cycle for the electrochemical HER catalyzed by the nickel metalloporphyrins **[1-H]** and **[3]**. On the basis of density functional theory (DFT) calculations, referenced to values from experimental cyclic voltammetry to enhance the quantitative accuracy, we propose mechanisms for the HER in the presence of weak or strong acid. Our calculations indicate that **[1-H]** and **[3]** evolve H_2 through key phlorin intermediates, in which the *meso* carbon of the porphyrin is protonated, and that no nickel-hydride complexes are formed. Spectroelectrochemical experiments provide evidence of the phlorin intermediate formed via protonation of the dianionic species $[\mathbf{3}]^{2-}$. Moreover, simulated cyclic voltammograms (CVs) based on the proposed mechanism, in conjunction with the calculated reduction potentials, pK_a's, and free energy barriers, provide further support of this mechanism through agreement with experimental CVs.

Results and Discussion

Electronic Structure of [3]. The relative free energies for various charge, spin, and structural states of **[3]** were calculated using DFT. The most stable form of $[\mathbf{3}]^{0}$ contains a puckered porphyrin ring (denoted bent hereafter) as a closed-shell singlet. A structure in which the pyrrolic nitrogens are coplanar with the nickel center (denoted flat hereafter) is the most stable form of $[\mathbf{3}]^{-}$. The single unpaired electron in the doublet $[\mathbf{3}]^{-}$ is localized on the nickel in the more stable flat geometry, generating a formally Ni(I) species upon reduction with a Mulliken spin density on the nickel center of $\rho_{Ni} \approx 1$. The less-stable bent porphyrin geometry is a Ni(II) porphyrin radical species with the unpaired electron localized on the porphyrin and $\rho_{Ni} \approx 0$. The most stable form of $[\mathbf{3}]^{2-}$ is the flat triplet, in which one reducing electron is localized on the nickel center ($\rho_{Ni} \approx 1$) and the other reducing electron is localized on the porphyrin, consistent with our previous work (21). The more-stable flat triplet can be described as a Ni(I) porphyrin radical, whereas the less-stable bent triplet, which corresponds to $\rho_{Ni} \approx 0$, is a Ni(II) porphyrin diradical, in which both unpaired electrons are localized on the porphyrin.

We considered four protonation sites for protonated **[3]**, denoted **[3-H]**: the nickel center, producing $[\mathbf{3\text{-}H_{Ni}}]$; a pyrrolic nitrogen, producing $[\mathbf{3\text{-}H_{N}}]$; a *meso* carbon, producing $[\mathbf{3\text{-}H_{C}}]$; and the π-electrons of a pyrrole, producing $[\mathbf{3\text{-}H_{pyr}}]$. Note that $[\mathbf{3\text{-}H_{pyr}}]$ is analogous to an intermediate proposed recently for HER catalysis by Pd and Cu tetraferrocenylporphyrin complexes (24); however, our calculations indicate that protonation occurs at the C2 carbon rather than at the face of the pyrrole. For the three relevant charge states of **[3]**, the thermodynamically favored protonation site is at the *meso* carbon position, forming a phlorin complex that is 5.5, 15.6, and 15.7 kcal/mol lower in free energy than the next most stable species for the neutral, monoanionic, and dianionic species, respectively (*SI Appendix*, Table S4). This result differs from our previous finding for the cobalt analog of **[3]**, where the cobalt-hydride was the thermodynamically preferred protonated complex in the neutral form (23). As with deprotonated **[3]**, the Ni(II) species have bent structures but the Ni(I) species have flat structures for protonated **[3]**. The neutral phlorin $[\mathbf{3\text{-}H_{C}}]^{0}$ is calculated to be a bent doublet with the spin density of the unpaired electron localized on the ligand rather than the metal center, indicating a Ni(II) phlorin radical, where the phlorin ring has an effective charge of −2. Thus, protonation of flat $[\mathbf{3}]^{-}$, a Ni(I) complex, at the *meso* carbon position is accompanied by an additional intramolecular ET from the metal to the porphyrin, oxidizing Ni(I) to Ni(II), as well as a structural change in the porphyrin ring from flat to bent.

Similarly, protonation of flat $[\mathbf{3}]^{2-}$ at the *meso* carbon position is also accompanied by intramolecular ET from the metal to the porphyrin and the associated structural change in the porphyrin ring. The anionic phlorin $[\mathbf{3\text{-}H_{C}}]^{-}$ is calculated to be a bent singlet, with a Ni(II) center and an effective charge of −3 on the phlorin ring. For protonation of the flat triplet $[\mathbf{3}]^{2-}$ species to result in the closed-shell phlorin $[\mathbf{3\text{-}H_{C}}]^{-}$, in which all electrons are paired, one unpaired electron in the flat triplet $[\mathbf{3}]^{2-}$ must undergo a spin flip to produce the flat open-shell singlet $[\mathbf{3}]^{2-}$, which is only slightly higher in free energy. Owing to the greater spin-orbit coupling between spin states on the metal center than on the organic ligands, this spin flip is most likely to occur for the unpaired electron localized on nickel (25). Intramolecular ET within the flat open-shell singlet oxidizes Ni(I) to Ni(II) and is accompanied by the structural change within the porphyrin ring from flat to bent, producing a bent closed-shell singlet.

This analysis of $[\mathbf{3}]^{-}$ and $[\mathbf{3}]^{2-}$ indicates that PT reactions to the *meso* carbon in flat Ni(I) species are effectively PCET reactions. The intramolecular ET can occur first, forming the bent geometries in a sequential ET–PT reaction, or the ET and PT can occur concertedly. We were unable to model the sequential PT–ET reaction because we could not identify minimum-energy flat phlorin complexes. Similar behavior was found for **[1-H]**, as discussed below.

Electronic Structure of [1-H]. The electronic, geometric, and thermodynamic properties of the various charge and spin states of **[1-H]** are similar to those of **[3]**. The neutral $[\mathbf{1\text{-}H}]^{0}$ is a closed-shell singlet Ni(II) in the bent structure. Upon reduction to $[\mathbf{1\text{-}H}]^{-}$, the most stable structure is a doublet with a flat geometry and $\rho_{Ni} = 0.98$, indicating a Ni(I) species. Further reduction to $[\mathbf{1\text{-}H}]^{2-}$ preferentially yields a flat triplet Ni(I) porphyrin radical structure ($\rho_{Ni} = 1.02$). These results are consistent with the results for **[3]** in that the first reducing electron is localized on the metal center and the second reducing electron is localized on the ligand. The calculations imply that the *meso* carbon (position 20 in Fig. 1) is the most likely proton acceptor for intramolecular PT from the carboxylic acid of both $[\mathbf{1\text{-}H}]^{-}$ and $[\mathbf{1\text{-}H}]^{2-}$ and is particularly thermodynamically favorable for the dianionic species, with a reaction free energy of −18.4 kcal/mol (*SI Appendix*, Tables S5 and S6). The inclusion of a water bridge between the carboxylic acid and the metal center does not significantly alter the thermodynamic favorability of PT to the *meso* carbon. Thus, the present calculations indicate that a phlorin intermediate is required for H_2 evolution and that formation of a nickel-hydride is not thermodynamically favorable.

Analogous to the above analysis for **[3]**, PT reactions to the *meso* carbon in the flat Ni(I) anionic and dianionic **[1-H]** species are effectively intramolecular PCET reactions because they involve intramolecular ET from the nickel center to the ligand, forming a Ni(II) phlorin species. Again the intramolecular ET can occur first, forming the bent geometries, denoted $[\mathbf{1'\text{-}H}]^{-}$ and $[\mathbf{1'\text{-}H}]^{2-}$, in a sequential ET–PT reaction, or the ET and PT

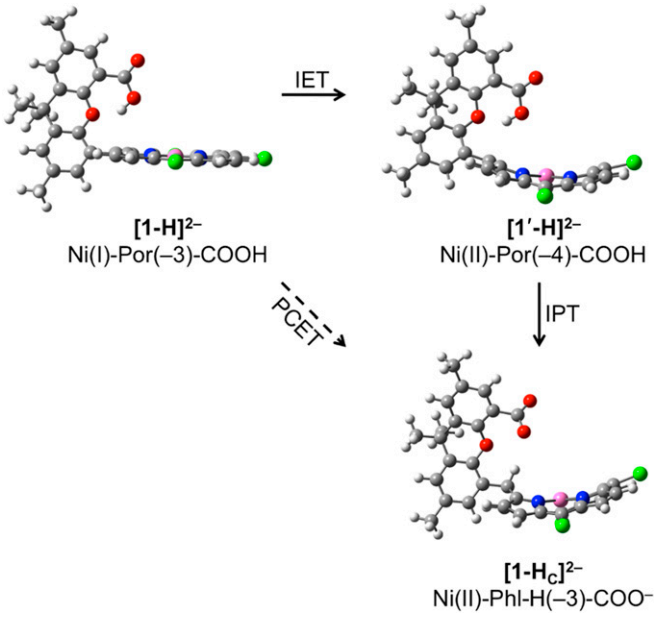

Fig. 2. Depiction of the structures for the intramolecular PCET reaction for **[1-H]**. The labels show the formal oxidation state of the nickel center and the porphyrin (Por) or phlorin (Phl-H), as well as the protonation state of the hanging carboxylic acid (COOH). The IET arrow includes a spin flip of the unpaired electron on the nickel of the flat triplet to generate the flat open-shell singlet $[\mathbf{1\text{-}H}]^{2-}$, followed by IET from the nickel to the porphyrin ring to produce the bent closed-shell singlet $[\mathbf{1'\text{-}H}]^{2-}$. The IPT arrow includes proton transfer from the carboxylic acid to the *meso* carbon to produce the bent closed-shell singlet $[\mathbf{1\text{-}H_C}]^{2-}$. The net PCET reaction is thermodynamically downhill by 18.4 kcal/mol.

can occur concertedly. Formation of the bent singlet $[\mathbf{1'\text{-}H}]^{2-}$ also requires a spin flip, analogous to **[3]**. Assuming the sequential ET–PT mechanism, we calculated the transition states associated with intramolecular PT from the hangman moiety to the closest *meso* carbon after intramolecular ET for both the anionic and dianionic complexes, producing $[\mathbf{1\text{-}H_C}]^{-}$ and $[\mathbf{1\text{-}H_C}]^{2-}$, respectively. Starting with the bent structures $[\mathbf{1'\text{-}H}]^{-}$ and $[\mathbf{1'\text{-}H}]^{2-}$, we calculated intramolecular PT free energy barriers of $\Delta G^{\ddagger}_{PT}$ = 16.3 kcal/mol and $\Delta G^{\ddagger}_{PT}$ = 6.1 kcal/mol, respectively. Using transition state theory, the corresponding PT rate constants are k_{PT} = 7.1 s^{-1} and $k_{PT} = 2.1 \times 10^{8}$ s^{-1}, respectively, at 298.15 K. On the basis of the relative free energy barriers to PT, the second reduction to produce the dianion is presumably necessary to enable intramolecular PT to form the phlorin. The PCET reaction for the dianion is depicted in Fig. 2.

In addition to the intramolecular PT that can occur within **[1-H]**, external acid can also be used to form a doubly protonated complex, denoted **[1-HH]**. For all charge states considered, protonation at the metal center forming a nickel-hydride is thermodynamically unfavorable compared with protonation at the *meso* carbon and carboxylate positions (*SI Appendix*, Table S10). This result suggests that regardless of acid strength, phlorin complexes will always be preferred over metal-hydrides, in contrast to the analogous cobalt complex that was hypothesized to evolve H_2 via a phlorin with weak acid and via a metal-hydride with strong acid (23).

Cyclic Voltammetry, Reduction Potentials, and pK_a Determinations. CVs recorded in acetonitrile for **[1-H]** and **[3]**, referenced to the standard reduction potential ferrocenium/ferrocene (Fc^{+}/Fc), are depicted in Fig. 3. As shown previously (21), CVs of **[3]** exhibit two reversible waves with midpoint potentials $E_{1/2}$ = –1.27 V and $E_{1/2}$ = –1.83 V, assigned to the reduction of $[\mathbf{3}]^{0}$ and $[\mathbf{3}]^{-}$, respectively. The CVs of **[1-H]** also exhibit two reversible waves with $E_{1/2}$ = –1.37 V and $E_{1/2}$ = –1.99 V, assigned to the reduction of $[\mathbf{1\text{-}H}]^{0}$ and $[\mathbf{1}]^{2-}$, respectively, as well as a central irreversible couple with peak potential E_p = –1.8 V. In the presence of benzoic acid (pK_a = 20.7) (26), the central irreversible wave of **[1-H]** and the second reversible wave of **[3]** become catalytic (Fig. 3 *A* and *C*). When titrated with tosic acid (pK_a = 8.0) (27), the first reversible waves of **[1-H]** and **[3]** become catalytic (Fig. 3 *B* and *D*). Bulk electrolysis of **[3]** with tosic acid at –1.2 V generated H_2 at 85% faradaic efficiency, similar to previous experiments of **[3]** with benzoic acid (21). These experiments suggest that H_2 evolution is catalyzed by **[1-H]** and **[3]** in benzoic acid and tosic acid, although H_2 could also be formed by other reduced macrocycles, such as Ni chlorin, Ni bacteriochlorin, or Ni isobacteriochlorin species. Using the initial $[\mathbf{1\text{-}H}]^{0}/[\mathbf{1\text{-}H}]^{-}$ reduction as a reference, reduction potentials calculated with DFT are given in Table 1 and *SI Appendix*, Table S11. Comparison with available experimental values for **[1-H]** and **[3]** lead to an average error of only 13 mV. This high level of agreement with experiment provides validation for the chosen computational methods.

Calculated pK_a's are required to complete the analysis of the HER mechanisms by **[1-H]** and **[3]**. Analysis of the experimental CVs generated in tosic acid and benzoic acid provides information about the pK_a's of certain protonated forms of **[3]** and **[1-H]** (see *SI Appendix* for details). On the basis of this analysis and calculations of absolute pK_a's, the pK_a of $[\mathbf{3}\text{-}\boldsymbol{H_C}]^{0}$ is estimated to be 15.0, where the italicized proton is removed. Using this value as a reference for additional calculations, the calculated pK_a's of $[\mathbf{3}\text{-}\boldsymbol{H_C}]^{-}$, $[\mathbf{1\text{-}H}\boldsymbol{H_C}]^{0}$, and $[\mathbf{1}\text{-}\boldsymbol{H}\mathbf{H_C}]^{-}$ are 35.9, 14.7, and 21.4, respectively. These computed values are consistent with the experimental values (*SI Appendix*, Table S12).

To provide more reliable pK_a's of $[\mathbf{1}\text{-}\boldsymbol{H}]^{0}$ and $[\mathbf{1}\text{-}\boldsymbol{H}]^{-}$, a second reference was used. To obtain this experimental value, we recorded

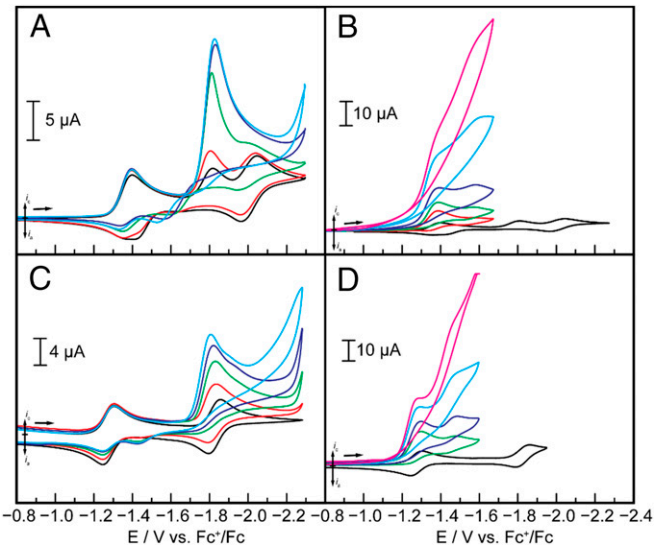

Fig. 3. Cyclic voltammetry of **[1-H]** and **[3]** in benzoic and tosic acids in 0.1 M $TBAPF_6$/acetonitrile electrolyte at a glassy carbon electrode with a scan rate of 0.1 V/s. (*A*) CVs of 0.3 mM **[1-H]** in the presence of 0 (black), 0.16 (red), 0.40 (green), 0.80 (dark blue), and 2.0 (light blue) mM benzoic acid. (*B*) CVs of 0.4 mM **[1-H]** in the presence of 0 (black), 0.40 (red), 1.0 (green), 2.0 (dark blue), 5.0 (light blue), and 10.0 (magenta) mM tosic acid. (*C*) CVs of 0.4 mM **[3]** in the presence of 0 (black), 0.20 (red), 0.40 (green), 0.80 (dark blue), and 2.0 (light blue) mM benzoic acid. (*D*) CVs of 0.4 mM **[3]** in the presence of 0 (black), 1.0 (green), 2.0 (dark blue), 5.0 (light blue), and 10.0 (magenta) mM tosic acid. Note that some CVs of **[1-H]** with benzoic acid (*A*) exhibit minor curve crossing, which is thought to be an artifact of background subtraction. No crossing is observed for the uncorrected CVs.

Table 1. Calculated reduction potentials

Oxidized species	Reduced species	E°
$[\mathbf{1\text{-}H}]^0$	$[\mathbf{1\text{-}H}]^-$	−1.37 (−1.37)*
$[\mathbf{1\text{-}H}]^-$	$[\mathbf{1\text{-}H}]^{2-}$	−1.85
$[\mathbf{1'\text{-}H}]^-$	$[\mathbf{1\text{-}H}]^{2-}$	−1.78
$[\mathbf{1\text{-}H}]^-$	$[\mathbf{1\text{-}H_C}]^{2-}$	−1.05
$[\mathbf{1\text{-}H_C}]^-$	$[\mathbf{1\text{-}H_C}]^{2-}$	−0.81
$[\mathbf{1\text{-}H_C}]^{2-}$	$[\mathbf{1\text{-}H_C}]^{3-}$	−1.96
$[\mathbf{1}]^-$	$[\mathbf{1}]^{2-}$	−1.40 (−1.42)†
$[\mathbf{1}]^{2-}$	$[\mathbf{1}]^{3-}$	−2.01 (−1.99)
$[\mathbf{3}]^0$	$[\mathbf{3}]^-$	−1.26 (−1.27)‡
$[\mathbf{3}]^-$	$[\mathbf{3}]^{2-}$	−1.83 (−1.83)‡
$[\mathbf{3}]^{2-}$	$[\mathbf{3}]^{3-}$	−2.61
$[\mathbf{1\text{-}HH_C}]^0$	$[\mathbf{1\text{-}HH_C}]^-$	−0.66
$[\mathbf{1\text{-}HH_C}]^-$	$[\mathbf{1\text{-}HH_C}]^{2-}$	−1.93
$[\mathbf{3\text{-}H_C}]^0$	$[\mathbf{3\text{-}H_C}]^-$	−0.59
$[\mathbf{3\text{-}H_C}]^-$	$[\mathbf{3\text{-}H_C}]^{2-}$	−1.86

Values given in volts vs. Fc^+/Fc in acetonitrile. Experimental values of $E_{1/2}$ are given in parentheses, as obtained from ref. 21. See *SI Appendix*, Table S11 for additional calculated values.

*$E_{1/2}([\mathbf{1\text{-}H}]^0/[\mathbf{1\text{-}H}]^-)$ was used as the reference and agrees by construction.

†Complex $[\mathbf{1}]^-$ is in the bent-down geometry, ∼2 kcal/mol lower in free energy than the corresponding bent-up structure.

‡Calculated values corrected from ref. 21.

CVs of $[\mathbf{1}]^-$ (generated by treatment with K_2CO_3) in acetonitrile with varying concentrations of benzoic acid. The CVs (*SI Appendix*, Fig. S1*A*) show that as the benzoic acid concentration is increased, the midpoint potential for the reversible first reduction wave shifts anodically from that of $[\mathbf{1}]^-$ (−1.42 V) to that of $[\mathbf{1\text{-}H}]^0$ (−1.37 V). Simulated fits of the experimental CVs yield an equilibrium constant of 17 ± 3 for protonation of the carboxylate group of $[\mathbf{1}]^-$ by benzoic acid, which corresponds to a pK_a of 21.9 ± 0.1 for $[\mathbf{1\text{-}}\boldsymbol{H}]^0$. The p$K_a$'s of other $[\mathbf{1\text{-}}\boldsymbol{H}]$ species with various charges and with the removed proton at various sites were calculated using this pK_a for $[\mathbf{1\text{-}}\boldsymbol{H}]^0$ as a reference. The pK_a's of $[\mathbf{1\text{-}}\boldsymbol{H}]^0$ and $[\mathbf{1\text{-}}\boldsymbol{H}]^-$ were subsequently used in the calculation of the free energy of H_2 self-elimination from $[\mathbf{1\text{-}HH_C}]^-$ and $[\mathbf{1\text{-}HH_C}]^{2-}$ with thermodynamic cycles. See *SI Appendix* for further details.

Hydrogen Evolution Mechanisms. The HER mechanisms for **[3]** can be deduced from the calculated reduction potentials, pK_a's, and relative free energies. For H_2 production with tosic acid and benzoic acid, the CVs show catalysis occurring at the $[\mathbf{3}]^0/[\mathbf{3}]^-$ couple (−1.27 V) and the $[\mathbf{3}]^-/[\mathbf{3}]^{2-}$ couple (−1.83 V), respectively (Fig. 3 *D* and *C*). Protonation of $[\mathbf{3}]^-$ by tosic acid is thermodynamically downhill by 9.5 kcal/mol. The resulting phlorin product, $[\mathbf{3\text{-}H_C}]^0$, is easily reduced to $[\mathbf{3\text{-}H_C}]^-$ at the $[\mathbf{3}]^0/[\mathbf{3}]^-$ potential. Reaction of $[\mathbf{3\text{-}H_C}]^-$ with tosic acid to eliminate H_2 is thermodynamically downhill by 4.8 kcal/mol, regenerating the neutral $[\mathbf{3}]^0$ catalyst. Unlike tosic acid, benzoic acid is unlikely to protonate $[\mathbf{3}]^-$ because it is thermodynamically uphill by 7.8 kcal/mol. Therefore, reduction to $[\mathbf{3}]^{2-}$ is required, consistent with the experimental CVs. Protonation of $[\mathbf{3}]^{2-}$ by benzoic acid to form $[\mathbf{3\text{-}H_C}]^-$ is thermodynamically downhill by 20.8 kcal/mol. Although H_2 production from $[\mathbf{3\text{-}H_C}]^-$ reacting with tosic acid is thermodynamically favorable, such a reaction is 12.5 kcal/mol uphill in free energy with benzoic acid. Therefore, an additional reduction from $[\mathbf{3\text{-}H_C}]^-$ to $[\mathbf{3\text{-}H_C}]^{2-}$ is necessary. The calculated reduction potential for this process, −1.86 V, is only slightly negative of the calculated $[\mathbf{3}]^-/[\mathbf{3}]^{2-}$ potential, indicating that such a mechanism is plausible. H_2 production from reaction of $[\mathbf{3\text{-}H_C}]^{2-}$ with benzoic acid is thermodynamically downhill by 1.3 kcal/mol, regenerating the monoanion $[\mathbf{3}]^-$. Thus, the HER mechanism for **[3]** is proposed to involve a phlorin intermediate for both weak and strong acids (*SI Appendix*, Fig. S2).

The proposed HER mechanisms for **[1-H]** are depicted in Fig. 4. First we focus on the mechanism with a weak acid, specifically benzoic acid. According to experiment, solutions of **[1-H]** and benzoic acid evolve H_2 at −1.8 V (Fig. 3*A*). After initial reduction to $[\mathbf{1\text{-}H}]^-$ (shown in purple brackets in Fig. 4), the following possible steps were determined to be unlikely on the basis of thermodynamics: an intramolecular PCET reaction to $[\mathbf{1\text{-}H_C}]^-$, which is thermodynamically unfavorable by 5.7 kcal/mol, and direct protonation to form $[\mathbf{1\text{-}HH_C}]^0$, which is thermodynamically unfavorable by 8.2 kcal/mol. The proposed mechanism in Fig. 4 indicates that $[\mathbf{1\text{-}H}]^-$ is electrochemically reduced to $[\mathbf{1\text{-}H}]^{2-}$, with a calculated $E^\circ = -1.85$ V, which is consistent with the experimentally measured $E_p = -1.8$ V. Note that we cannot rule out the possibility that $[\mathbf{1\text{-}H}]^-$ is reduced directly to $[\mathbf{1\text{-}H_C}]^{2-}$ in a concerted electrochemical PCET reaction, with a calculated standard reduction potential of $E^\circ = -1.05$ V; as discussed below, however, the simulated CVs support the $[\mathbf{1\text{-}H}]^-/[\mathbf{1\text{-}H}]^{2-}$ reduction step.

The subsequent intramolecular PCET reaction from $[\mathbf{1\text{-}H}]^{2-}$ to $[\mathbf{1\text{-}H_C}]^{2-}$ could occur concertedly (dotted diagonal line in Figs. 2 and 4), which is thermodynamically downhill by 18.4 kcal/mol, or sequentially via an ET–PT mechanism. The ET–PT mechanism starts with intramolecular ET, accompanied by a structural change in the porphyrin ring from flat to bent, with a reaction free energy $\Delta G^\circ_{ET} = 5.8$ kcal/mol, followed by intramolecular PT with a reaction free energy $\Delta G^\circ_{PT} = -24.2$ kcal/mol and a free energy barrier $\Delta G^{\ddagger}_{PT} = 6.1$ kcal/mol. The initial intramolecular ET reaction could be viewed as the electronic charge redistribution resulting from a thermal fluctuation that leads to the bent conformation of the porphyrin ring. These PCET steps could be explored further with theoretical methods that examine the relative rate constants for the sequential and concerted mechanisms (6).

Electrochemical reduction of $[\mathbf{1\text{-}H_C}]^{2-}$ to $[\mathbf{1\text{-}H_C}]^{3-}$ requires additional potential slightly beyond $E_p = -1.8$ V; however, protonation of the carboxylate group in $[\mathbf{1\text{-}H_C}]^{2-}$ by benzoic acid to form $[\mathbf{1\text{-}HH_C}]^-$ is thermodynamically favorable by 1.0 kcal/mol. H_2 production by reaction of $[\mathbf{1\text{-}HH_C}]^-$ with benzoic acid is thermodynamically unfavorable by 8.1 kcal/mol, and H_2 self-elimination is thermodynamically unfavorable by 9.7 kcal/mol. Reduction to $[\mathbf{1\text{-}HH_C}]^{2-}$, which occurs at a calculated standard potential of −1.93 V, is therefore likely to occur before H_2 production. Reduction of $[\mathbf{1\text{-}HH_C}]^-$ is compatible with the experimentally measured $E_p = -1.8$ V because of the anodic shifting that can occur as a result of subsequent catalytic steps, as supported by simulated CVs (discussed below). H_2 production by reaction of $[\mathbf{1\text{-}HH_C}]^{2-}$ with benzoic acid is thermodynamically favorable by 4.9 kcal/mol, and self-elimination of H_2 is thermodynamically favorable by 2.4 kcal/mol. Self-elimination may be favored by the structural proximity of the two hydrogen nuclei, which are separated by 1.89 Å. For the self-elimination mechanism, the cycle is completed by reprotonation of the carboxylate of $[\mathbf{1}]^{2-}$, reforming $[\mathbf{1\text{-}H}]^-$ (shown in purple brackets in Fig. 4).

Next we explore the HER mechanism in strong acid. Solutions of **[1-H]** and tosic acid catalyze H_2 production at the $[\mathbf{1\text{-}H}]^0/[\mathbf{1\text{-}H}]^-$ potential of −1.37 V (Fig. 3*B*). Protonation of $[\mathbf{1\text{-}H}]^-$ with tosic acid directly yields $[\mathbf{1\text{-}HH_C}]^0$ with $\Delta G^\circ_{PT} = -9.1$ kcal/mol. As discussed above, the DFT calculations indicate that $[\mathbf{1\text{-}H}]^-$ is flat and $[\mathbf{1\text{-}HH_C}]^0$ is bent, implying that such protonation also requires a structural change of the porphyrin ring from flat to bent and the accompanying intramolecular ET from the Ni center to the porphyrin ring. At the catalytic potential of −1.37 V, $[\mathbf{1\text{-}HH_C}]^0$ is easily reduced to $[\mathbf{1\text{-}HH_C}]^-$. H_2 production by reaction of $[\mathbf{1\text{-}HH_C}]^-$ with tosic acid is thermodynamically favorable by 9.2 kcal/mol, forming the original $[\mathbf{1\text{-}H}]^0$ complex (shown in green brackets in Fig. 4). Flowcharts depicting all of the possible elementary steps toward H_2 evolution are shown in *SI Appendix*, Figs. S3 and S4.

We emphasize that the quantitative free energy differences are expected to exhibit errors on the order of ∼3 kcal/mol from a

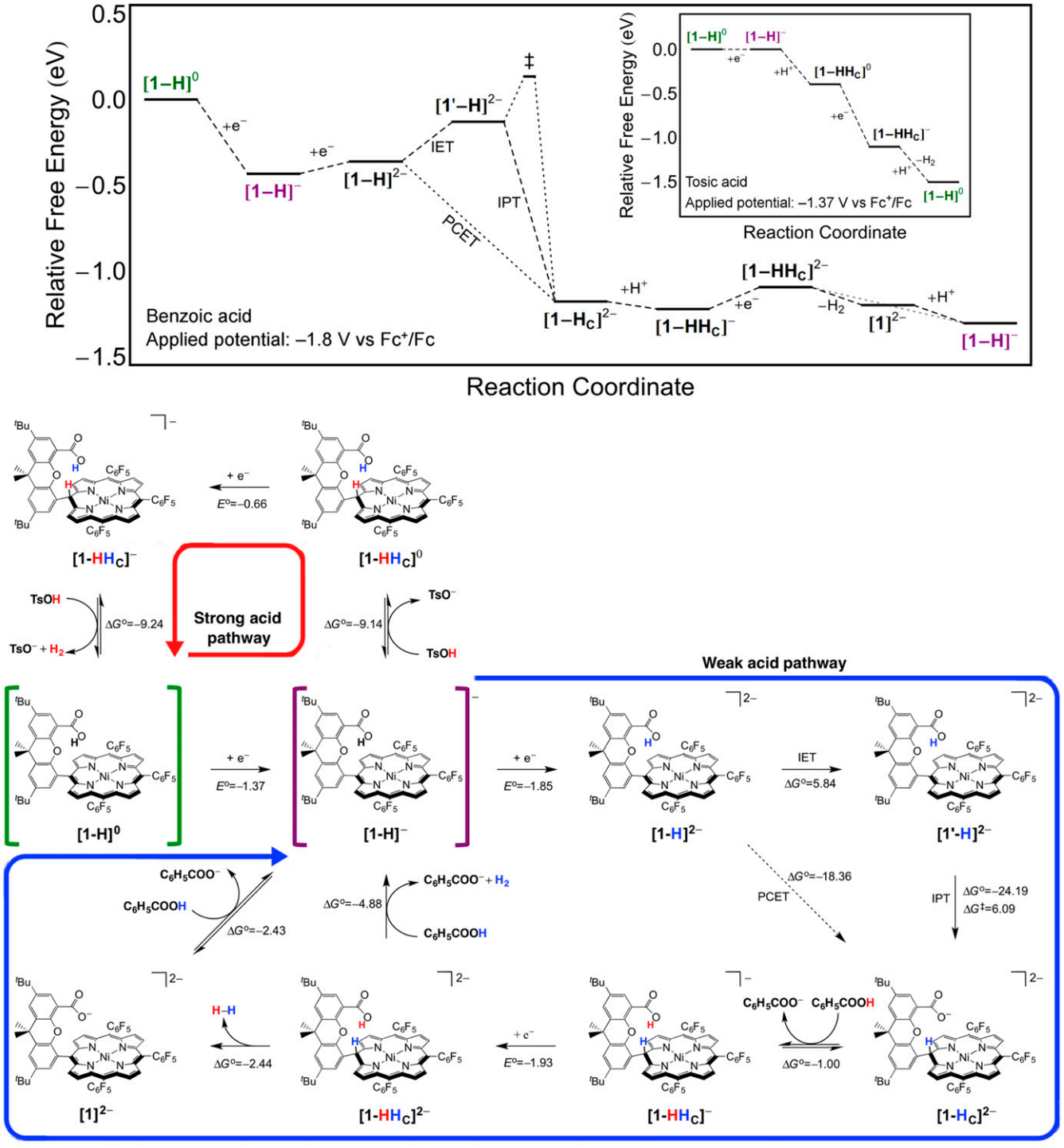

Fig. 4. Free energy diagrams (*Top*) for H_2 production catalyzed by **[1-H]** with benzoic acid (C_6H_5COOH, $pK_a = 20.7$) and an applied potential of –1.8 V vs. Fc^+/Fc and tosic acid (TsOH, $pK_a = 8.0$) with an applied potential of –1.37 V vs. Fc^+/Fc (*Inset*). The chosen applied potentials, which define the zero for the free energy changes associated with reduction steps, correspond to the peaks of the catalytic waves in the CVs. Complete mechanistic cycle of proposed mechanisms (*Bottom*), starting from $[\mathbf{1\text{-}H}]^0$ (shown in green brackets). Reduction potentials are listed in volts vs. Fc^+/Fc, and free energies are listed in kcal/mol. Proposed cycles in strong (red arrow) and weak (blue arrow) acid regimes begin with reduction to $[\mathbf{1\text{-}H}]^-$ (shown in purple brackets). With benzoic (weak) acid, additional reduction is required to form $[\mathbf{1\text{-}H}]^{2-}$. The subsequent intramolecular PCET step is thermodynamically favorable and can occur either concertedly (dotted line) or sequentially via intramolecular ET from the nickel to the porphyrin to form the bent structure $[\mathbf{1'\text{-}H}]^{2-}$ followed by intramolecular PT to produce the phlorin $[\mathbf{1\text{-}H_C}]^{2-}$. Protonation from benzoic acid at the carboxylate forms $[\mathbf{1\text{-}HH_C}]^-$, which is subsequently reduced. H_2 is evolved from $[\mathbf{1\text{-}HH_C}]^{2-}$, either via self-elimination to the deprotonated $[\mathbf{1}]^{2-}$ or by reaction with benzoic acid, forming $[\mathbf{1\text{-}H}]^-$. With tosic (strong) acid, protonation of $[\mathbf{1\text{-}H}]^-$ yields the phlorin $[\mathbf{1\text{-}HH_C}]^0$, which is rapidly reduced at the operating potential. The phlorin formation involves an analogous PCET step as shown for the weak acid pathway, but it is not shown explicitly for the strong acid pathway. H_2 is evolved by reaction of $[\mathbf{1\text{-}HH_C}]^-$ with tosic acid, forming the neutral $[\mathbf{1\text{-}H}]^0$. Note that other branches leading to Ni chlorin, Ni bacteriochlorin, and Ni isobacteriochlorin species are not shown but may be thermodynamically favorable and possibly nonproductive toward H_2 catalysis.

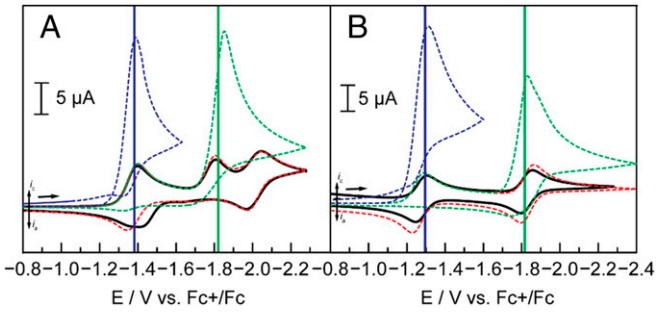

Fig. 5. Experimental (black curve) and simulated (dotted curves) CVs of (*A*) 0.34 mM **[1-H]** and (*B*) 0.30 mM **[3]**. The simulated curves correspond to the reaction in the absence of external acid (red curve), in the presence of 1 mM tosic acid (blue curve), or in the presence of 1 mM benzoic acid (green curve). The vertical lines correspond to the experimentally measured catalytic peak positions for tosic acid (blue line) or benzoic acid (green line). Parameters used for simulations are tabulated in *SI Appendix*, Tables S13 and S14.

combination of factors such as the puckering of the porphyrin, the side for protonation by external acid, the DFT functional and basis set, the pK_a references, and the replacement of the *tert*-butyl and pentafluorophenyl groups, which could lead to minor structural differences. For example, calculation of the relative free energies of the species depicted in Fig. 2 with the pentafluorophenyl groups indicates that the free energies differences are the same to within 2.4 kcal/mol. The qualitative mechanistic insights, however, are expected to be insensitive to these factors, as shown by the agreement of the CV simulations with the experimental data and the experimental detection of the theoretically predicted phlorin intermediate discussed below.

Cyclic Voltammetry Simulations. To support the validity of the computed HER mechanisms proposed above, CV simulations were performed for **[1-H]** and **[3]** in the absence of acid and in the presence of tosic and benzoic acids (Fig. 5). Reduction potentials for all electrochemical ET steps in the simulations were fixed at the values computed using DFT, and the equilibrium constants for all homogeneous chemical steps were based on differences in calculated reduction potentials, pK_a's, and thermodynamic cycles for H_2 generation (*SI Appendix*, Tables S13 and S14). These parameters were not fit to the experimental data, although slight refinement would improve the agreement between the simulated and experimental CVs. The simulated CV of **[1-H]** in the absence of external acid (red dotted curve in Fig. 5*A*) shows reasonable agreement with the experimental CV (solid black curve), because it reproduces most of the CV features at appropriate peak potentials. The simulated mechanism assumed two consecutive reductions to $\mathbf{[1\text{-}H]^{2-}}$, followed by sequential intramolecular ET–PT to the phlorin $\mathbf{[1\text{-}H_C]^{2-}}$. Reprotonation of the carboxylate is assumed to occur by neutral $\mathbf{[1\text{-}H]^0}$ in solution in the absence of external acid. Note that the large shoulder on the return scan for the Ni(II/I) couple is not reproduced in the simulated CV. This discrepancy is likely due to the use of the calculated –1.40 V value for the $\mathbf{[1]^-/[1]^{2-}}$ reduction potential, which is too close to the $\mathbf{[1\text{-}H]^0/[1\text{-}H]^-}$ potential of –1.37 V to be properly resolved in the simulation. Previous simulations that did capture the shoulder did so by leaving the $\mathbf{[1]^-/[1]^{2-}}$ potential as a free parameter, resulting in a value of –1.45 V for the couple (21). A difference of 0.05 V is within the accuracy of the DFT calculations, and all other CV features are well reproduced using the DFT results.

The CV simulations of **[1-H]** in the presence of tosic acid or benzoic acid assumed the mechanisms depicted in Fig. 4. The blue dotted curve in Fig. 5*A* shows the simulation when the concentration of tosic acid is set to 1 mM, corresponding to the proposed mechanism for strong acid in Fig. 4 (red arrow). The large increase in current at the $\mathbf{[1\text{-}H]^0/[1\text{-}H]^-}$ reduction potential is consistent with the experimental observation of catalytic H_2 generation at that potential (Fig. 3*B*). The green dotted curve in Fig. 5*A* shows the simulation when the concentration of benzoic acid is set to 1 mM, corresponding to the proposed mechanism for weak acid in Fig. 4 (blue arrow). H_2 is evolved via protonation of $\mathbf{[1\text{-}HH_C]^{2-}}$ or by self-elimination, necessitating reduction of $\mathbf{[1\text{-}HH_C]^-}$ at a calculated standard reduction potential of E^o = –1.93 V. The simulated CV exhibits a large increase in current near the central irreversible peak (E_p = –1.8 V), which again is consistent with experimental results (Fig. 3*A*) despite the more negative calculated reduction potential for the $\mathbf{[1\text{-}HH_C]^-/[1\text{-}HH_C]^{2-}}$ couple. A similar level of agreement between the CV simulations and the experimentally generated CVs was found for **[3]** in the presence of tosic acid or benzoic acid (Fig. 5*B*). All of the CV simulations presented in Fig. 5 neglected the possibility of concerted intramolecular PCET; however, alternative simulations that included this possibility both exclusively as well as in addition to the stepwise pathway all agreed with the experimental data to the same extent. Thus, the CV simulations were not able to distinguish between the concerted and sequential intramolecular PCET mechanisms.

We emphasize that the CV simulations for **[1-H]** required a total of 38 parameters: 20 were fixed to the DFT results without any adjustment, 4 were assumed to be diffusion limited, 4 were obtained from experimental trumpet plots, and the remaining 10 corresponded to rate constants that were not available via DFT and therefore were adjusted to fit the experimental CVs. Upon simulation of the CVs, the rate constants used as free parameters were confirmed to correspond to physically reasonable values, and those that did not depend on the external acid were constrained to be the same for all acids studied. Although these CV simulations do not definitively prove the validity of the mechanistic cycles proposed in this study, they do demonstrate their plausibility compared with experimental results.

Spectroelectrochemical Observation of Nickel Phlorin Anion. To experimentally observe phlorin formation from a nickel porphyrin, thin-layer UV-visible spectroelectrochemical experiments were carried out using complex **[3]** in acetonitrile. When no potential is applied, the absorption spectrum of the neutral Ni(II) porphyrin $\mathbf{[3]^0}$ is observed (black curve in Fig. 6*A*), with the most notable features being two well-resolved Q bands at 520 and 555 nm. When a potential at –1.3 V is applied, the spectrum of $\mathbf{[3]^-}$ (red curve) is observed, featuring a lower intensity of the Q bands and the appearance of new peaks at 608 and 841 nm, which are typical for one-electron reduced nickel porphyrins (28–30).

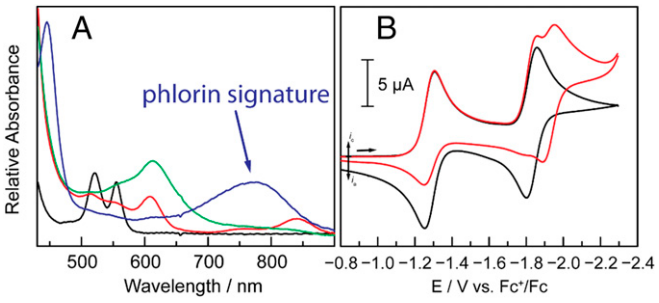

Fig. 6. (*A*) Absorption spectra of **[3]** acquired using thin-layer spectroelectrochemistry in 0.1 M $TBAPF_6$/acetonitrile electrolyte. Spectra taken before electrolysis (black), after electrolysis at –1.3 V vs. Fc^+/Fc (red), after electrolysis at –1.9 V vs. Fc^+/Fc in the absence of external acid (green), and after electrolysis at –1.9 V vs. Fc^+/Fc in the presence of 10 mM phenol (blue). (*B*) CVs of 0.4 mM of **[3]** without acid (black curve) and in the presence of 1 mM phenol (red curve).

The spectrum observed when a potential of *ca.* –1.9 V is applied in the absence of acid is characterized by the appearance of a broader, slightly more intense band at 613 nm (green curve), with no absorption bands observed in the near-infrared, and it is therefore assigned to the doubly reduced Ni porphyrin $[\mathbf{3}]^{2-}$. However, when phenol (pK_a = 29.1) (31) is added and a potential of *ca.* –1.9 V is applied, a very broad peak centered at 769 nm is observed (blue curve). This peak is consistent with the spectral features reported for metallophlorins (32, 33), including those of nickel phlorins (30).

Phenol is strong enough to protonate $[\mathbf{3}]^{2-}$ with ΔG^{o}_{PT} = –9.3 kcal/mol; however, the generation of H_2 from $[\mathbf{3\text{-}H_C}]^{2-}$ with phenol is calculated to be thermodynamically uphill by 10.2 kcal/mol. These calculations suggest that a buildup of a phlorin intermediate should occur under these conditions and therefore be detectable via spectroelectrochemical methods. This buildup of phlorin intermediate is confirmed by the CV of **[3]** and phenol (Fig. 6*B*), in which a peak tentatively assigned to the phlorin reduction $[\mathbf{3\text{-}H_C}]^{-}$/ $[\mathbf{3\text{-}H_C}]^{2-}$ is observed at $E_{1/2}$ = –1.92 V (calculated to be E^{o} = –1.86 V) without H_2 evolution. The UV-visible spectrum provides strong evidence for the phlorin intermediate predicted by our previous computational study of the analogous cobalt hangman porphyrins, as well as the current computational results for the nickel porphyrins.

Conclusions

In this paper, DFT calculations were used to propose mechanisms for H_2 evolution by molecular electrocatalysts **[3]** and **[1-H]** in the presence of weak or strong acid. For **[1-H]** in weak acid, the catalytic pathway begins with two electrochemical reduction steps: First the nickel center is reduced and then the porphyrin ring is reduced. The next step is a PCET reaction that could occur either concertedly or via a sequential ET–PT mechanism, in which intramolecular ET from the nickel to the porphyrin ring is accompanied by a structural change in the porphyrin ring from flat to bent, followed by intramolecular PT from the carboxylic acid to the *meso* carbon of the porphyrin. The net PCET reaction, which results in a phlorin dianion, is thermodynamically favorable, as is the subsequent reprotonation of the carboxylate by the acid. Following another electrochemical reduction, which further reduces the phlorin ring, H_2 evolution via either self-elimination or reaction with the acid is thermodynamically favorable. For **[1-H]** in strong acid, the catalytic pathway begins with only a single electrochemical reduction step, which reduces the nickel, followed by a PCET reaction composed of intramolecular ET from the nickel to the porphyrin ring and protonation of the *meso* carbon by the acid, resulting in a neutral phlorin. Following another electrochemical reduction, which produces a phlorin anion, H_2 evolution via reaction with the acid is thermodynamically favorable. The HER mechanisms for **[3]**, which lacks the carboxylic acid hanging group, are analogous in weak and strong acid except that the *meso* carbon is protonated by external acid rather than by the carboxylic acid hanging group in weak acid.

Further support for the proposed mechanisms is provided by a comparison of CV simulations to experimentally generated CVs. For the CV simulations, 20 out of the 38 parameters (*SI Appendix*, Table S13) were fixed to values obtained from DFT calculations of reduction potentials and pK_a's, as well as reaction free energies and free energy barriers for intramolecular PT. Eight of the remaining parameters were fixed on other grounds, and only the remaining 10 parameters were adjusted. The resulting CV simulations are in good agreement with the experimentally generated CVs for **[1-H]** and **[3]** in the absence of acid and in the presence of benzoic acid or tosic acid. In particular, the catalytic peaks are all found to be within 0.03 V of the experimental peaks. This level of agreement provides compelling support for the proposed mechanisms.

These proposed mechanisms are unusual in that the active species for H_2 evolution is a phlorin instead of a metal-hydride, which has been presumed to be the active species for most other H_2-evolving molecular electrocatalysts. According to the proposed mechanisms, the C–H bond in the phlorin behaves similarly to the more traditional metal-hydride, and H^- can react with acid or with the carboxylic acid of the hanging group to produce H_2. The possibility of an active phlorin intermediate was first proposed for the analogous cobalt hangman H_2 evolution catalysts (23). More recently, metallophlorin species have been suggested as intermediates in the electocatalytic generation of H_2 by copper and palladium porphyrins (24). The present work indicates that phlorin formation is also structurally and thermodynamically favored over metal-hydride formation for the nickel hangman catalysts. Specifically, considering PT from the carboxylic acid group of $[\mathbf{1\text{-}H}]^{2-}$, the PT donor–acceptor distance is shorter by 0.78 Å for PT to the *meso* carbon of the porphyrin than to the nickel center, and the reaction free energy is −18.4 kcal/mol for PT to the *meso* carbon and 5.4 kcal/mol for PT to the nickel center. Note that storing formal hydride equivalents at carbon centers is also used in other chemical and biological processes, such as reactions involving the reduction of NAD^+ (nicotinamide adenine dinucleotide) to generate NADH (34, 35), and it has been demonstrated that the heterolytic bond dissociation energy of the C4–H bond in NADH derivatives is considerably smaller than those of typical sp^3 C–H bonds (36). However, the nickel hangman porphyrin catalysts are uncommon in exhibiting an implied preference for protonating a carbon over a metal center, suggesting that the metal's role is to influence the energetics and conformation of the porphyrin rather than serving as a site of protonation. This lack of metal protonation also raises the possibility of H_2 electrocatalysis from free-base porphyrins that contain no coordinated metal.

In addition, the present work provides experimental evidence for a phlorin intermediate through spectroelectrochemical measurements of **[3]** in the presence of phenol, which according to our calculations can protonate the *meso* carbon of $[\mathbf{3}]^{2-}$ without evolving H_2. The spectroelectrochemical measurements at an applied potential expected to produce the dianion $[\mathbf{3}]^{2-}$ show the buildup up of a species with spectroscopic features that are in agreement with those reported by Kadish and coworkers (30) for nickel phlorin anions produced via the protonation of electrogenerated Ni(II) porphyrin dianions. This spectral observation provides strong experimental evidence for the feasibility of stable phlorin formation from the nickel complexes studied in this work. Although a phlorin intermediate has been detected experimentally for **[3]**, it has not yet been shown experimentally to produce H_2 under acidic conditions. Production of H_2 could require additional protonation and reduction steps, and other possibly nonproductive pathways leading to Ni chlorin, Ni bacteriochlorin, and Ni isobacteriochlorin species could occur. Future experimental and theoretical work will be needed to fully characterize the phlorin intermediate and investigate additional potential mechanisms, as well as explore the possibility of catalysis from free-base porphyrins. The ability to store reducing equivalents within porphyrins through phlorin intermediates holds the potential for unique chemistry and has significant implications for the design of effective catalysts for other energy conversion processes.

Computational and Experimental Methods

DFT calculations were performed with the Gaussian 09 program and a double-ζ basis set with polarization and diffuse functions (37). Geometry optimizations were performed with implicit acetonitrile solvent using the conductor-like polarizable continuum method. The *tert*-butyl and pentafluorophenyl groups were truncated to methyl and chlorine groups, respectively, for computational tractability. After benchmarking with seven different functionals (*SI Appendix*, Tables S1–S3), B3P86 (38, 39) was used for the full analysis for consistency with our previous work (21). Long-range corrected functionals may be more accurate for determining electron localization upon reduction but gave similar results in the benchmarking. Note that the open-shell singlet states contain significant spin contamination and therefore are not considered reliable

(*SI Appendix*, Table S3), but spin contamination in the calculated triplet states was found to be negligible. Restricted open-shell DFT or other higher-level ab initio calculations could be used to explore the relative energies among different spin states more accurately.

Reduction potentials and pK_a's were calculated in acetonitrile with respect to experimental references. All reduction potentials were calculated relative to the experimentally determined half-wave potential ($E_{1/2}$) for the reversible $[1\text{-H}]^0/[1\text{-H}]^-$ couple vs. Fc^+/Fc in acetonitrile and are considered to be standard reduction potentials E°. Comparison with peak potentials is therefore approximate due to experimental conditions that affect peak position. See *SI Appendix* for additional computational details and benchmarking.

Electrochemical measurements were performed in a nitrogen-atmosphere glovebox. All CVs were background-corrected, recorded at room temperature with iR compensation, and referenced the Fc^+/Fc couple using an internal standard. Bulk electrolysis was performed in a gas-tight electrochemical cell; the amount of H_2 gas produced in the headspace was analyzed by gas chromatography. Thin-layer spectroelectrochemistry experiments were performed as above in a 0.5-mm path length quartz cuvette. CVs were simulated with the DigiElch 7 software (40). The parameters used in data fitting were set to experimental and theoretical values. See *SI Appendix* for additional experimental details.

ACKNOWLEDGMENTS. We thank Ryan Murphy and Christopher Lemon for providing complex **[3]** and Guillaume Passard, Soumya Ghosh, and Mioy Huynh for useful discussions. B.H.S. is grateful to the Alexander von Humboldt Foundation for postdoctoral support during the writing of this paper. The computational work was supported by Center for Chemical Innovation of the National Science Foundation Solar Fuels Grant CHE-1305124 (to B.H.S. and S.H.-S.). This work was also supported by US Department of Energy Office of Science, Office of Basic Energy Sciences Energy Frontier Research Centers program Award DE-SC0009758 (to A.G.M., D.K.D., and D.G.N.).

1. Lewis NS, Nocera DG (2006) Powering the planet: Chemical challenges in solar energy utilization. *Proc Natl Acad Sci USA* 103(43):15729–15735.
2. Nocera DG (2009) Chemistry of personalized solar energy. *Inorg Chem* 48(21):10001–10017.
3. Schneider J, Jia H, Muckerman JT, Fujita E (2012) Thermodynamics and kinetics of CO_2, CO, and H^+ binding to the metal centre of CO_2 reduction catalysts. *Chem Soc Rev* 41(6):2036–2051.
4. Costentin C, Robert M, Savéant J-M (2013) Catalysis of the electrochemical reduction of carbon dioxide. *Chem Soc Rev* 42(6):2423–2436.
5. Hammes-Schiffer S (2012) Proton-coupled electron transfer: Classification scheme and guide to theoretical methods. *Energy Environ Sci* 5:7696–7703.
6. Hammes-Schiffer S (2015) Proton-coupled electron transfer: Moving together and charging forward. *J Am Chem Soc* 137(28):8860–8871.
7. Cukier RI (1996) Proton-coupled electron transfer reactions: Evaluation of rate constants. *J Phys Chem* 100:15428–15443.
8. Mayer JM (2004) Proton-coupled electron transfer: A reaction chemist's view. *Annu Rev Phys Chem* 55:363–390.
9. Huynh MHV, Meyer TJ (2007) Proton-coupled electron transfer. *Chem Rev* 107(11): 5004–5064.
10. Hammes-Schiffer S, Soudackov AV (2008) Proton-coupled electron transfer in solution, proteins, and electrochemistry. *J Phys Chem B* 112(45):14108–14123.
11. Hammes-Schiffer S, Stuchebrukhov AA (2010) Theory of coupled electron and proton transfer reactions. *Chem Rev* 110(12):6939–6960.
12. Wilson AD, et al. (2007) Nature of hydrogen interactions with Ni(II) complexes containing cyclic phosphine ligands with pendant nitrogen bases. *Proc Natl Acad Sci USA* 104(17):6951–6956.
13. Barton BE, Rauchfuss TB (2008) Terminal hydride in [FeFe]-hydrogenase model has lower potential for H_2 production than the isomeric bridging hydride. *Inorg Chem* 47(7):2261–2263.
14. DuBois DL, Bullock RM (2011) Molecular electrocatalysts for the oxidation of hydrogen and the production of hydrogen – The role of pendant amines as proton relays. *Eur J Inorg Chem* (7):1017–1027.
15. O'Hagan M, et al. (2011) Moving protons with pendant amines: Proton mobility in a nickel catalyst for oxidation of hydrogen. *J Am Chem Soc* 133(36):14301–14312.
16. Horvath S, Fernandez LE, Soudackov AV, Hammes-Schiffer S (2012) Insights into proton-coupled electron transfer mechanisms of electrocatalytic H_2 oxidation and production. *Proc Natl Acad Sci USA* 109(39):15663–15668.
17. Dempsey JL, Brunschwig BS, Winkler JR, Gray HB (2009) Hydrogen evolution catalyzed by cobaloximes. *Acc Chem Res* 42(12):1995–2004.
18. Small YA, DuBois DL, Fujita E, Muckerman JT (2011) Proton management as a design principle for hydrogenase-inspired catalysts. *Energy Environ Sci* 4:3008–3020.
19. Kaeffer N, Chavarot-Kerlidou M, Artero V (2015) Hydrogen evolution catalyzed by cobalt diimine-dioxime complexes. *Acc Chem Res* 48(5):1286–1295.
20. Lee CH, Dogutan DK, Nocera DG (2011) Hydrogen generation by hangman metalloporphyrins. *J Am Chem Soc* 133(23):8775–8777.
21. Bediako DK, et al. (2014) Role of pendant proton relays and proton-coupled electron transfer on the hydrogen evolution reaction by nickel hangman porphyrins. *Proc Natl Acad Sci USA* 111(42):15001–15006.
22. Roubelakis MM, Bediako DK, Dogutan DK, Nocera DG (2012) Proton-coupled electron transfer kinetics for the hydrogen evolution reaction of hangman porphyrins. *Energy Environ Sci* 5:7737–7740.
23. Solis BH, et al. (2014) Theoretical analysis of cobalt hangman porphyrins: Ligand dearomatization and mechanistic implications for hydrogen evolution. *ACS Catal* 4:4516–4526.
24. Sirbu D, Turta C, Gibson EA, Benniston AC (2015) The ferrocene effect: Enhanced electrocatalytic hydrogen production using meso-tetraferrocenyl porphyrin palladium(II) and copper(II) complexes. *Dalton Trans* 44(33):14646–14655.
25. Fedorov DG, Koseki S, Schmidt MW, Gordon MS (2003) Spin-orbit coupling in molecules: Chemistry beyond the adiabatic approximation. *Int Rev Phys Chem* 22(3):551–592.
26. Fourmond V, Jacques P-A, Fontecave M, Artero V (2010) H_2 evolution and molecular electrocatalysts: Determination of overpotentials and effect of homoconjugation. *Inorg Chem* 49(22):10338–10347.
27. Hu X, Brunschwig BS, Peters JC (2007) Electrocatalytic hydrogen evolution at low overpotentials by cobalt macrocyclic glyoxime and tetraimine complexes. *J Am Chem Soc* 129(29):8988–8998.
28. Lexa D, Momenteau M, Mispelter J, Savéant J-M (1989) Does one-electron transfer to nickel(ii) porphyrins involve the metal or the porphyrin ligand? *Inorg Chem* 28(1): 30–35.
29. Kadish KM, Franzen MM, Han BC, Araullo-McAdams C, Sazou D (1991) Factors determining the site of electroreduction in nickel metalloporphyrins. Spectral characterization of Ni(I) porphyrins, Ni(II) porphyrin π-anion radicals, and Ni(II) porphyrin π-anion radicals with some Ni(I) character. *J Am Chem Soc* 113(2):512–517.
30. Fang Y, et al. (2015) Electrochemical and spectroelectrochemical studies of diphosphorylated metalloporphyrins. Generation of a phlorin anion product. *Inorg Chem* 54(7):3501–3512.
31. Kütt A, et al. (2008) Pentakis(trifluoromethyl)phenyl, a sterically crowded and electron-withdrawing group: synthesis and acidity of pentakis(trifluoromethyl)benzene, -toluene, -phenol, and -aniline. *J Org Chem* 73(7):2607–2620.
32. Lanese JG, Wilson GS (1972) Electrochemical studies of zinc tetraphenylporphin. *J Electrochem Soc* 119(8):1039–1043.
33. Kadish KM, et al. (1987) Electrochemical and spectroelectrochemical studies of nickel(II) porphyrins in dimethylformamide. *Inorg Chem* 27(7):1198–1204.
34. Belenky P, Bogan KL, Brenner C (2007) NAD^+ metabolism in health and disease. *Trends Biochem Sci* 32(1):12–19.
35. Pollak N, Dölle C, Ziegler M (2007) The power to reduce: Pyridine nucleotides–small molecules with a multitude of functions. *Biochem J* 402(2):205–218.
36. Zhu X-Q, et al. (2003) Determination of the C4-H bond dissociation energies of NADH models and their radical cations in acetonitrile. *Chemistry* 9(4):871–880.
37. Frisch MJ, et al. (2009) Gaussian 09. *Revision* C:1.
38. Perdew JP (1986) Density-functional approximation for the correlation energy of the inhomogeneous electron gas. *Phys Rev B Condens Matter* 33(12):8822–8824.
39. Becke AD (1993) Density-functional thermochemistry. III. The role of exact exchange. *J Chem Phys* 98(7):5648–5652.
40. Rudolph M (2003) Digital simulations on unequally spaced grids. Part 2. Using the box method by discretisation on a transformed equally spaced grid. *J Electroanal Chem* 543(1):23–29.